Trans-ruthenium(II) complexes for photoactivated cChemotherapy: from design to anticancer activity

Verbeet, W.

Appendix I: General methods

I.1 Photoreactor for synthesis of dissymmetric complexes

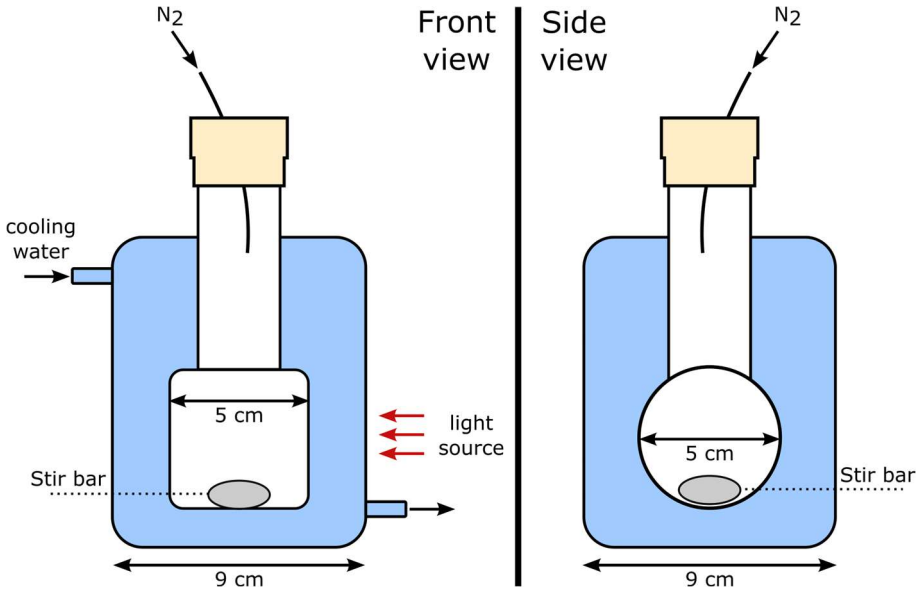

Figure I.1 Schematic representation of water-cooled photoreactor.

I.2 Photochemistry

I.2.1 Determination of molar extinction coefficients

The molar extinction coefficients (ε) of the reported compounds were determined according to the following procedure. Three stock samples of the compound were prepared with a known mass. Following dissolution in the same solvent used for absorbance experiments, the UV-Vis absorbance spectra between 200 and 800 nm were measured for 5 dilutions of each stock solution at 25 °C. Linear regression of the maximum absorbance at the ^{1}MLCT band of every measurement provided the molar extinction coefficient according to the Lambert-Beer law.

I.2.2 Actinometry

According to standard protocol, ferrioxalate actinometry was used to determine the photon flux (in mol/s) of the blue (λ_{irr} = 435 nm) and green (λ_{irr} = 505 nm) LEDs used in this work.[1,2] In short, the cuvette used for the photoreactions was charged freshly prepared solution of $K_3Fe(C_2O_4)_3 \cdot 3\ H_2O$ (3 mL, 150 mM in 50 mM H_2SO_4). The solution was stirred for 2 minutes at 25 °C to ensure thermal stability, followed by irradiation (vertical beam, pathlength = 3

cm) for a given time. A portion of the irradiated sample (2 mL) was transferred to a 10 mL volumetric flask containing an aqueous solution of 1,10-phenanthroline (4 mL, 5.55 mM) and 1 ml of a solution of glacial acetic acid (1.76 M), sodium hydroxide (0.71 mM) and sodium sulfate (0.53 mM). After filling the volumetric flask to 10 mL, the absorbance spectrum of the resulting ferrous tris-1,10-phenanthroline $[Fe(phen)_3]^{2+}$ solution was measured by UV-Vis spectroscopy. With the absorbance at 510 nm and the molar absorption coefficient (ε = 11500 $M^{-1}cm^{-1}$) for $[Fe(phen)_3]^{2+}$ in water, the amount of formed Fe^{2+} after irradiation of a given time ($d[Fe^{2+}]/dt$) could be calculated. This slope (as visualized in Figure I.2) was then used to calculate the photon flux (ϕ) of the respective LEDs with equation I.1:

$$\varphi = \frac{d[Fe^{2+}]}{dt\left(1-10^{-A_{ref}}\right)\varphi_{ref}} \qquad (I.1)$$

in which $\left(1-10^{-A_{ref}}\right)$ is the photon absorption probability of the solution and φ_{ref} is the reference quantum yield at the irradiated wavelength of the ferrioxalate actinometer to generate Fe^{2+}.[1] Since the length of the vertical irradiation beam pathway is 3 cm, A_{ref} equals $A'_{ref} \times 3$ where A'_{ref} is the absorbance of the non-irradiated actinometer $K_3Fe(C_2O_4)_3 \cdot 3H_2O$ (150 mM in 50 mM H_2SO_4) at the irradiation wavelength of the LED, measured in a cuvette with a 1 cm pathlength. Using equation II.1, ϕ was 307.6 nmol/s for the 435 nm LED (I = 13.5 mW/cm^2) and 25.8 nmol/s for the 505 nm LED (I = 12.0 mW/cm^2).

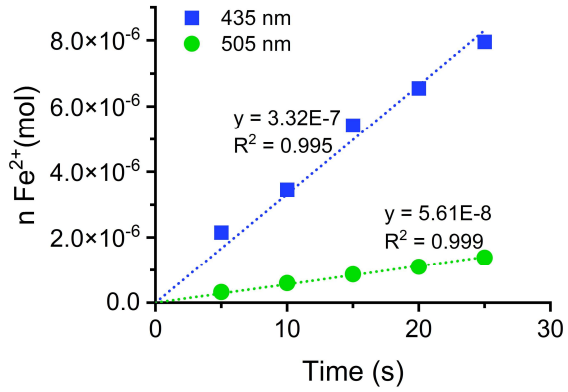

Figure I.2 Plot of Fe^{2+} evolution from ferrioxalate actinometer when irradiated with the LEDs used within the photoirradiation setup.

Since the ferrioxalate actinometer has a quantum yield below 1% when irradiated with λ_{irr} >570 nm, it is not suitable for determining the photon flux of a light source with a maximum output at higher wavelength. Therefore, the photon flux of the red LED (λ_{irr} = 625 nm) (ϕ_{625}) used was determined indirectly using equation I.2:

$$\varphi_{625} = \frac{\varphi_{ref} \times E_{ref}}{E_{625}} \times \frac{I_{625}}{I_{ref}} \qquad (I.2)$$

in which ϕ_{ref} is the photon flux of a reference LED in mol per second, E_{ref}/E_{625} is the photon energy of the reference or 625 nm LED in Joule and I_{ref}/I_{625} is the irradiance of the used LEDs in mW per cm^2. Using equation I.2, ϕ_{625} was 423.5 nmol/s for the 625 nm LED (I = 11.3 mW/cm^2). The emission spectra of the LEDs (used in UV-Vis absorbance measurements) and lamps (used in ^{1}H-NMR photosubstitution experiments and preparation of dissymmetric complexes) are shown in Figure I.3.

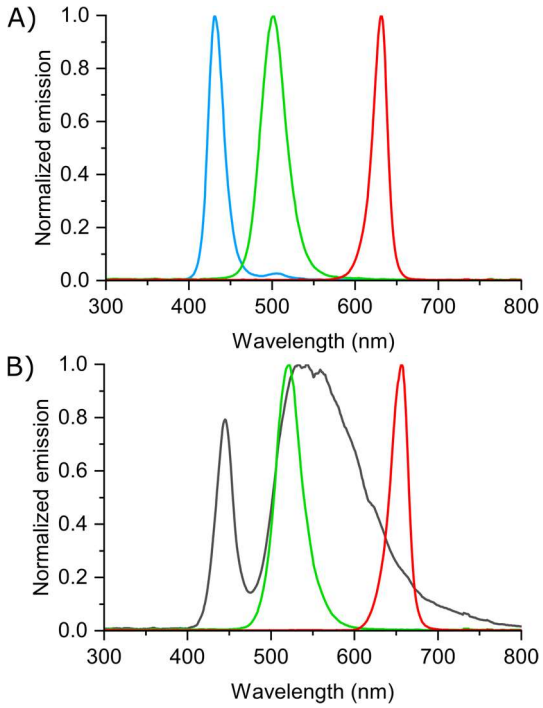

Figure I.3 Normalized emission spectra of used LEDs (A; 435 nm in blue, 505 nm in green, 625 nm in red; obtained from Mouser Electronics) and lamps (B; white in grey, 530 nm in green, 650 nm in red; obtained from HepatoChem).

I.2.3 Photosubstitution quantum yield

For symmetric complexes: The photosubstitution reactions of the symmetric complexes reported in this work all follow a sequential two-step mechanism according to the general equation **R** → **I** → **P**, in which a reagent **R** in converted into a photoproduct **P** through intermediate **I**. Therefore, global fitting of the time-dependent evolution of the UV-Vis absorption spectra with a sequential first-order kinetic model using the Glotaran software package was performed as previously described by Meijer and Bonnet.[3,4] This approach provided the fitted UV-Vis absorption spectra of all species as well as the time-evolution of

the relative concentrations. Using the known molar extinction coefficients of **R** (ε_R), the molar extinction coefficients of **I** (ε_I) and **P** (ε_P) were calculated. From the known starting concentration of **R**, the time-evolution of the relative concentrations and the molar extinction coefficient of all species, the time evolutions of n_R, n_i and n_P were derived. The average absorbance between two consecutive UV-Vis measurements $(A_{\lambda,irr})_{avg}$ at t_i and t_{i+1}, at the irradiation wavelength λ_{irr} was then calculated according to equation II.3:

$$\left(A_{\lambda,irr}\right)_{avg} = \frac{\left(A_{\lambda,irr}\right)_i + \left(A_{\lambda,irr}\right)_{i+1}}{2} \qquad (I.3)$$

According to equation I.4, the number of moles of photons absorbed by the reagent between two consecutive UV-Vis measurements ($\Delta t = t_{i+1} - t_i$) $q_{i,R}$ was calculated. Here $\varphi_{\lambda,irr}$ is the photon flux at the irradiation wavelength (λ,irr) and $\left(1\text{-}10^{-3\left(A_{\lambda,irr}\right)_{avg}}\right)$ is the photon absorption probability. Because the sample was irradiated from the top of the UV-Vis cuvette (vertical beam, pathlength = 3 cm), the photon absorption probability is obtained by multiplying $(A_{\lambda,irr})_{avg}$ by 3.

$$q_{i,R} = \left(\frac{A_R}{\left(A_{\lambda,irr}\right)_{avg}}\right)_i \times \left(1\text{-}10^{-3\left(A_{\lambda,irr}\right)_{avg}}\right) \times \varphi_{\lambda,irr} \times \Delta t \qquad (I.4)$$

The total number of moles of photons absorbed by the **R** at time t since t = 0, $Q_{i,R}(t)$, was calculated according I.5.

$$Q_{i,R}(t) = \Sigma_{t=0}^{i} q_{i,R} \qquad (I.5)$$

When plotting n_R *vs.* $Q_{i,R}$, the slope provided the quantum yield of the first photosubstitution step φ_1. Similarly, the resulting slope of plotting n_P *vs.* $Q_{i,I}$ provided the quantum yield of the second step φ_2.

For dissymmetric complexes: As the dissymmetric complexes follow a "branched" sequential first-order pathway that can be described by the equation **R** → **I'** + **I"** → **P**, fitting to a general sequential model can only provide overall reaction rates. Therefore, targeted fitting was used to describe the system more accurately and provided the time-evolution of the relative concentrations for all species with the irradiation wavelength λ_{irr} being 435 nm and 505 nm. Since the molar extinction coefficients of **I'**, **I"** and **P** were calculated from the symmetric complexes, the time-evolution of n_R, $n_{I'}$, $n_{I''}$ and n_P could be readily derived. Subsequently, the total number of photons absorbed by **R**, **I'** and **I"** at time t since t = 0 was calculated. The resulting slope of plotting $n_{I'}$ *vs.* $Q_{i,R}$ and $n_{I''}$ *vs.* $Q_{i,R}$ provided the quantum yield of the first steps $\varphi_{R\rightarrow I'}$ and $\varphi_{R\rightarrow I''}$. The slopes of the plotting n_P *vs.* $Q_{i,I'}$ and n_P *vs.* $Q_{i,I''}$ provided the quantum yield of the second steps $\varphi_{R\rightarrow I'}$ and $\varphi_{R\rightarrow I''}$.

Since the photosubstitution experiments with 625 nm irradiation generally show significantly less spectral difference, targeted fitting does not provide satisfactorily results.

Therefore, the time-evolution of the relative concentrations for all species were calculated using simultaneous equation matrix method (equation I.8).[5] Importantly, the molar extinction coefficients of the individual species should not be identical at the selected wavelengths.

$$A_\lambda(t) = \varepsilon_{R,\lambda}C_R + \varepsilon_{I',\lambda}C_{I'} + \varepsilon_{I'',\lambda}C_{I''} + \varepsilon_{P,\lambda}C_P \quad \text{(I.6)}$$

$$\begin{vmatrix} A_1 \\ A_2 \\ A_3 \\ A_4 \end{vmatrix}_t = \begin{vmatrix} \varepsilon_{R,1} & \varepsilon_{I',1} & \varepsilon_{I'',1} & \varepsilon_{P,1} \\ \varepsilon_{R,2} & \varepsilon_{I',2} & \varepsilon_{I'',2} & \varepsilon_{P,2} \\ \varepsilon_{R,3} & \varepsilon_{I',3} & \varepsilon_{I'',3} & \varepsilon_{P,3} \\ \varepsilon_{R,4} & \varepsilon_{I',4} & \varepsilon_{I'',4} & \varepsilon_{P,4} \end{vmatrix}_t \times \begin{vmatrix} C_R \\ C_{I'} \\ C_{I''} \\ C_P \end{vmatrix}_t \quad \text{(I.7)}$$

$$\begin{vmatrix} C_R \\ C_{I'} \\ C_{I''} \\ C_P \end{vmatrix}_t = \begin{vmatrix} \varepsilon_{R,1} & \varepsilon_{I',1} & \varepsilon_{I'',1} & \varepsilon_{P,1} \\ \varepsilon_{R,2} & \varepsilon_{I',2} & \varepsilon_{I'',2} & \varepsilon_{P,2} \\ \varepsilon_{R,3} & \varepsilon_{I',3} & \varepsilon_{I'',3} & \varepsilon_{P,3} \\ \varepsilon_{R,4} & \varepsilon_{I',4} & \varepsilon_{I'',4} & \varepsilon_{P,4} \end{vmatrix}_t^{-1} \times \begin{vmatrix} A_1 \\ A_2 \\ A_3 \\ A_4 \end{vmatrix}_t \quad \text{(I.8)}$$

I.2.4 Phosphorescence and singlet oxygen generation quantum yield

The quantum yields of phosphorescence and singlet oxygen generation were determined using a custom-built setup and experimental procedure as previously reported.[6–8] The compounds were dissolved in aerated acetonitrile (3 mL) and transferred into a fluorescence cuvette (Helma Analytics, light path 1 × 1 cm). The absorbance spectra at 268 K were recorded using Agilent Cary 60 UV-Vis spectrometer. Emission spectroscopy was performed at 298 K by irradiating the sample using 450 nm fiber-coupled laser (LRD-0450, Laserglow) set to 80 mW at the cuvette as determined with a power meter (PM100USB, Thorlabs). The phosphorescence of the complexes was recorded between 530 nm to 900 nm using a UV-Vis spectrometer (Avantes 2048L Starline), with an acquisition time of 100 ms. The phosphorescence of singlet oxygen (around 1275 nm) was recorded between 1200 nm to 1350 nm using a NIR spectrometer (Avantes NIR256-1.7TEC, detector set at −12 °C), with an acquisition time of 10 s. For phosphorescence quantum yield (φ_p) determination, $[Ru(bpy)_3]Cl_2$ was used as reference (φ_p = 0.018 in aerated acetonitrile).[9] For singlet oxygen generation quantum yield (φ_Δ) determination, perinaphthenone was used as a reference (φ_p = 0.98 ± 0.07 in aerated acetonitrile) and $[Ru(bpy)_3]Cl_2$ as validation (φ_p = 0.57 ± 0.06 in aerated acetonitrile).[10,11] All spectral data was processed with OriginPro 9.1 and Microsoft Office Excel 2016.

I.2.5 Photosubstitution followed by ^{1}H-NMR

An aliquot of compound (1.5 mg) was dissolved in acetone-d6 and diluted further with D_2O to the desired ratio, with a total volume of 650 µl. A portion (550 µl) was transferred into an NMR tube and a "dark" ^{1}H-NMR spectrum was measured at 293 K. The NMR tube was then irradiated with a lamp of indicated (Figure I.3) outside of the NMR, and spectra were recorded intermittently at different time intervals to monitor the photoreaction.

I.3 Cell culture

General information

The human U-87 MG cells (glioblastoma cells) were purchased from ATCC (American Type Culture Collection, Manassas, Virginia, US). Human U251 (glioblastoma cells) cells were kindly provided by Rob C. Hoeben via Sabrina van der Zanden, LUMC, Leiden, the Netherlands. Human cancer cell line A549 (human lung carcinoma) and A375 (human epidormoid carcinoma) were distributed by the European Collection of Cell Cultures (ECACC) and purchased from Sigma Aldrich. Dulbecco's Modified Eagle Medium (DMEM, with phenol red, without glutamine), Glutamine-S (GM; 200 mM), MTT salt was purchased from Sigma Aldrich or Bio-connect. Fetal calf serum (FCS) was purchased from Hyclone. Penicillin and streptomycin were purchased from Duchefa and were diluted to a 100 mg/mL penicillin/streptomycin solution (P/S). Trypsin and OptiMEM (without phenol red) were purchased from Gibco Life Technologies. Trypan blue (0.4% in 0.81% sodium chloride and 0.06% potassium phosphate dibasic solution) was purchased from BioRad. Plastic disposable flasks and 96-well plates for cytotoxicity assays were purchased from Sarstedt. Cells were counted by using a BioRad TC20™ automated cell counter with BioRad cell-counting slides. Cells were inspected with an Olympus IX81 microscope. UV-vis measurements for analysis of 96-well plates were performed with a M1000 Tecan Reader, Tecan Trading AG, Switzerland).

Cell culture under normoxia and hypoxia

Cells were cultured in DMEM complete (Dulbecco's Modified Eagle Medium (DMEM) with phenol red) supplemented with 1% v/v GM, 0.1% v/v P/S and 10% v/v FCS. Cells were incubated at 37°C at 5% CO_2 atmosphere and subcultured upon reaching 80-90% confluency (approximately twice per week). Cells were converted into hypoxic phenotype by incubation in a hypoxic incubator at t = 37°C under atmosphere of >1% O_2 with 5% CO_2 for at least 10 days prior use. Cells were cultured for a maximum of 8 weeks for all biological experiments.

Cell-irradiation setup

96-well plates were irradiated using described in detail earlier.[12] In short, the 96-well plates were placed on Ditabis thermostate fitted with two flat-bottemed micro-plate thremoblocks and a 96-LED array was placed directly on top of the plates (with lid). For irradiation under hypoxic conditions, the 96-LED array was place on top of the plates inside the hypoxic incubator and irradiation was only started upon stabilization of the >1% O_2 atmosphere.

Cytotoxicity assay

For each photocytotoxicity experiment, three plates were prepared and treated identically. One to test the cytotoxicity in dark and green (520 ± 35 nm, 17.1 mW/cm^2 for 30 min, 30.78

J/cm^2) and red (630 ± 24 nm, 31.3 mW/cm^2 for 60 min, 114.84 J/cm^2) light. Cells were seeded at t = 0 h in 96-well plates in the respective density according to Table I.1 (100 µL), respectively in OptiMEM supplemented with 2.5% v/v FCS, 0.1% v/v P/S, and 1.0% v/v GM (OptiMEM complete) and incubated for 24 h at 37 °C and 5.0% CO_2.

Table I.1 Seeding density in 96-well plate for the respective cell lines given in cells/well cultured under normoxic (NX) or hypoxic (HX) conditions.

Cell line	*Condition*	*Density (cells/well)*
A375	NX	4.000
	HX	4.000
A549	NX	5.000
	HX	5.000
U87MG	NX	6.000
	HX	7.000
U251	NX	6.000

Only the inner 60 wells were used for seeding, the outer wells were equipped with 100 µL OptiMEM to prevent border effects during irradiation. At t = 24 h, aliquots (100 µL) of six different concentrations of freshly prepared stock solutions of the compounds in OptiMEM complete were added to the wells in triplicate and incubated for additional 24 h. Dimethylsulfoxide (DMSO) was used to dissolve the compounds in such amounts that the maximum v/v% of DMSO per well did not exceed 0.5%. At t = 48 h, medium was aspired and exchanged against fresh OptiMEM medium and the plates were irradiated with the cell-irradiation setup while the control plate was kept in the dark. After irradiation, all the plates were incubated in the dark for further 48 h. After an overall incubation time of 72 h, cell viability was measured either using 10 µL of a MTT solution (5 mg/mL for A375 NX & HX and A549 NX & HX or 3 mg/mL for U-87 NX & HX in PBS) or via a modified MTT (EZ4U kit, Bio-Connect, BI-5000 for U251 cells) was added into each well. The mixture was incubated for 3 h under humanified conditions. The absorbance in each well was read at λ = 570 nm for MTT or 492 and 620 nm for EZ4U using M1000 Tecan reader.

The absorbance data per compound per concentration was averaged over three identical wells (technical replicates, $n_t = 3$) in Excel and was exported to GraphPad Prism. Relative cell populations were calculated by dividing the average absorbance of the treated wells by the average absorbance of the untreated wells. To ensure no light induced cytotoxicity occurred during the experiment, the maximum difference in cell viability between the untreated irradiated and non-irradiated control wells was 10%. The resulting data each biological replicate was fitted using the dose-response two parameter Hill slope equation (equation I.9), to obtain the half-maximal effective concentration (EC_{50}, defined as the drug concentration needed to reduced cell viability by 50% compared to the untreated control).

$$Y = 100/\left(1 + 10^{\log(EC_{50} - X) \times \text{Hill Slope}}\right) \quad \text{(I.9)}$$

The reported EC_{50} values (from at least three biological replicates) are expressed as the mean ± 95% confidence interval. Statistical significance between the irradiated groups and the dark control was evaluated by a two-way ANOVA test with the Dunnett's Multiple Comparison Test.

I.4 References

(1) Calvert, J. G.; Pitts, J. N. *Photochemistry*; Wiley: New York, NY, 1966.

(2) Demas, J. N.; Bowman, W. D.; Zalewski, E. F.; Velapoldi, R. A. *J. Phys. Chem.* **1981**, *85* (19), 2766–2771.

(3) Snellenburg, J. J.; Laptenok, S. P.; Seger, R.; Mullen, K. M.; Stokkum, I. H. M. V. *J. Stat. Soft.* **2012**, *49* (3).

(4) Meijer, M. S.; Bonnet, S. *Inorg. Chem.* **2019**, *58* (17), 11689–11698.

(5) Attia, K. A. M.; Elabasawy, N. M.; Abolmagd, E. *Future Journal of Pharmaceutical Sciences* **2017**, *3* (2), 163–167.

(6) Zhou, X.-Q.; Busemann, A.; Meijer, M. S.; Siegler, M. A.; Bonnet, S. *Chem. Commun.* **2019**, *55* (32), 4695–4698.

(7) Partanen, S. B.; Erickson, P. R.; Latch, D. E.; Moor, K. J.; McNeill, K. *Environ. Sci. Technol.* **2020**, *54* (6), 3316–3324.

(8) Ossola, R.; Jönsson, O. M.; Moor, K.; McNeill, K. *Chem. Rev.* **2021**, *121* (7), 4100–4146.

(9) Suzuki, K.; Kobayashi, A.; Kaneko, S.; Takehira, K.; Yoshihara, T.; Ishida, H.; Shiina, Y.; Oishi, S.; Tobita, S. *Phys. Chem. Chem. Phys.* **2009**, *11* (42), 9850.

(10) Schmidt, R.; Tanielian, C.; Dunsbach, R.; Wolff, C. *Journal of Photochemistry and Photobiology A: Chemistry* **1994**, *79* (1–2), 11–17.

(11) Abdel-Shafi, A. A.; Beer, P. D.; Mortimer, R. J.; Wilkinson, F. *Phys. Chem. Chem. Phys.* **2000**, *2* (14), 3137–3144.

(12) Hopkins, S. L.; Siewert, B.; Askes, S. H. C.; Veldhuizen, P.; Zwier, R.; Heger, M.; Bonnet, S. *Photochem Photobiol Sci* **2016**, *15* (5), 644–653.

Appendix II: Supporting Information for Chapter 2

II.1 Characterization of novel compounds

II.1.1 Amine-products

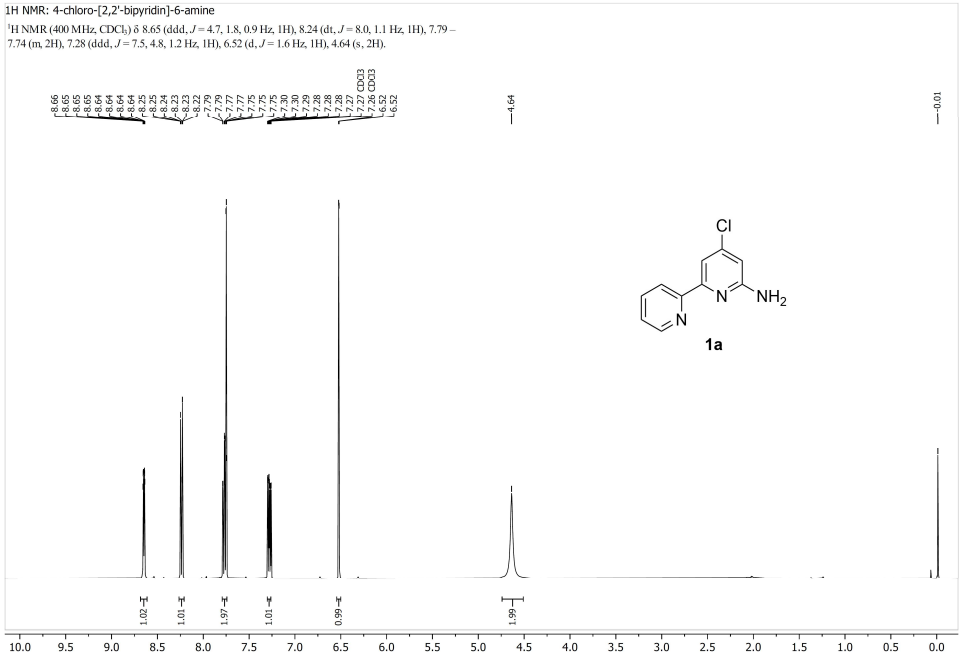

Figure II.1 ^{1}H-NMR of **1a** in $CDCl_3$.

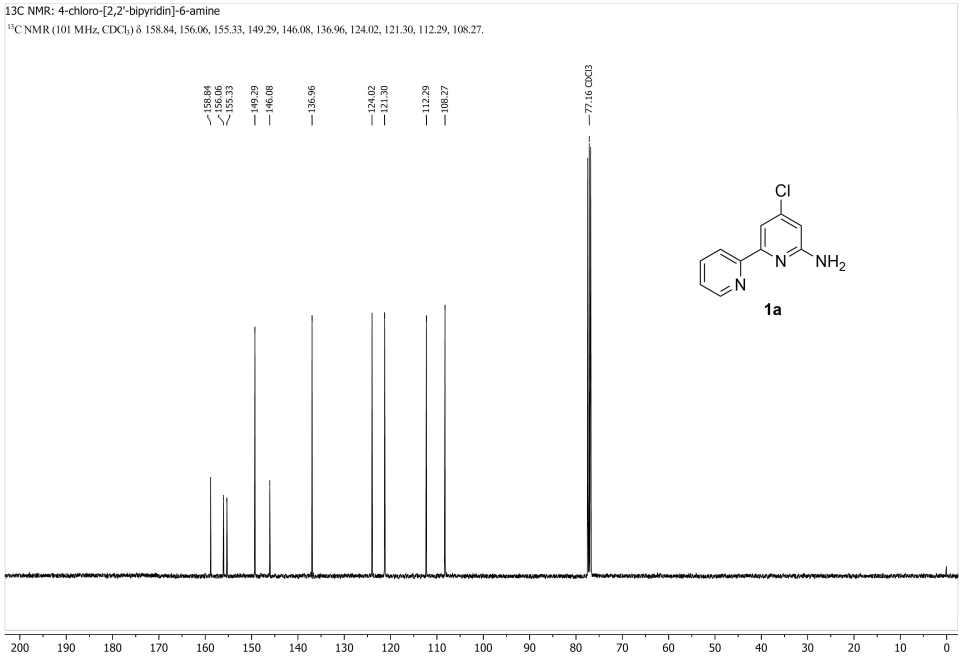

Figure II.2 ^{13}C-NMR of **1a** in $CDCl_3$.

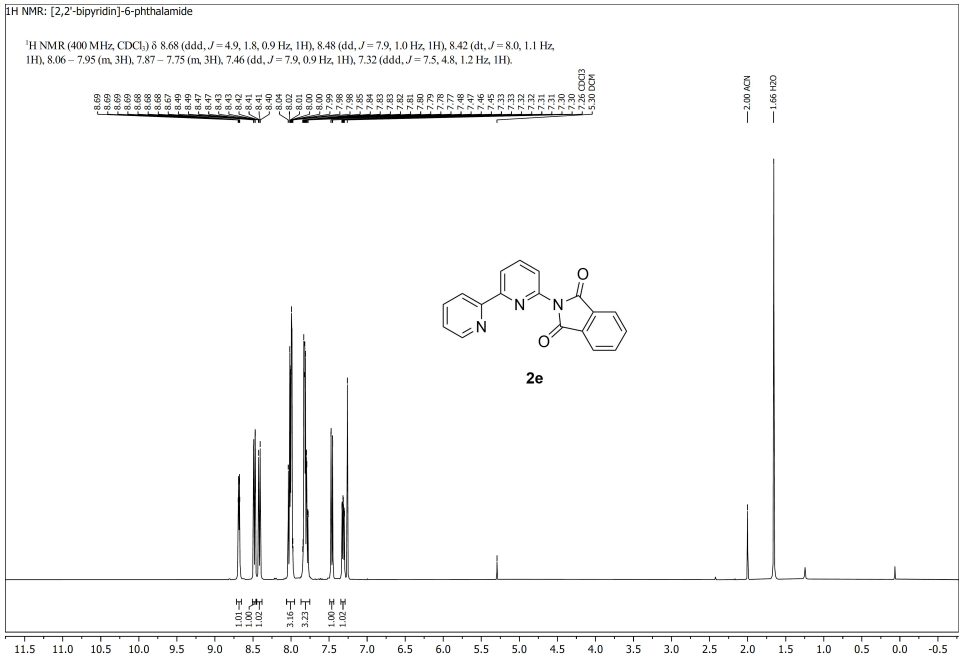

Figure II.3 ^{1}H-NMR of **2e** in $CDCl_3$.

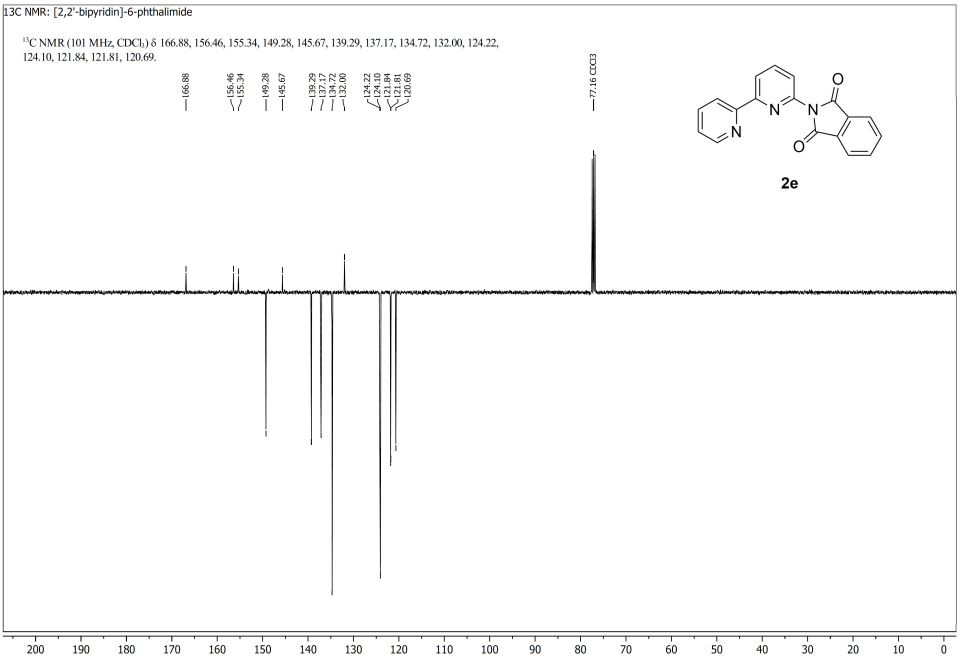

Figure II.4 ^{13}C-NMR of **2e** in $CDCl_3$.

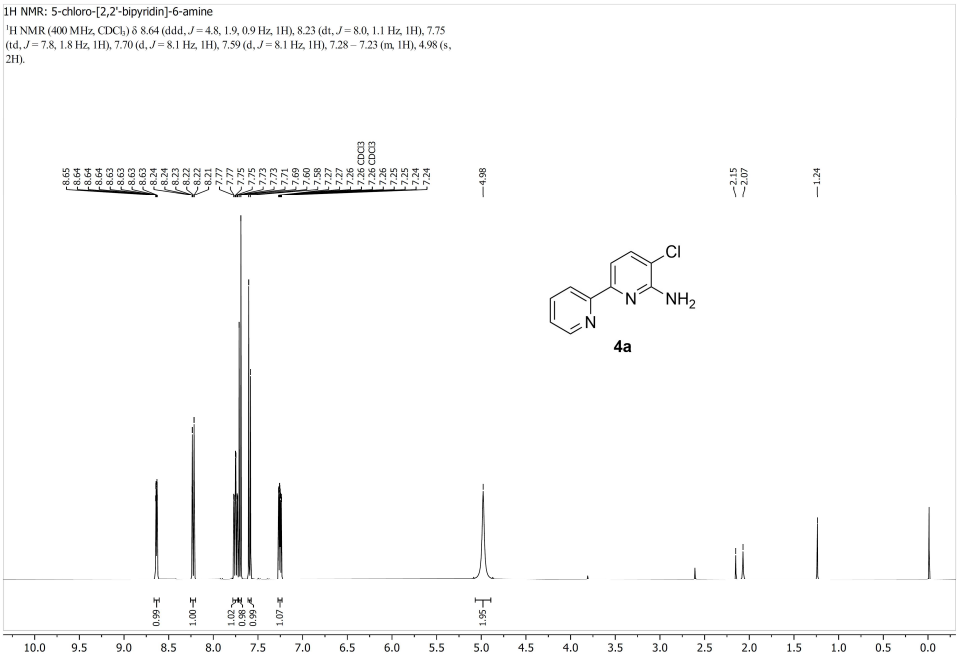

Figure II.5 ^{1}H-NMR of **4a** in $CDCl_3$.

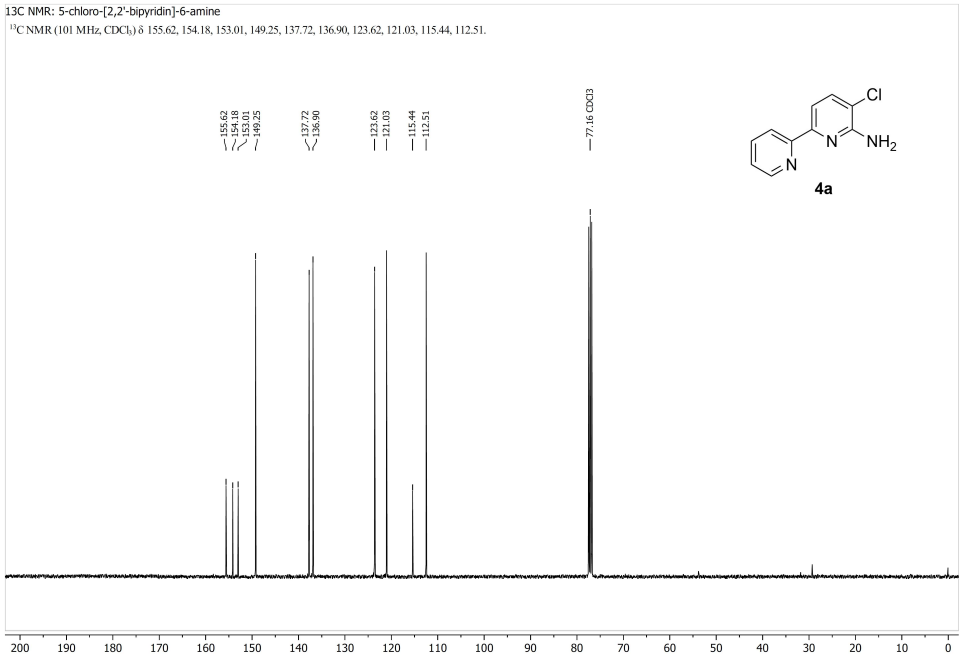

Figure II.6 ^{13}C-NMR of **4a** in $CDCl_3$.

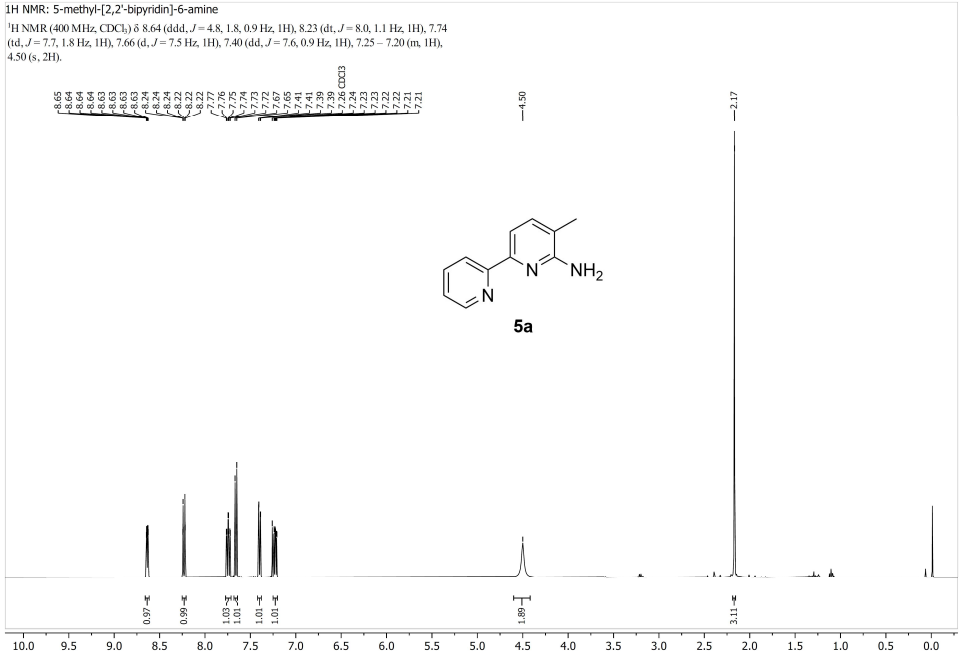

Figure II.7 ^{1}H-NMR of **5a** in $CDCl_3$.

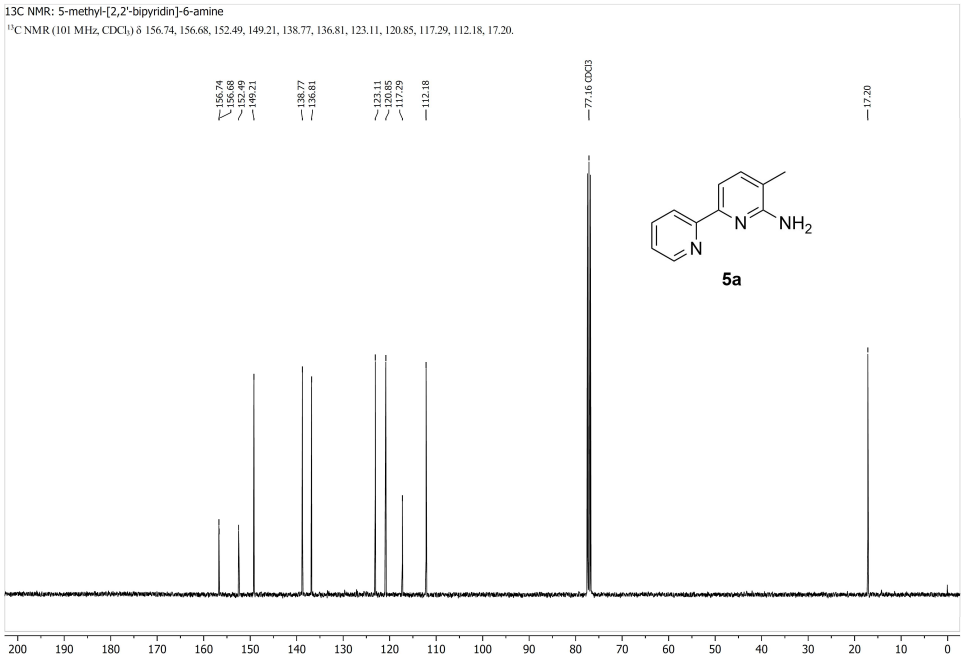

Figure II.8 ^{13}C-NMR of **5a** in $CDCl_3$.

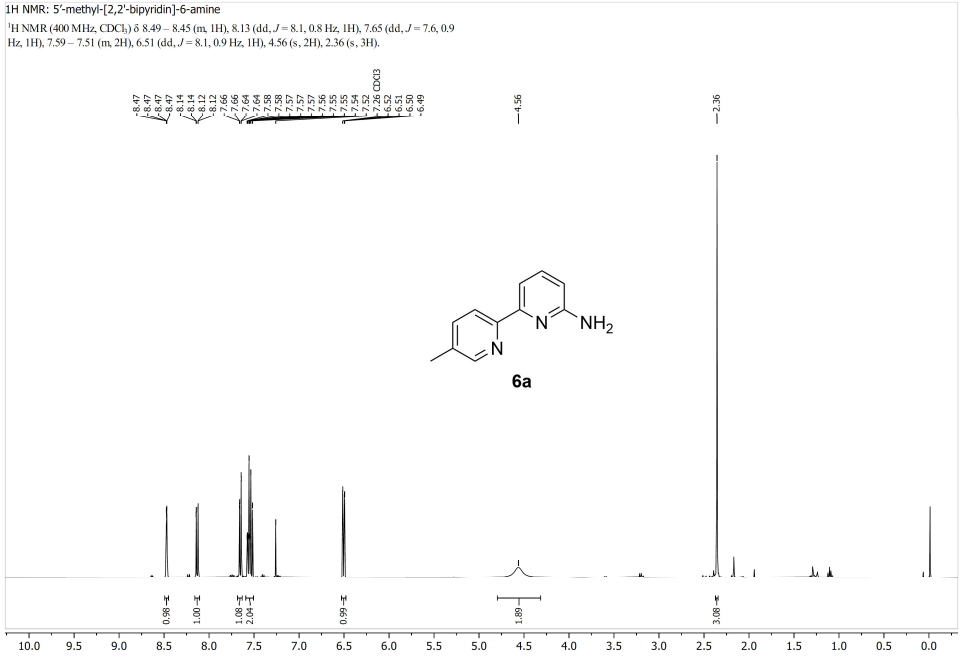

Figure II.9 ^{1}H-NMR of **6a** in $CDCl_3$.

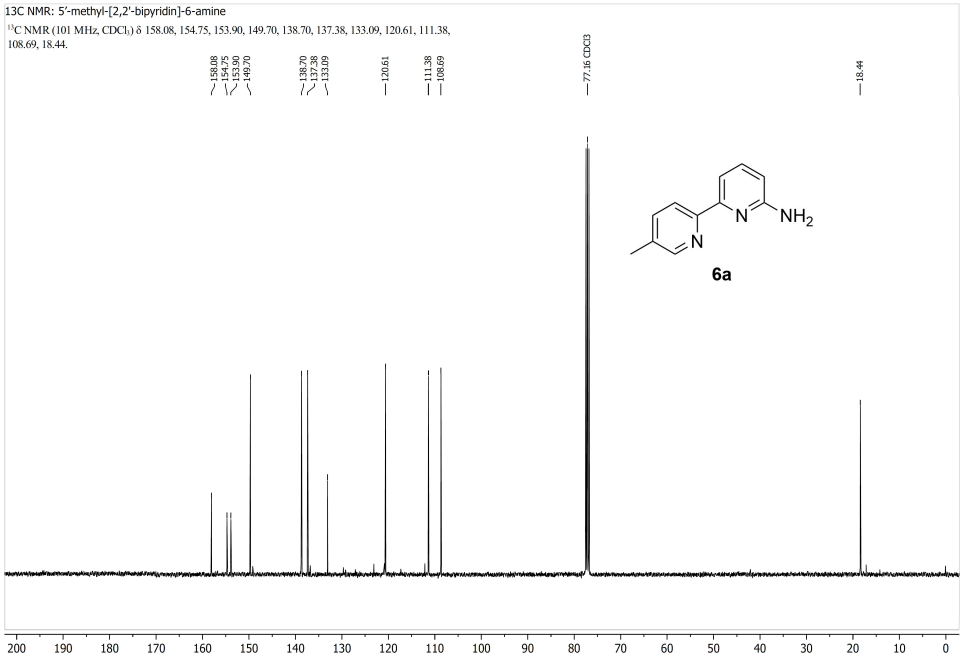

Figure II.10 ^{13}C-NMR of **6a** in $CDCl_3$.

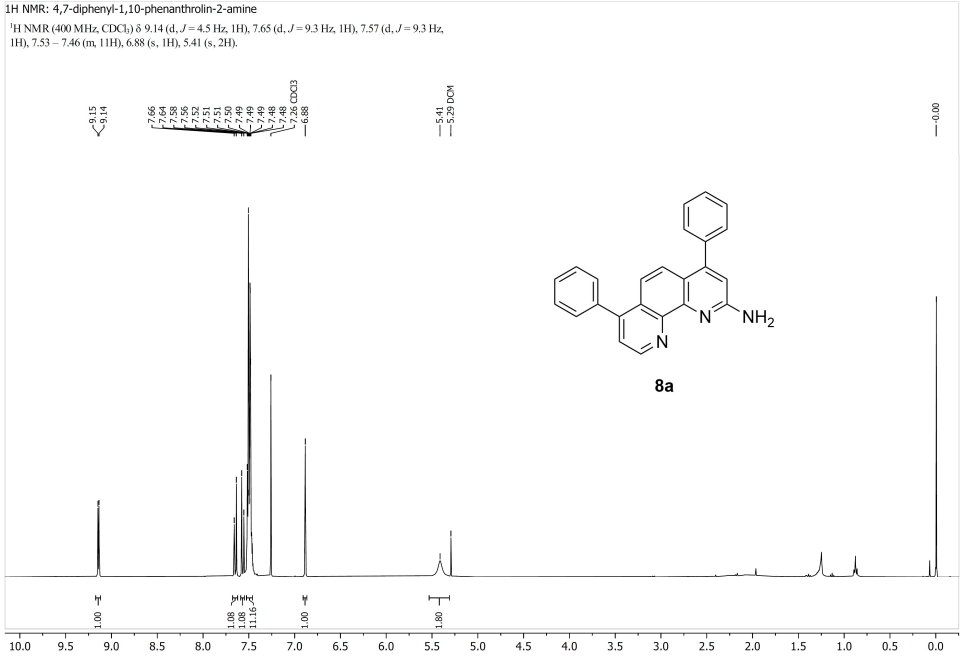

Figure II.11 ^{1}H-NMR of **8a** in $CDCl_3$.

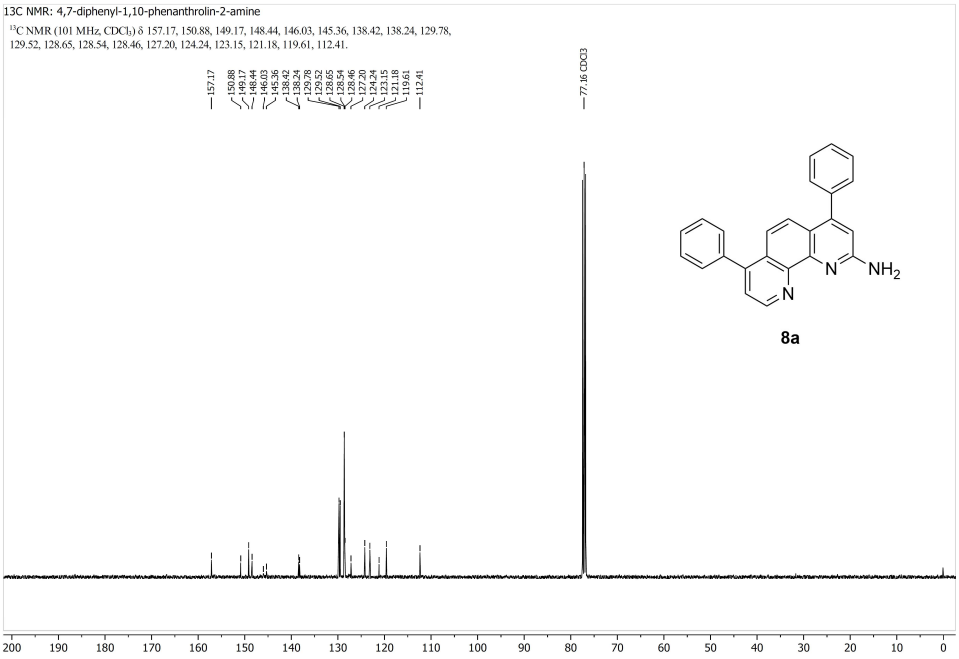

Figure II.12 ^{13}C-NMR of **8a** in $CDCl_3$.

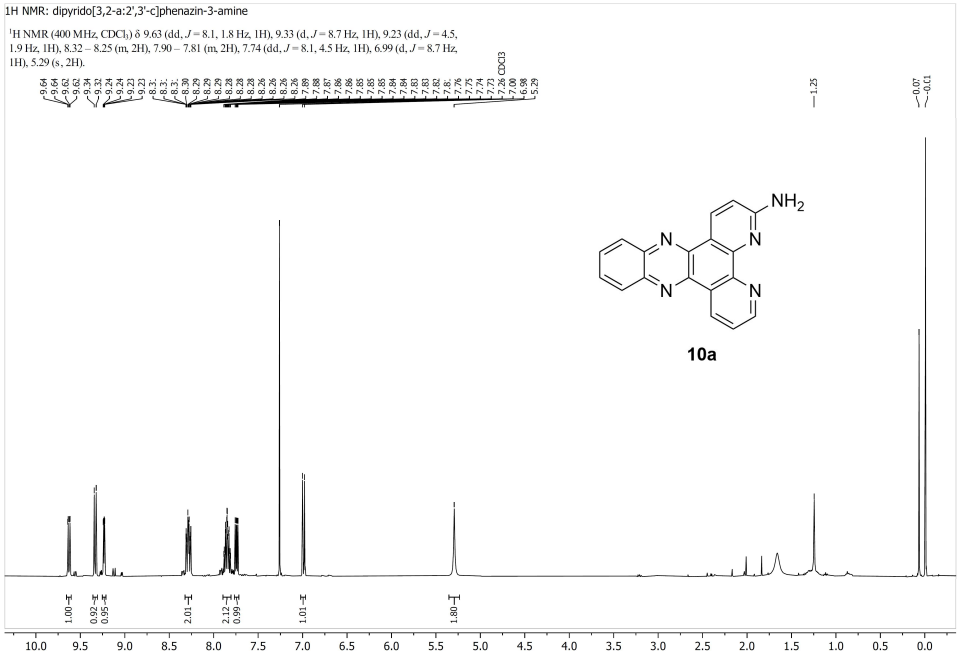

Figure II.13 ^{1}H-NMR of **10a** in $CDCl_3$.

II

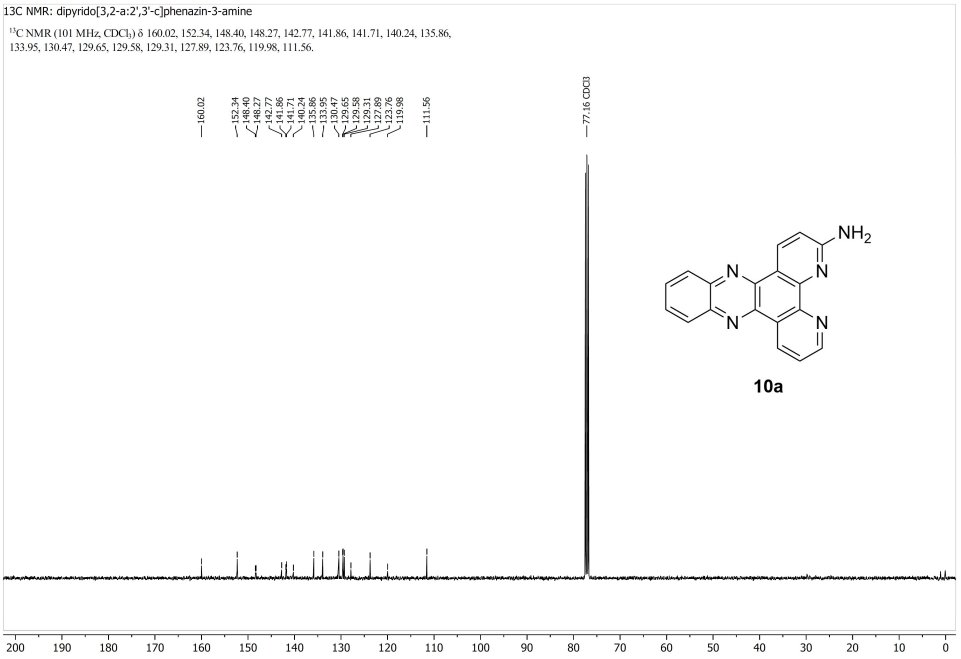

Figure II.14 ^{13}C-NMR of **10a** in $CDCl_3$.

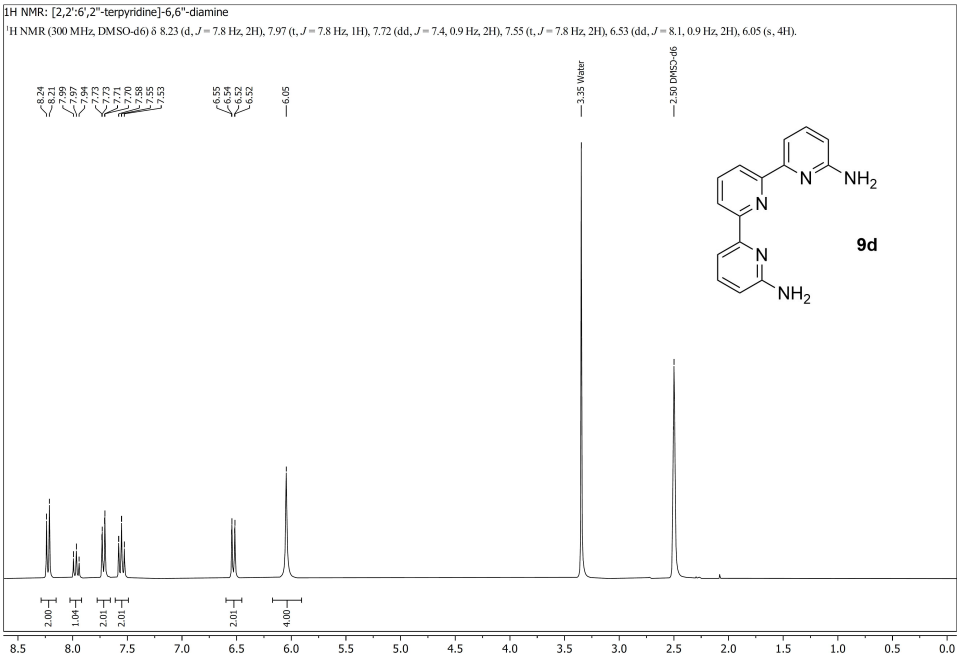

Figure II.15 ^{1}H-NMR of **9d** in DMSO-d_6.

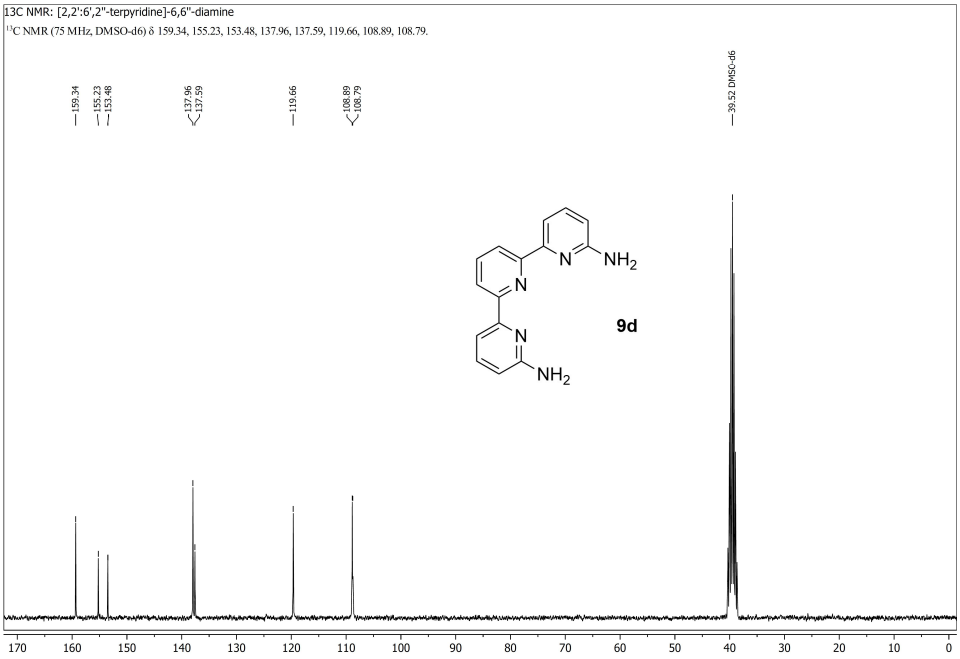

Figure II.16 ^{13}C-NMR of **9d** in DMSO-d_6.

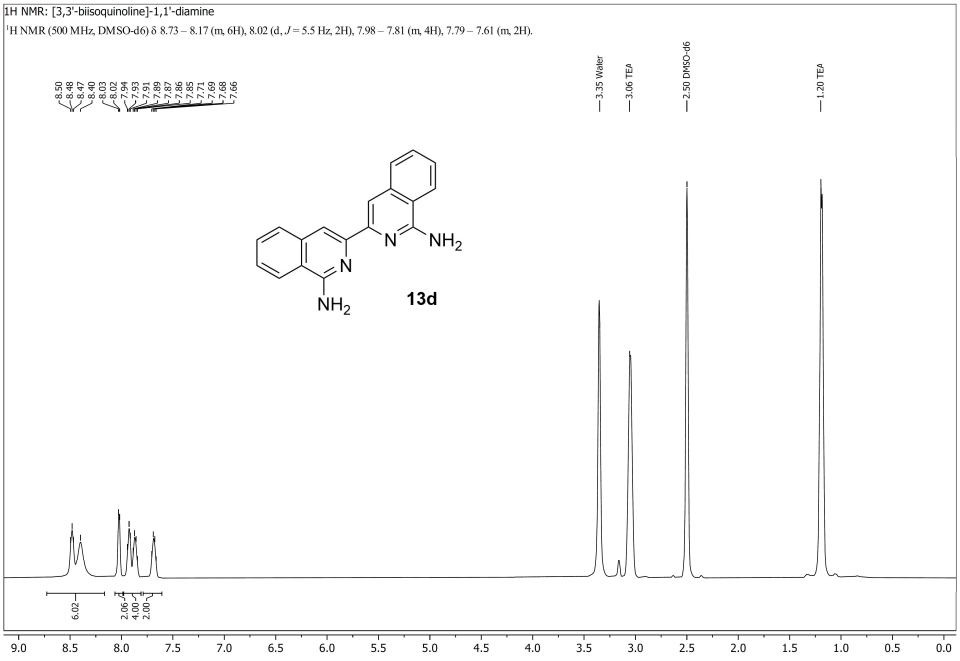

Figure II.17 ^{1}H-NMR of **13d** in DMSO-d_6.

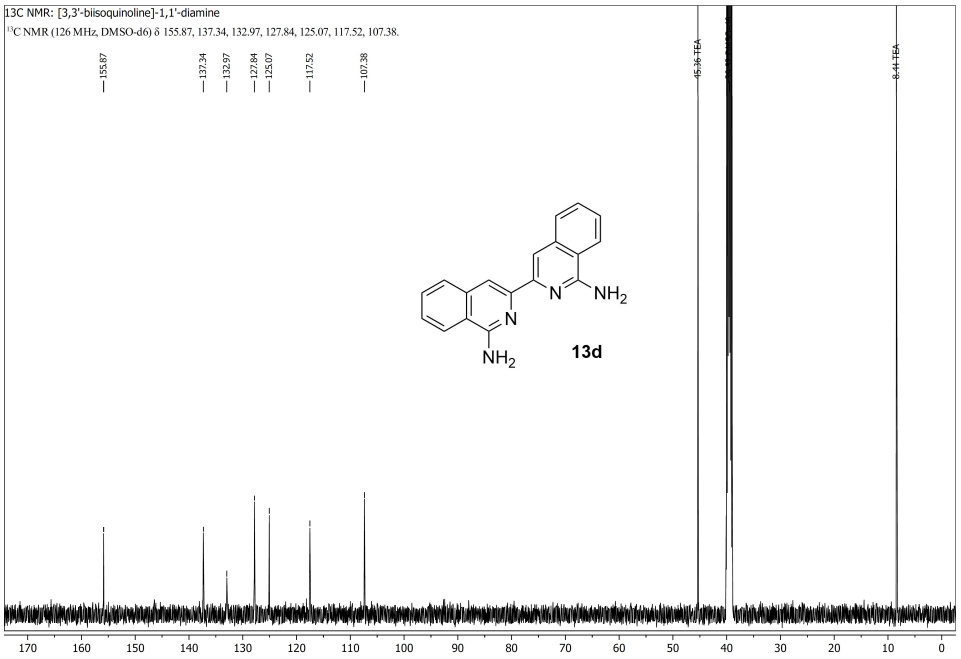

Figure II.18 ^{13}C-NMR of **13d** in DMSO-d_6.

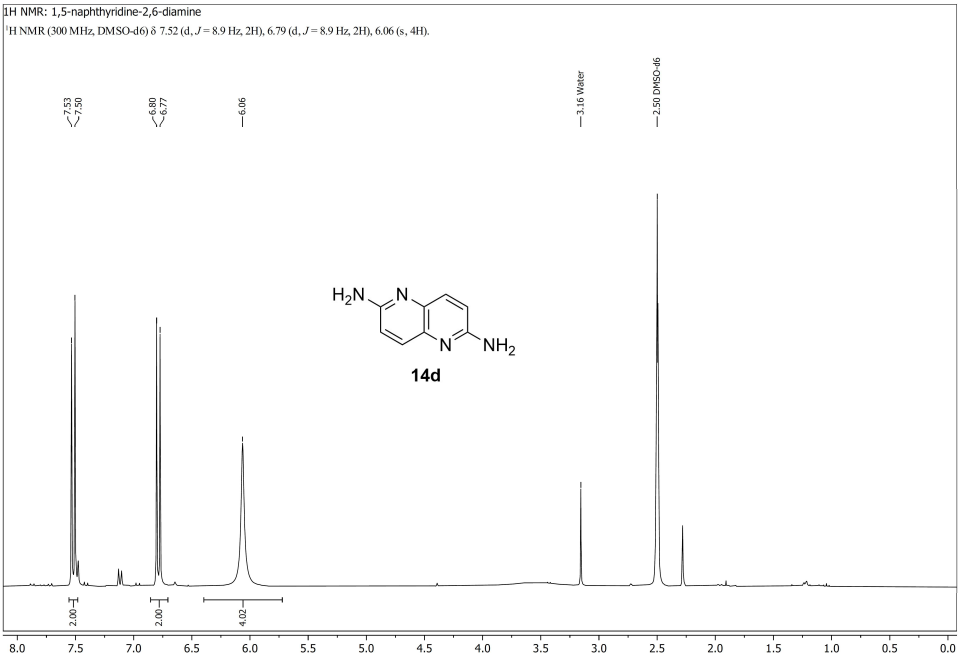

Figure II.19 ^{1}H-NMR of **14d** in DMSO-d_6.

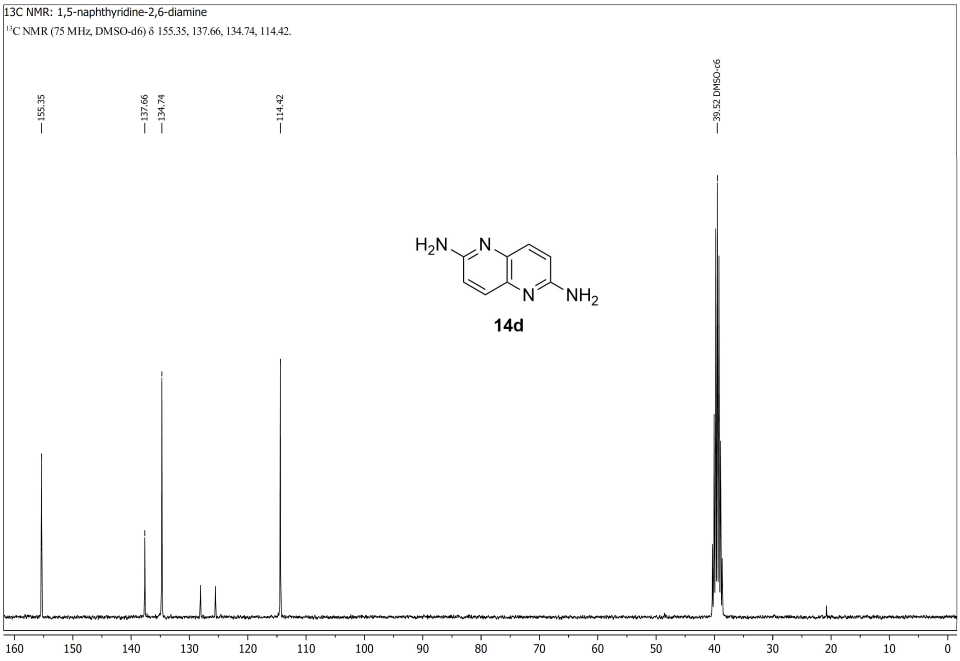

Figure II.20 ^{13}C-NMR of **14d** in DMSO-d_6.

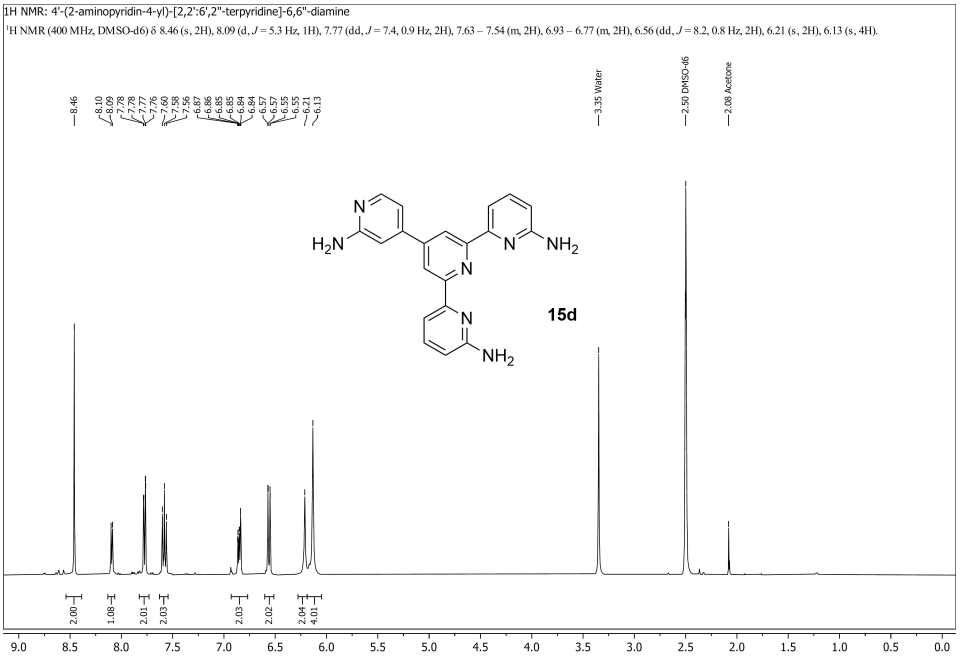

Figure II.21 ^{1}H-NMR of **15d** in $CDCl_3$.

II

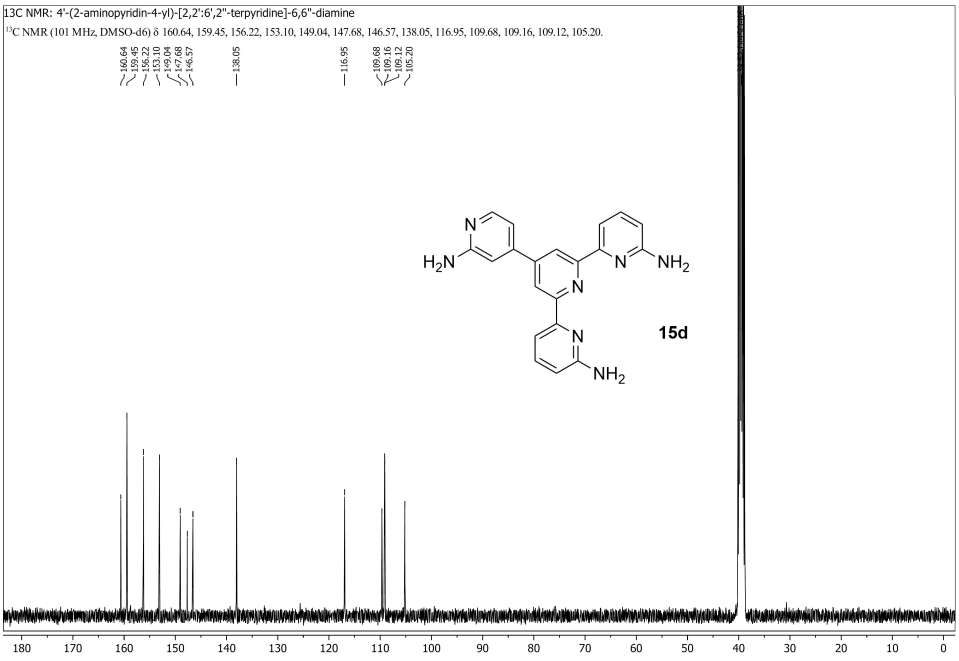

Figure II.22 ^{13}C-NMR of **15d** in $CDCl_3$.

II.1.2 Precursors

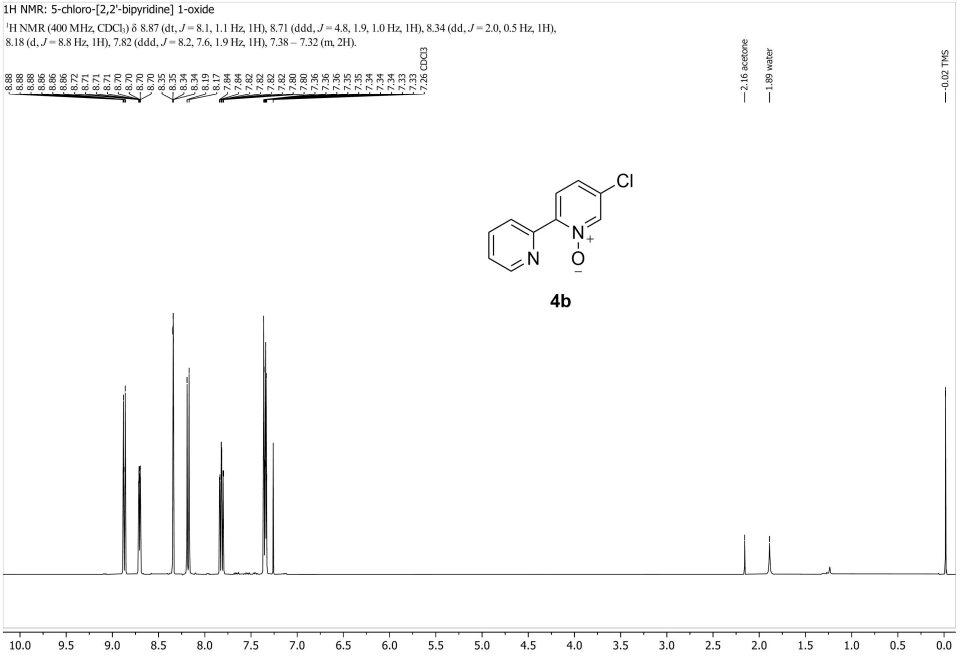

Figure II.23 ^{1}H-NMR of **4b** in $CDCl_3$.

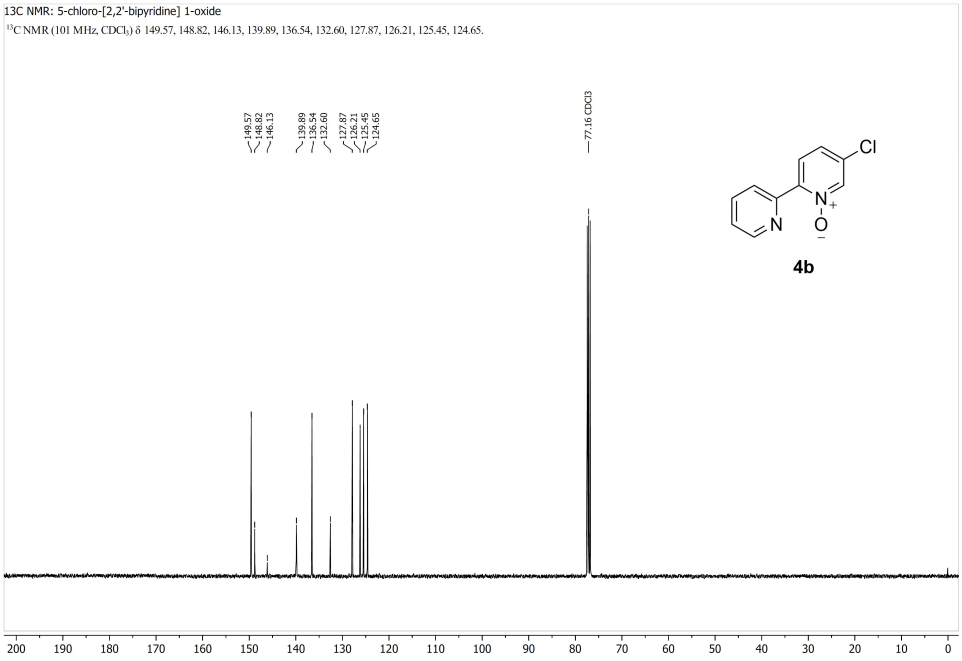

Figure II.24 ^{13}C-NMR of **4b** in $CDCl_3$.

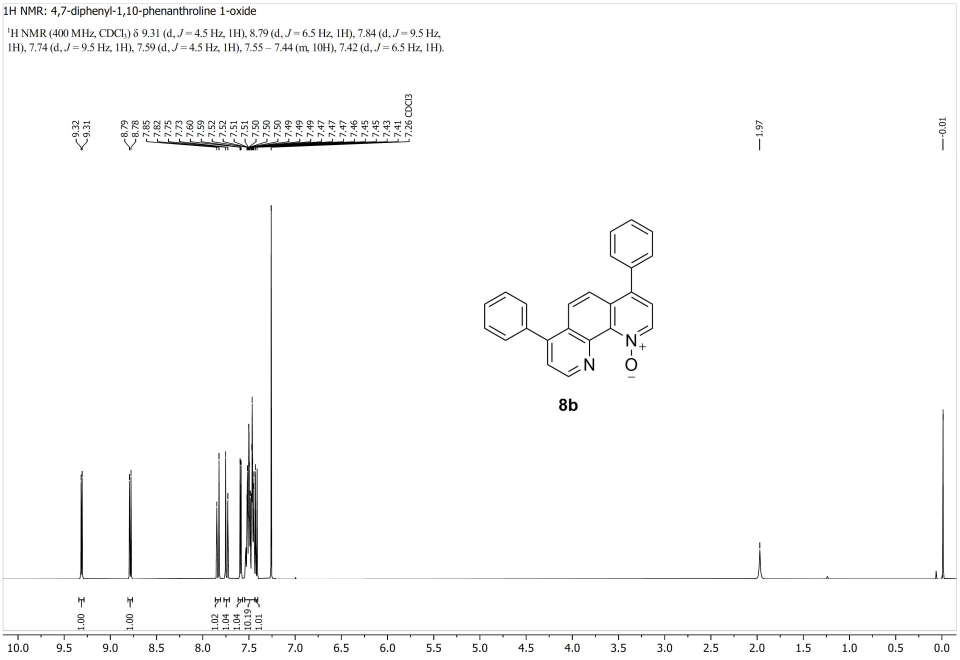

Figure II.25 ^{1}H-NMR of **8b** in $CDCl_3$.

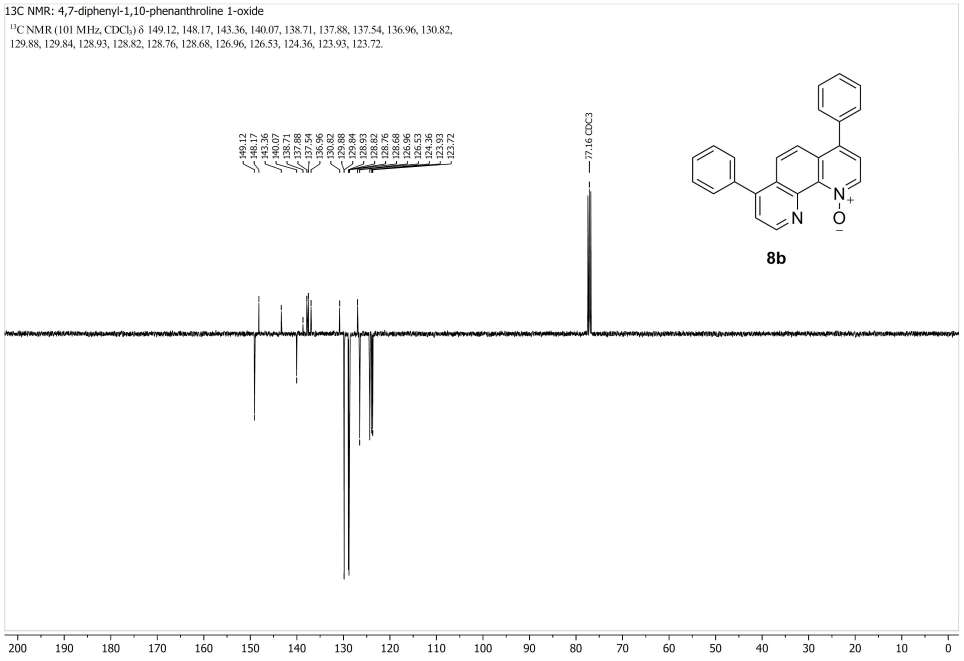

Figure II.26 ^{13}C-NMR of **8b** in $CDCl_3$.

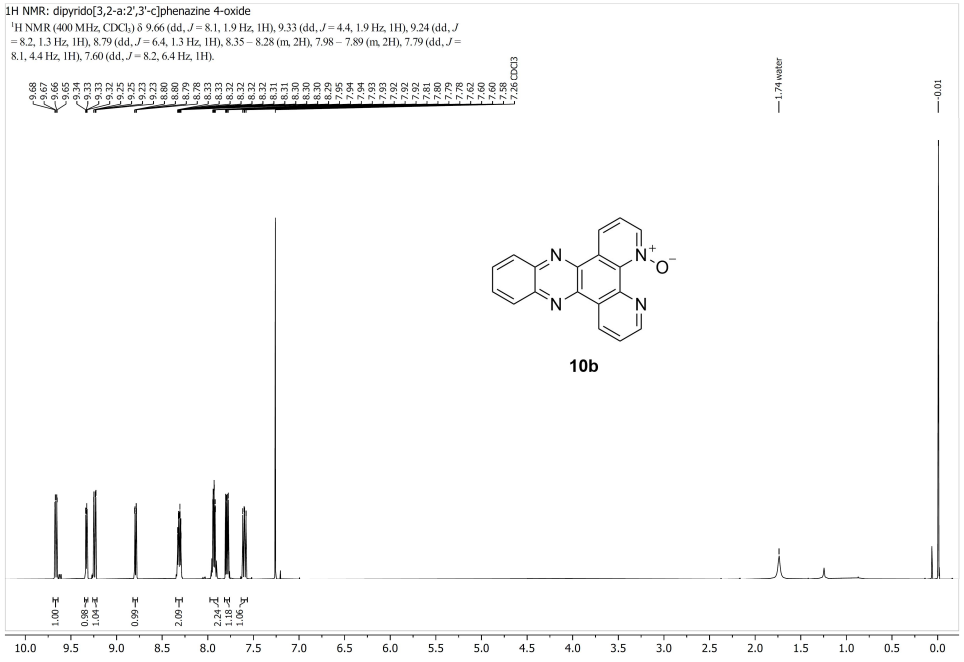

Figure II.27 ^{1}H-NMR of **10b** in $CDCl_3$.

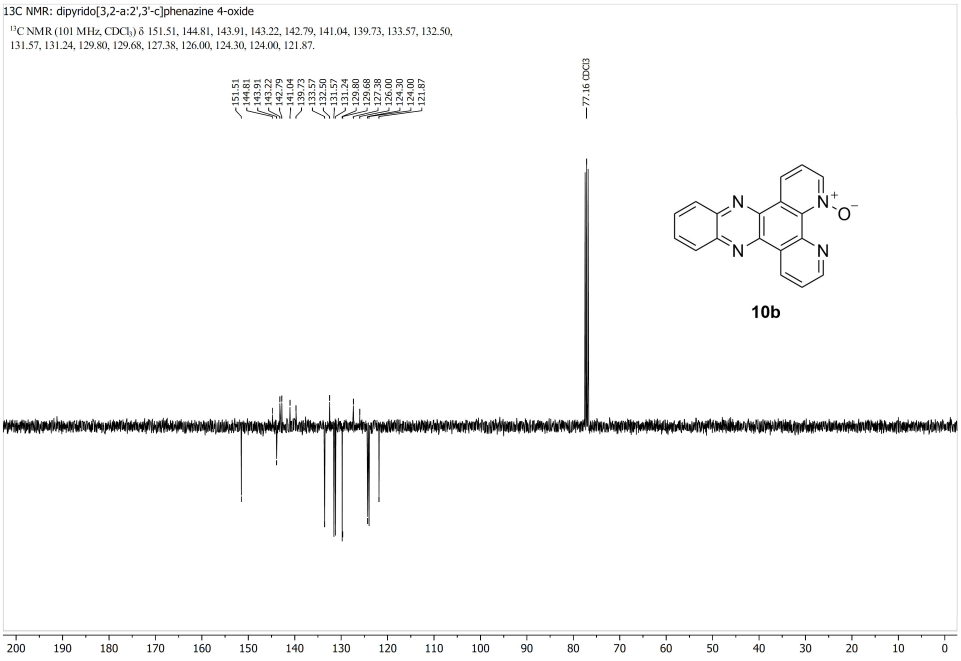

Figure II.28 ^{13}C-NMR of **10b** in $CDCl_3$.

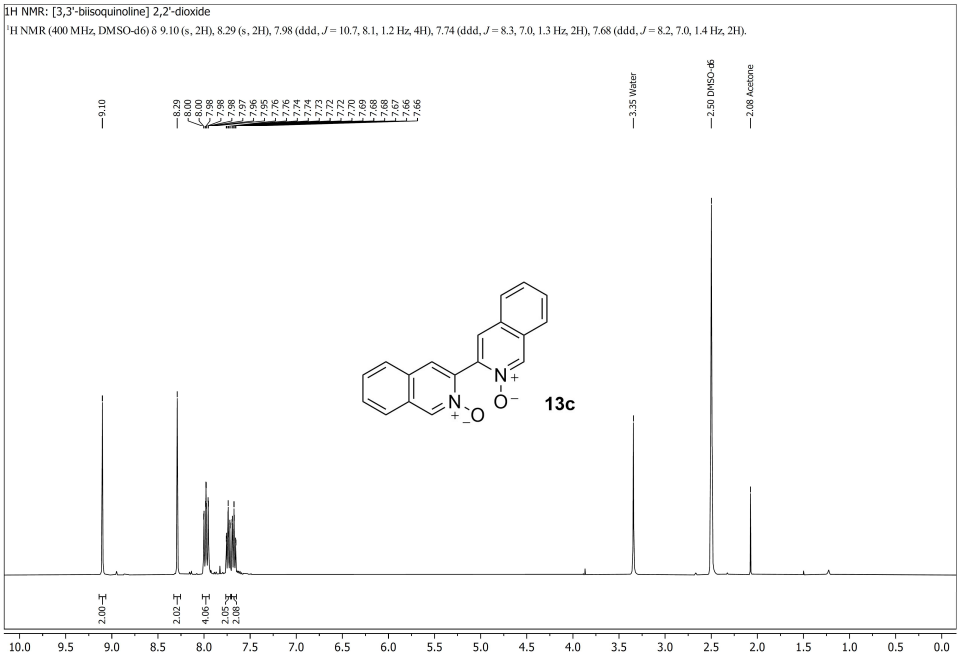

Figure II.29 ^{1}H-NMR of **13c** in DMSO-d_6.

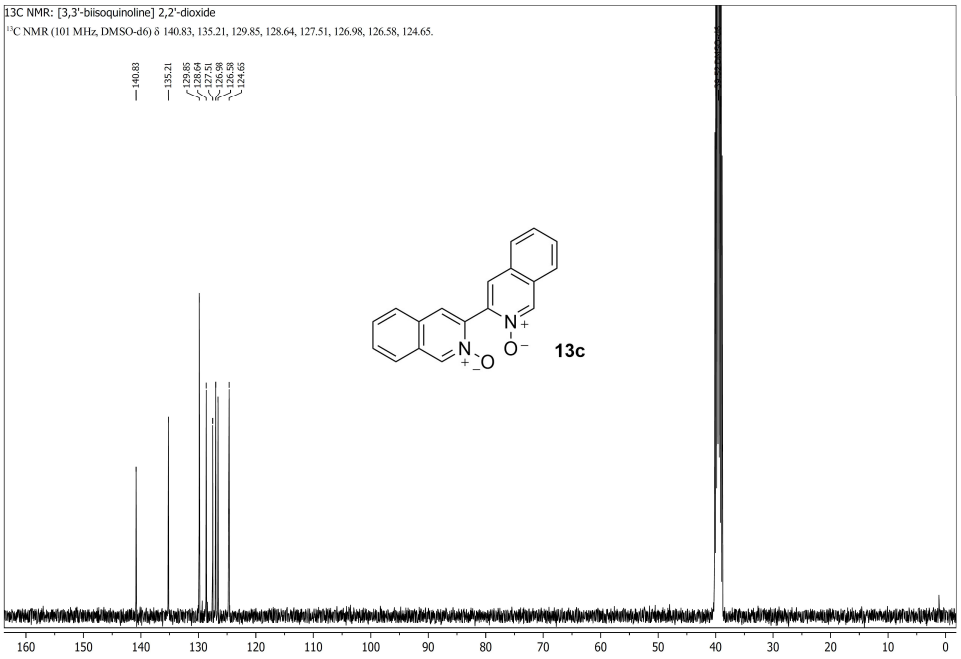

Figure II.30 ^{13}C-NMR of **13c** in DMSO-d_6.

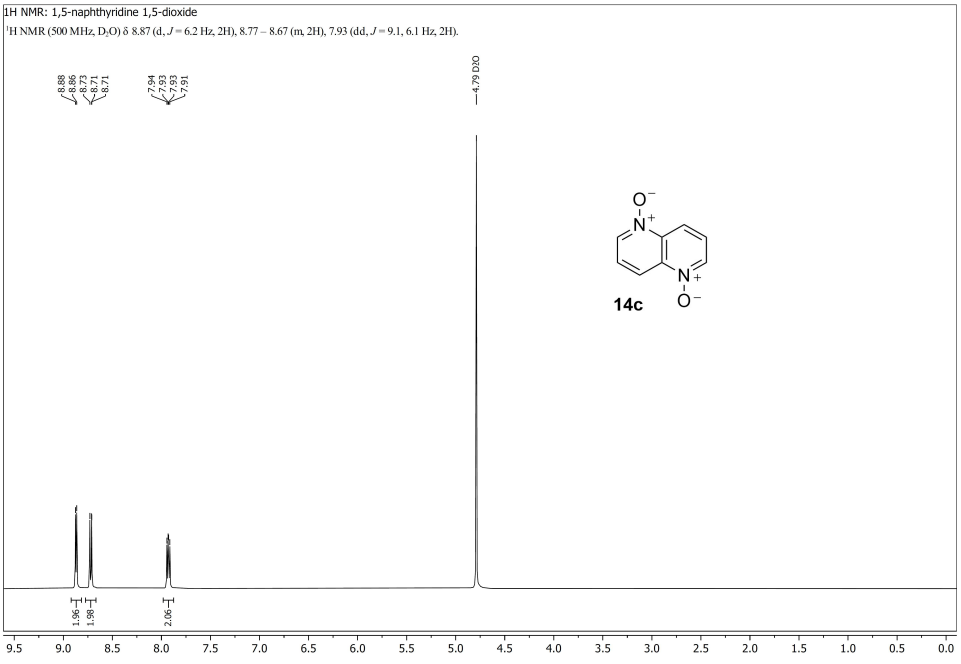

Figure II.31 ^{1}H-NMR of **14c** in DMSO-d_6.

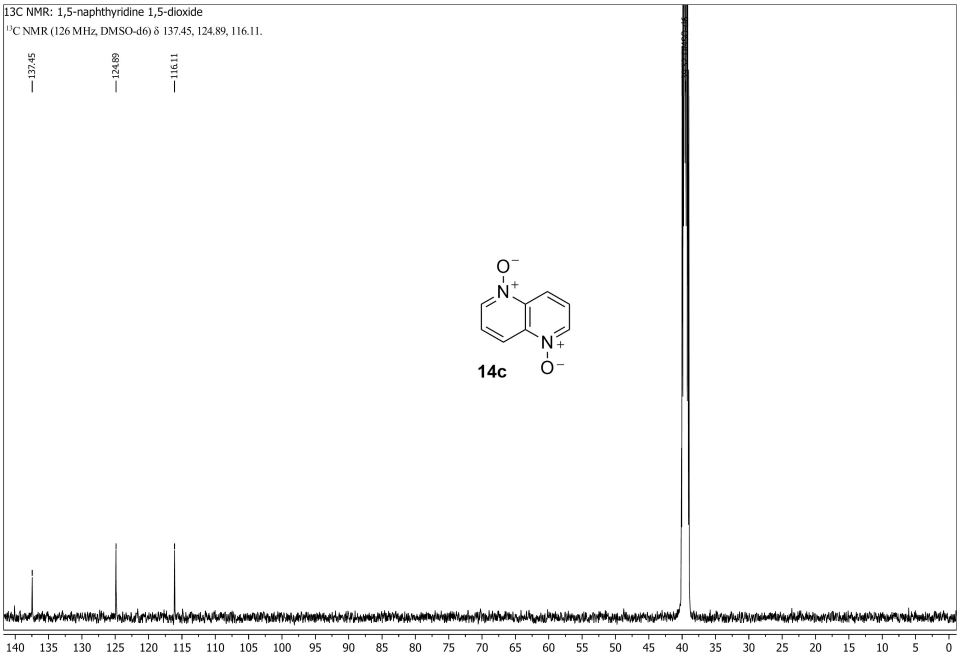

Figure II.32 ^{13}C-NMR of **14c** in DMSO-d_6.

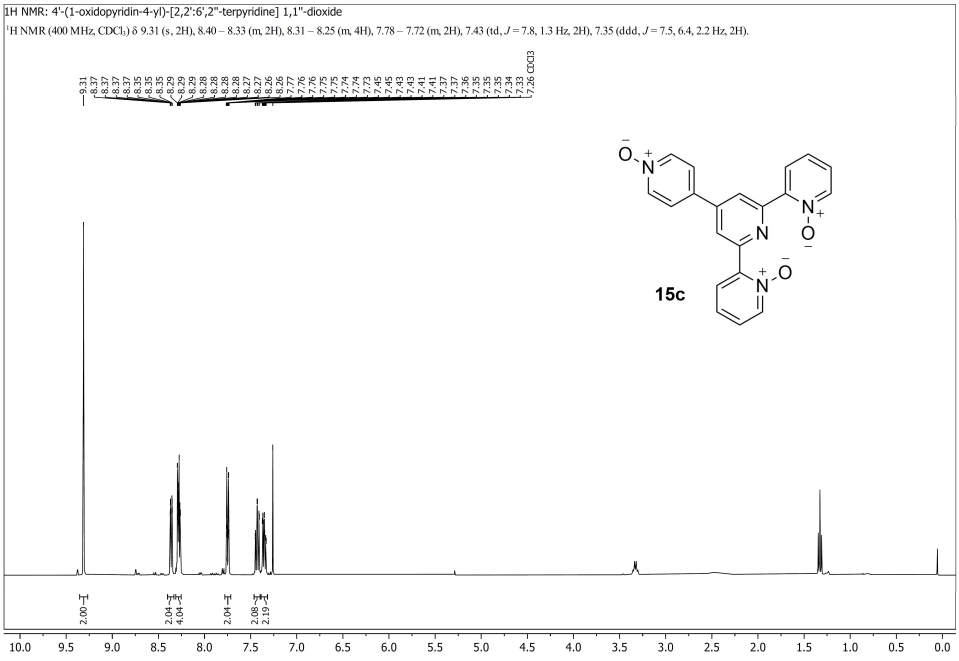

Figure II.33 ^{1}H-NMR of **15c** in $CDCl_3$.

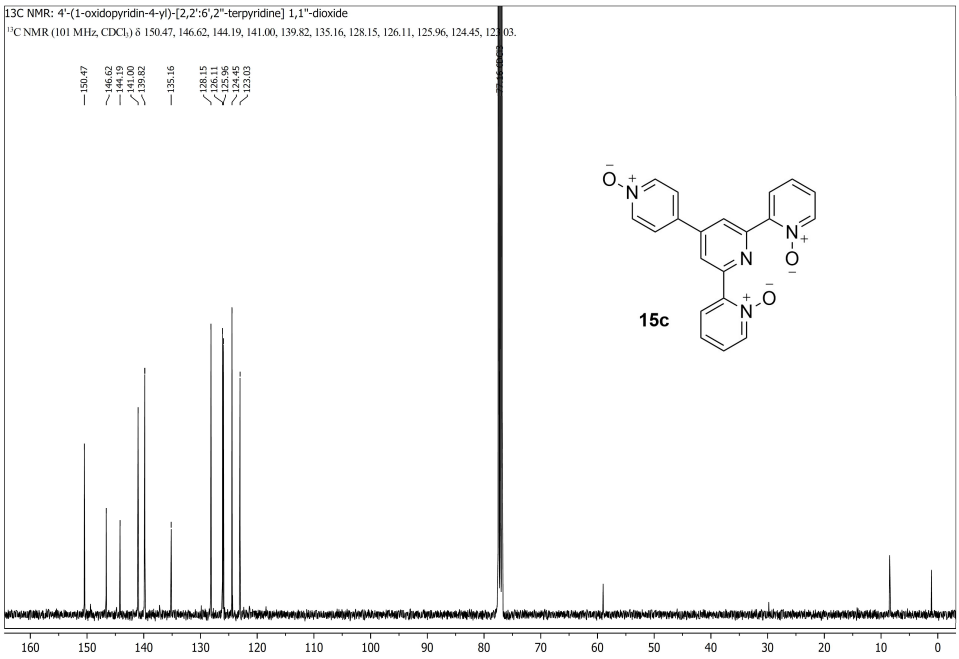

Figure II.34 ^{13}C-NMR of **15c** in $CDCl_3$.

Appendix III: Supporting information for Chapter 3

III.1 Single crystal X-ray crystallography

Experimental details

For [**2b**]$(PF_6)_2$ and [**3b**]$(PF_6)_2$, all reflection intensities were measured at 110(2) K using a SuperNova diffractometer (equipped with Atlas detector and the Cryojet system by Oxford Instruments for temperature control during data collection) with either Mo *Kα* radiation (λ = 0.71073 Å) for [**2b**]$(PF_6)_2$ or Cu *Kα* radiation (λ = 1.54178 Å) for [**3b**]$(PF_6)_2$ under the program CrysAlisPro (Version CrysAlisPro 1.171.42.49, Rigaku OD, 2022). All reflection intensities for [**1a**]$(PF_6)_2$, [**1b**]$(PF_6)_2$ and [**4b**]$(PF_6)_2$ were measured at 110.00(10) K using a Rigaku XtaLAB Synergy R (equipped with a rotating-anode X-ray source, HyPix-6000HE detector and the Cryostream 1000 system by Oxford Cryosystems for temperature control during data collection) with Cu *Kα* radiation (λ = 1.54178 Å) under the program CrysAlisPro (Version CrysAlisPro 1.171.42.49, Rigaku OD, 2022). The same program was used to refine the cell dimensions and for data reduction. The structures were solved with the program SHELXS-2018/3 (Sheldrick, 2018) and was refined on F^2 with SHELXL-2018/3 (Sheldrick, 2018). Numerical absorption correction based on gaussian integration over a multifaceted crystal model was performed using CrysAlisPro for the data of [**2b**]$(PF_6)_2$. Analytical numeric absorption correction using a multifaceted crystal was applied using CrysAlisPro for the data of [**1a**]$(PF_6)_2$, [**1b**]$(PF_6)_2$, [**3b**]$(PF_6)_2$ and [**4b**]$(PF_6)_2$. The H atoms were placed at calculated positions using the instructions AFIX 23, AFIX 43, AFIX 83 or AFIX 137 with isotropic displacement parameters having values 1.2 or 1.5 U_{eq} of the attached C or O atoms.

The structure of [**1a**]$(PF_6)_2$ is disordered. The Ru complex is found at both sites of twofold axial and mirror symmetries, and thus must be disordered. Overall, the occupancy factor must be constrained to be 0.25. The PF_6^- counterion is found disordered over two orientations while also being located at one site of mirror symmetry, and thus the sum of the occupancy factors for both orientations must be constrained to 0.5. Since the target compound does not have the 2/m symmetry, the whole molecule had to be modelled with an occupancy factor of 0.25. Even though EADP constraints were used to minimize the number of parameters to refine, it was not sufficient enough to increase the data-to-parameter ratio.

The structure of [**1b**]$(PF_6)_2$ is partly disordered. One of the two coordinated Hmte ligands and both PF_6^- counterions are disordered over either two (counterions) or three (Htme) orientations. All occupancy factors can be retrieved from the final .cif file.

For [**2b**]$(PF_6)_2$, the asymmetric unit contains ½ Ru complex (the Ru complex is found at one site of mirror symmetry, and only half is crystallographically independent) and two

disordered ½ PF_6^- counterions (one counterion is found at one site of inversion symmetry and the other counterion is found at one site of mirror symmetry). The structure is pseudomerohedrally twinned. The twin relationship is given by the matrix M: 0 1 0 / 1 0 0 / 0 0 -1, and the BASF scale factor refines to 0.1054(8).

The structure of [**3b**]$(PF_6)_2$ is partially disordered. One of the two PF_6^- counterions is disordered over two orientations, and the occupancy factor of the major component of the disorder refines to 0.523(8). The structure was refined as an inversion twin, and the Flack and Hooft parameters refine to 0.088(9) and 0.088(1), respectively.

The structure of [**4b**]$(PF_6)_2$ is partly disordered. The axial pyridine and thioether ligands can be coordinated on both sides of the equatorial ligand, and the occupancy factor of the major component of the disorder refines to 0.775(5). One of the two PF_6^- counterions is also disordered over two orientations, and the occupancy factor of the major component of the disorder refines to 0.574(13). The crystal that was mounted on the diffractometer was non-merohedrally twinned, and the two twin components are related by a twofold rotation along [0.55 0.00 0.83]. The BASF scale factor refines to 0.4949(16).

Table III.1 Crystallographic data for the crystal structures presented in this work.

	[**1a**](PF$_6$)$_2$	[**1b**](PF$_6$)$_2$	[**2b**](PF$_6$)$_2$
Chemical formula	$C_{26}H_{31}N_5O_2RuS_2$·2(F_6P)	$C_{27}H_{33}N_5O_2RuS_2$ ·$C_{18}H_{15}OP$·2(F_6P)	$C_{25}H_{23}N_7Ru$·2(F_6P)
M_r	900.69	1192.98	812.51
Crystal system	Monoclinic	Triclinic	Orthorhombic
Space group	*C2/m*	*P*-1	*P*nma
Cell lengths (*a, b, c*)(Å)	17.4981 (3), 11.4857 (3), 8.26232 (13)	8.50398 (15), 10.1685 (2), 28.0138 (4	15.3570 (5), 15.3124 (4), 12.5014 (4)
Cell angles (α, β, γ)(◦)	90, 98.1669 (17), 90	90.2939 (15), 92.6335 (14), 96.7146 (16)	90, 90, 90
Cell volume (Å^3)	1643.70 (6)	2403.14 (7)	2939.74 (15)
Z	2	2	4
μ (mm^{-1})	6.94	5.24	0.75
Crystal size (mm)	0.09 × 0.06 × 0.02	0.11 × 0.05 × 0.02	0.11 × 0.10 × 0.08
Temperature (K)	110(2)	110	110(2)
Diffractometer	XtaLAB Synergy R, HyPix	XtaLAB Synergy R, HyPix	SuperNova, Dual, Cu at zero, Atlas detector
Radiation type	Cu *Kα*	Cu *Kα*	Mo *Kα*
T_{min}, T_{max}	0.663, 0.875	0.629, 0.901	0.885, 1.000
No. of measured, independent and observed [$I > 2\sigma(I)$] reflections	19522, 1695, 1629	47520, 9445, 8464	28602, 3687, 3405
R_{int}	0.034	0.030	0.063
$(\sin\theta/\lambda)_{max}$ (Å^{-1})	0.616	0.616	0.650
$R[F^2 > 2\sigma(F^2)]$, $wR(F^2)$, S	0.040, 0.113, 1.06	0.034, 0.087, 1.04	0.036, 0.083, 1.09
No. of reflections	1695	9945	3687
No. of parameters	311	817	347
No. of restraints	729	842	542
H-atom treatment	H-atom parameters constrained	H-atom parameters constrained	H-atom parameters constrained
$\Delta\rho_{max}$, $\Delta\rho_{min}$ (e Å^{-3})	0.61, -0.60	0.81, -0.70	0.95, -0.53

	[**3b**](PF$_6$)$_2$	[**4b**](PF$_6$)$_2$
Chemical formula	$C_{31}H_{27}N_7Ru\cdot 2(F_6P)$	$C_{29}H_{30}N_6ORuS\cdot 2(F_6P)$
M_r	888.60	901.66
Crystal system	Orthorhombic	Monoclinic
Space group	$P2_12_12_1$	$P2_{1/c}$
Cell lengths (*a, b, c*)(Å)	8.72848 (13), 9.82300 (13), 37.8019 (5)	18.8561 (8), 8.4130 (3), 20.9072 (11)
Cell angles (α, β, γ)(°)	90, 90, 90	90, 95.833 (4), 90
Cell volume (Å^3)	3241.13 (8)	3299.5 (3)
Z	4	4
μ (mm^{-1})	5.83	6.33
Crystal size (mm)	0.33 × 0.07 × 0.03	0.13 × 0.01 × 0.01
Temperature (K)	110(2)	110(2)
Diffractometer	SuperNova, Dual, Cu at zero, Atlas detector	XtaLAB Synergy R, HyPix
Radiation type	Cu *Kα*	Cu *Kα*
T_{min}, T_{max}	0.388, 0.879	0.697, 0.938
No. of measured, independent and observed [$I > 2\sigma(I)$] reflections	26948, 6263, 5958	24143, 6978, 4115
R_{int}	0.036	0.090
(sin θ/λ)$_{max}$ (Å^{-1})	0.616	0.598
$R[F^2 > 2\sigma(F^2)]$, $wR(F^2)$, S	0.026, 0.061, 1.04	0.057, 0.133, 0.88
No. of reflections	6263	6978
No. of parameters	538	589
No. of restraints	279	487
H-atom treatment	H-atom parameters constrained	H-atom parameters constrained
$\Delta\rho_{max}$, $\Delta\rho_{min}$ (e Å^{-3})	0.52, -0.47	1.112, -1.17

III.2 Photochemistry

III.2.1 Molar extinction coefficient determination

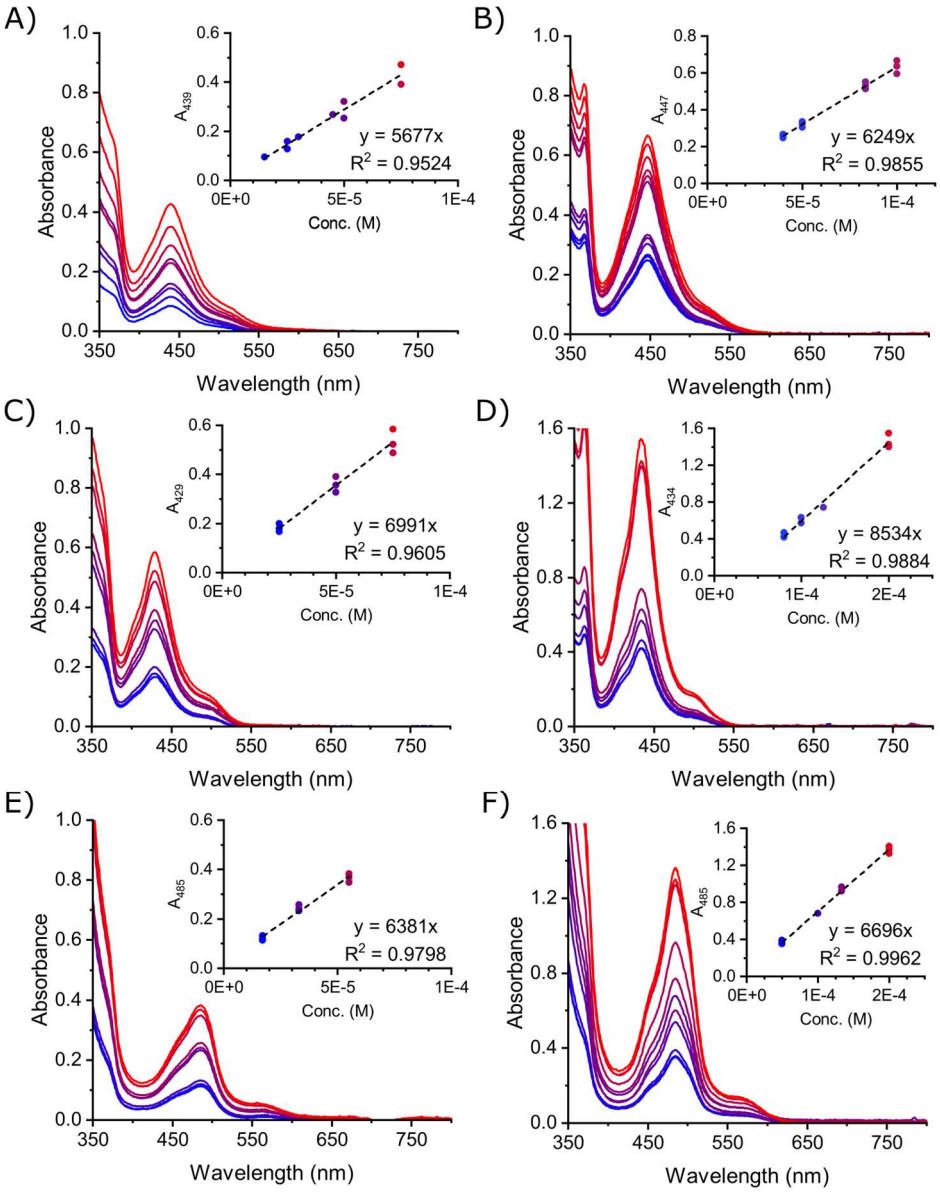

Figure III.1 UV-Vis absorbance spectra of complexes at different concentrations in 3 ml 20% acetone in H_2O at 298 K (l = 1 cm). Insets depict absorption at λ_{max} at different concentrations. A) [**1a**]$(PF_6)_2$: $\varepsilon = 5.68 \times 10^3$ M^{-1} cm^{-1} at 439 nm. B) [**1b**]$(PF_6)_2$: $\varepsilon = 6.25 \times 10^3$ M^{-1} cm^{-1} at 447 nm. C) [**2a**]$(PF_6)_2$: $\varepsilon = 6.99 \times 10^3$ M^{-1} cm^{-1} at 429 nm. D) [**2b**]$(PF_6)_2$: $\varepsilon = 8.53 \times 10^3$ M^{-1} cm^{-1} at 434 nm. E) [**3a**]$(PF_6)_2$: $\varepsilon = 6.38 \times 10^3$ M^{-1} cm^{-1} at 485 nm. F) [**3b**]$(PF_6)_2$: $\varepsilon = 6.70 \times 10^3$ M^{-1} cm^{-1} at 485 nm.

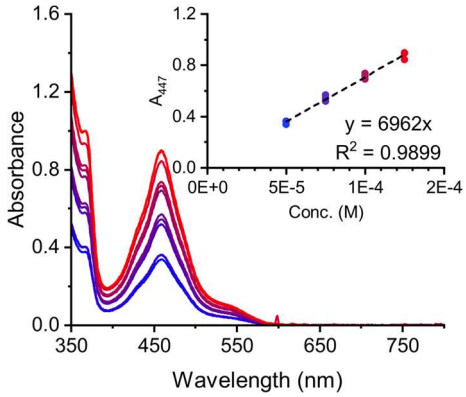

Figure III.2 UV-Vis absorbance spectra of [**4b**]$(PF_6)_2$ at different concentrations in 3 ml 20% acetone in H_2O at 298 K (l = 1 cm). Insets depict absorption at λ_{max} at different concentrations; $\varepsilon = 6.96 \times 10^3\ M^{-1}\ cm^{-1}$ at 447 nm.

III.2.2 Photosubstitution quantum yield measurements

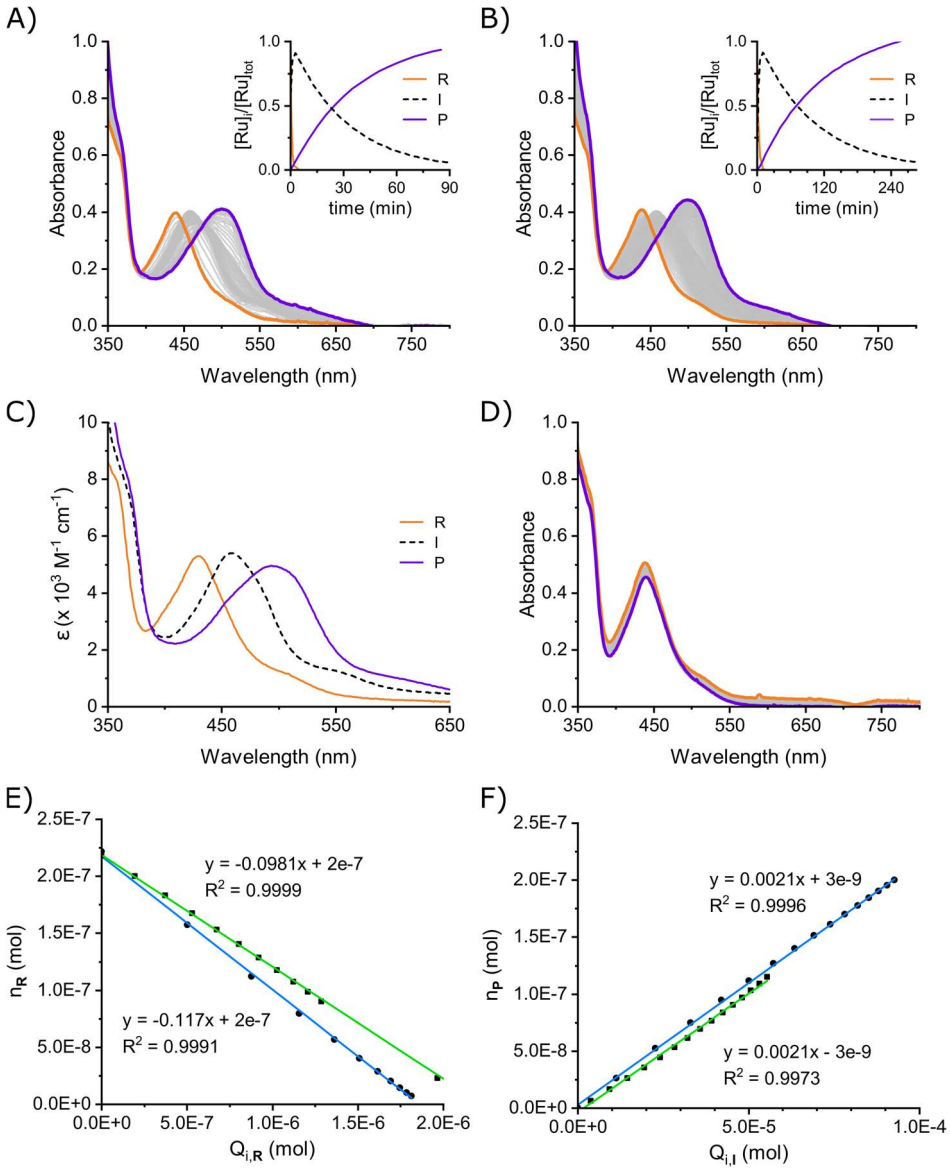

Figure III.3 Graphs for photosubstitution quantum yield for [**1a**]$(PF_6)_2$ at 298 K in 20% acetone in H_2O. Time-evolution of UV-Vis absorbance upon irradiation with A) 435 nm (photon flux = 5.09×10^{-8} mol/s) for 85 min at 73.8 µM and B) 505 nm (photon flux = 2.95×10^{-8} mol/s) for 285 min at 72.8 µM (from orange to purple). C) Globally fitted UV-Vis absorption spectra of [**1a**]$^{2+}$ (R; orange line), the intermediate [**5a**]$^{2+}$ (I; black dashed) and the photoproduct [**8a**]$^{2+}$ (P; purple line). D) Absorption spectra of [**1a**]$(PF_6)_2$ in the dark for 15 h (from orange to purple). E) Plot of n_R against $Q_{i,R}$ used to calculate the first step photosubstitution quantum yield. F) Plot of n_P against $Q_{i,I}$ used to calculate the second step photosubstitution quantum yield.

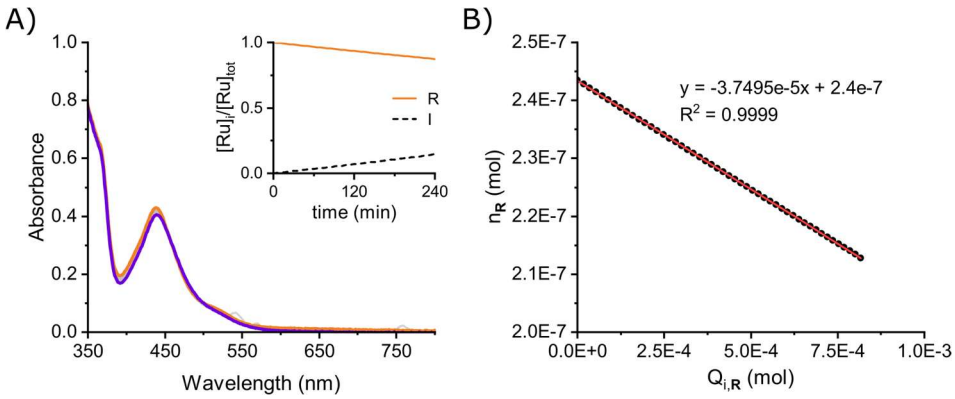

Figure III.4 Graphs for photosubstitution quantum yield for [**1a**]$(PF_6)_2$ at 298 K in 20% acetone in H_2O. A) Time-evolution of UV-Vis absorbance upon irradiation with 625 nm (photon flux = 4.85×10^{-7} mol/s) for 4 h at 81.2 µM (from orange to purple). B) Plot of $n_{\mathbf{R}}$ against $Q_{i,\mathbf{R}}$ used to calculate the first step photosubstitution quantum yield.

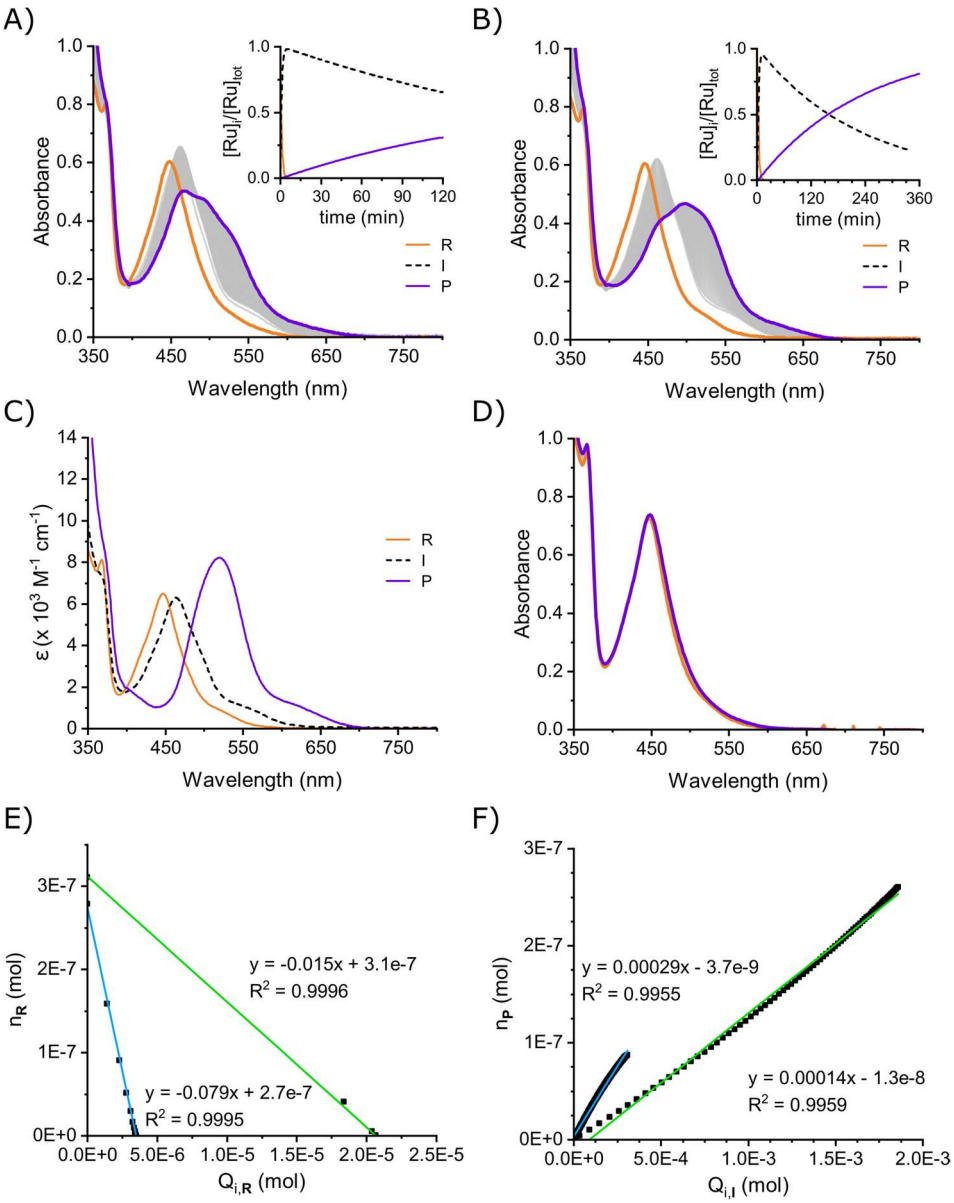

Figure III.5 Graphs for photosubstitution quantum yield for [**1b**](PF$_6$)$_2$ at 298 K in 20% acetone in H$_2$O. Time-evolution of UV-Vis absorbance upon irradiation with A) 435 nm (photon flux = 5.70 × 10^{-8} mol/s) for 120 min at 90.7 µM and B) 505 nm (photon flux = 2.28 × 10^{-7} mol/s) for 360 min at 100.7 µM (from orange to purple). C) Globally fitted UV-Vis absorption spectra of [**1b**](PF$_6$)$_2$ (R; orange line), the intermediate [**5b**]$^{2+}$ (I; black dashed) and the photoproduct [**8b**]$^{2+}$ (P; purple line). D) Absorption spectra of [**1b**](PF$_6$)$_2$ in the dark for 12 h (from orange to purple). E) Plot of n_R against $Q_{i,R}$ used to calculate the first step photosubstitution quantum yield. F) Plot of n_P against $Q_{i,I}$ used to calculate the second step photosubstitution quantum yield.

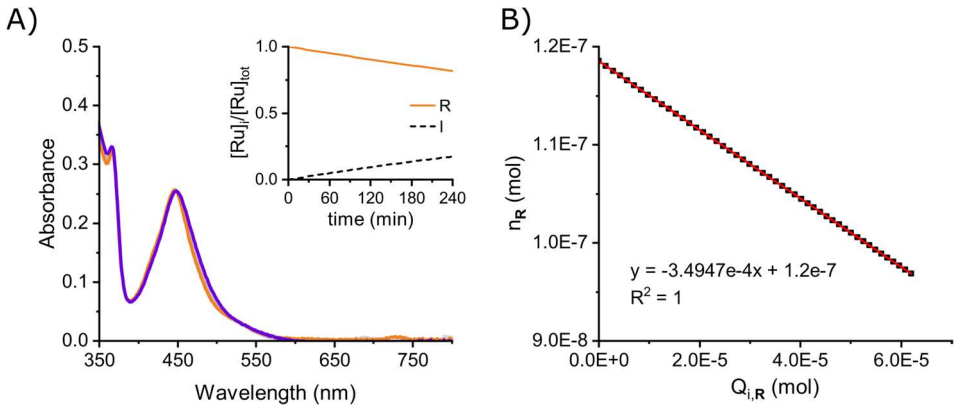

Figure III.6 Graphs for photosubstitution quantum yield for [**1b**]$(PF_6)_2$ at 298 K in 20% acetone in H_2O. A) Time-evolution of UV-Vis absorbance upon irradiation with 625 nm (photon flux = 4.83×10^{-7} mol/s) for 4 h at 44.4 µM (from orange to purple). B) Plot of $n_{\mathbf{R}}$ against $Q_{i,\mathbf{R}}$ used to calculate the first step photosubstitution quantum yield.

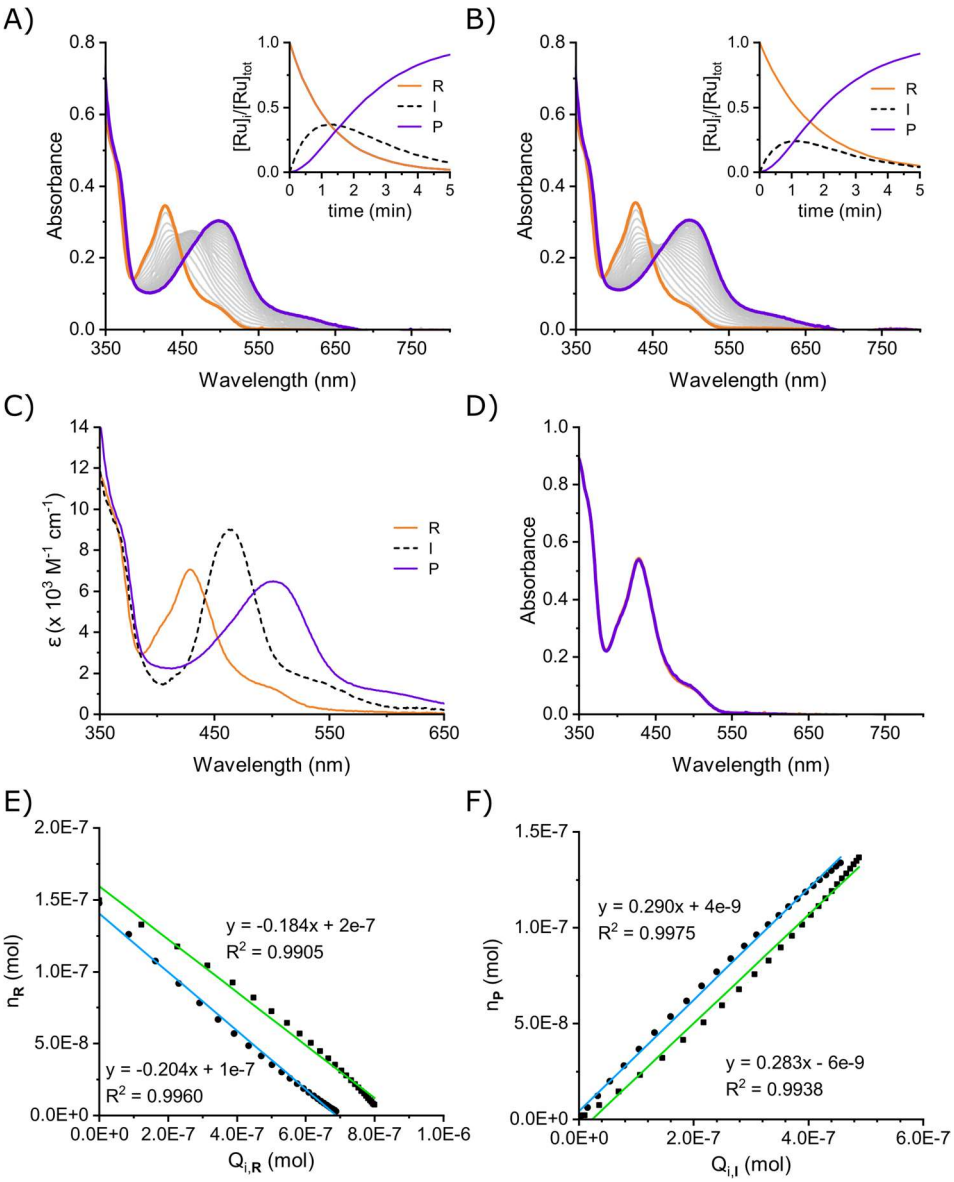

Figure III.7 Graphs for photosubstitution quantum yield for [**2a**]$(PF_6)_2$ at 298 K in 20% acetone in H_2O. Time-evolution of UV-Vis absorbance upon irradiation with A) 435 nm (photon flux = 8.54×10^{-9} mol/s) for 5 min at 49.2 µM and B) 505 nm (photon flux = 2.92×10^{-8} mol/s) for 5 min at 49.9 µM (from orange to purple). C) Globally fitted UV-Vis absorption spectra of [**2a**]$(PF_6)_2$ (R; orange line), the intermediate [**6a**]$^{2+}$ (I; black dashed) and the photoproduct [**8a**]$^{2+}$ (P; purple line). D) Absorption spectra of [**2a**]$(PF_6)_2$ in the dark for 130 min (from orange to purple). E) Plot of n_R against $Q_{i,R}$ used to calculate the first step photosubstitution quantum yield. F) Plot of n_P against $Q_{i,I}$ used to calculate the second step photosubstitution quantum yield.

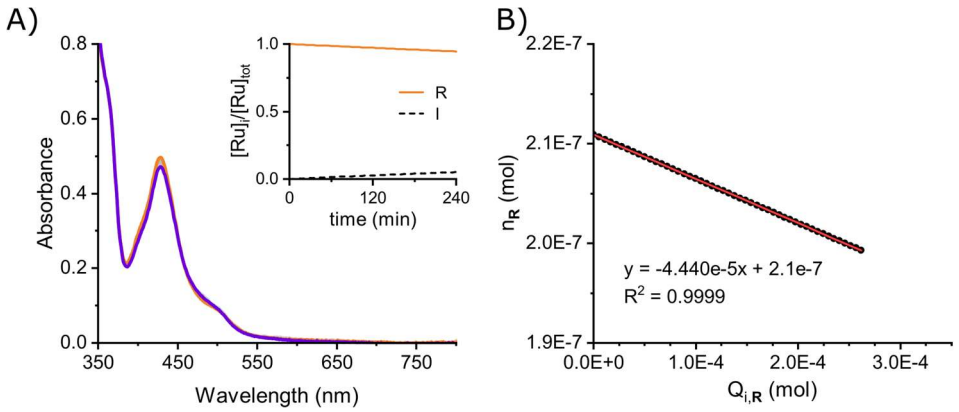

Figure III.8 Graphs for photosubstitution quantum yield for [**2a**]$(PF_6)_2$ at 298 K in 20% acetone in H_2O. A) Time-evolution of UV-Vis absorbance upon irradiation with 625 nm (photon flux = 4.85×10^{-7} mol/s) for 4 h at 70.3 µM (from orange to purple). B) Plot of $n_{\mathbf{R}}$ against $Q_{i,\mathbf{R}}$ used to calculate the first step photosubstitution quantum yield.

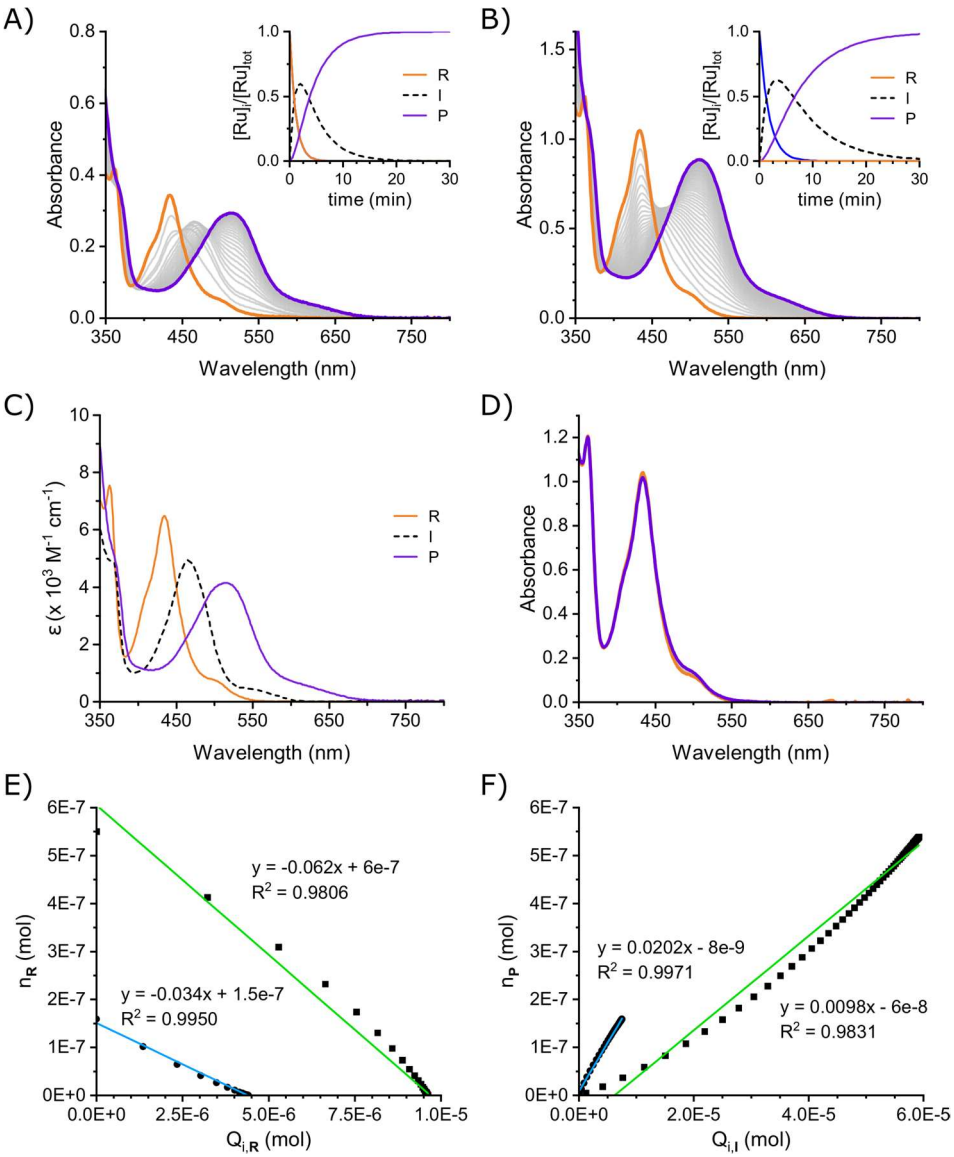

Figure III.9 Graphs for photosubstitution quantum yield for [**2b**]$(PF_6)_2$ at 298 K in 20% acetone in H_2O. Time-evolution of UV-Vis absorbance upon irradiation with A) 435 nm (photon flux = 5.70×10^{-8} mol/s) for 30 min at 53.0 μM and B) 505 nm (photon flux = 2.28×10^{-7} mol/s) for 30 min at 183 μM) (from orange to purple). C) Globally fitted UV-Vis absorption spectra of [**2b**]$(PF_6)_2$ (R; orange line), the intermediate [**6b**]$^{2+}$ (Int; black dashed) and the photoproduct [**8b**]$^{2+}$ (P; purple line). D) Absorption spectra of [**2b**]$(PF_6)_2$ in the dark for 130 min (from orange to purple). E) Plot of n_R against $Q_{i,R}$ used to calculate the first step photosubstitution quantum yield. F) Plot of n_P against $Q_{i,I}$ used to calculate the second step photosubstitution quantum yield.

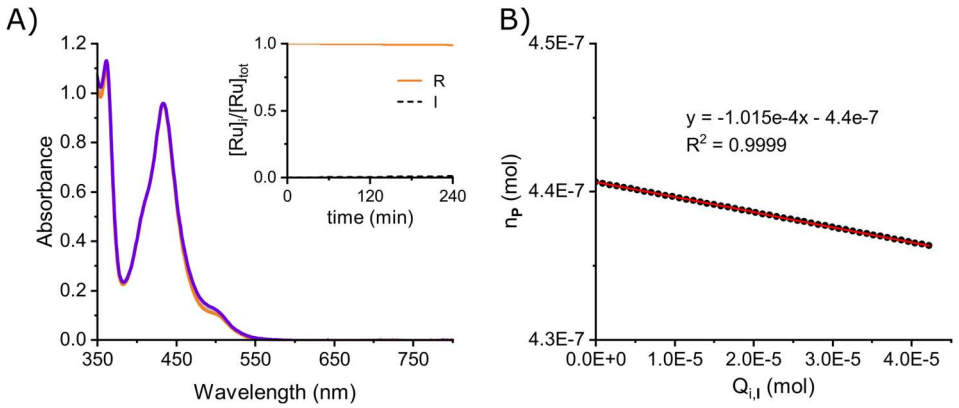

Figure III.10 Graphs for photosubstitution quantum yield for [**2b**]$(PF_6)_2$ at 298 K in 20% acetone in H_2O. A) Time-evolution of UV-Vis absorbance upon irradiation with 625 nm (photon flux = 4.84×10^{-7} mol/s) for 4 h at 147 µM (from orange to purple). B) Plot of $n_{\mathbf{R}}$ against $Q_{i,\mathbf{R}}$ used to calculate the first step photosubstitution quantum yield.

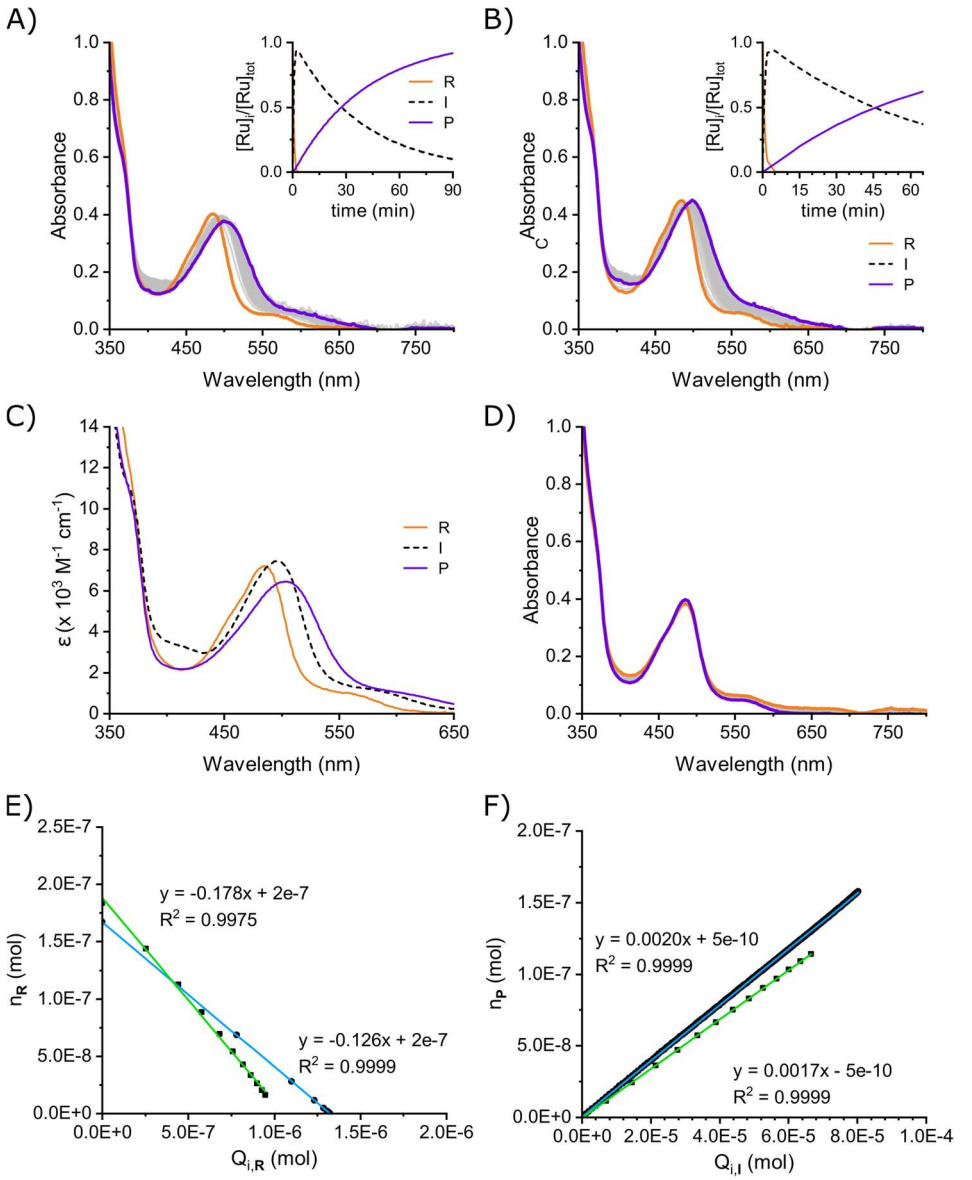

Figure III.11 Graphs for photosubstitution quantum yield for [**3a**](PF$_6$)$_2$ at 298 K in 20% acetone in H$_2$O. Time-evolution of UV-Vis absorbance upon irradiation with A) 435 nm (photon flux = 5.27 × 10^{-8} mol/s) for 100 min at 55.7 µM and B) 505 nm (photon flux = 2.95 × 10^{-8} mol/s) for 65 min at 61.1 µM) (from orange to purple). C) Globally fitted UV-Vis absorption spectra of [**3a**](PF$_6$)$_2$ (R; orange line), the intermediate [**7a**]$^{2+}$ (I; black dashed) and the photoproduct [**8a**]$^{2+}$ (P; purple line). D) Absorption spectra of [**3a**](PF$_6$)$_2$ in the dark for 260 min (from orange to purple). E) Plot of n_R against $Q_{i,R}$ used to calculate the first step photosubstitution quantum yield. F) Plot of n_P against $Q_{i,I}$ used to calculate the second step photosubstitution quantum yield.

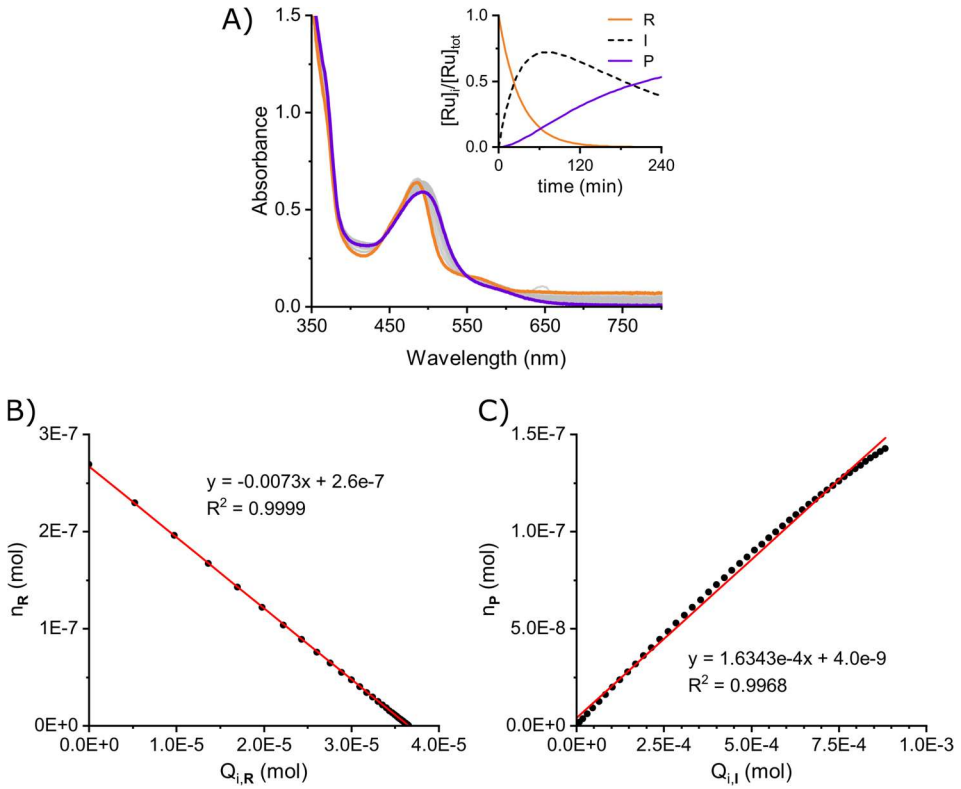

Figure III.12 Graphs for photosubstitution quantum yield for [**3a**]$(PF_6)_2$ at 298 K in 20% acetone in H_2O. A) Time-evolution of UV-Vis absorbance upon irradiation with 625 nm (photon flux = 4.85×10^{-7} mol/s) for 4 h at 89.6 µM (from orange to purple). B) Plot of n_R against $Q_{i,R}$ used to calculate the first step photosubstitution quantum yield. C) Plot of n_P against $Q_{i,I}$ used to calculate the second step photosubstitution quantum yield.

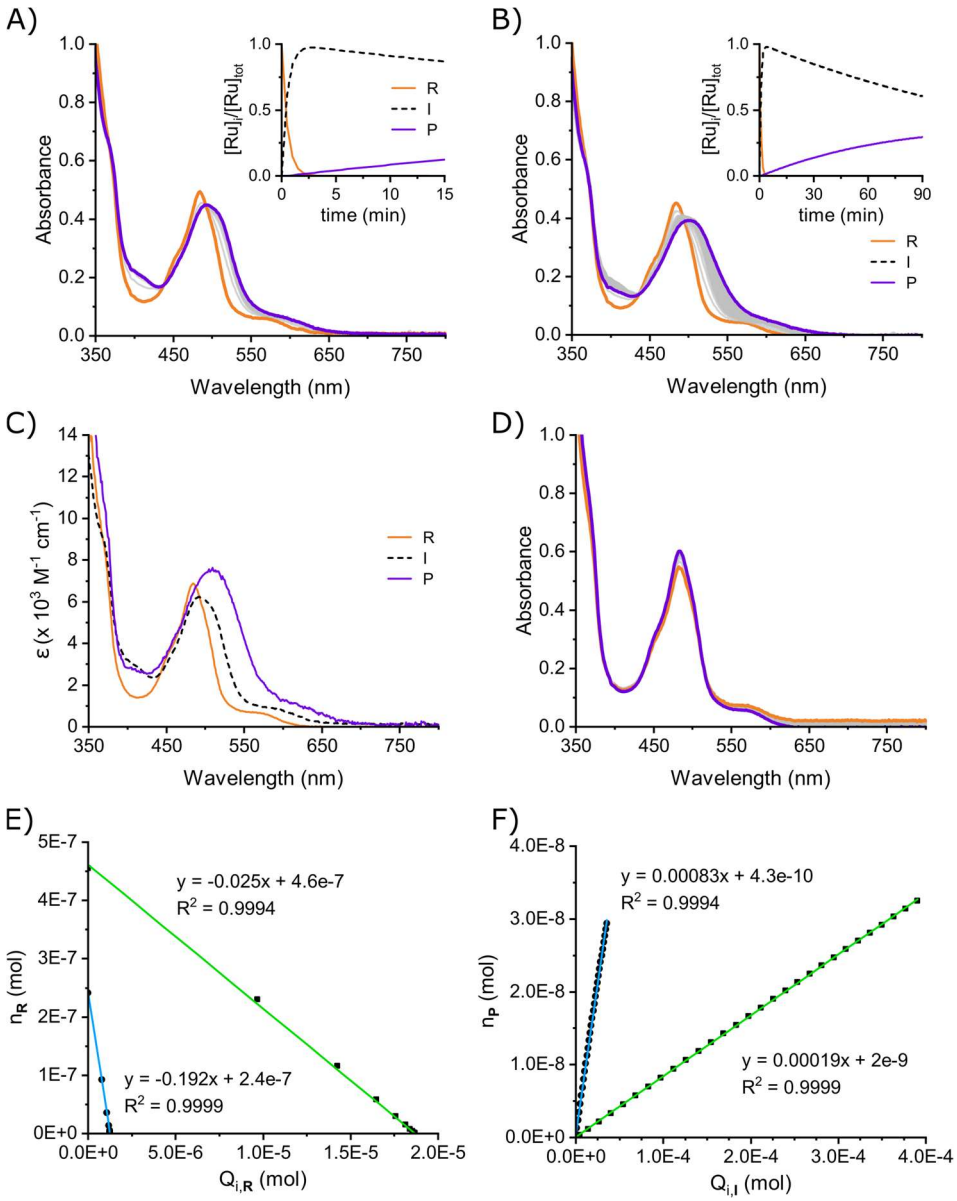

Figure III.13 Graphs for photosubstitution quantum yield for [**3b**](PF$_6$)$_2$ at 298 K in 20% acetone in H$_2$O. Time-evolution of UV-Vis absorbance upon irradiation with A) 435 nm (photon flux = 5.70 × 10^{-8} mol/s) for 15 min at 72.9 μM and B) 505 nm (photon flux = 2.28 × 10^{-7} mol/s) for 90 min at 137.8 μM) (from orange to purple). C) Globally fitted UV-Vis absorption spectra of [**3b**](PF$_6$)$_2$ (R; orange line), the intermediate [**7b**]$^{2+}$ (Int; black dashed) and the photoproduct [**8b**]$^{2+}$ (P; purple line). D) Absorption spectra of [**3b**](PF$_6$)$_2$ in the dark for 15 h (from orange to purple). E) Plot of n_R against $Q_{i,R}$ used to calculate the first step photosubstitution quantum yield. F) Plot of n_P against $Q_{i,I}$ used to calculate the second step photosubstitution quantum yield.

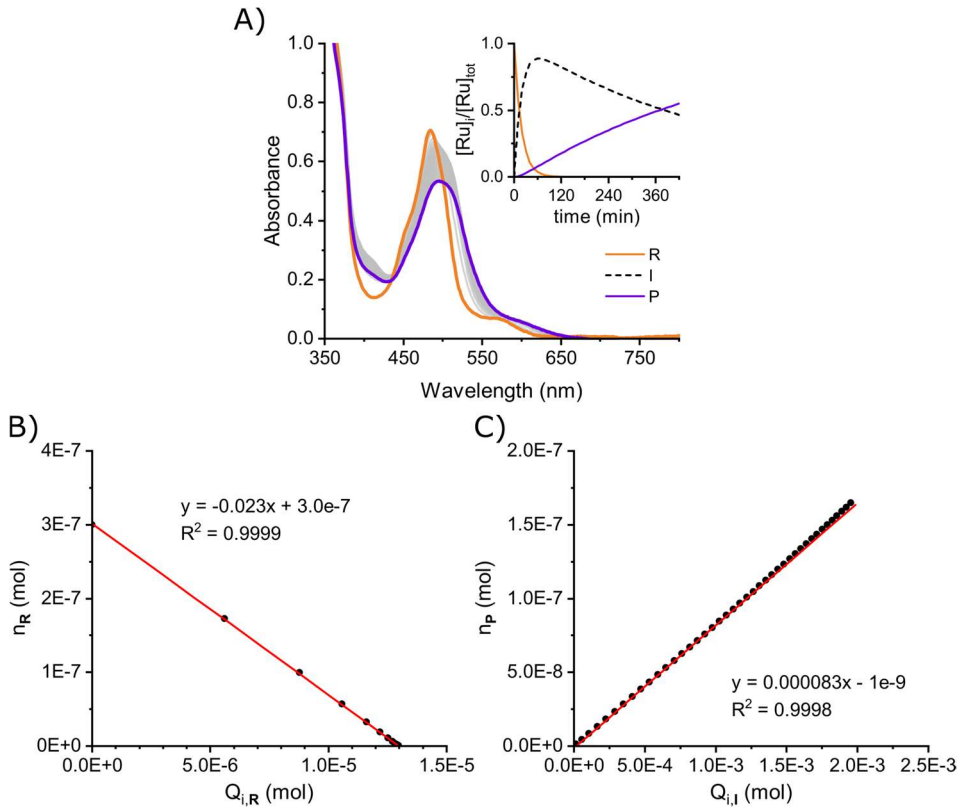

Figure III.14 Graphs for photosubstitution quantum yield for [**3b**]$(PF_6)_2$ at 298 K in 20% acetone in H_2O. A) Time-evolution of UV-Vis absorbance upon irradiation with 625 nm (photon flux = 4.24×10^{-7} mol/s) for 7 h at 100.0 µM (from orange to purple). B) Plot of n_R against $Q_{i,R}$ used to calculate the first step photosubstitution quantum yield. C) Plot of n_P against $Q_{i,I}$ used to calculate the second step photosubstitution quantum yield.

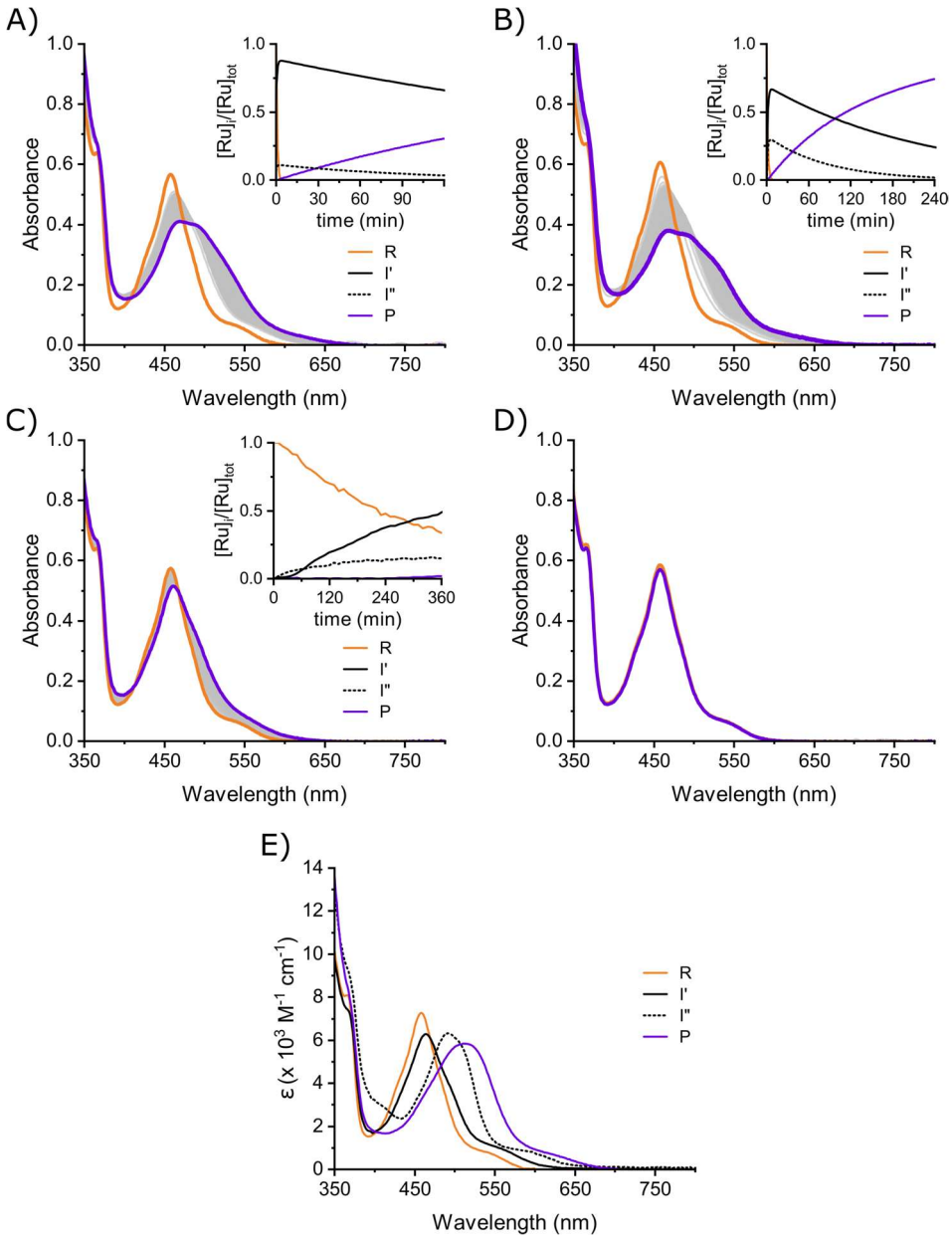

Figure III.15 Time-evolution of UV-Vis absorbance of [**4b**]$(PF_6)_2$ at 298 K in 20% acetone in H_2O when irradiated with A) 435nm (photon flux = 3.29×10^{-7} mol/s; 84.1 µM; 120 min), B) 505nm (photon flux = 2.00×10^{-7} mol/s; 83.3 µM; 240 min), C) 625 nm (photon flux = 4.24×10^{-7} mol/s; 84.1 µM; 360 min) and D) in the dark (84.1 µM; 12 h) (from orange to purple). E) Globally fitted UV-Vis absorption spectra of [**4b**]$(PF_6)_2$ (R; orange line), [**5b**]$^{2+}$ (I'; black solid), [**7b**]$^{2+}$ (I''; black dashed) and [**8b**]$^{2+}$ (P; purple line).

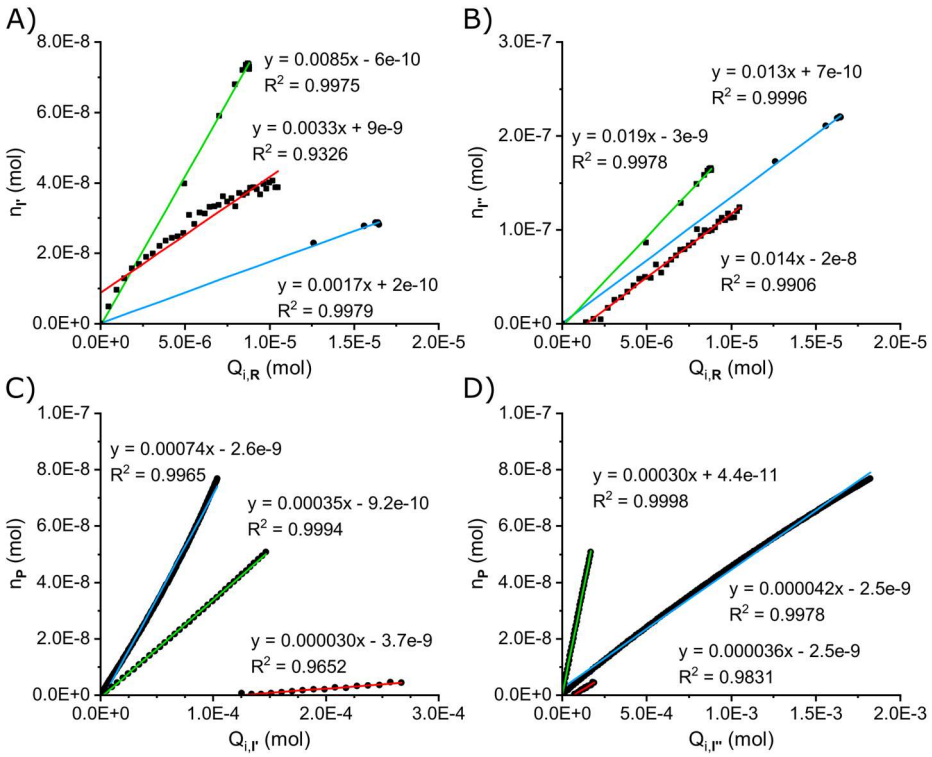

Figure III.16 Graphs for photosubstitution quantum yields for [**4b**]$(PF_6)_2$ at 298 K in 20% acetone in H_2O upon irradiation with 435 nm, 505 nm or 625 nm. A) [**4b**]$^{2+}$ → [**7b**]$^{2+}$ ($\varphi_{1,S}$). B) [**4b**]$^{2+}$ → [**5b**]$^{2+}$ ($\varphi_{1,N}$). C) [**7b**]$^{2+}$ → [**8b**]$^{2+}$ ($\varphi_{2,S}$). D) [**5b**]$^{2+}$ → [**8b**]$^{2+}$ ($\varphi_{1,N}$).

III.2.3 ^{1}H-NMR photosubstitution

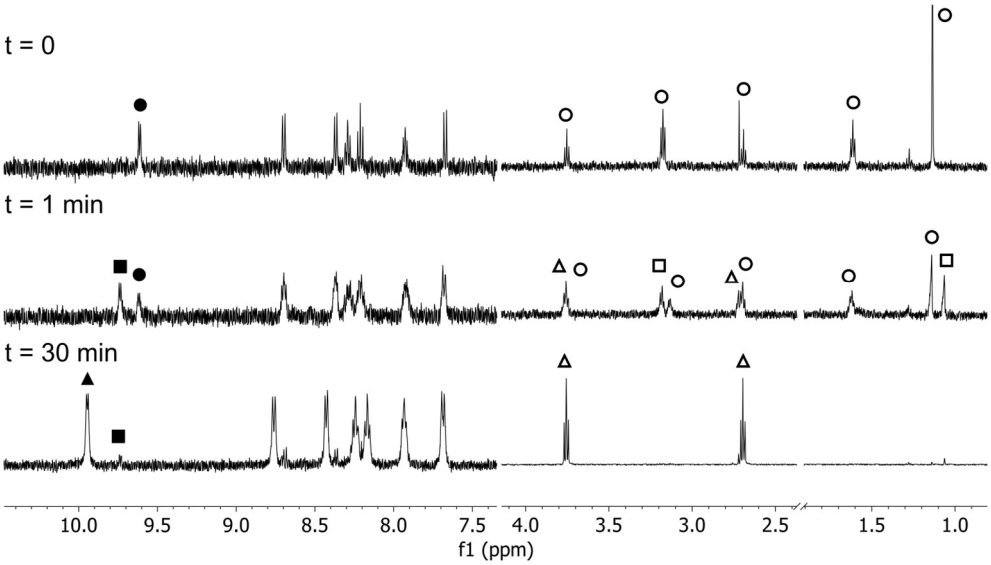

Figure III.17 ^{1}H-NMR spectra evolution of [**1a**](PF$_6$)$_2$ (● for complex, ○ for MTE) in 1/5 acetone-d6/D$_2$O at 298 K during irradiation with white light. Symbols indicate intermediate (■ for complex, □ for MTE), photoproduct (▲) and free MTE (△).

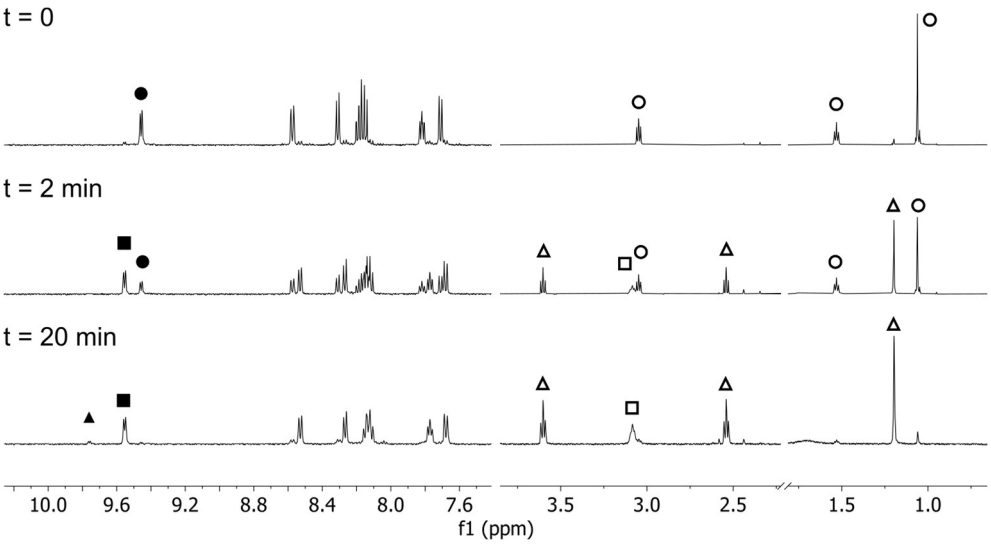

Figure III.18 ^{1}H-NMR spectra evolution of [**1b**](PF$_6$)$_2$ (● for complex, ○ for MTE) in 1/5 acetone-d6/D$_2$O at 298 K during irradiation with 530 nm. Symbols indicate intermediate (■ for complex, □ for MTE), photoproduct (▲) and free MTE (△).

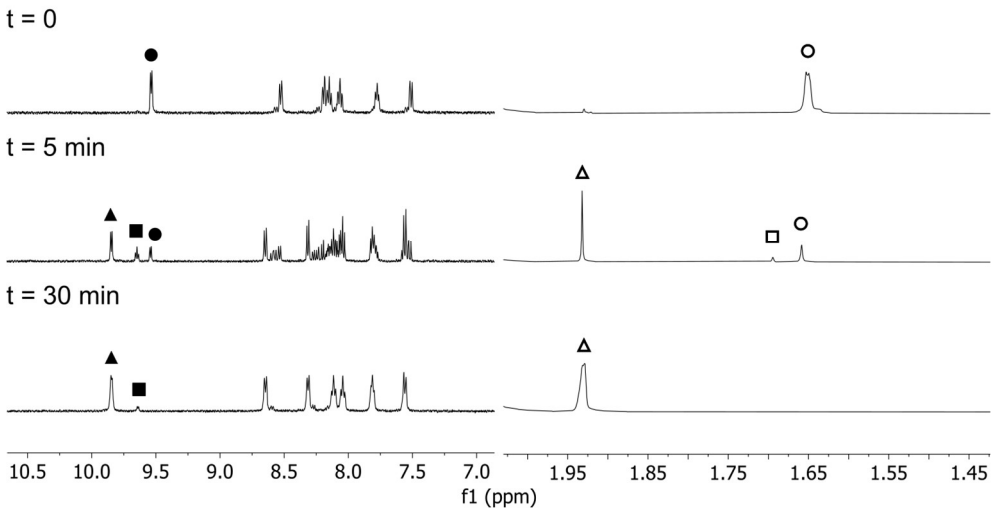

Figure III.19 ^{1}H-NMR spectra evolution of [**2a**](PF$_6$)$_2$ (● for complex, ○ for ACN) in 1/5 acetone-d6/D$_2$O at 298 K during irradiation with white light. Symbols indicate intermediate (■ for complex, □ for ACN), photoproduct (▲) and free ACN (△).

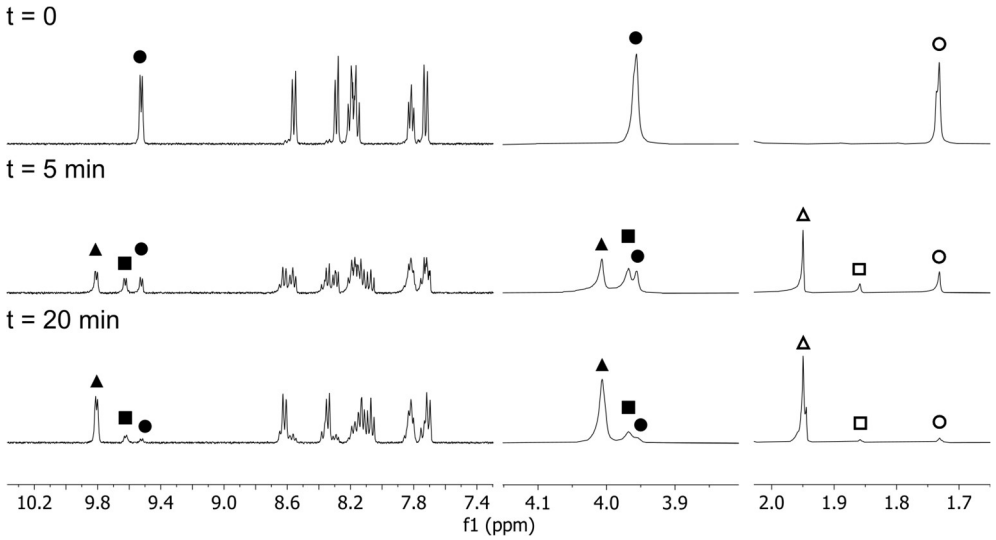

Figure III.20 ^{1}H-NMR spectra evolution of [**2b**](PF$_6$)$_2$ (● for complex, ○ for ACN) in 1/3 acetone-d6/D$_2$O at 298 K during irradiation with 530 nm. Symbols indicate intermediate (■ for complex, □ for ACN), photoproduct (▲) and free ACN (△).

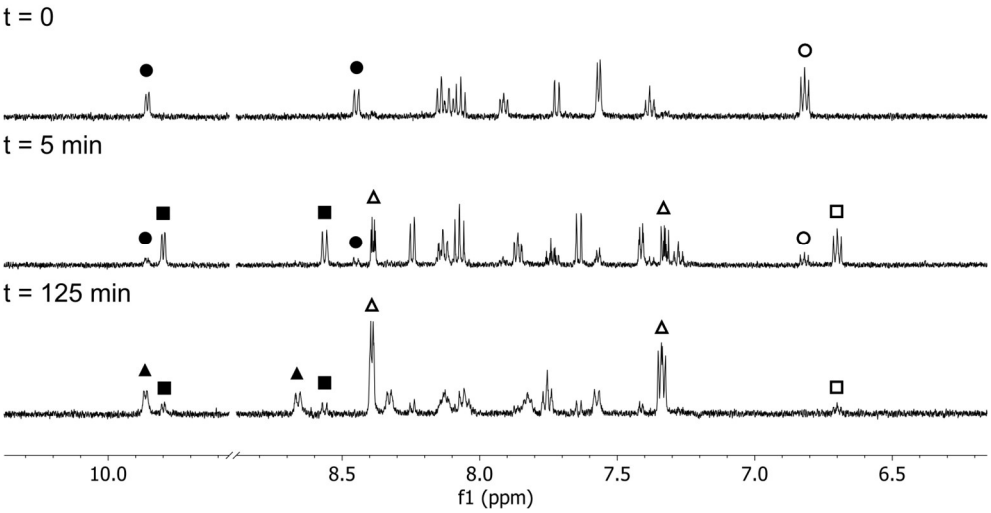

Figure III.21 ^{1}H-NMR spectra evolution of [**3a**]$(PF_6)_2$ (● for complex, ○ for pyridine) in 1/5 acetone-d6/D_2O at 298 K during irradiation with white light. Symbols indicate intermediate (■ for complex, □ for pyridine), photoproduct (▲) and free pyridine (△).

III.3 Characterization of synthesized compounds

V.3.1 $[Ru(L)(MTE)_2](PF_6)_2$ [1a]$(PF_6)_2$

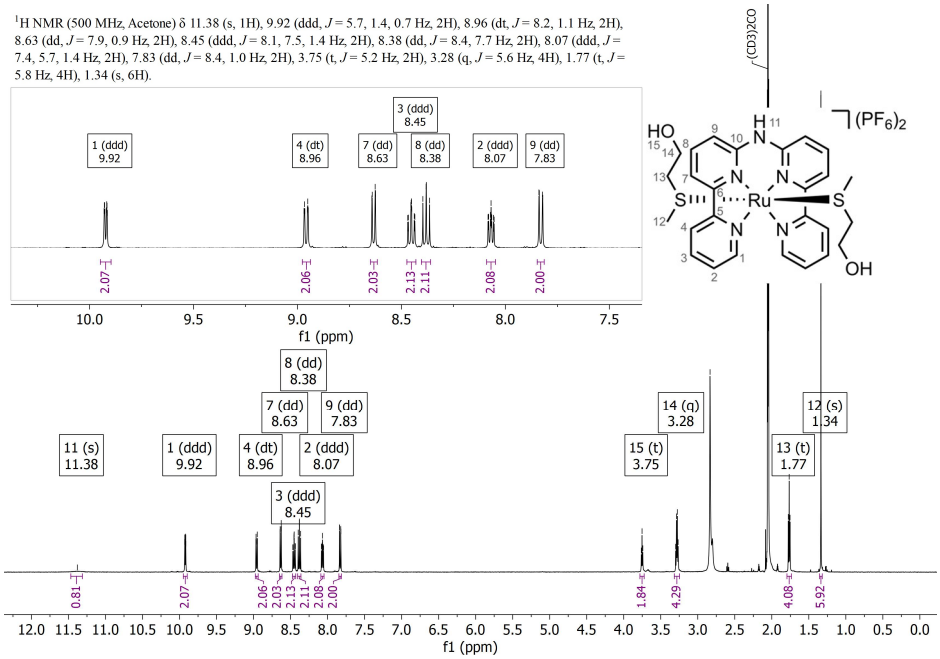

Figure III.22 ^{1}H-NMR of [**1a**]$(PF_6)_2$ in Acetone-d_6.

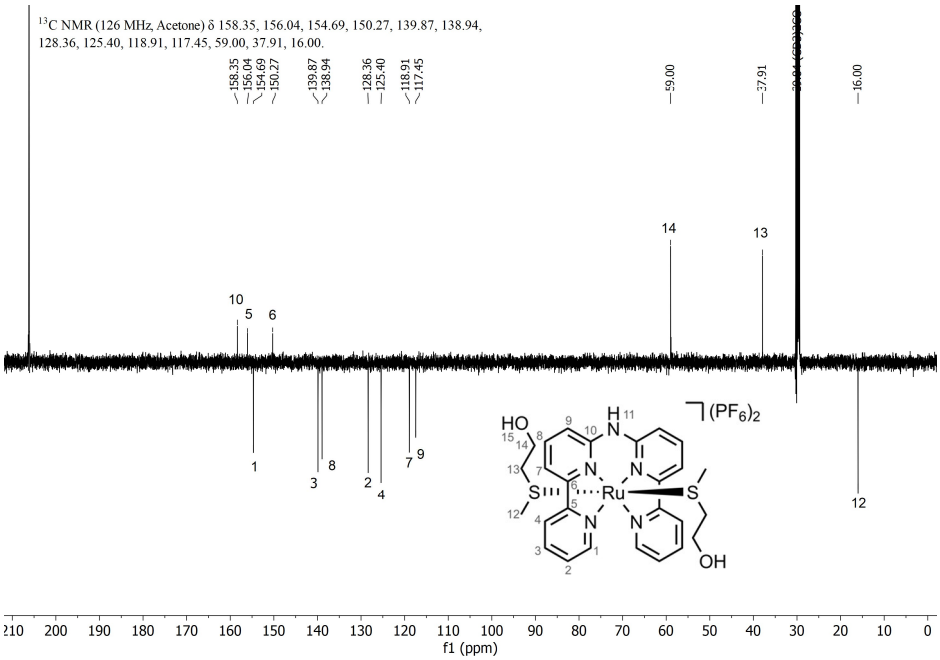

Figure III.23 ^{13}C-APT-NMR of [**1a**]$(PF_6)_2$ in Acetone-d_6.

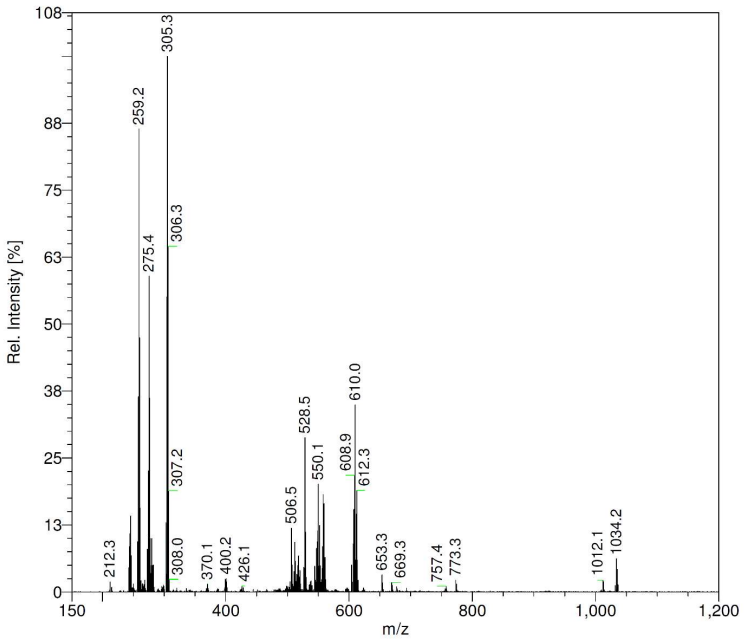

Figure III.24 ESI-MS of [**1a**](PF$_6$)$_2$. Calculated for $[C_{26}H_{31}N_5O_2RuS_2]^{2+}$: 305.6 m/z; $[C_{26}H_{31}N_5O_2RuS_2–H]^{+}$: 610.1 m/z; $[C_{26}H_{31}N_5O_2RuS_2–C_3H_8OS]^{2+}$: 259.5 m/z; $[C_{26}H_{31}N_5O_2RuS_2–C_3H_8OS+C_4HO\ ]^{2+}$: 275.5 m/z.

V.3.2 [Ru(L)(ACN)$_2$](PF$_6$)$_2$ [2a](PF$_6$)$_2$

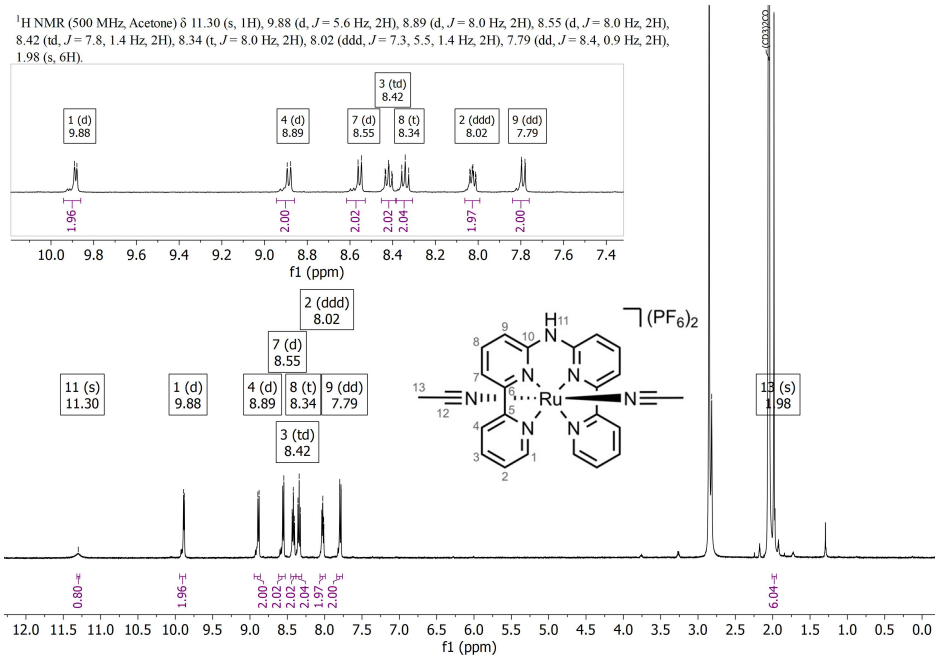

Figure III.25 ^{1}H-NMR of [**2a**](PF$_6$)$_2$ in Acetone-*d$_6$*.

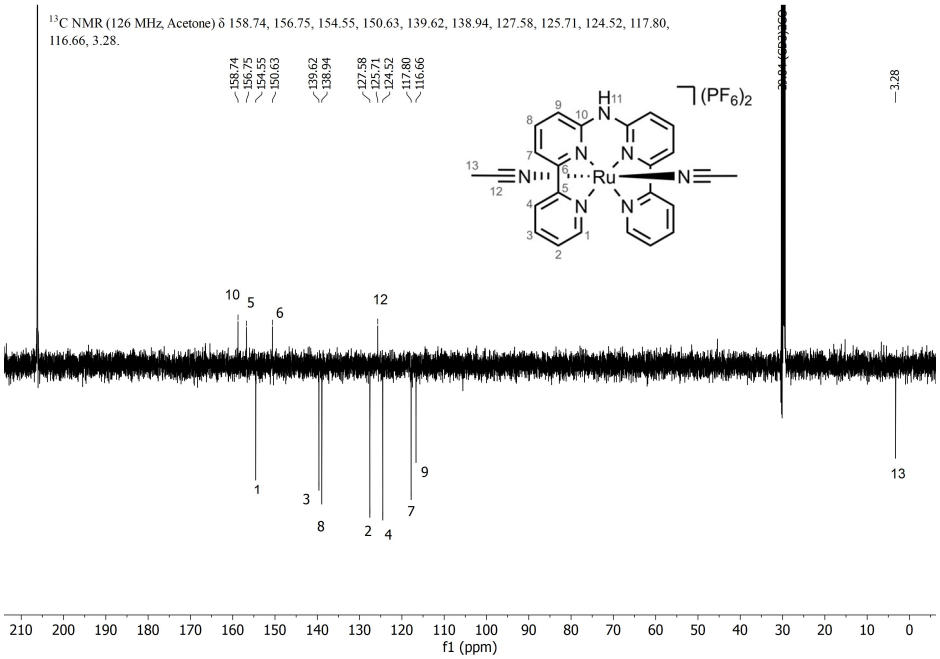

Figure III.26 ^{13}C-APT-NMR of [**2a**](PF$_6$)$_2$ in Acetone-*d*$_6$.

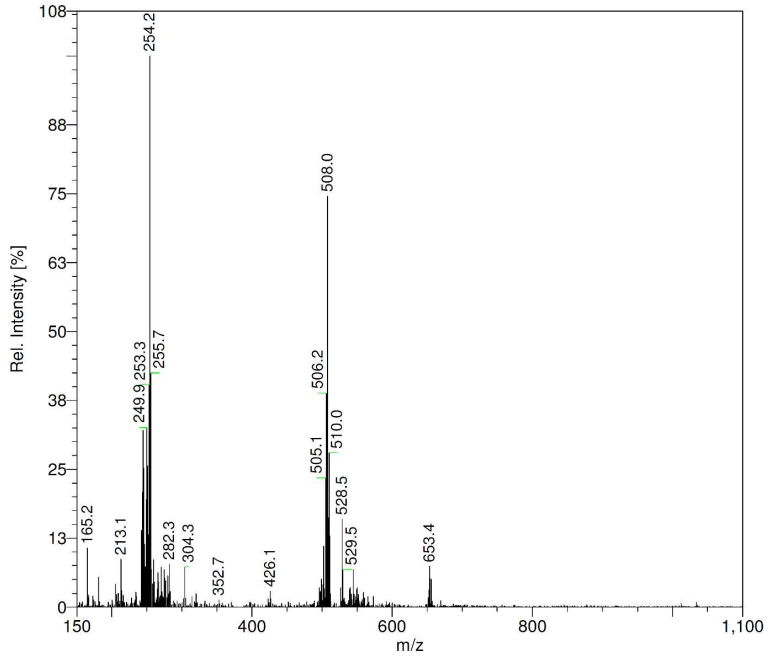

Figure III.27 ESI-MS of [**2a**](PF$_6$)$_2$. Calculated for [$C_{24}H_{21}N_7Ru$]$^{2+}$: 254.5 m/z; [$C_{24}H_{21}N_7Ru$–H]$^{+}$: 508.1 m/z.

V.3.3 [Ru(L)(Py)$_2$](PF$_6$)$_2$ [3a](PF$_6$)$_2$

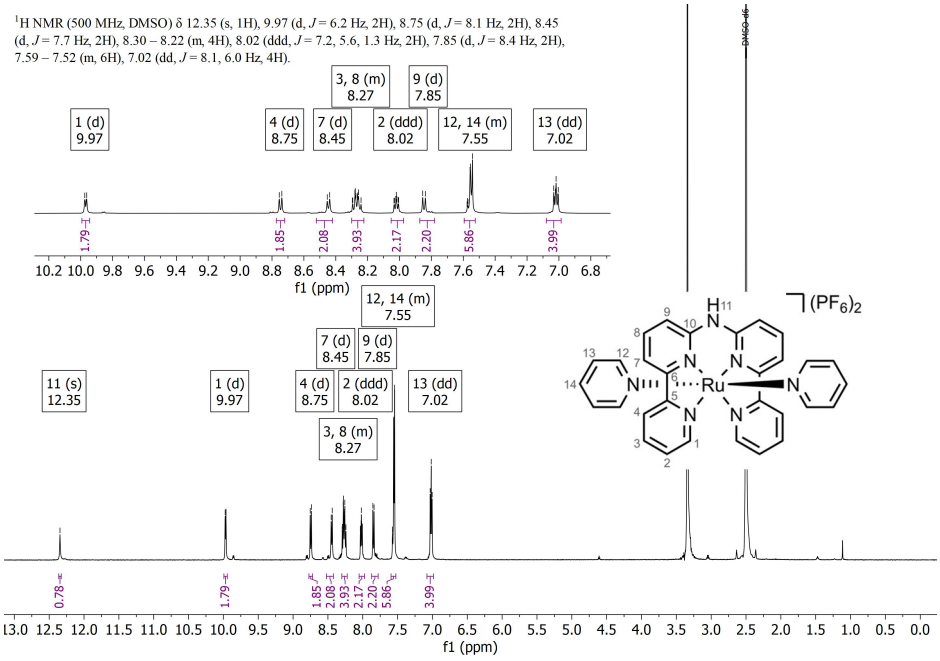

Figure III.28 ^{1}H-NMR of [**3a**](PF$_6$)$_2$ in Acetone-d_6.

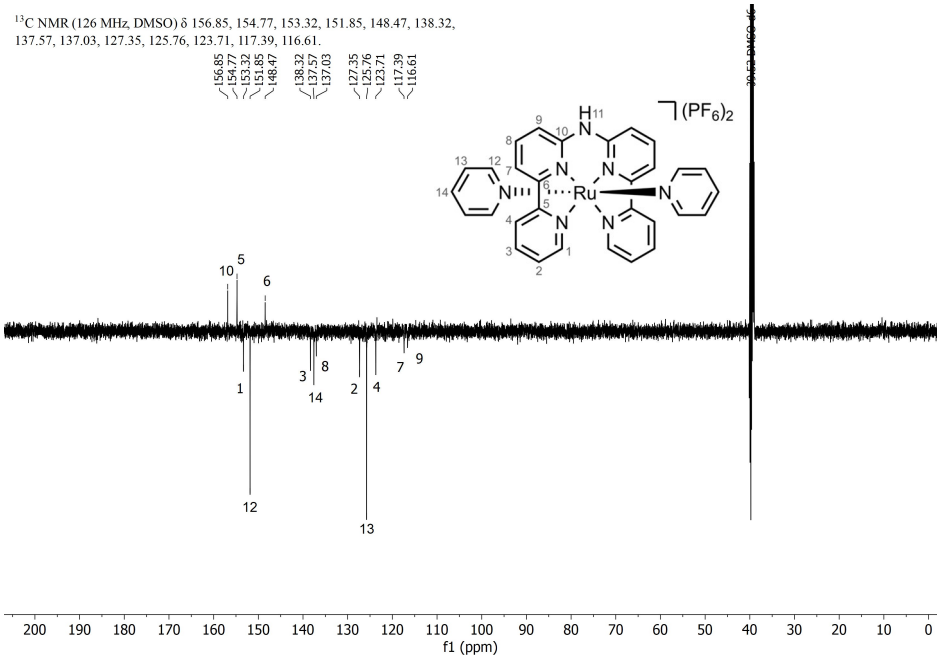

Figure III.29 ^{13}C-APT-NMR of [**3a**](PF$_6$)$_2$ in Acetone-d_6.

III

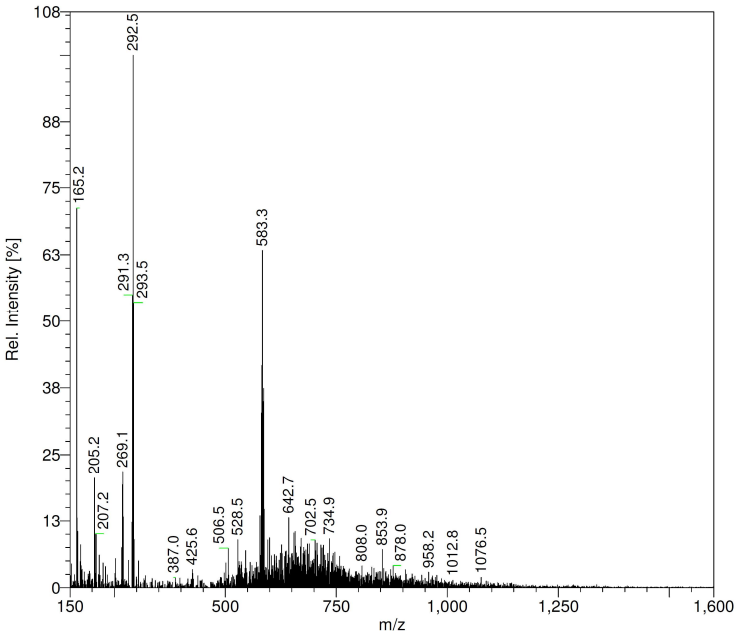

Figure II.30 ESI-MS of [**3a**]$(PF_6)_2$. Calculated for $[C_{30}H_{25}N_7Ru]^{2+}$: 292.6 m/z; $[C_{30}H_{25}N_7Ru–H]^{+}$: 584.3 m/z.

V.3.4 [Ru(MeL)(MTE)$_2$]$(PF_6)_2$ [1b]$(PF_6)_2$

^{1}H NMR (400 MHz, Acetone) δ 9.85 (ddd, J = 5.7, 1.6, 0.8 Hz, 2H), 8.92 (dt, J = 8.1, 1.1 Hz, 2H), 8.66 (dd, J = 7.9, 0.9 Hz, 2H), 8.47 – 8.37 (m, 5H), 8.08 – 7.99 (m, 5H), 4.22 (s, 3H), 3.75 (t, J = 5.2 Hz, 2H), 3.27 (q, J = 5.6 Hz, 4H), 1.80 (t, J = 5.8 Hz, 4H), 1.36 (s, 6H).

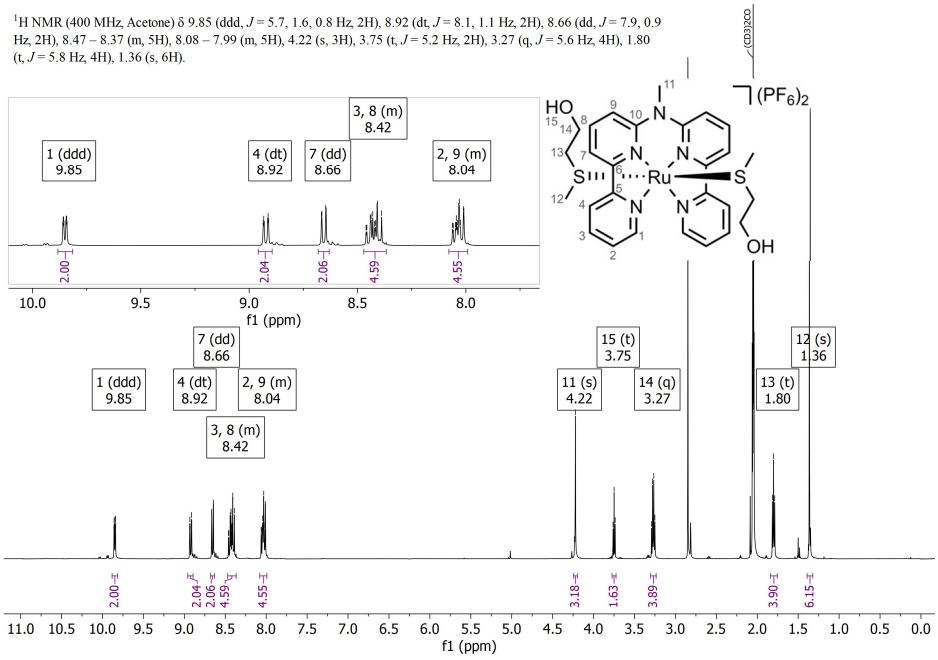

Figure III.31 ^{1}H-NMR of [**1b**]$(PF_6)_2$ in Acetone-d_6.

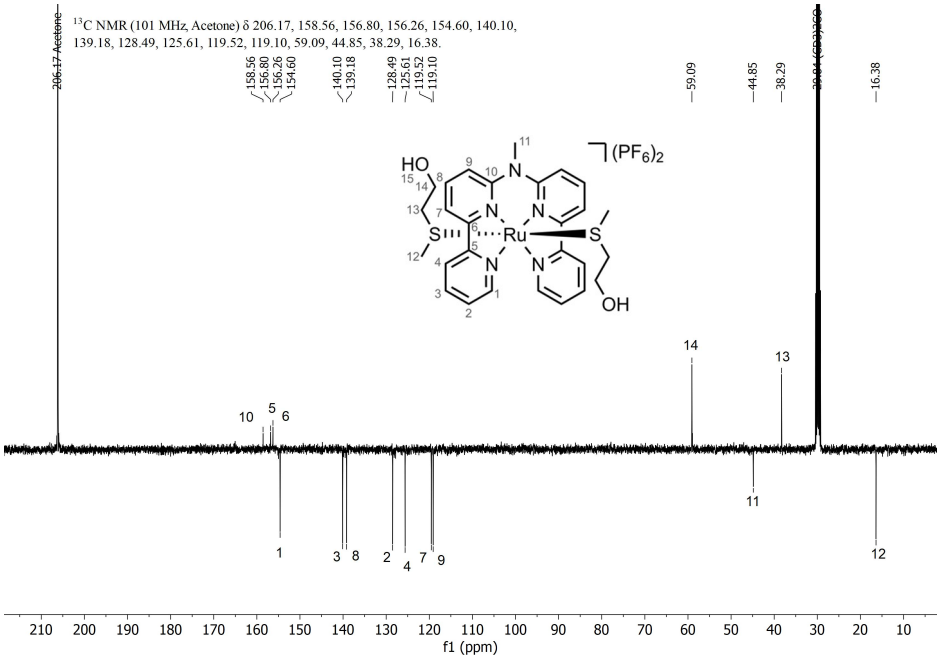

Figure III.32 ^{13}C-APT-NMR of [**1b**](PF$_6$)$_2$ in Acetone-*d*$_6$.

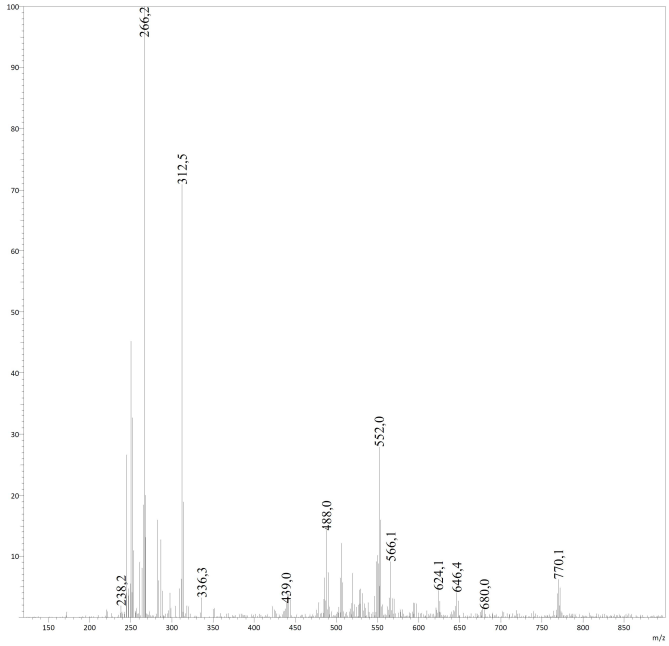

Figure III.33 ESI-MS of [**1b**](PF$_6$)$_2$. Calculated for $[C_{27}H_{33}N_5O_2RuS_2]^{2+}$: 312.6 m/z; $[C_{27}H_{33}N_5O_2RuS_2–C_3H_8OS]^{2+}$: 266.5 m/z; $[C_{27}H_{33}N_5O_2RuS_2–C_3H_8OS+H_2O]^{+}$: 551.1 m/z.

V.3.5 [Ru(MeL)(ACN)$_2$](PF$_6$)$_2$ [2b](PF$_6$)$_2$

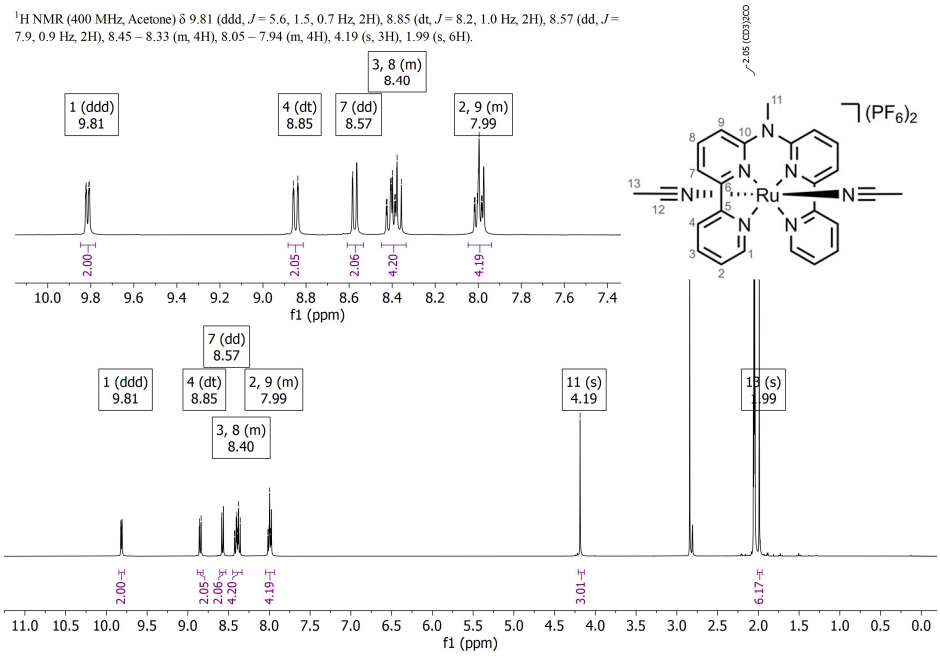

Figure III.34 ^{1}H-NMR of [**2b**](PF$_6$)$_2$ in Acetone-d_6.

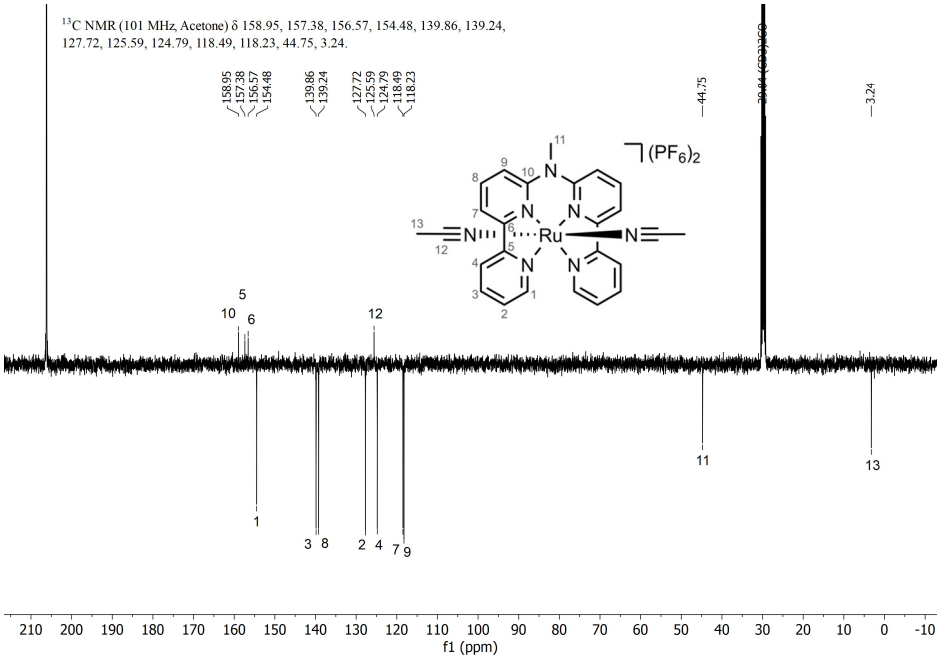

Figure III.35 ^{13}C-APT-NMR of [**2b**](PF$_6$)$_2$ in Acetone-d_6.

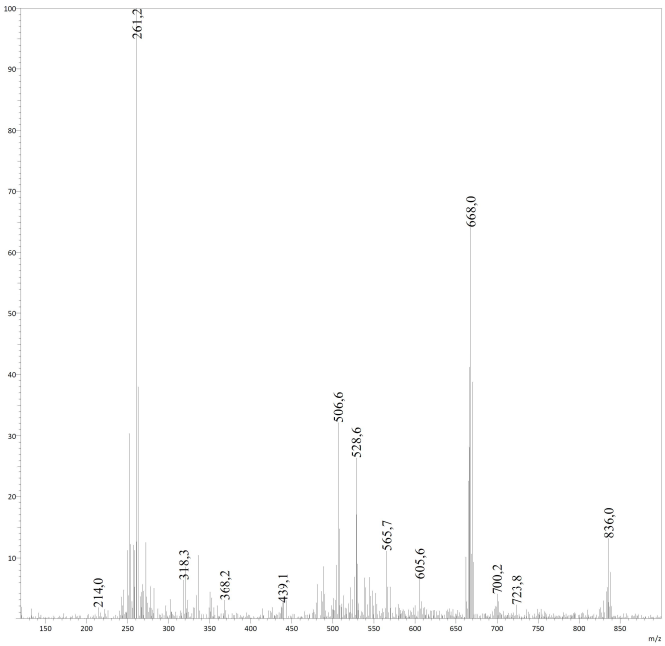

Figure III.36 ESI-MS of [**2b**](PF$_6$)$_2$. Calculated for [$C_{25}H_{23}N_7Ru$]$^{2+}$: 261.5 m/z; [$C_{25}H_{23}N_7Ru$+PF_6]$^+$: 668.1 m/z.

V.3.6 [Ru(MeL)(Py)$_2$](PF$_6$)$_2$ [3b](PF$_6$)$_2$

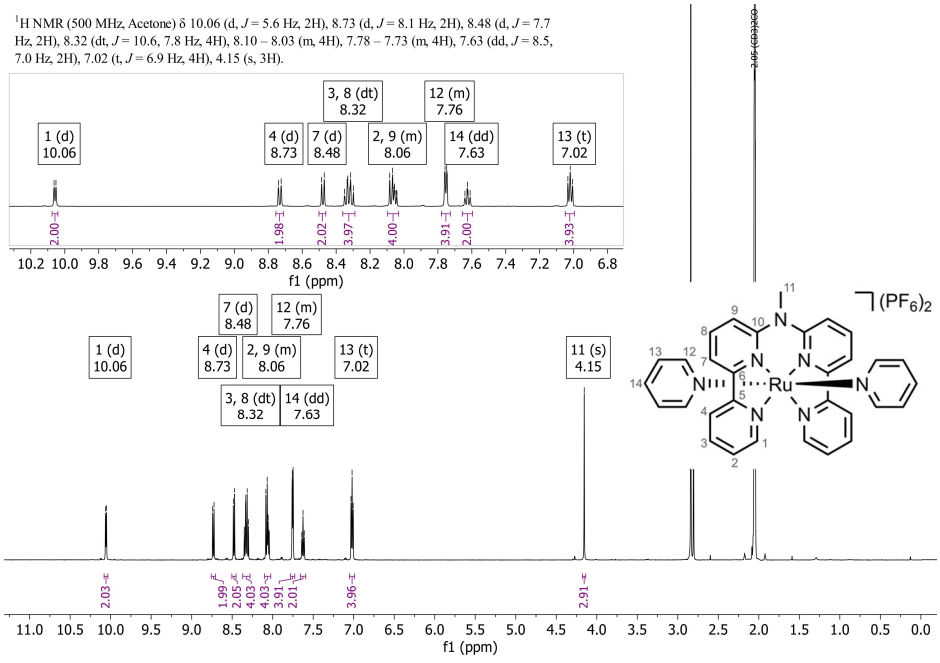

Figure III.37 ^{1}H-NMR of [**3b**](PF$_6$)$_2$ in Acetone-d_6.

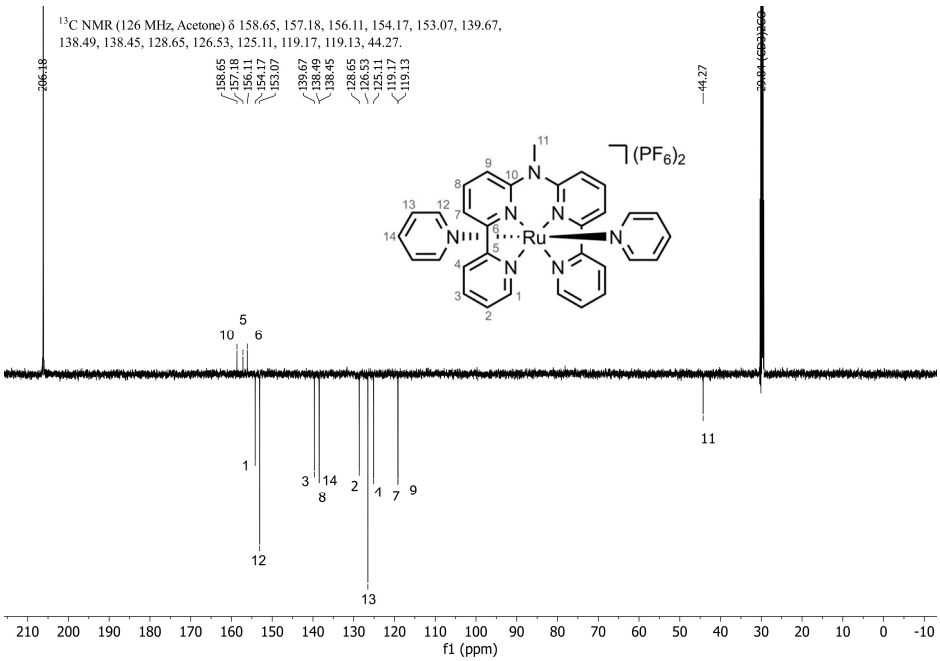

Figure III.38 ^{13}C-APT-NMR of [**3b**](PF$_6$)$_2$ in Acetone-*d*$_6$.

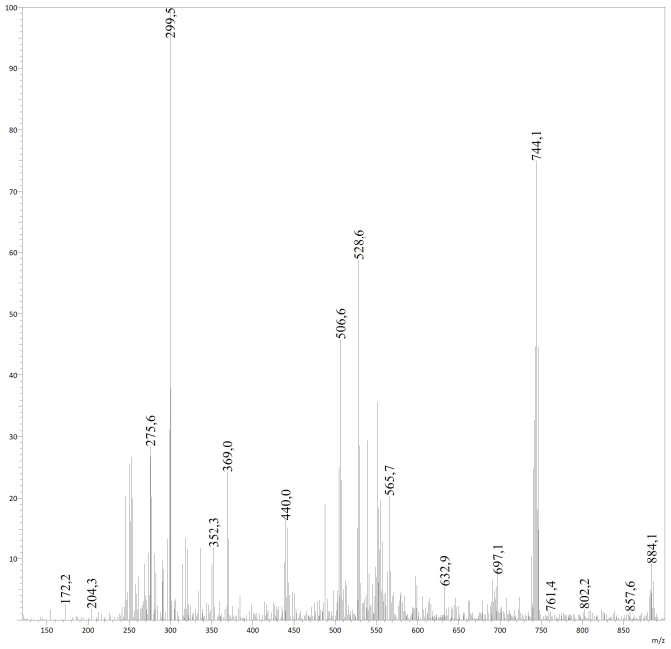

Figure III.39 ESI-MS of [**3b**](PF$_6$)$_2$. Calculated for [C$_{31}$H$_{27}$N$_7$Ru]$^{2+}$: 299.6 m/z; [C$_{31}$H$_{27}$N$_7$Ru+PF$_6$]$^+$: 744.1 m/z

V.3.7 [Ru(MeL)(Py)(MTE)](PF$_6$)$_2$ [4b](PF$_6$)$_2$

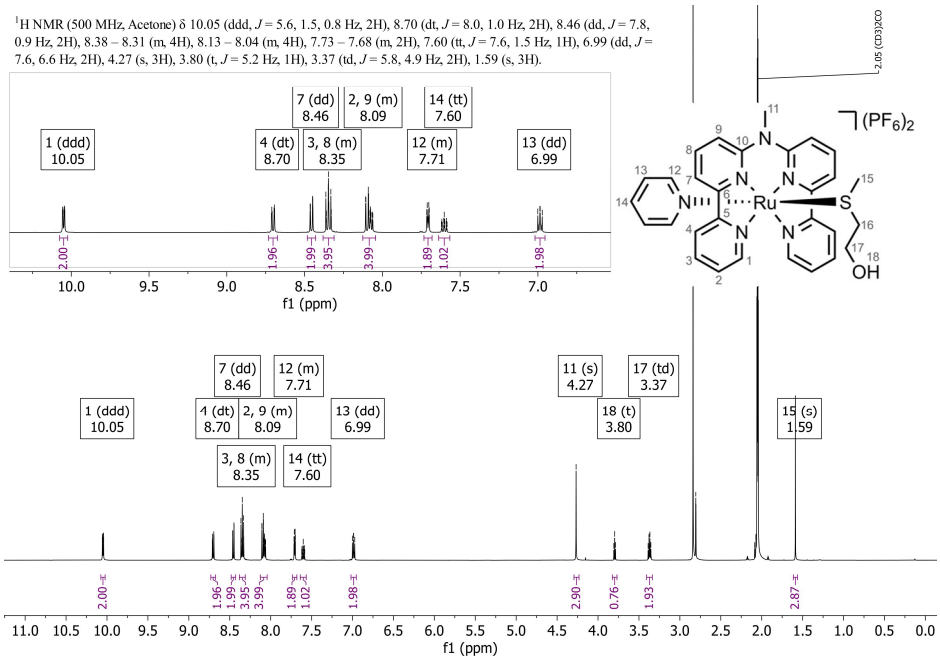

Figure III.40 ^{1}H-NMR of [**4b**](PF$_6$)$_2$ in Acetone-*d*$_6$.

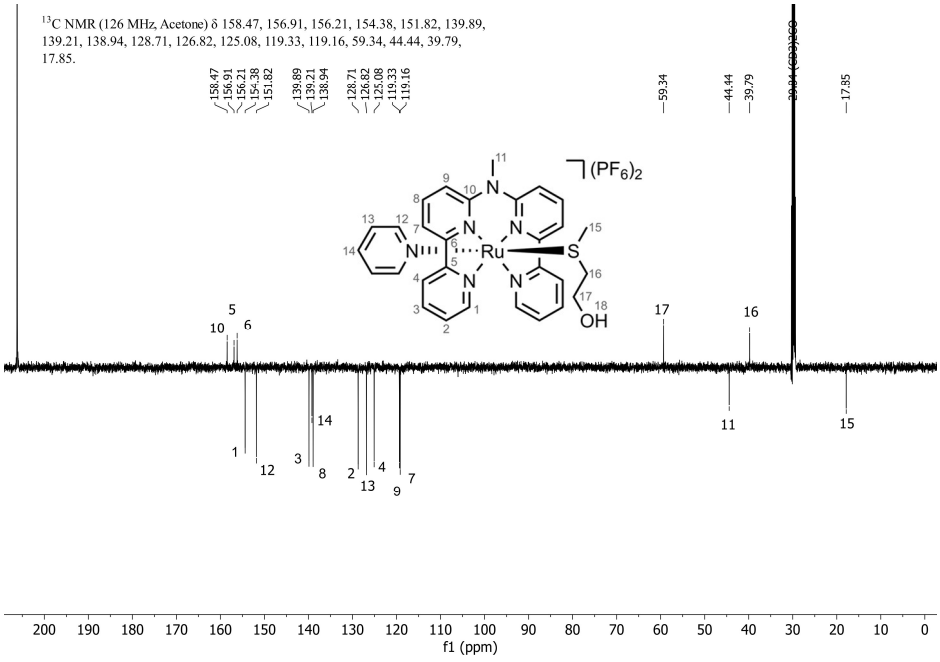

Figure III.41 ^{13}C-APT-NMR of [**4b**](PF$_6$)$_2$ in Acetone-*d*$_6$.

III

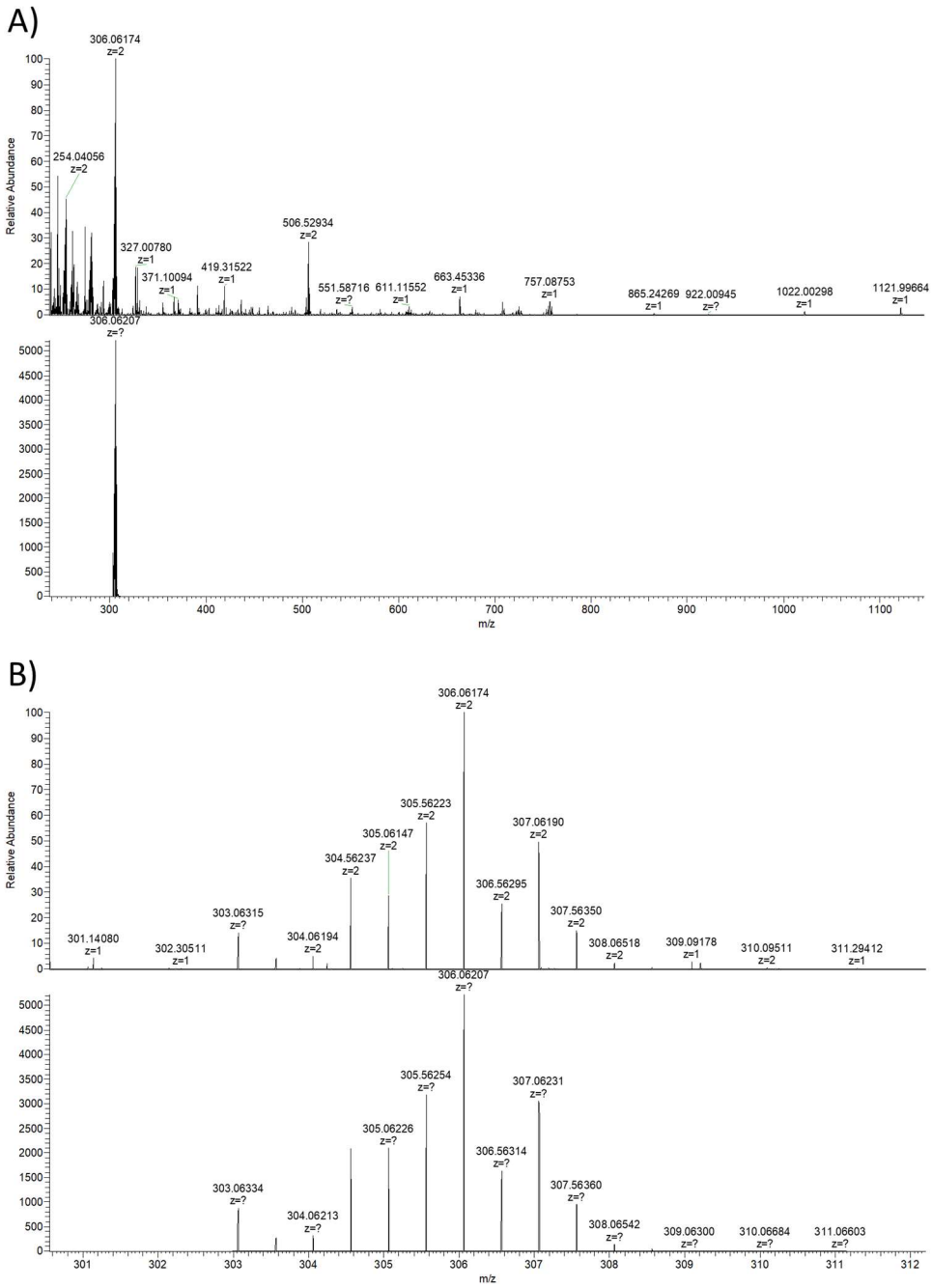

Figure III.42 HRMS of [**4b**]$(PF_6)_2$. A) *Top* measured and *bottom* calculated for $[C_{29}H_{30}N_6ORuS]^{2+}$. B) Zoom between 301 and 312 m/z. *Top* measured and *bottom* calculated for $[C_{29}H_{30}N_6ORuS]^{2+}$.

Appendix IV: Supporting information for Chapter 4

IV.1 Photochemistry

IV.1.1 Molar extinction coefficient determination

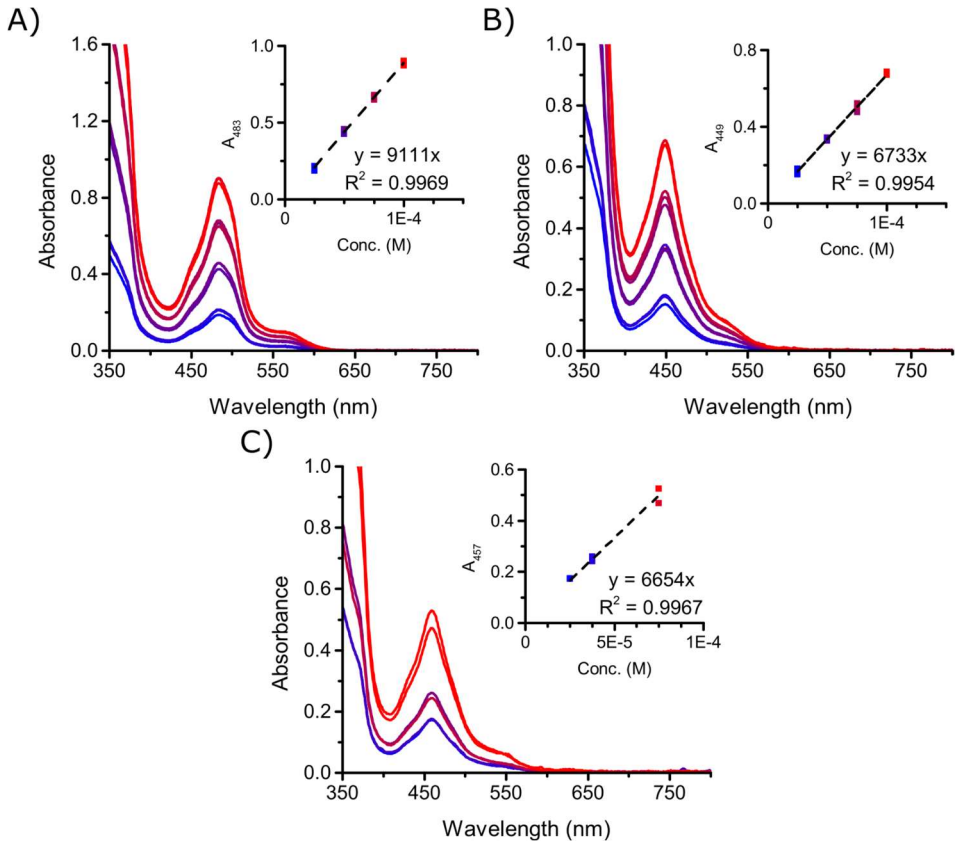

Figure IV.1 UV-Vis spectra of [**1**](PF$_6$)$_2$, [**2**](PF$_6$)$_2$ and [**3**](PF$_6$)$_2$ at different concentrations in 3 ml 50% acetone in H_2O at 298 K (l = 1 cm). Insets depicted absorption at λ_{max}. A) [**1**](PF$_6$)$_2$: ε = 9.11 x 10^3 $M^{-1}cm^{-1}$ at 483 nm. B) [**2**](PF$_6$)$_2$: ε = 67.3 x 10^3 M^{-1} cm^{-1} at 449 nm. C) [**3**](PF$_6$)$_2$: ε = 6.65 x 10^3 M^{-1} cm^{-1} at 457 nm.

IV.1.2 Photosubstitution quantum yield measurements

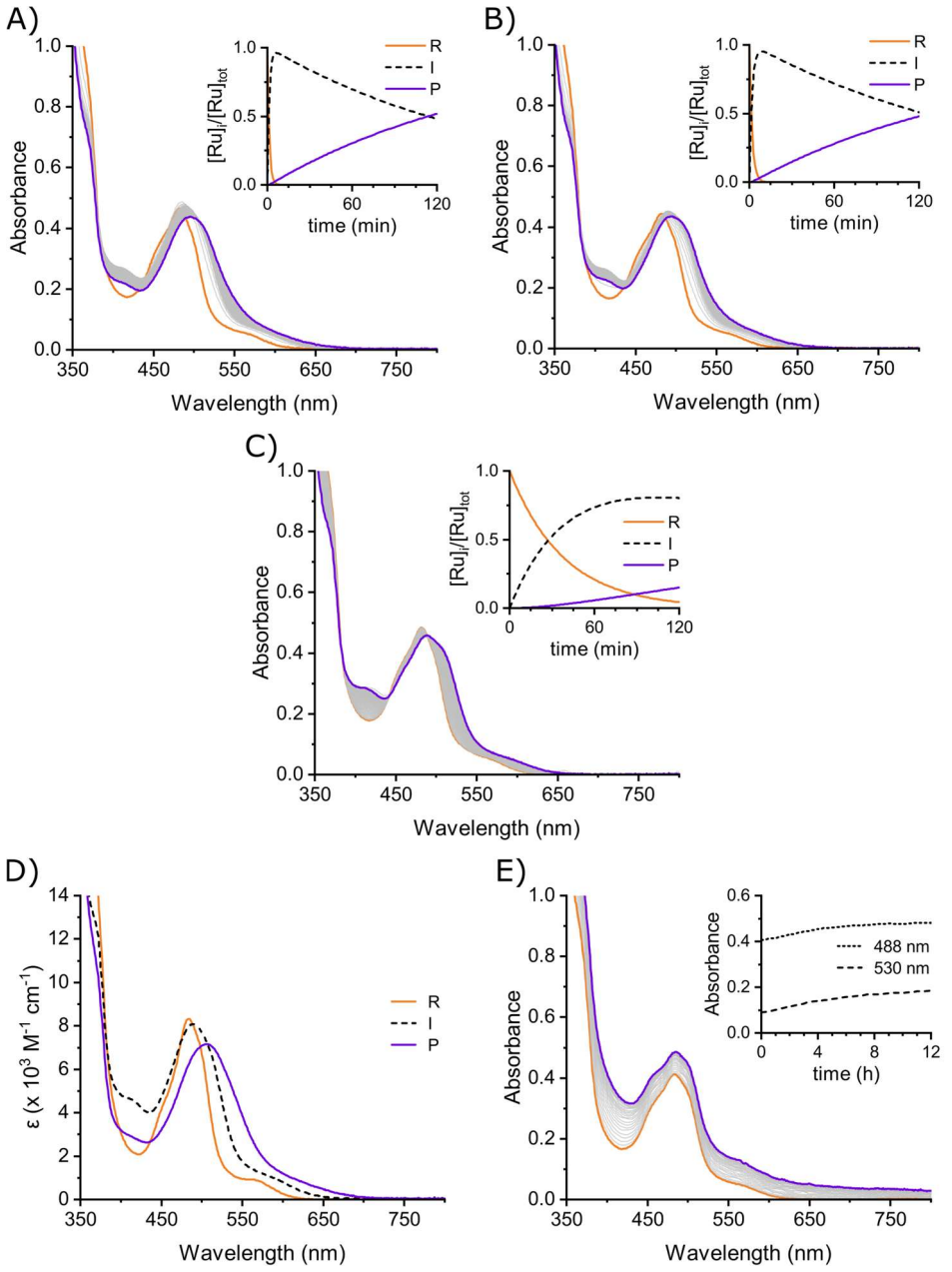

Figure IV.2 Absorbance measurements for [**1**]$(PF_6)_2$ at 59.4 µM in 50% acetone in H_2O at 298 K. Time-evolution of UV-Vis absorption upon irradiation for 120 min with A) 435 nm (photon flux = 3.26 × 10^{-7} mol/s), B) 505 nm (photon flux = 2.27 × 10^{-7} mol/s) and C) 625 nm (photon flux = 4.32 × 10^{-7} mol/s) (from orange to purple). D) Globally fitted UV-Vis absorption spectra of [**1**]$(PF_6)_2$ (R; orange), the mono-aqua intermediate [**6**]$^{2+}$ (I; black dashed) and the bis-aqua photoproduct [**8**]$^{2+}$ (P; purple). E) Absorption spectra of [**1**]$(PF_6)_2$ in the dark for 12 h (from orange to purple).

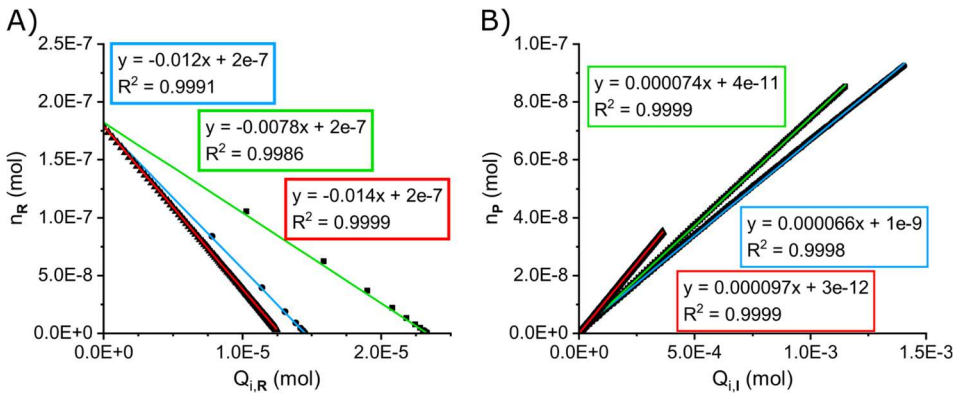

Figure IV.3 Plots for determination photosubstitution quantum yield of $\varphi_{1,N}$ (A) and $\varphi_{2,N}$ (B) for [**1**]$(PF_6)_2$ at 59.4 μM in 50% acetone in H_2O at 298 K upon irradiation with 435 nm (blue), 505 nm (green) and 625 nm (red).

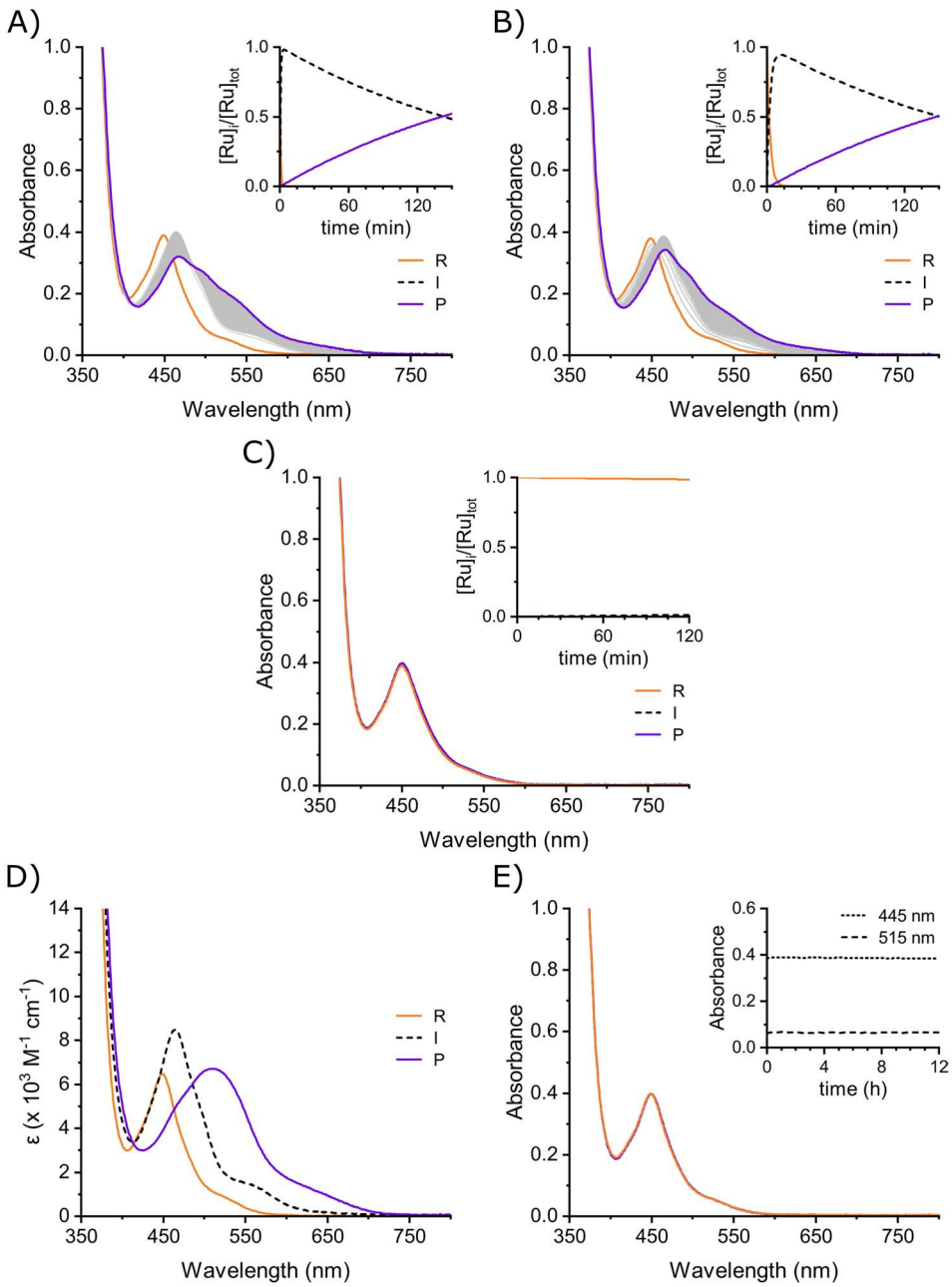

Figure IV.4 Absorbance measurements for [**2**]$(PF_6)_2$ at 61.0 µM in 50% acetone in H_2O at 298 K. Time-evolution of UV-Vis absorption upon irradiation for 150 min with A) 435 nm (photon flux = 3.26×10^{-7} mol/s), B) 505 nm (photon flux = 2.27×10^{-7} mol/s) and C) 625 nm (photon flux = 4.32×10^{-7} mol/s) (from orange to purple). D) Globally fitted UV-Vis absorption spectra of [**2**]$(PF_6)_2$ (R; orange), the mono-aqua intermediate [**7**]$^{2+}$ (I; black dashed) and the bis-aqua photoproduct [**8**]$^{2+}$ (P; purple). E) Absorption spectra of [**2**]$(PF_6)_2$ in the dark for 12 h (from orange to purple).

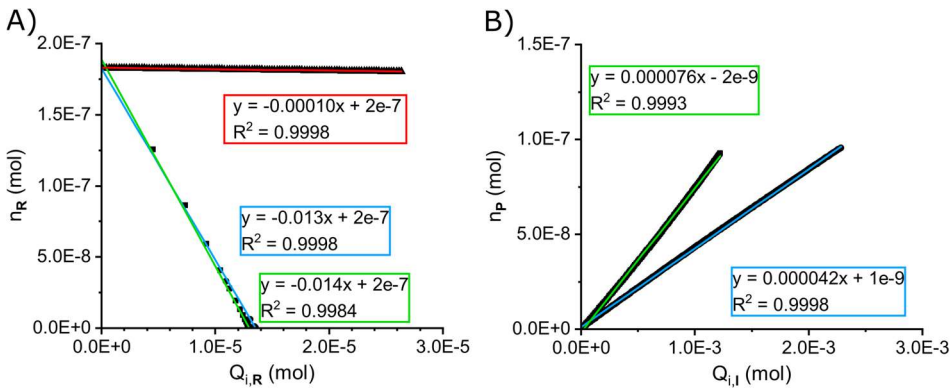

Figure IV.5 Plots for determination photosubstitution quantum yield $\varphi_{1,S}$ (A) and $\varphi_{2,S}$ (B) for [**2**](PF$_6$)$_2$ at 61.0 µM in 50% acetone in H_2O at 298 K upon irradiation with 435 nm (blue), 505 nm (green) and 625 nm (red).

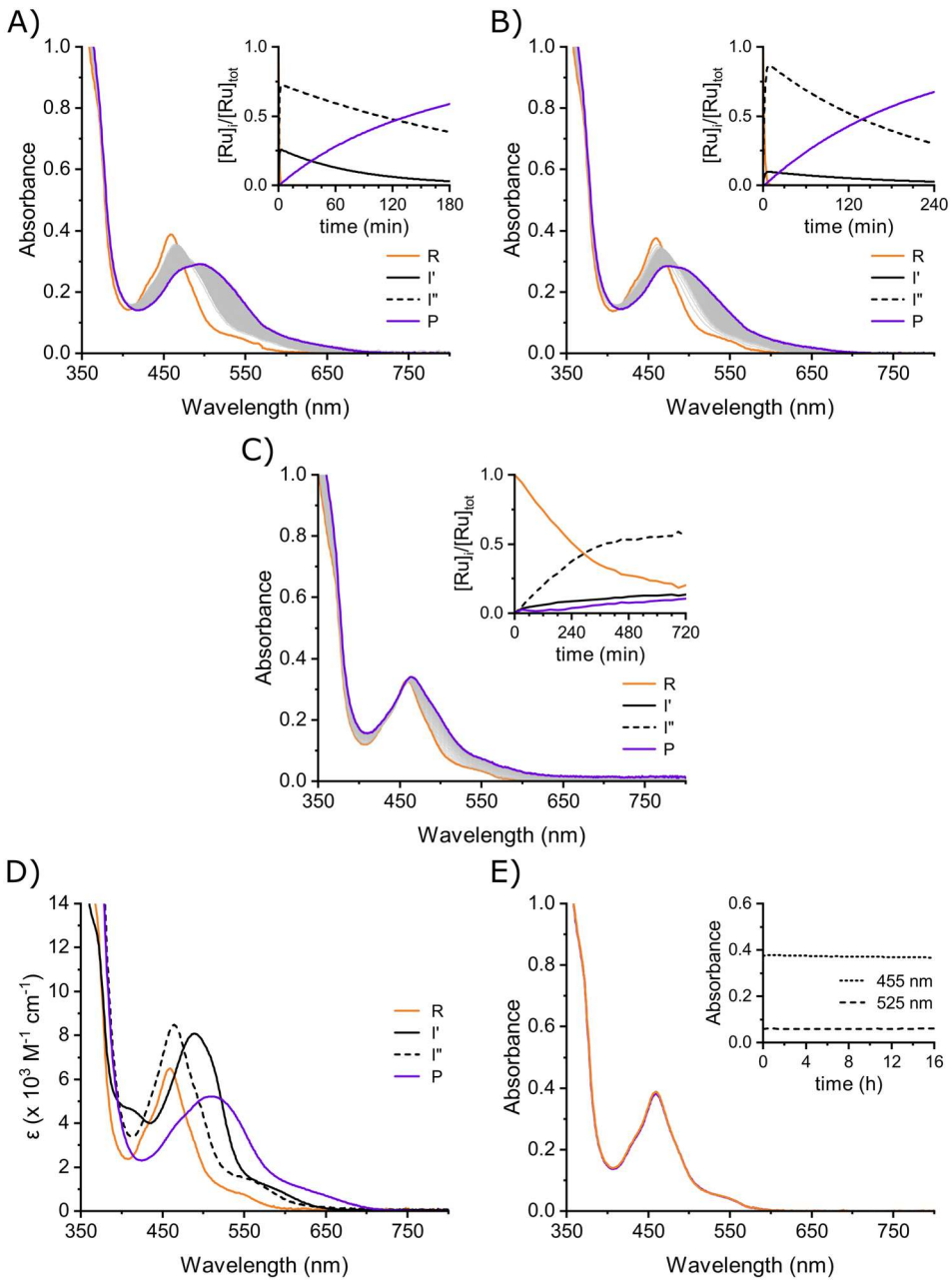

Figure IV.6 Absorbance measurements for [**3**]$(PF_6)_2$ at 56.2 µM in 1:1 acetone:H_2O at 298 K. Time-evolution of UV-Vis absorption upon irradiation with A) 435 nm for 180 min (photon flux = 3.25 × 10^{-7} mol/s), B) 505 nm for 240 min (photon flux = 2.27 × 10^{-7} mol/s) and C) 625 nm for 720 min (photon flux = 4.24 × 10^{-7} mol/s) (from orange to purple). D) Globally fitted UV-Vis absorption spectra of [**1**]$(PF_6)_2$ (R; orange line), the mono-aqua intermediates [**6**]$^{2+}$ (I''; black dashed) and [**7**]$^{2+}$ (I'; solid black)

and the bis-aqua photoproduct $[\mathbf{8}]^{2+}$ (P; purple line). E) Absorption spectra of $[\mathbf{3}](PF_6)_2$ in the dark for 16 h (from orange to purple).

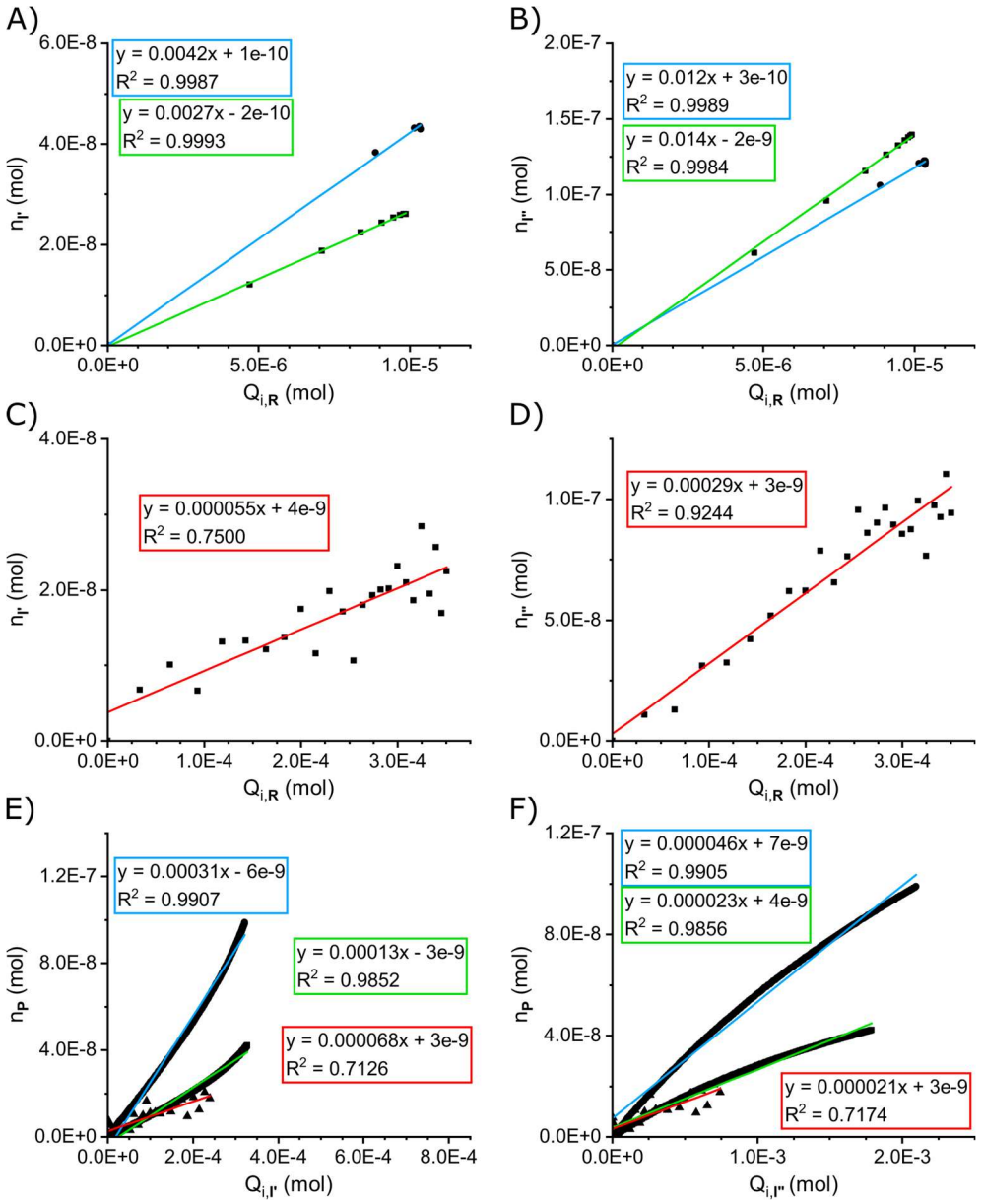

Figure IV.7 Plots for determination photosubstitution quantum yield $\varphi_{1,S}$ (A, C), $\varphi_{1,N}$ (B, D), $\varphi_{2,N}$ (E) and $\varphi_{2,S}$ (F) for $[\mathbf{3}](PF_6)_2$ at 56.2 µM in 50% acetone in H_2O at 298 K upon irradiation with 435 nm (blue), 505 nm (green) and 625 nm (red).

IV.1.3 Singlet oxygen generation quantum yield measurement

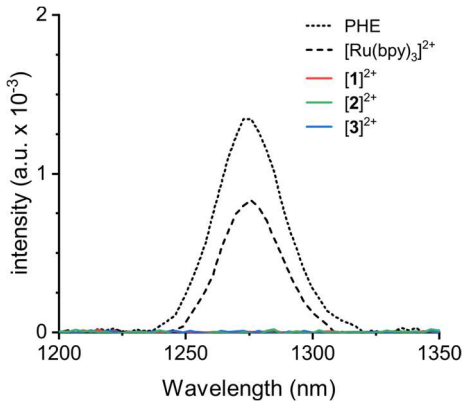

Figure IV.8 Near-infrared emission spectra of $^1O_2$ phosphorescence (λ_{em} = 1275 nm) sensitized by [**1**]$(PF_6)_2$ – [**3**]$(PF_6)_2$, $[Ru(bpy)_3]Cl_2$ and perinaphthenone (PHE) in aerated acetonitrile at 298 K under blue light irradiation (450 nm, 80 mW/cm^2).

Table IV.1 Data for the determination of singlet oxygen generation quantum yields in aerated acetonitrile.

Compound	Abs. (450 nm)	Integrated intensity	φ_Δ ($^1O_2$)
Perinaphthenone	0.0960	0.0439	0.98
$[Ru(bpy)_3]Cl_2$	0.1073	0.0266	0.53
[**1**]$(PF_6)_2$	0.1049	0.0004	<0.01
[**2**]$(PF_6)_2$	0.1127	0.0004	<0.01
[**3**]$(PF_6)_2$	0.1159	0.0001	<0.01

IV.1.4 Photosubstitution followed by ^{1}H-NMR

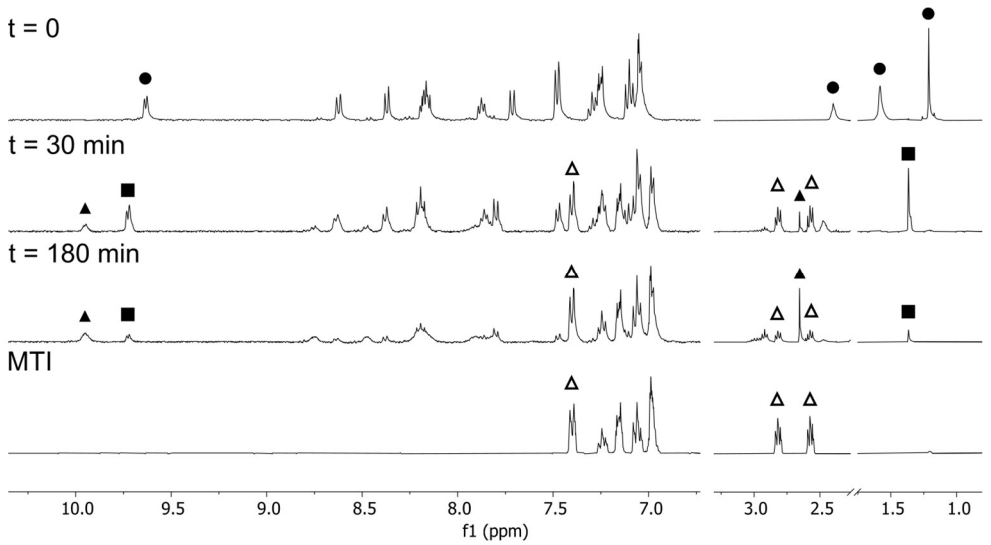

Figure IV.9 Time-evolution of ^{1}H-NMR spectra of [**2**](PF$_6$)$_2$ (●) in 1:5 D$_2$O:Acetone-D6 upon irradiation with 530 nm. Symbols indicate intermediate [**7**]$^{2+}$ (■), photoproduct [**8**]$^{2+}$ (▲) and MTI (Δ).

IV.1.5 Photoactivation in biological media

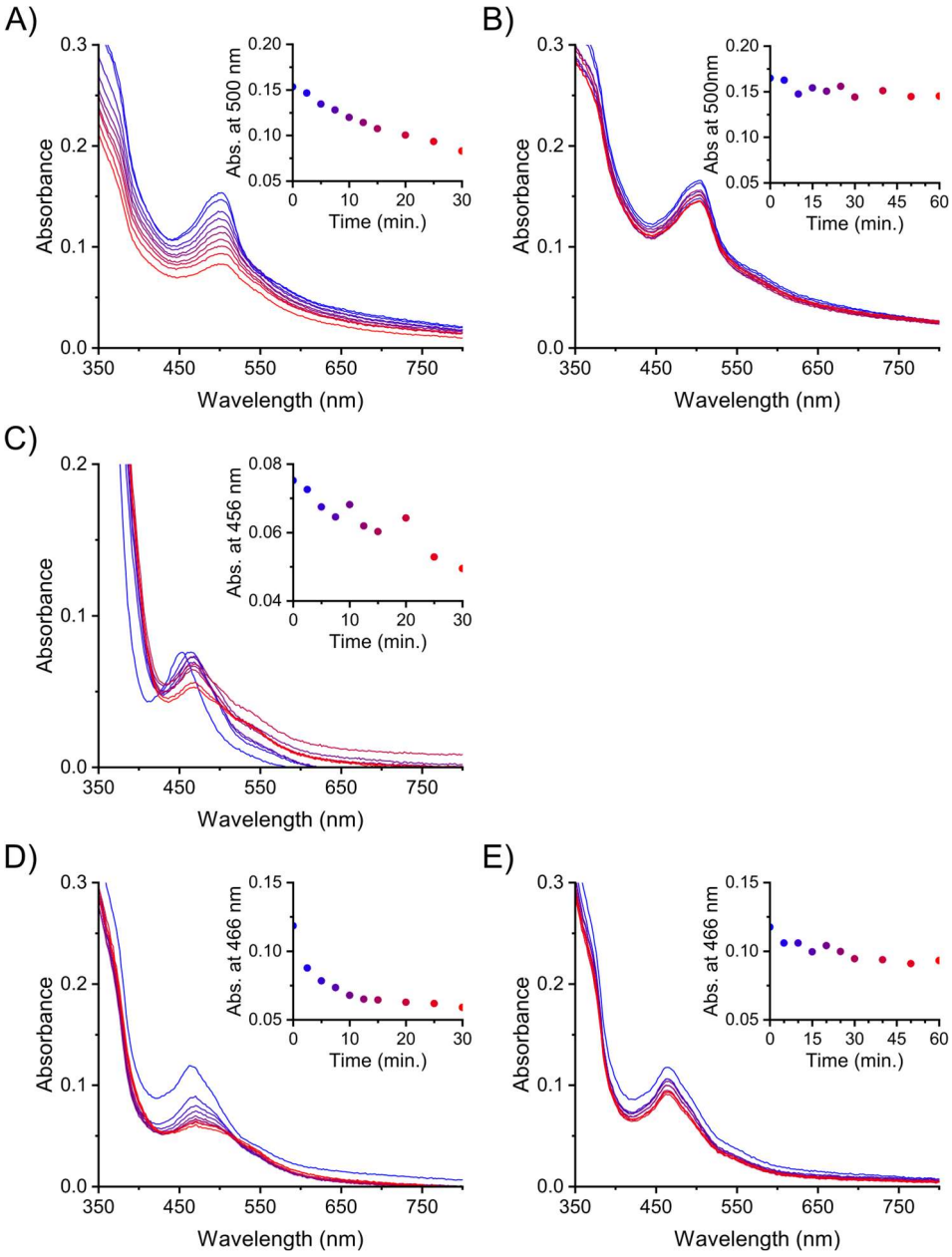

Figure IV.10 Time-evolution (blue to red) of UV-Vis absorbance spectra of [**1**]Cl_2 (A, B), [**2**]Cl_2 (C) and [**3**]Cl_2 (D, E) in OptiMEM complete media + 0.14% DMSO upon irradiation with green (A, C, D; 520 ± 35 nm; 17.1 mW · cm^{-2}) and red (B, E; 630 ± 24 nm, 31.3 mW · cm^{-2}) light array at 37 °C (conc. = 5×10^{-5} M; v = 200 µL).

IV.2 Cytotoxicity

Table IV.2 Cytotoxicity in the dark and under irradiation with green (520 nm) and red (630 nm) light in normoxic (21% O_2) and hypoxic (1% O_2) conditions.[a]

		[**1**]Cl_2					[**2**]Cl_2					[**3**]Cl_2				
Cell line	% O_2	EC_{50}, dark CI_{95} (μM)	EC_{50}, 520 CI_{95} (μM)	PI_{520}[b]	EC_{50}, 630 CI_{95} (μM)	PI_{630}[b]	EC_{50}, dark CI_{95} (μM)	EC_{50}, 520 CI_{95} (μM)	PI_{520}[b]	EC_{50}, 630 CI_{95} (μM)	PI_{630}[b]	EC_{50}, dark CI_{95} (μM)	EC_{50}, 520 CI_{95} (μM)	PI_{520}[b]	EC_{50}, 630 CI_{95} (μM)	PI_{630}[b]
A375	21%	6.38 ±3.29	0.53 ±0.38	12	1.38 ±0.61	4.6	0.95 ±0.18	0.74 ±0.17	1.3	1.03 ±0.32	0.9	2.35 ±1.62	0.27 ±0.12	8.7	1.20 ±0.49	2.0
	1%	19.7 ±4.26	0.93 ±0.49	21	1.99 ±1.68	10	0.84 ±1.29	1.10 ±0.65	0.8	0.78 ±1.77	1.1	3.47 ±2.03	0.22 ±0.15	16	2.17 ±0.86	1.6
A549	21%	9.81 ±5.90	0.45 ±0.19	22	1.80 ±0.78	5.5	6.63 ±2.67	2.55 ±1.43	2.6	4.21 ±1.30	1.6	3.66 ±0.61	1.10 ±0.36	3.3	3.15 ±0.96	1.2
	1%	19.5 ±4.39	0.60 ±0.43	33	1.43 ±1.15	14	0.65 ±1.50	1.10 ±0.93	0.6	0.66 ±0.28	1.0	2.98 ±0.70	0.37 ±0.18	8.1	2.04 ±1.08	1.5
U87MG	21%											>75	7.51 ±4.26	>10	13.8 ±11.5	>5.5
	1%											>75	3.13 ±2.70	>24	8.44 ±7.86	>8.9
U251	21%											14.4 ±3.16	7.39 ±2.29	2.0	12.3 ±5.87	1.2

[a] Metabolic activity inhibition effective concentrations (EC_{50} in μM) with 95% confidence interval (CI_{95} in μM) for [**1**]Cl_2, [**2**]Cl_2 and [**3**]Cl_2 on skin (A375), lung (A549) and glioblastoma (U87MG, U251) cancer cell lines. Irradiation was done with green light (520 ± 35 nm, dose = 30.78 J/cm^2) and red light (630 ± 24 nm, dose = 114.84 J/cm^2). Treatment-to-irradiation interval was 24 h. [b] Photo index (PI) = EC_{50}, dark/EC_{50}, light.

Table IV.3 Cytotoxicity in the dark and under irradiation with green (520 nm) and red (630 nm) light in normoxic (21% O_2) and hypoxic (1% O_2) conditions.[a]

		[**4**]Cl_2					STF	MTI	STF + MTI
Cell line	% O_2	EC_{50}, dark CI_{95} (μM)	EC_{50}, 520 CI_{95} (μM)	PI_{520}[b]	EC_{50}, 630 CI_{95} (μM)	PI_{630}[b]	EC_{50}, dark CI_{95} (μM)	EC_{50}, dark CI_{95} (μM)	EC_{50}, dark CI_{95} (μM)
A375	21%	>100	>100	-	>100	-	0.84 ±0.55	0.26 ±0.18	0.29 ±0.06
	1%	>100	>100	-	>100	-	2.40 ±1.00	1.97 ±0.89	0.92 ±0.32
A549	21%	>100	>100	-	>100	-	2.30 ±1.52	6.21 ±2.63	1.01 ±0.47
	1%	>100	>100	-	>100	-	4.94 ±0.96	0.91 ±0.38	0.47 ±0.23
U87MG	21%	>100	>100	-	>100	-	18.4 ±0.46	1.79 ±1.27	1.25 ±0.57
	1%	>100	>100	-	>100	-	>25	2.95 ±1.89	1.25 ±0.57
U251	21%	>100	>100	-	>100	-	2.53 ±1.55	4.71 ±2.33	0.49 ±0.22

[a] Metabolic activity inhibition effective concentrations (EC_{50} in μM) with 95% confidence interval (CI_{95} in μM) for [**1**]Cl_2, [**2**]Cl_2 and [**3**]Cl_2 on skin (A375), lung (A549) and glioblastoma (U87MG, U251) cancer cell lines. Irradiation was done with green light (520 ± 35 nm, dose = 30.78 J/cm^2) and red light (630 ± 24 nm, dose = 114.84 J/cm^2). Treatment-to-irradiation interval was 24 h. [b] Photo index (PI) = EC_{50}, dark/EC_{50}, light.

IV.3 Cellular uptake

Table IV.4 Cellular ruthenium uptake (in ng/ 10^6 cells and % of administered dose per 10^6 cells, both with standard deviation) determined by ICPMS in A375, U87MG and U251 incubated under normoxic (21% O_2) or hypoxic (1% O_2) conditions with [**1**]Cl_2 (2 µM), [**2**]Cl_2 (0.5 µM) and [**3**]Cl_2 (1 µM for A375, 5 µM for U87MG NX, 10 µM for U87MG HX and U251) for 24 hours in the dark.

		[**1**]Cl_2		[**2**]Cl_2		[**3**]Cl_2	
Cell line	% O_2	Ru content (ng/10^6cells)	% / 10^6cells	Ru content (ng/10^6cells)	% / 10^6cells	Ru content (ng/10^6cells)	% / 10^6cells
A375	21%	10.7 ± 2.75	19.3 ± 7.26	0.12 ± 0.02	0.99 ± 0.16	0.63 ± 0.08	2.73 ± 0.32
	1%	2.64 ± 1.47	5.89 ± 2.09	0.21 ± 0.01	1.37 ± 0.06	0.76 ± 0.34	2.50 ± 0.88
U87MG	21%	-	-	-	-	4.43 ± 1.05	7.86 ± 2.67
	1%	-	-	-	-	10.0 ± 3.53	7.03 ± 3.71
U251	21%	-	-	-	-	14.3 ± 6.61	11.3 ± 3.17

IV.4 Compound characterization

IV.4.1 [Ru(MeL)Cl_2] [**5**]

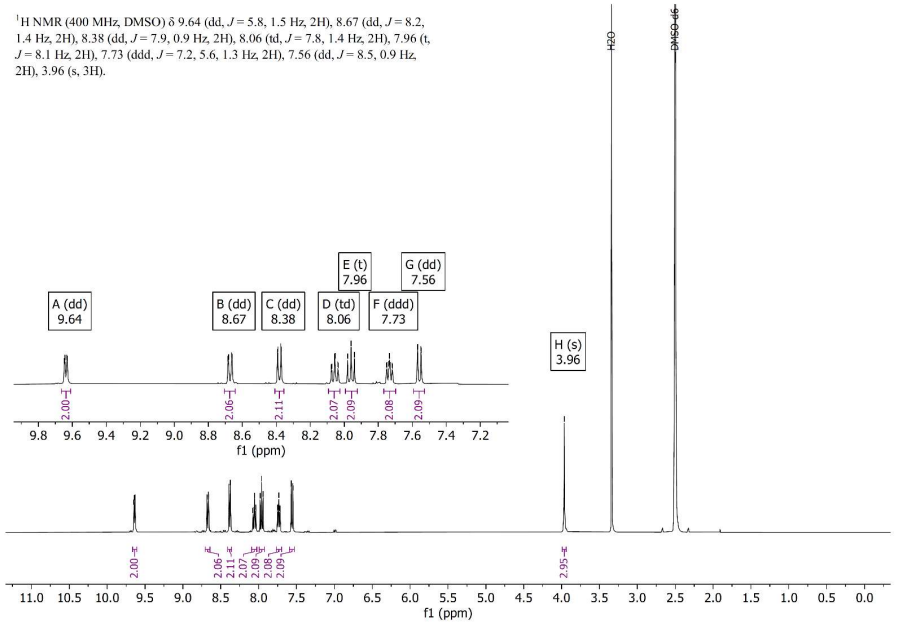

Figure IV.13 ¹H-NMR of [**5**] in DMSO-d_6.

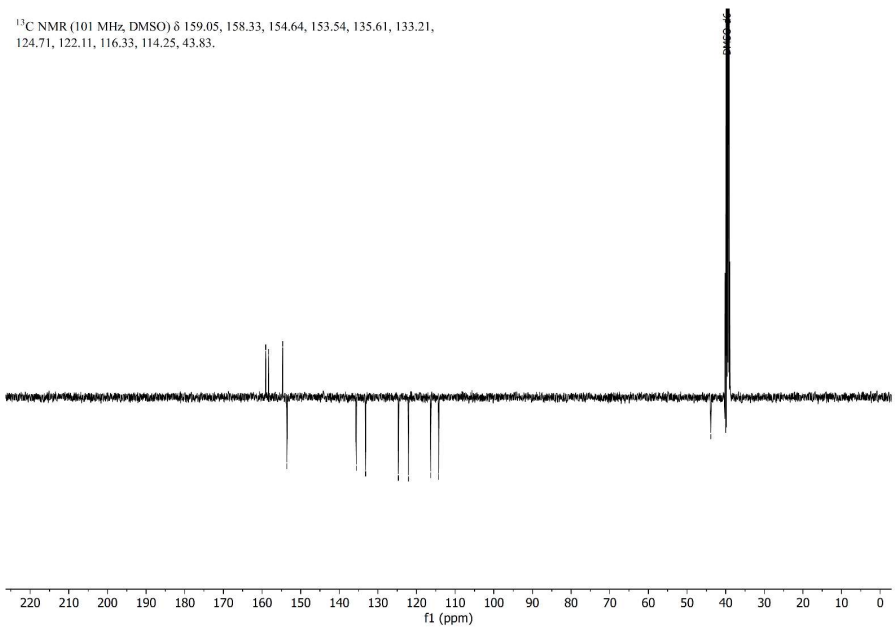

Figure IV.14 ^{13}C-APT-NMR of [**5**] in DMSO-d_6.

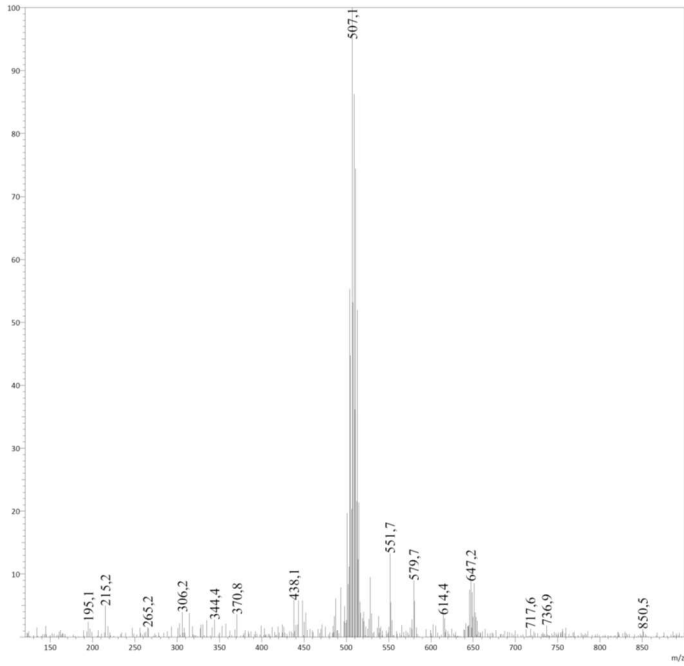

Figure IV.15 ESI-MS of [**5**]. Calculated for $[C_{21}H_{17}N_5RuCl + CH_3OH]^+$: 508.1 m/z.

IV.4.2 $[Ru(MeL)(STF\text{-}31)_2]^{2+}$ $[\mathbf{1}]^{2+}$

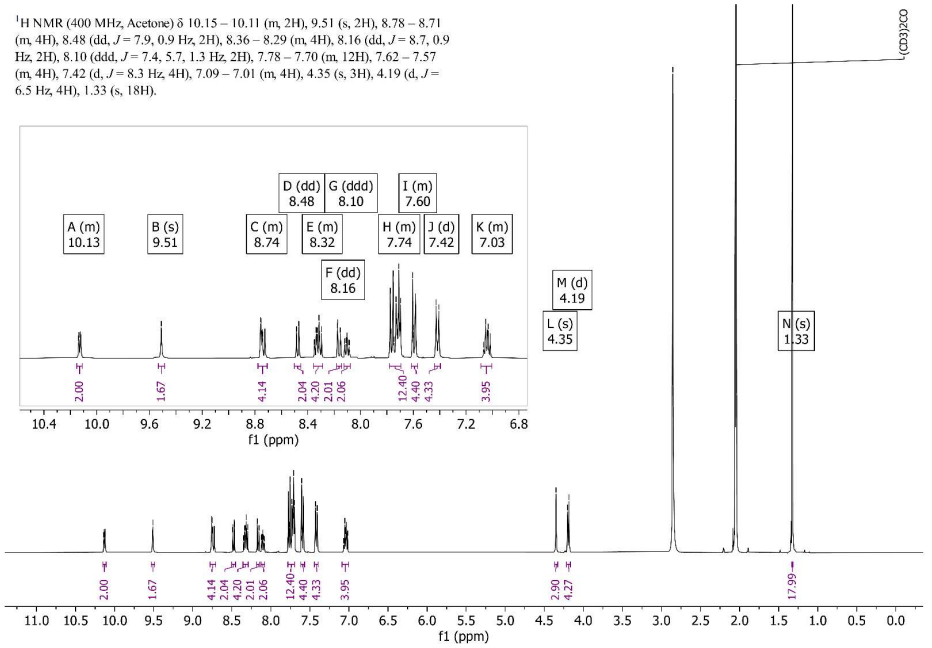

Figure IV.16 ^{1}H-NMR of $[\mathbf{1}](PF_6)_2$ in Acetone-d_6.

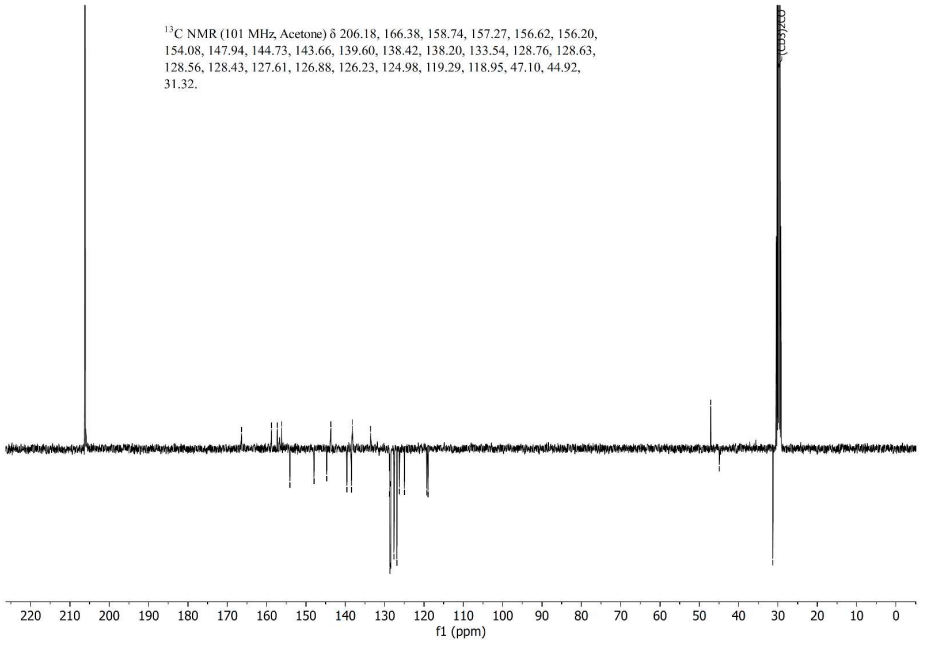

Figure IV.17 ^{13}C-APT-NMR of $[\mathbf{1}](PF_6)_2$ in Acetone-d_6.

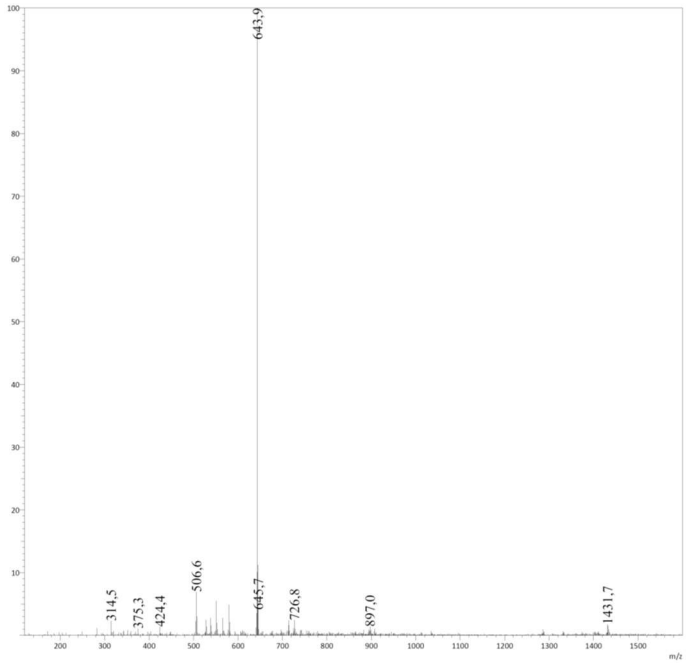

Figure IV.18 ESI-MS of [**1**]$(PF_6)_2$. Calculated for $[C_{67}H_{67}N_{11}O_6S_2Ru]^{2+}$: 643.7 m/z.

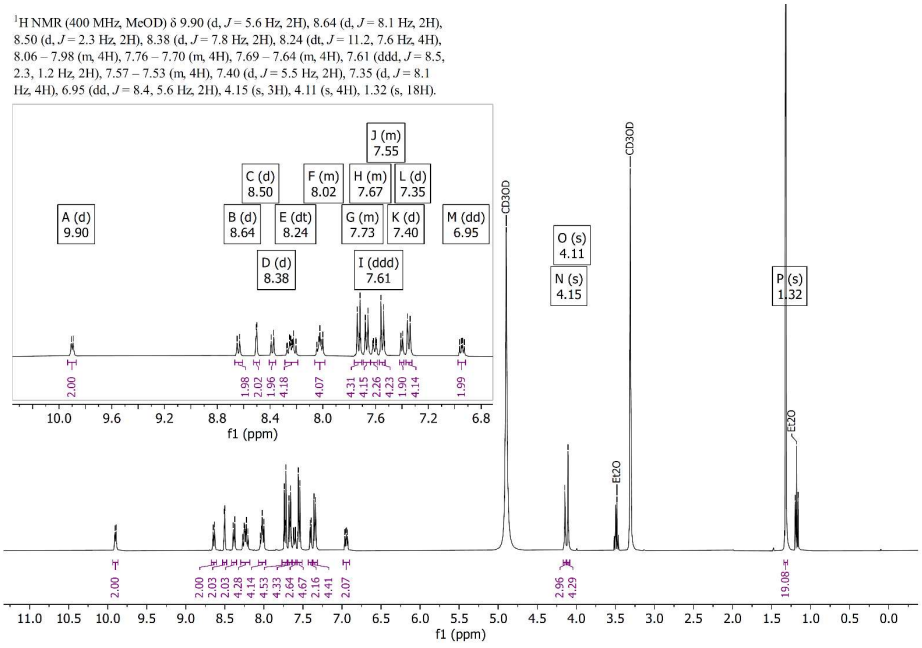

Figure IV.19 ^{1}H-NMR of [**1**]Cl_2 in MeOD.

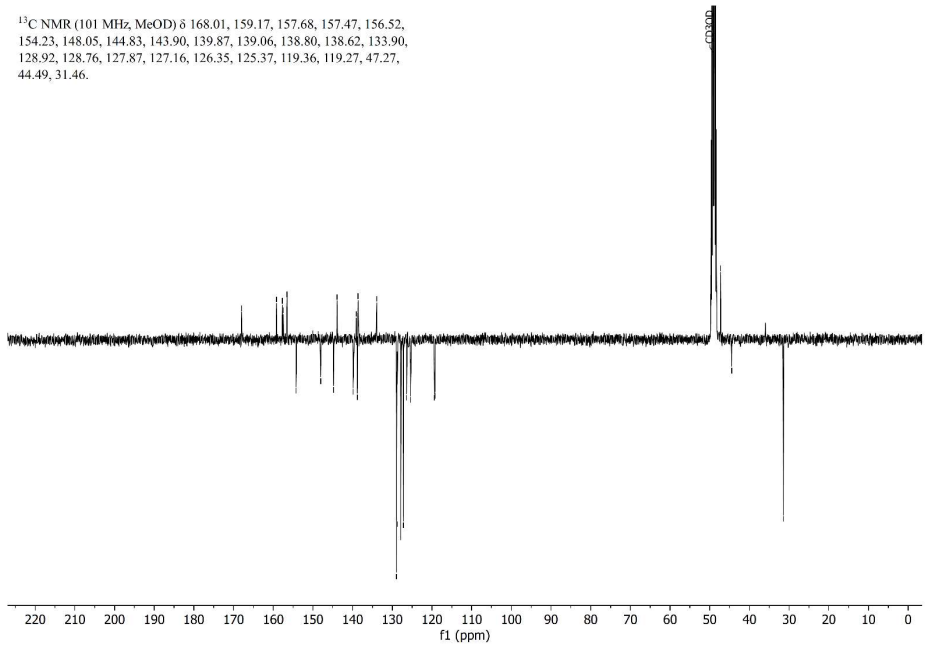

Figure IV.20 ^{13}C-APT-NMR of [**1**]Cl_2 in MeOD.

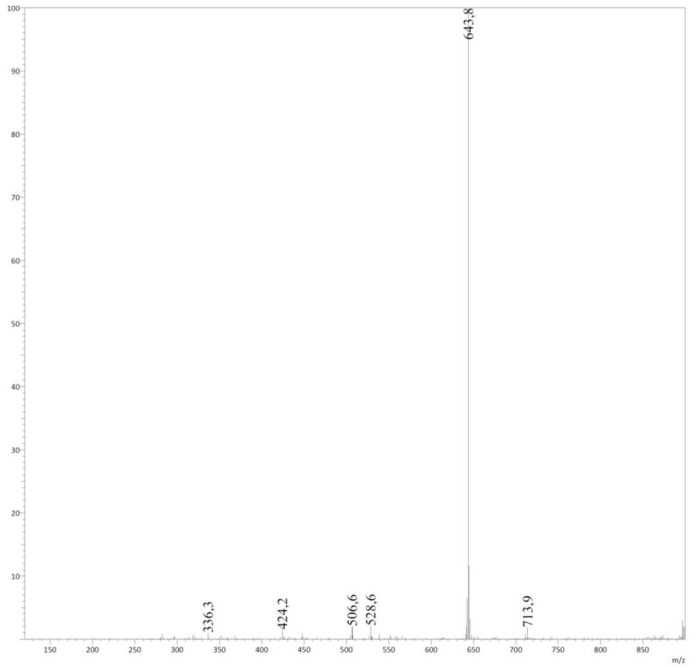

Figure IV.21 ESI-MS of [**1**]Cl_2. Calculated for $[C_{67}H_{67}N_{11}O_6S_2Ru]^{2+}$: 643.7 m/z.

IV.4.3 $[Ru(MeL)(MTI)_2]^{2+}$ $[\mathbf{2}]^{2+}$

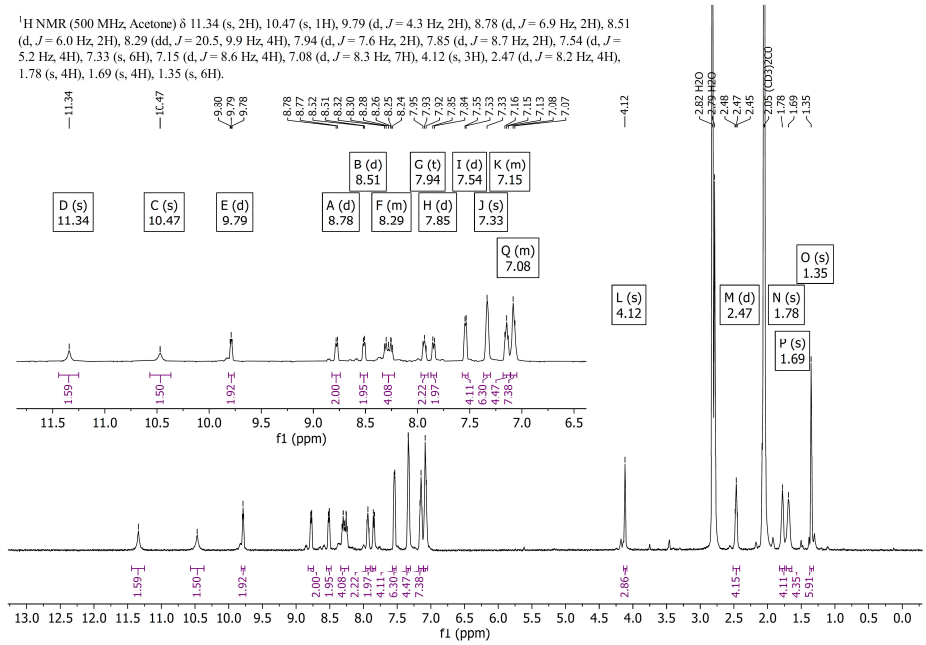

Figure IV.22 ^{1}H-NMR of $[\mathbf{2}](PF_6)_2$ in Acetone-d_6.

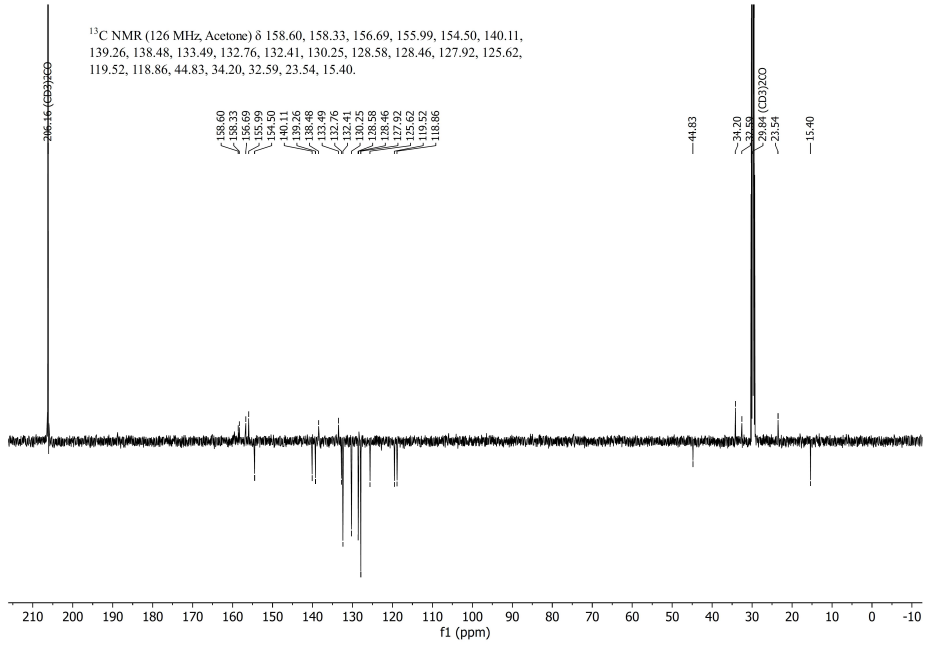

Figure IV.23 ^{13}C-APT-NMR of $[\mathbf{2}](PF_6)_2$ in Acetone-d_6.

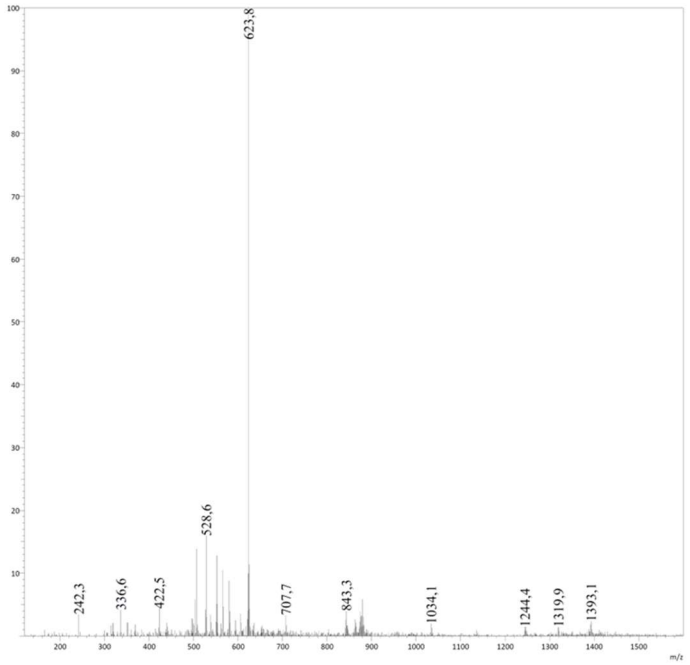

Figure IV.24 ESI-MS of [**2**](PF$_6$)$_2$. Calculated for $[C_{67}H_{59}N_{11}O_4S_2Ru]^{2+}$: 623.7 m/z.

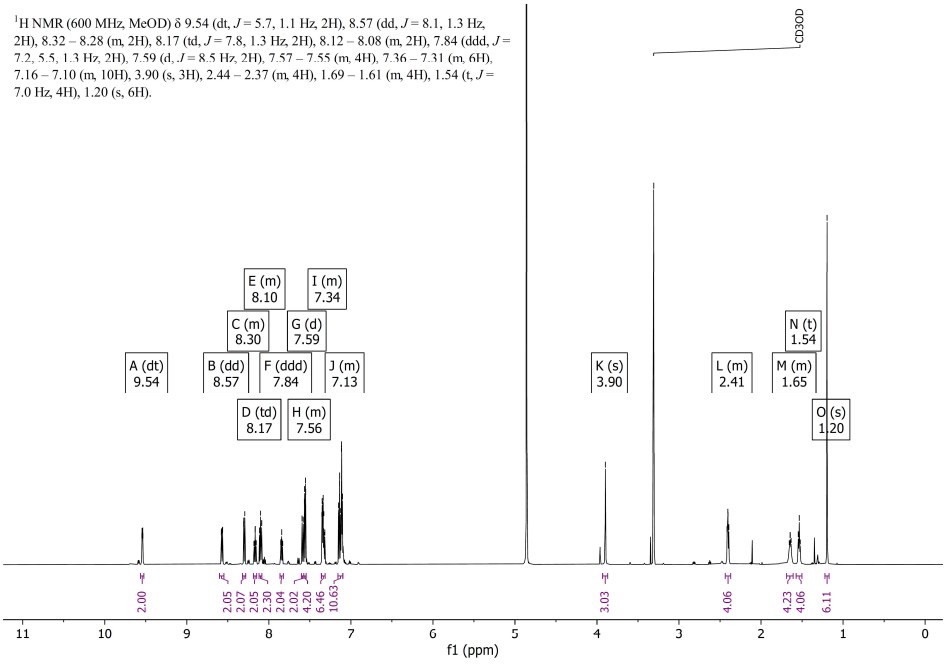

Figure IV.25 ^{1}H-NMR of [**2**]Cl$_2$ in MeOD.

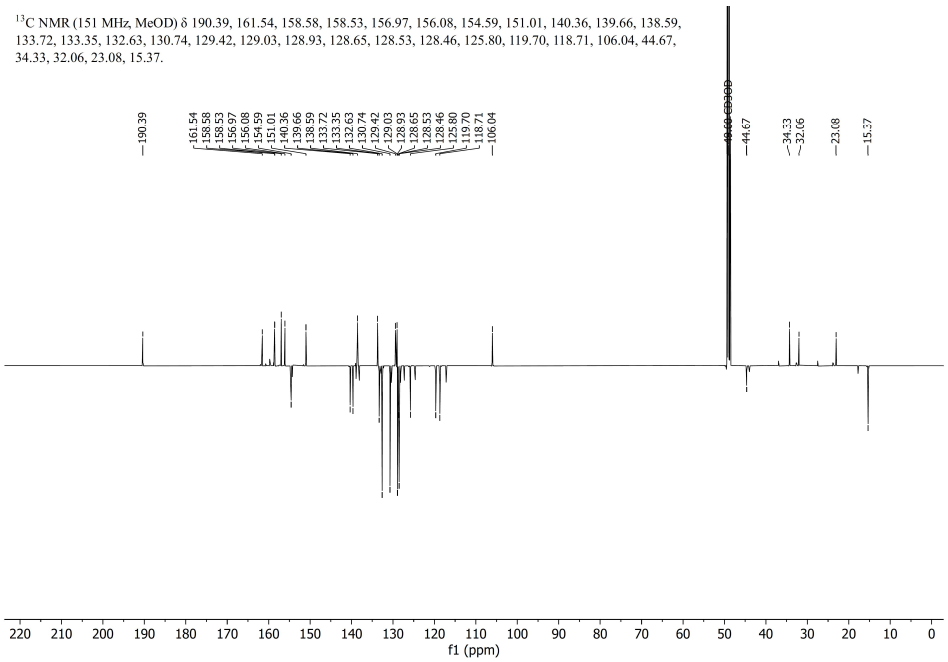

Figure IV.26 ^{13}C-APT-NMR of [**2**]Cl_2 in MeOD.

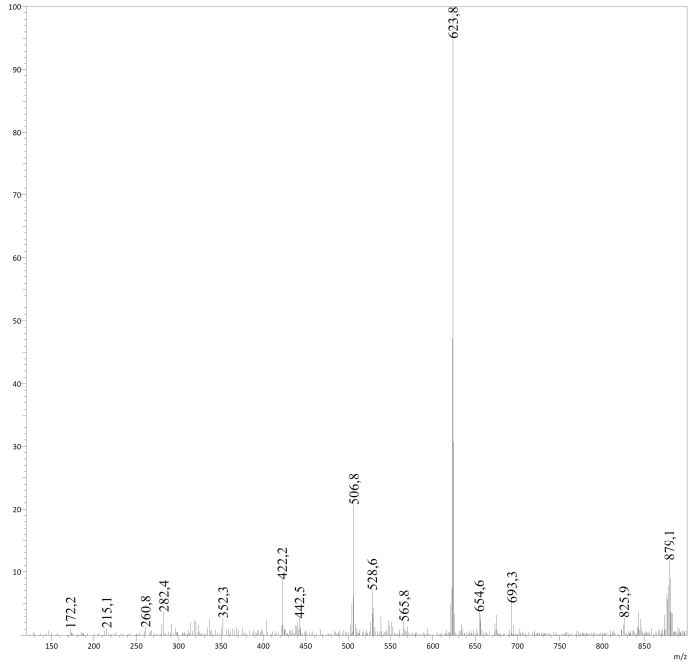

Figure IV.27 ESI-MS of [**2**]Cl_2. Calculated for $[C_{67}H_{59}N_{11}O_4S_2Ru]^{2+}$: 623.7 m/z.

IV.4.4 [Ru(MeL)(STF-31)(MTI)]$^{2+}$ [**3**]$^{2+}$

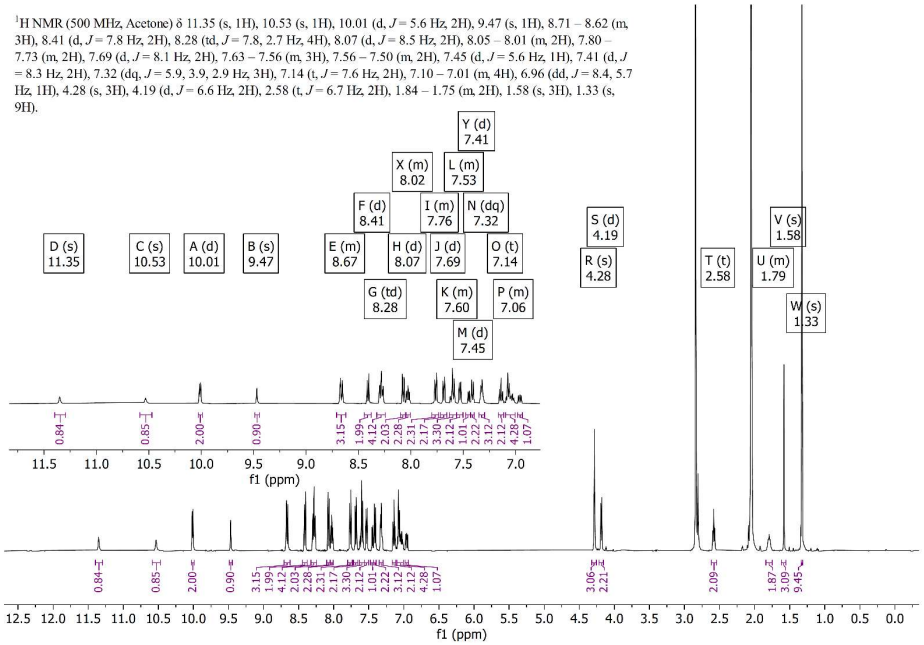

Figure IV.28 ¹H-NMR of [**3**](PF$_6$)$_2$ in Acetone-*d*$_6$.

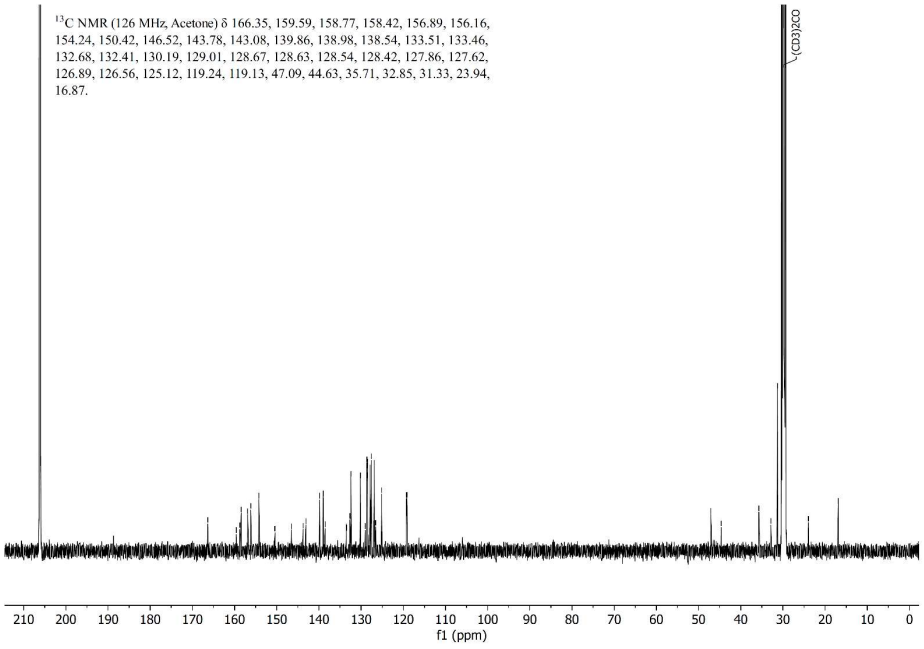

Figure IV.29 ¹³C-NMR of [**3**](PF$_6$)$_2$ in Acetone-*d*$_6$.

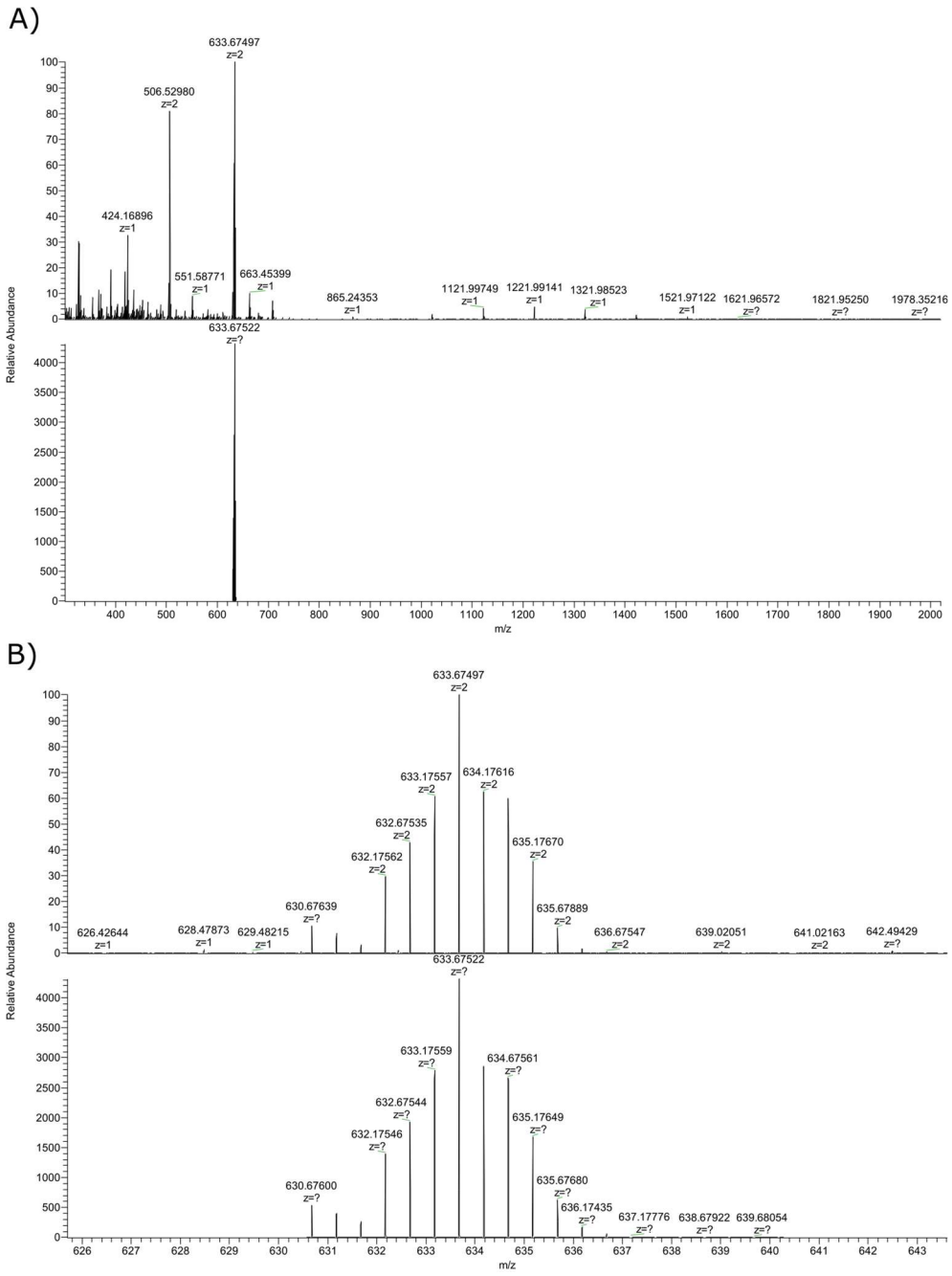

Figure IV.30 ESI-HRMS of [**3**]$(PF_6)_2$. Calculated for $[C_{67}H_{63}N_{11}O_5S_2Ru]^{2+}$: 633.6752 m/z. A) full range between 200 and 2000 m/z. B) zoom between 625 and 645 m/z.

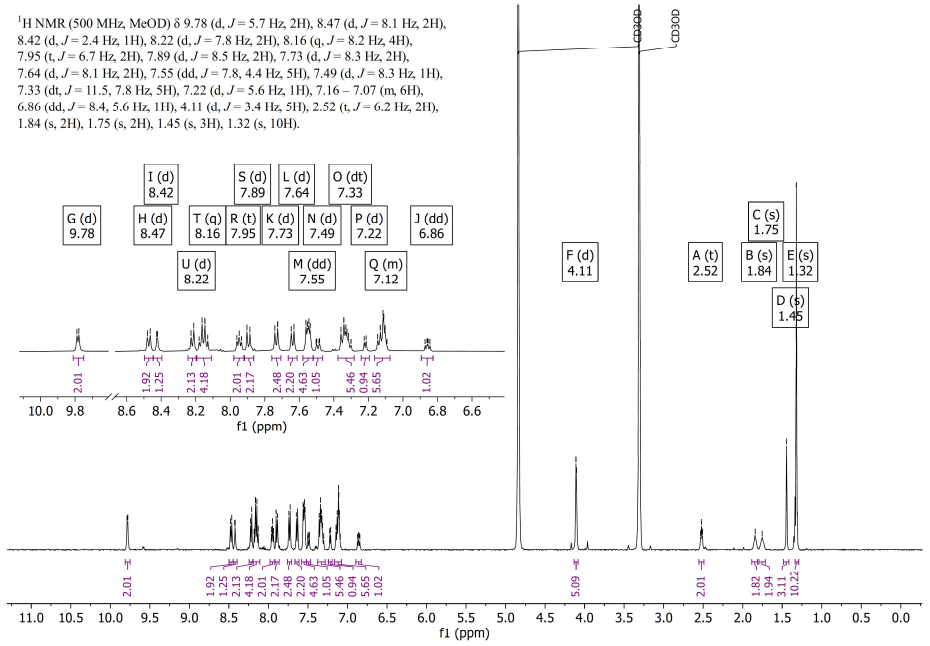

Figure IV.31 ^{1}H-NMR of [**3**]Cl_2 in MeOD.

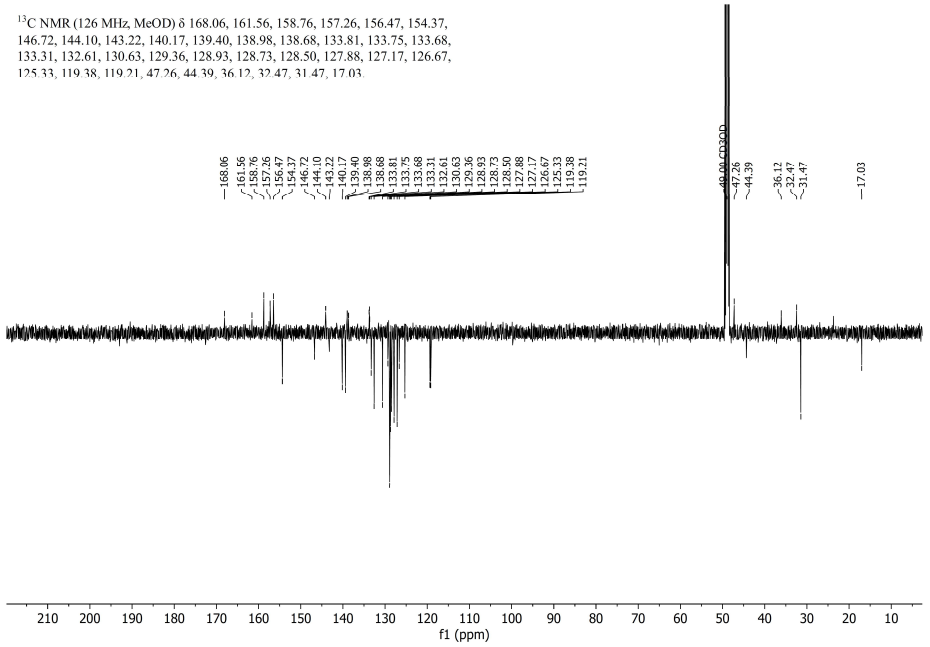

Figure IV.32 ^{13}C-APT-NMR of [**3**]Cl_2 in MeOD.

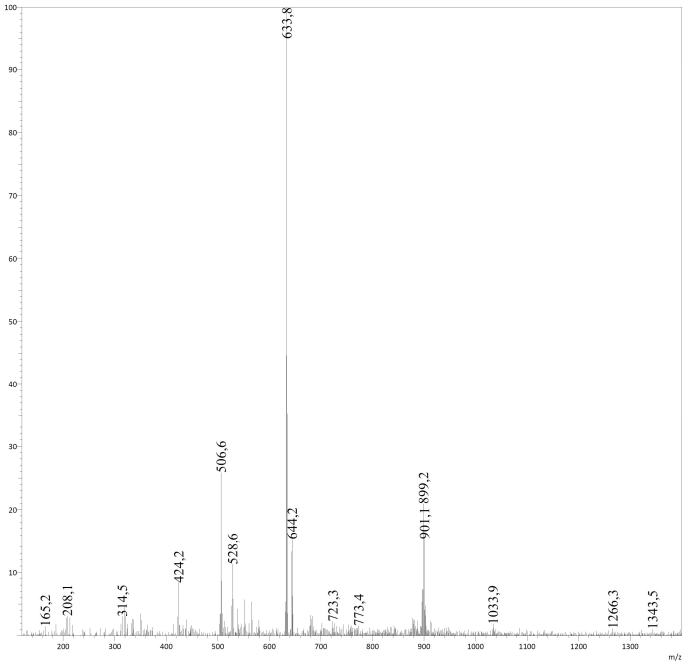

Figure IV.33 ESI-MS of [**3**]Cl_2. Calculated for $[C_{67}H_{63}N_{11}O_5S_2Ru]^{2+}$: 633.7 m/z.

IV.4.5 [Ru(MeL)(Py)(MTE)]Cl_2 [**4**]Cl_2

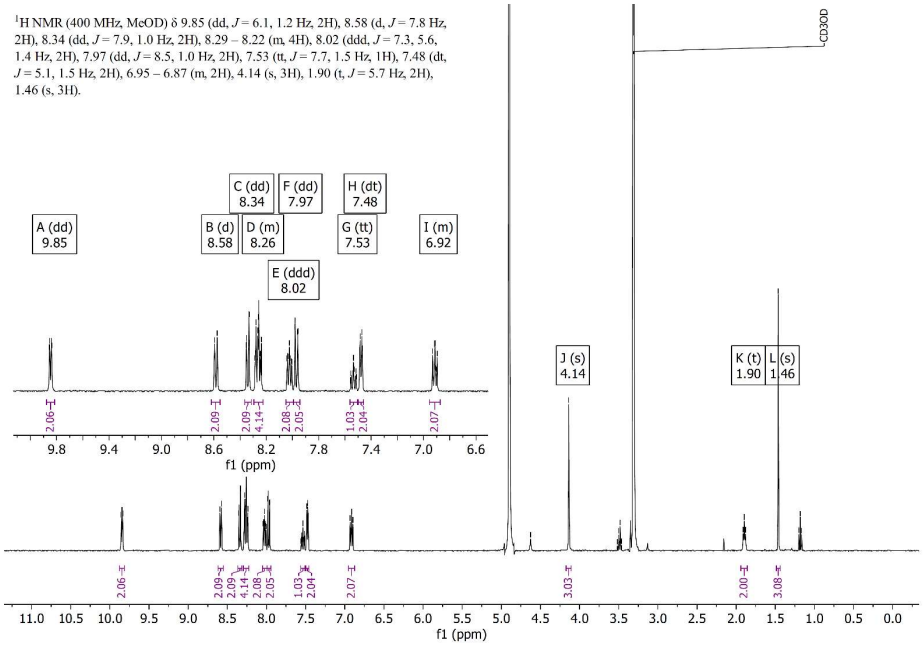

Figure IV.34 ¹H-NMR of [**4**]Cl_2 in MeOD.

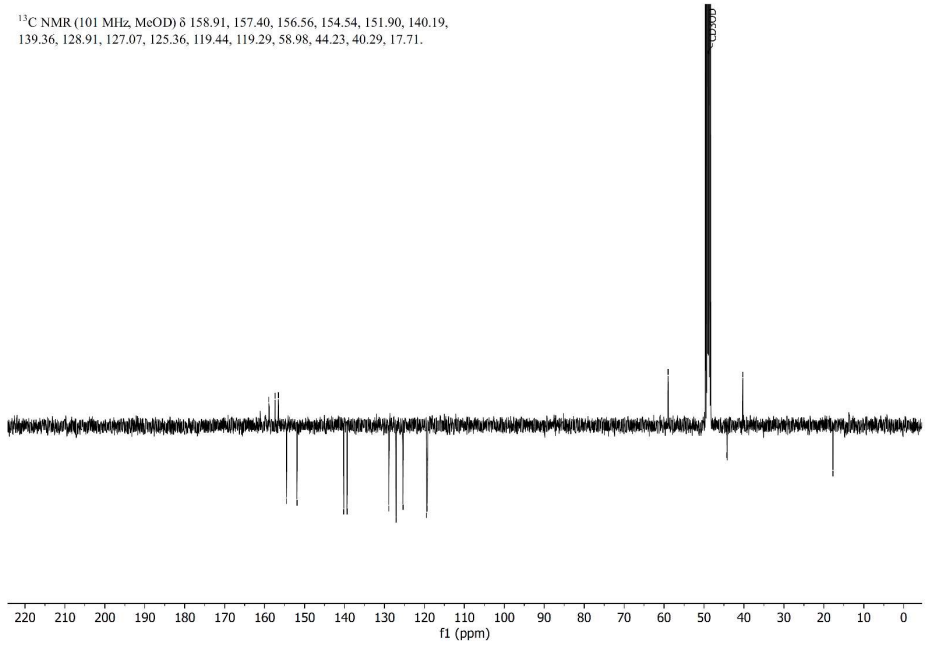

Figure IV.35 ^{13}C-APT-NMR of [**4**]Cl_2 in MeOD.

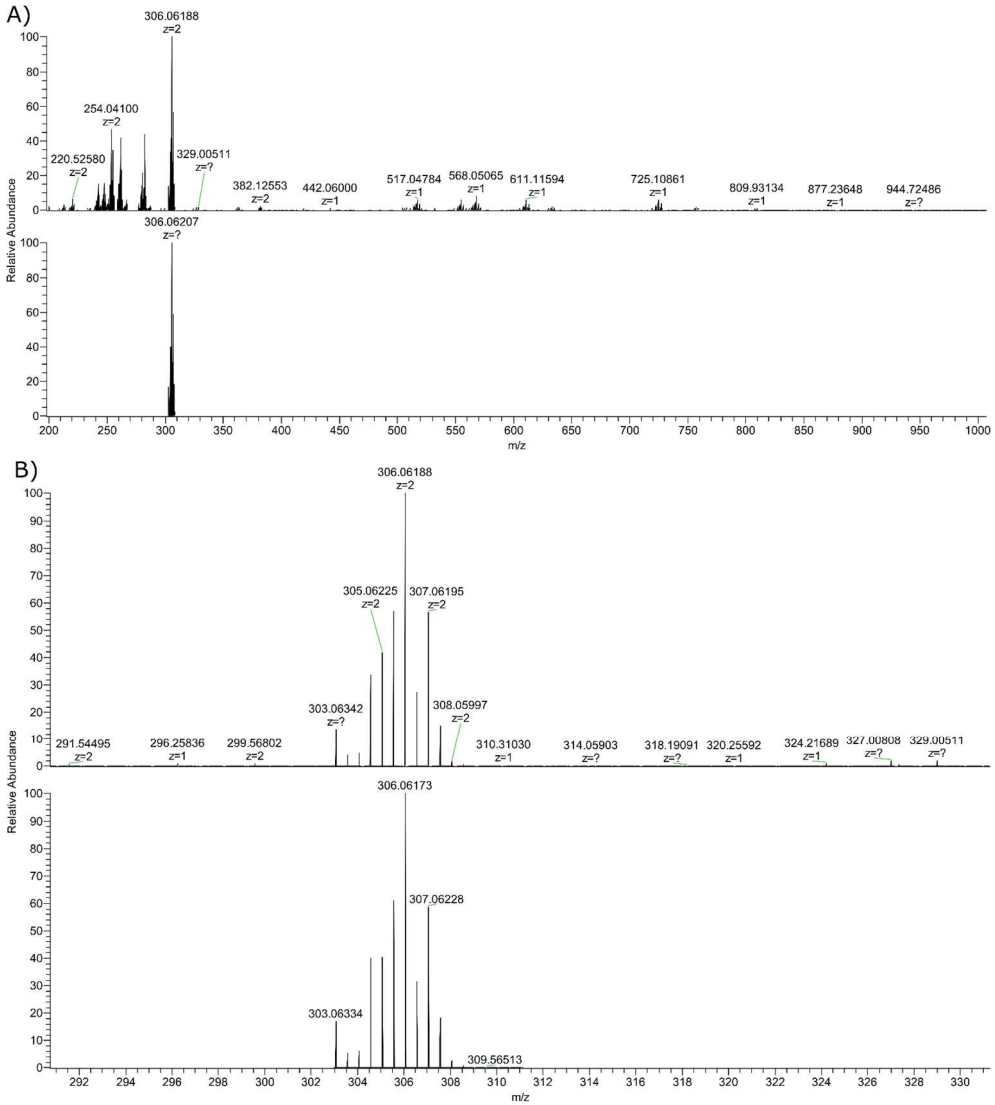

Figure IV.36 ESI-HRMS of [**4**]Cl_2. Calculated for $[C_{29}H_{30}N_6O_1S_1Ru]^{2+}$: 306.0617 m/z. A) full range between 200 and 1000 m/z. B) zoom between 291 and 331 m/z.

Appendix V: Supporting information for Chapter 5

V.1 Single crystal X-ray crystallography

Experimental details

For both [**24**]Cl_2 and [**26**]$(PF_6)_2$, all reflection intensities were measured at 110.00(10) K using a Rigaku XtaLAB Synergy R (equipped with a rotating-anode X-ray source and HyPix-6000HE detector) with Cu *K*α radiation (λ = 1.54178 Å) under the program CrysAlisPro (Version CrysAlisPro 1.171.42.49, Rigaku OD, 2022). The same program was used to refine the cell dimensions and for data reduction. The structure was solved and refined on F^2 with the program SHELXL-2018/3.[1] Analytical numeric absorption correction using a multifaceted crystal was applied using CrysAlisPro. The temperature of the data collection was controlled using the system Cryostream 1000 from Oxford Cryosystems). The H atoms were placed at calculated positions using the instructions AFIX 13, AFIX 23, AFIX 43, AFIX 137 or AFIX 147 with isotropic displacement parameters having values 1.2 or 1.5 U_{eq} of the attached C or O atoms.

For [**24**]Cl_2, the structure is partly disordered. The adamantyl fragment of the N3' moiety and one of the two lattice MeOH solvent molecules are disordered over two orientations, and the occupancy factors of the major components of the disorder refine to 0.621(4) and 0.512(11), respectively. For [**26**]$(PF_6)_2$, The structure is partly disordered. The coordinated pyridine, the adamantyl fragment, and the PF_6^- counterions are all disordered over two orientations. All occupancy factors of the major/minor components of the disorder can be retrieved from the final .cif file. The asymmetric unit contains three PF_6^- counterions located at three different sites: one site has one fully occupied counterion, another site has one half occupied counterion as it is found at one site of inversion symmetry, and the third site contains a heavily disordered and partly occupied counterion (the sum of the occupancies from the individual disordered components were constrained to be 0.5). The asymmetric unit also contains some amount of very disordered (and possibly partially occupied) lattice THF solvent molecules, and that contribution was removed from the final refinement using the SQUEEZE procedure in Platon.[2]

[1] Sheldrick, G.M., *Acta. Cryst.*, 2015, C71, 3-8, DOI: 10.1107/S2053229614024218
[2] Spek, A.L., *Acta. Cryst.*, 2009, D65, 148-155, DOI: 10.1107/S090744490804362X

Table V.1 Crystallographic data for the crystal structures presented in this work.

	[**24**]$(Cl)_2$	[**26**]$(PF_6)_2$
Chemical formula	$C_{51}H_{57}N_9O_2Ru·2(CH_4O)·2(Cl)$	$C_{41}H_{42}N_8ORu·2(F_6P)$
M_r	1064.11	1053.83
Crystal system	Triclinic	Triclinic
Space group	*P*-1	*P*-1
Cell lengths (*a, b, c*)(Å)	11.32203 (18) 12.2551 (2) 18.558899 (18)	9.3424 (2) 13.8428 (6) 19.7677 (6)
Cell angles (α, β, γ)(◦)	75.2897 (13) 82.2838 (12) 79.7078 (14)	99.089 (3) 94.080 (2) 95.336 (2)
Cell volume (Å^3)	2439.90 (6)	2503.82 (14)
Z	2	2
μ (mm^{-1})	4.06	3.89
Crystal size (mm)	0.17 × 0.03 × 0.03	0.28 × 0.04 × 0.04
Temperature (K)	110(10)	110(10)
Diffractometer	XtaLAB Synergy R, HyPix	XtaLAB Synergy R, HyPix
Radiation type	Cu *Kα*	Cu *Kα*
T_{min}, T_{max}	0.701, 0.914	0.603, 0.896
No. of measured, independent and observed [$I > 2\sigma(I)$] reflections	41896, 9545, 8928	36586, 9777, 8429
R_{int}	0.043	0.041
$(\sin\theta/\lambda)_{max}$ (Å^{-1})	0.616	0.616
$R[F^2 > 2\sigma(F^2)]$, $wR(F^2)$, S	0.038, 0.098, 1.07	0.056, 0.171, 1.03
No. of reflections	9545	9777
No. of parameters	730	920
No. of restraints	417	1212
H-atom treatment	H-atom parameters constrained	H-atom parameters constrained
$\Delta\rho_{max}$, $\Delta\rho_{min}$ (e Å^{-3})	1.02, -1.46	1.83, -1.05

V.2 Photochemistry

V.2.1 Molar extinction coefficient determination

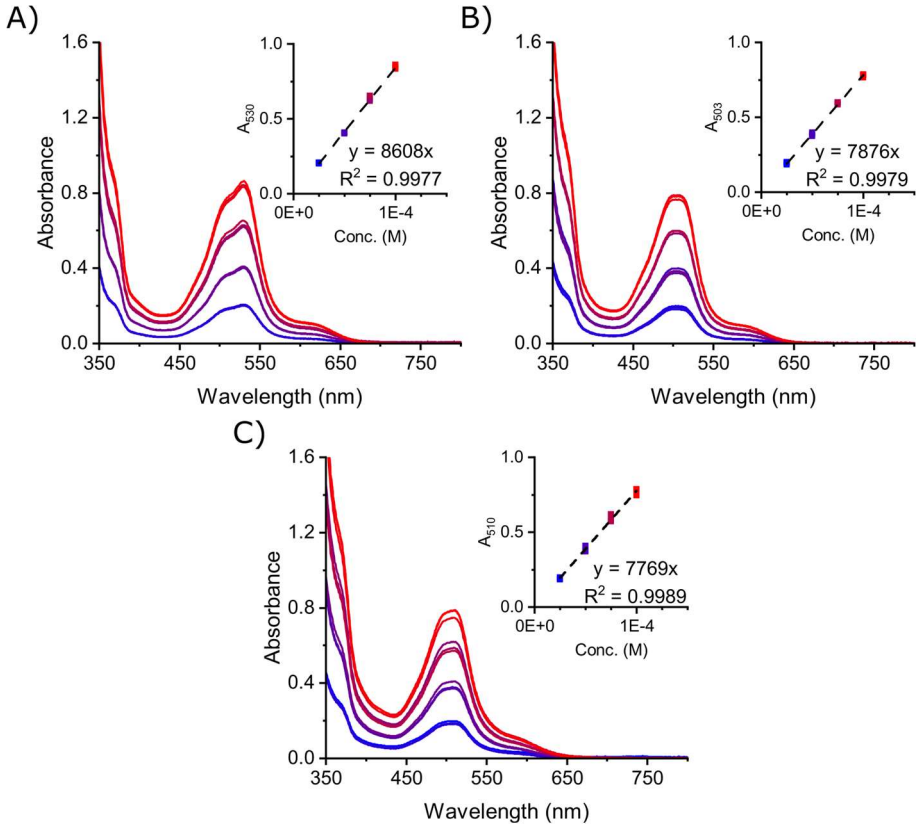

Figure V.1 UV-Vis spectra of [**24**](PF$_6$)$_2$ – [**26**](PF$_6$)$_2$ at different concentrations in 3 ml 50% acetone in H_2O at 298 K (l = 1 cm). Insets depict absorption at λ_{max} at different concentrations. A) [**24**](PF$_6$)$_2$: ε = 8.61 × 10^3 M^{-1} cm^{-1} at 530 nm. B) [**26**](PF$_6$)$_2$: ε = 7.88 × 10^3 M^{-1} cm^{-1} at 503 nm. C) [**25**](PF$_6$)$_2$: ε = 7.77 × 10^3 M^{-1} cm^{-1} at 510 nm.

V.2.2 Photosubstitution quantum yield measurements

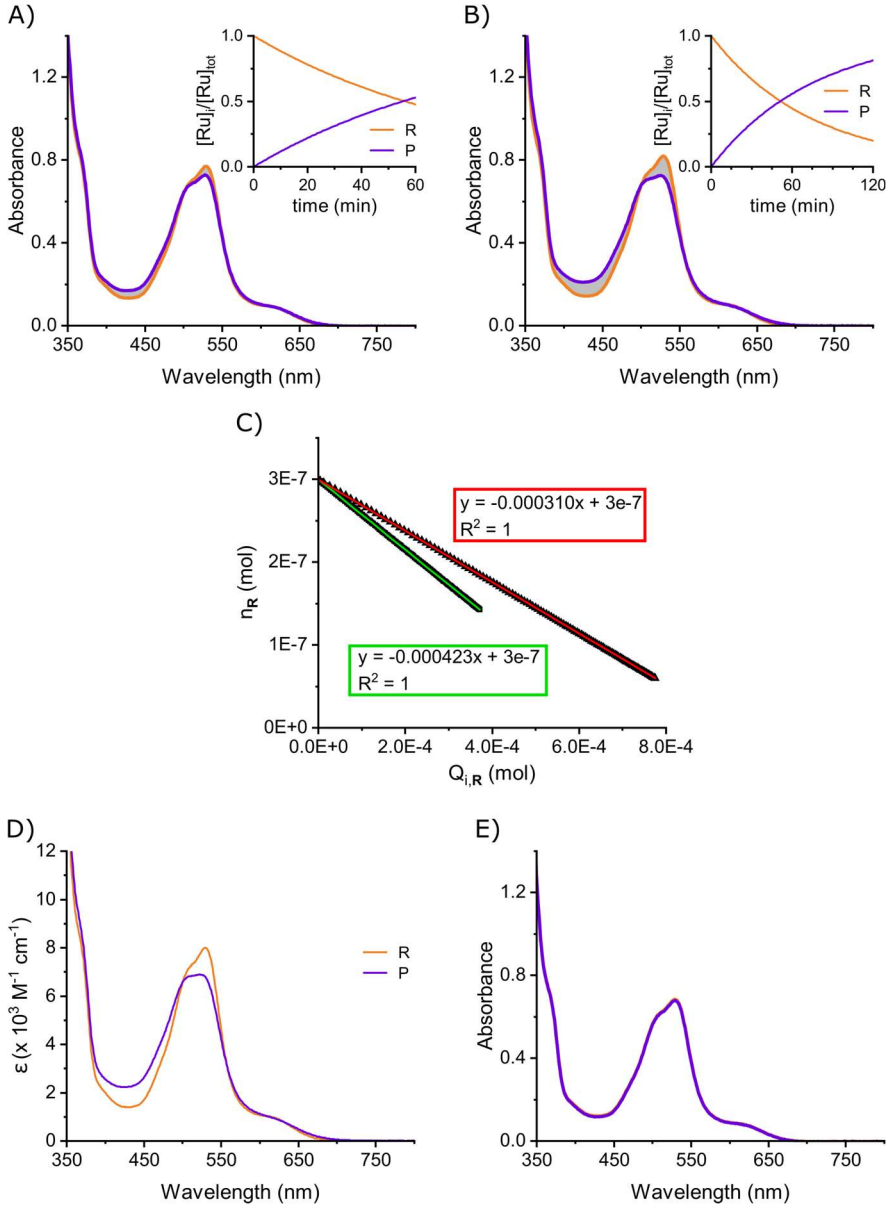

Figure V.2 Graphs for photosubstitution quantum yield for [**24**]$(PF_6)_2$ at 298 K in 50% acetone in H_2O. Time-evolution of UV-Vis absorption upon irradiation with A) 505 nm (photon flux = 1.42× 10^{-7} mol/s) for 60 min at 100 µM and B) 625 nm (photon flux = 4.76 × 10^{-7} mol/s) for 60 min at 100 µM (from orange to purple). C) Plot of n_R against $Q_{i,R}$ used to calculate the photosubstitution quantum yield. D) Globally fitted UV-Vis absorption spectra of [**24**]$(PF_6)_2$ (R; orange line) and the photoproduct (P; purple line). E) Absorption spectra of [**24**]$(PF_6)_2$ in the dark for 18 h (orange to purple).

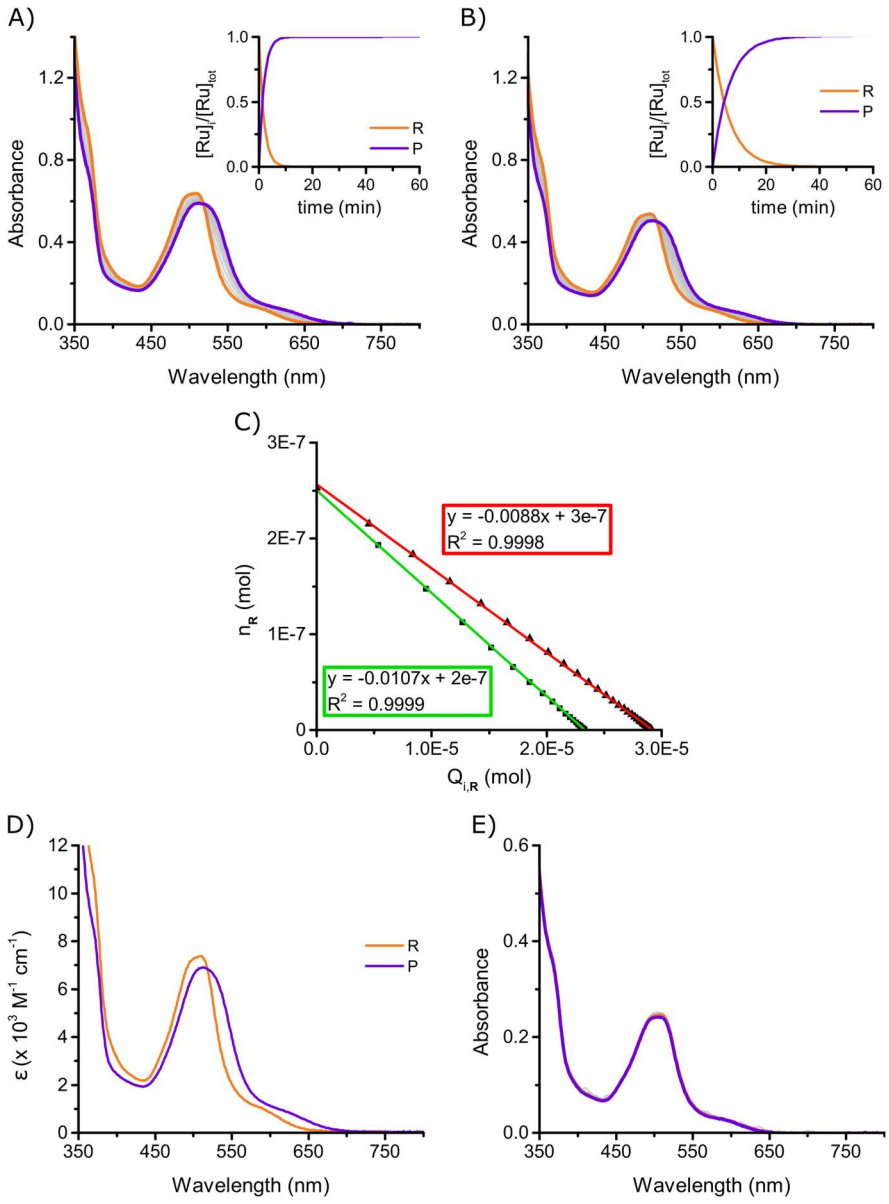

Figure V.3 Graphs for photosubstitution quantum yield for [**25**]$(PF_6)_2$ at 298 K in 50% acetone in H_2O. Time-evolution of UV-Vis absorption upon irradiation with A) 505 nm (photon flux = 2.09×10^{-7} mol/s) for 60 min at 84.3 µM and B) 625 nm (photon flux = 4.14×10^{-7} mol/s) for 60 min at 84.3 µM (from orange to purple). C) Plot of n_R against $Q_{i,R}$ used to calculate the photosubstitution quantum yield. D) Globally fitted UV-Vis absorption spectra of [**25**]$(PF_6)_2$ (R; orange line) and the photoproduct (P; purple line). E) Absorption spectra of [**25**]$(PF_6)_2$ in the dark for 16 h (from orange to purple).

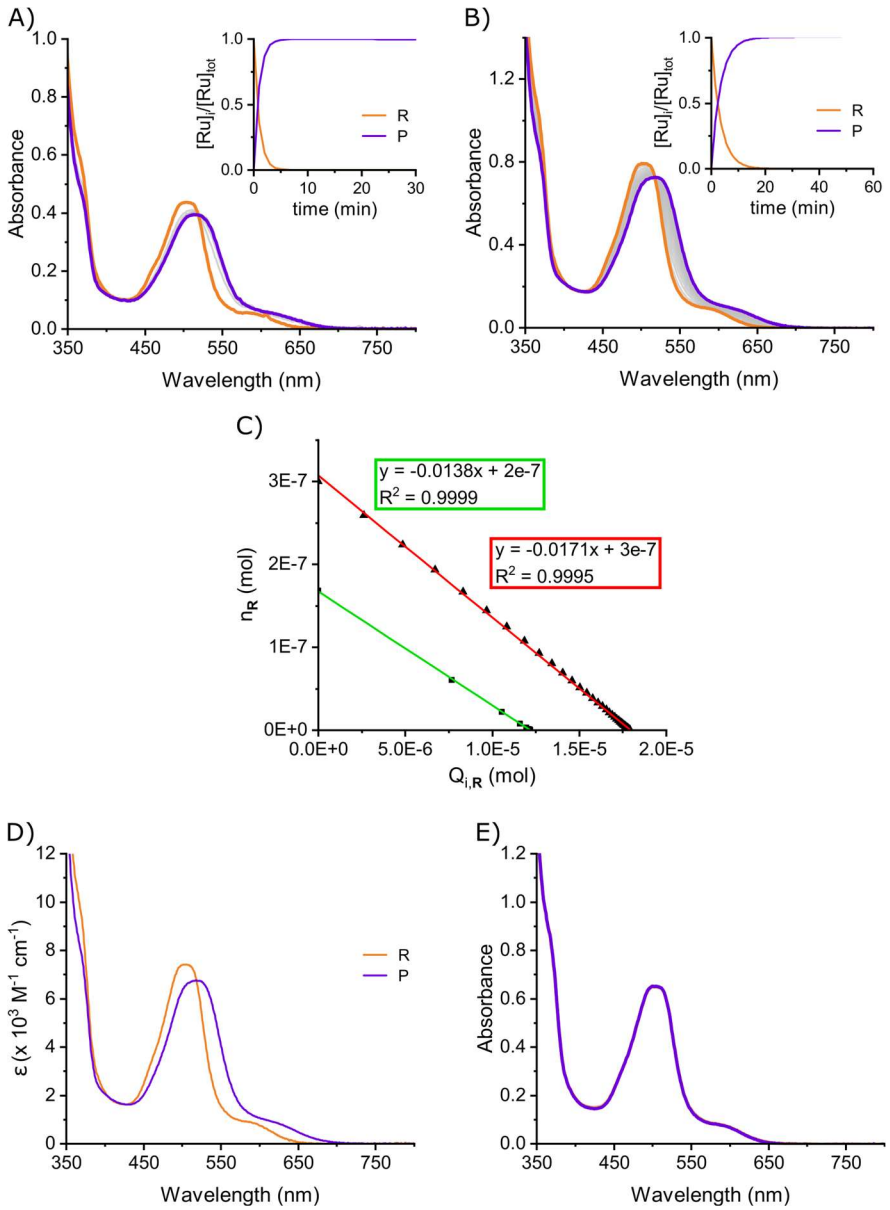

Figure V.4 Graphs for photosubstitution quantum yield for [**26**]$(PF_6)_2$ at 298 K in 50% acetone in H_2O. Time-evolution of UV-Vis absorption upon irradiation with A) 505 nm (photon flux = 2.02×10^{-7} mol/s) for 30 min at 56.0 μM and B) 625 nm (photon flux = 4.76×10^{-7} mol/s) for 60 min at 100 μM) (from orange to purple). C) Plot of n_R against $Q_{i,R}$ used to calculate the photosubstitution quantum yield. D) Globally fitted UV-Vis absorption spectra of [**26**]$(PF_6)_2$ (R; orange line) and the photoproduct (P; purple line). E) Absorption spectra of [**26**]$(PF_6)_2$ in the dark for 20 h (from orange to purple).

V.2.3 Phosphorescence and singlet oxygen generation quantum yield measurements

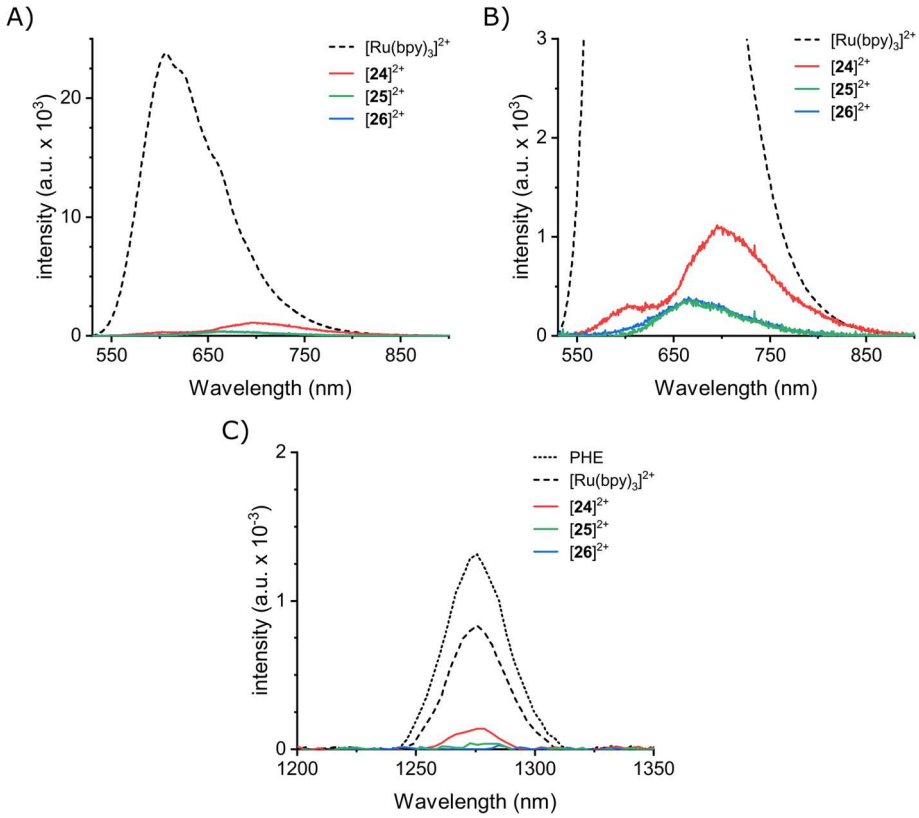

Figure V.5 A) Visible emission spectra of [**24**](PF$_6$)$_2$ – [**26**](PF$_6$)$_2$ and [Ru(bpy)$_3$]Cl$_2$ in aerated acetonitrile at 298 K under blue light irradiation (450 nm, 80 mW/cm^2) with B) being a focused version of A). C) Near-infrared emission spectra of $^1O_2$ phosphorescence (λ_{em} = 1275 nm) sensitized by [**24**](PF$_6$)$_2$ – [**26**](PF$_6$)$_2$, [Ru(bpy)$_3$]Cl$_2$ and perinaphthenone (PHE) in aerated acetonitrile at 298 K under blue light irradiation (450 nm, 80 mW/cm^2).

Table V.2 Data for the determination of phosphorescence and singlet oxygen generation quantum yields in aerated acetonitrile.

Compound	Abs. (450 nm)	Integrated intensity	φ_p	Abs. (450 nm)	Integrated intensity	φ_Δ ($^1O_2$)
Perinaphthenone	-	-	-	0.0960	0.0403	0.980
[Ru(bpy)$_3$]Cl$_2$	0.1071	2.56×10^6	0.018	0.1073	0.0265	0.577
[**24**](PF$_6$)$_2$	0.1024	1.39×10^5	0.00102	0.1077	0.0034	0.073
[**25**](PF$_6$)$_2$	0.0973	3.29×10^4	0.00025	0.0992	0.0002	<0.01
[**26**](PF$_6$)$_2$	0.1041	3.95×10^4	0.00029	0.1010	0.0002	<0.01

V.2.4 Mock irradiation experiment

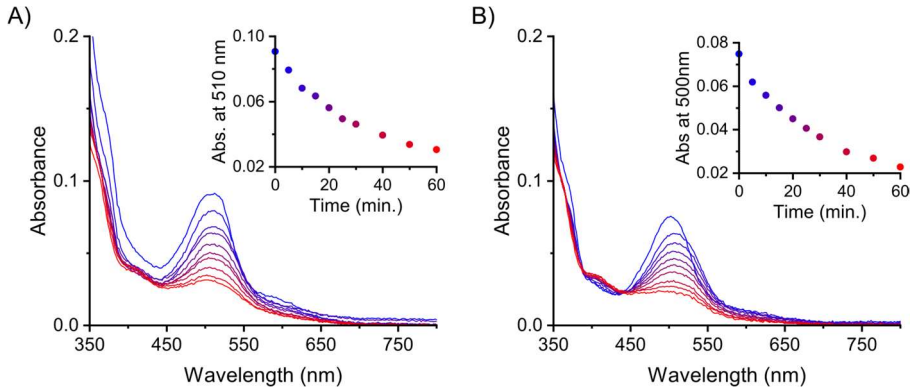

Figure V.6 Time-evolution (blue to red) of UV-Vis absorbance spectra of [**25**]Cl_2 (A) and [**26**]Cl_2 (B) in OptiMEM complete media + 0.14% DMSO upon irradiation with red (630 ± 24 nm, 31.3 mW/cm^2) light array at 37 °C (conc. = 5.0 × 10^{-5} M, v = 200 µL).

V.3 Cytotoxicity

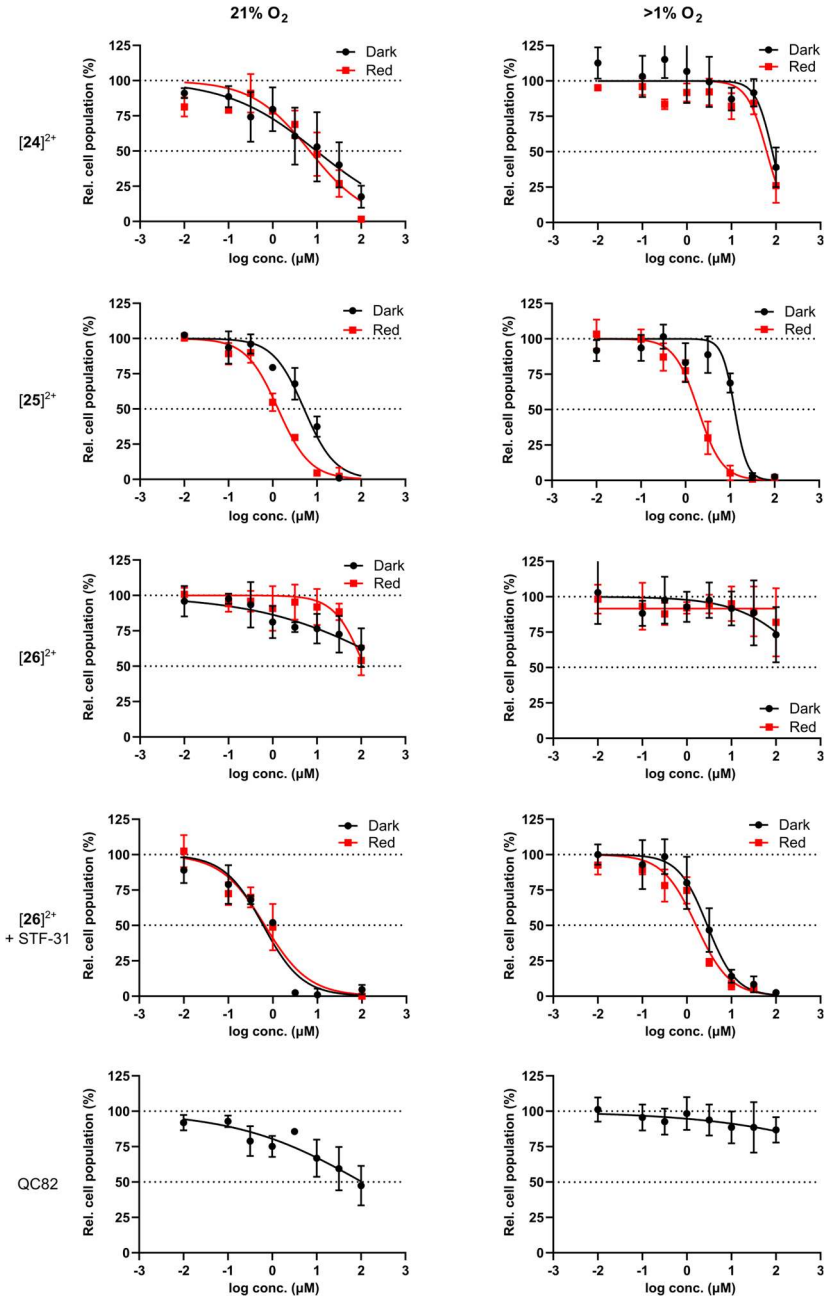

Figure V.7 Dose-response curves of [**24**]Cl_2 – [**26**]Cl_2, [**26**]Cl_2 + **STF31** (1:1 molar ratio), **QC82** and **STF31** in A375 cell line incubated in normoxic (21% O_2) and hypoxic (1% O_2) conditions in the dark (black curve) or with red light irradiation (630 nm, 58 J/cm^2, 31.3 mW/cm^2, 30 min). Data points are average of independent triplicate with error bars indicating 95% confidence intervals.

V.4 Characterization of synthesized compounds

V.4.1 6-bromo-4-chloro-2,2'-bipyridine, 2a

^{1}H NMR (400 MHz, $CDCl_3$) δ 8.67 (ddd, *J* = 5.0, 1.8, 1.0 Hz, 1H), 8.42 (d, *J* = 1.7 Hz, 1H), 8.39 (dt, *J* = 8.0, 1.1 Hz, 1H), 7.83 (td, *J* = 7.8, 1.8 Hz, 1H), 7.51 (d, *J* = 1.7 Hz, 1H), 7.35 (ddd, *J* = 7.5, 4.8, 1.1 Hz, 1H).

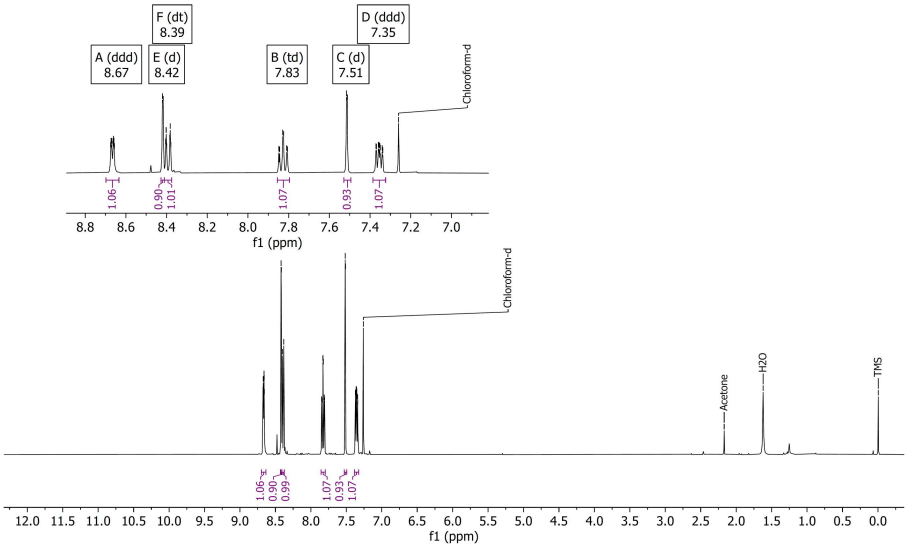

Figure V.8 ^{1}H-NMR of **2a** in $CDCl_3$.

^{13}C NMR (101 MHz, $CDCl_3$) δ 158.22, 153.49, 149.45, 146.53, 141.83, 137.29, 127.64, 124.95, 121.89, 120.56.

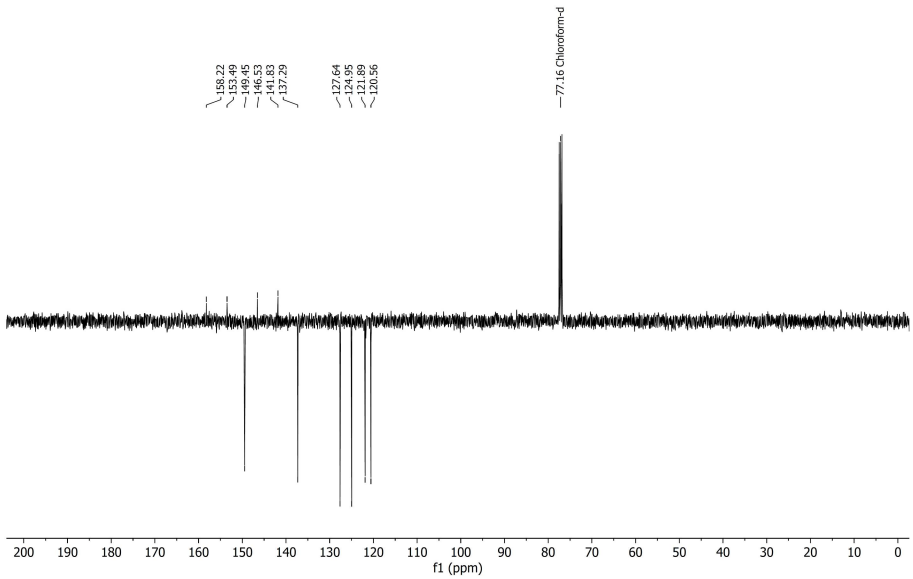

Figure V.9 ^{13}C-APT-NMR of **2a** in $CDCl_3$.

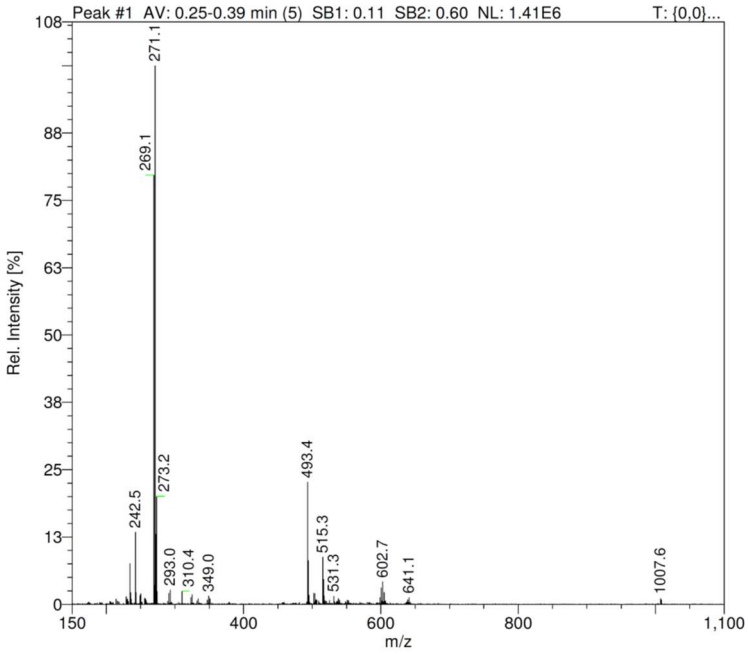

Figure V.10 ESI-MS of **2a**. Calculated for $[C_{10}H_6BrClN_2 + H^+]^{2+}$: 270.9 m/z.

V.4.2 6-bromo-5-chloro-2,2'-bipyridine, 2b

^{1}H NMR (850 MHz, $CDCl_3$) δ 8.66 (ddd, *J* = 4.7, 1.8, 1.0 Hz, 1H), 8.38 (dt, *J* = 7.9, 1.1 Hz, 1H), 8.35 (d, *J* = 8.2 Hz, 1H), 7.84 (d, *J* = 8.2 Hz, 1H), 7.82 (ddd, *J* = 7.9, 7.4, 1.8 Hz, 1H), 7.34 (ddd, *J* = 7.4, 4.7, 1.2 Hz, 1H).

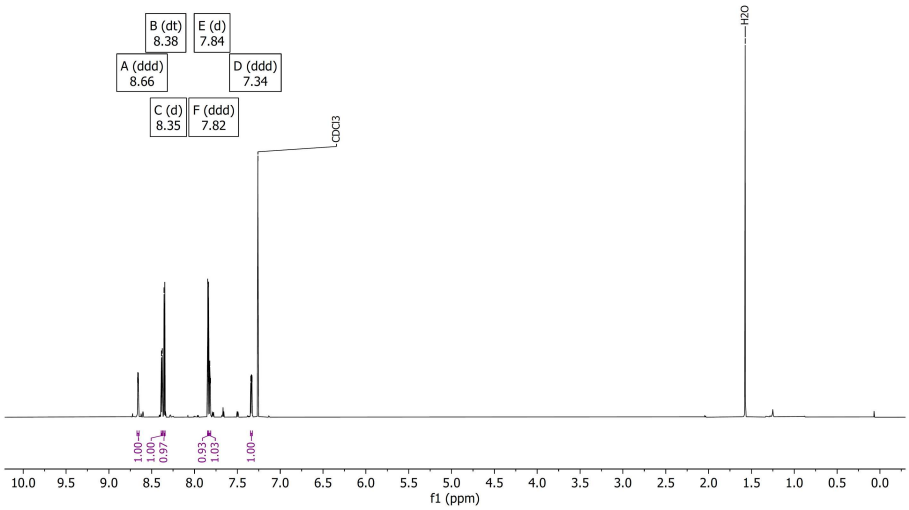

Figure V.11 ^{1}H-NMR of **2b** in $CDCl_3$.

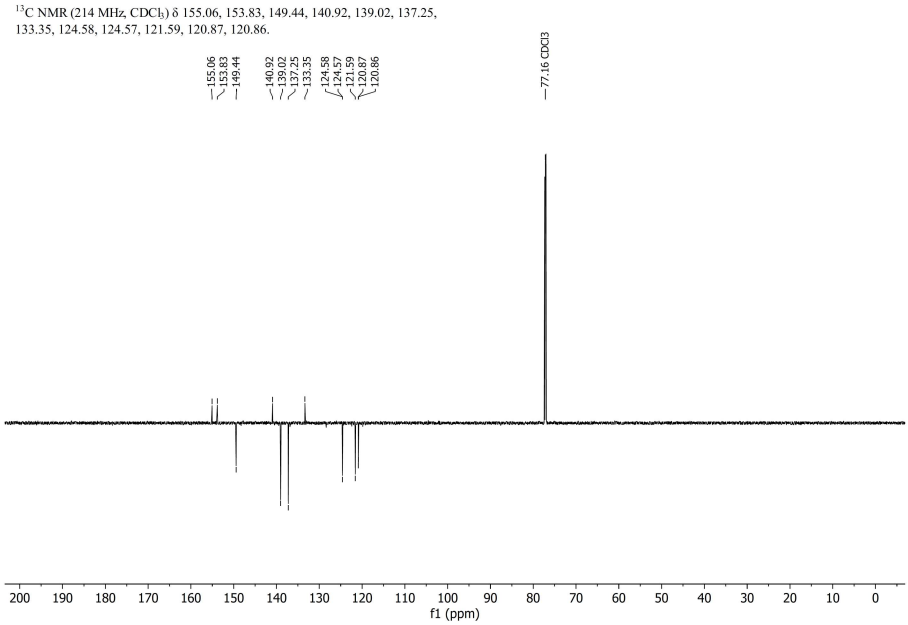

Figure V.12 ^{13}C-APT-NMR of **2b** in $CDCl_3$.

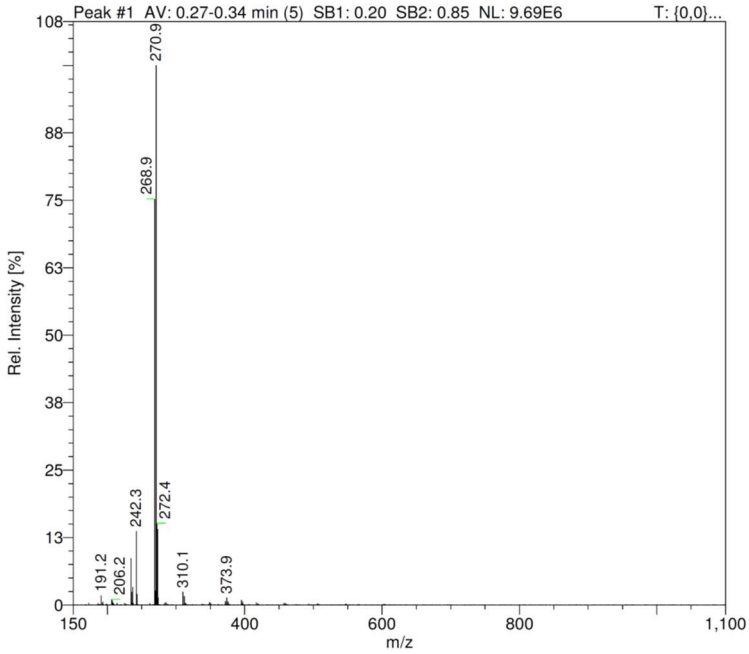

Figure V.13 ESI-MS of **2b**. Calculated for $[C_{10}H_6BrClN_2 + H^+]^+$: 270.9 m/z.

V.4.3 Bis(4-chloro-[2,2'-bipyridin]-6-yl)amine, 3a

^{1}H NMR (850 MHz, DMSO) δ 10.31 (s, 1H), 8.68 (d, J = 4.6 Hz, 2H), 8.27 (dt, J = 7.9, 1.1 Hz, 2H), 7.99 (td, J = 7.6, 1.8 Hz, 2H), 7.97 – 7.94 (m, 2H), 7.89 (d, J = 1.8 Hz, 2H), 7.48 (ddd, J = 7.4, 4.6, 1.1 Hz, 2H).

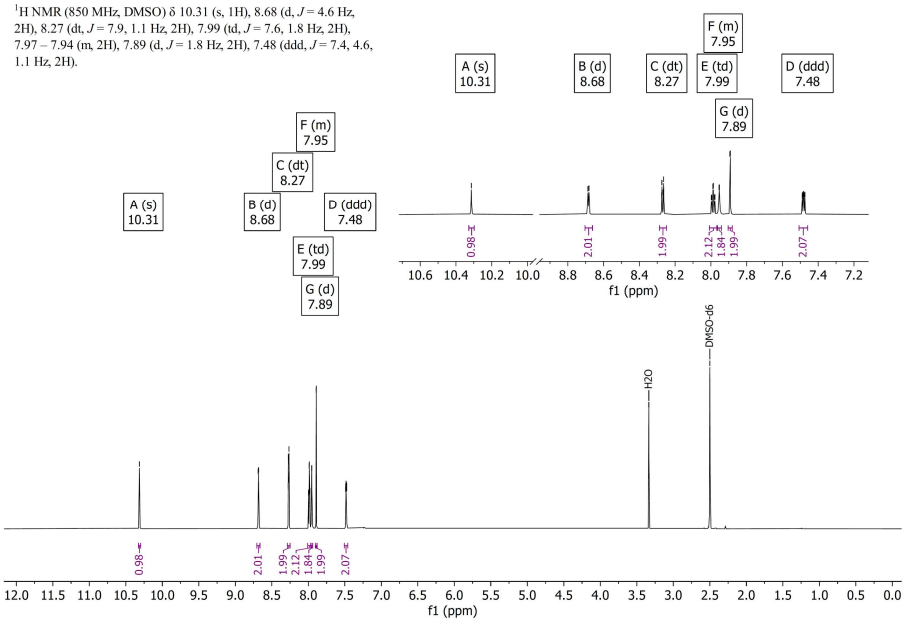

Figure V.14 ^{1}H-NMR of **3a** in DMSO-d_6.

^{13}C NMR (214 MHz, DMSO) δ 155.05, 154.29, 153.91, 149.44, 149.43, 144.51, 137.37, 124.73, 120.52, 113.05, 111.55.

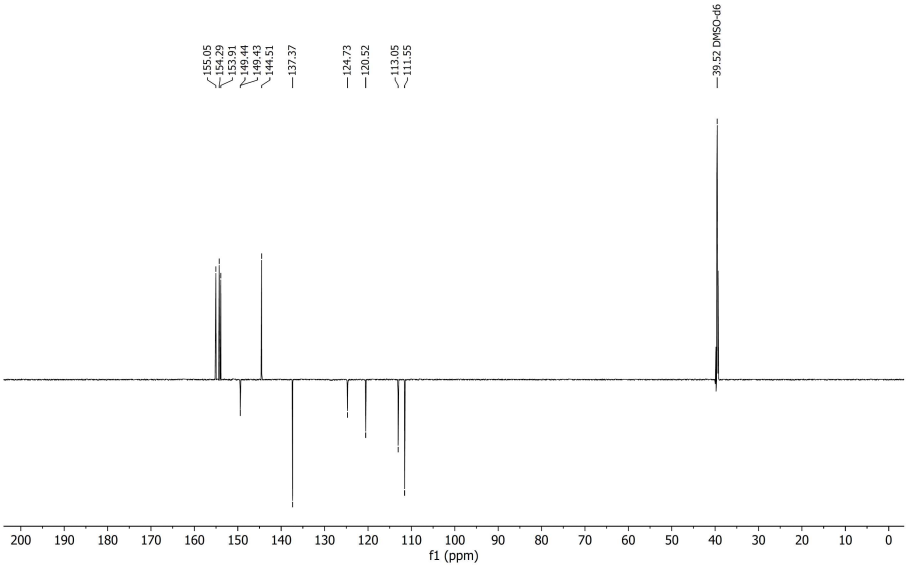

Figure V.15 ^{13}C-APT-NMR of **4a** in DMSO-d_6.

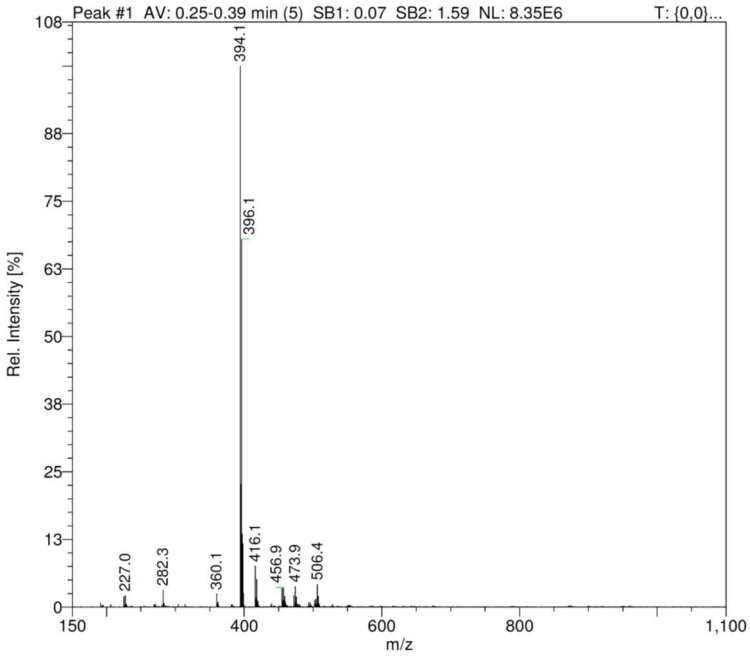

Figure V.16 ESI-MS of **3a**. Calculated for $[C_{20}H_{13}Cl_2N_5 + H^+]^+$: 394.1 m/z.

V.4.4 Bis(5-chloro-[2,2'-bipyridin]-6-yl)amine, 3b

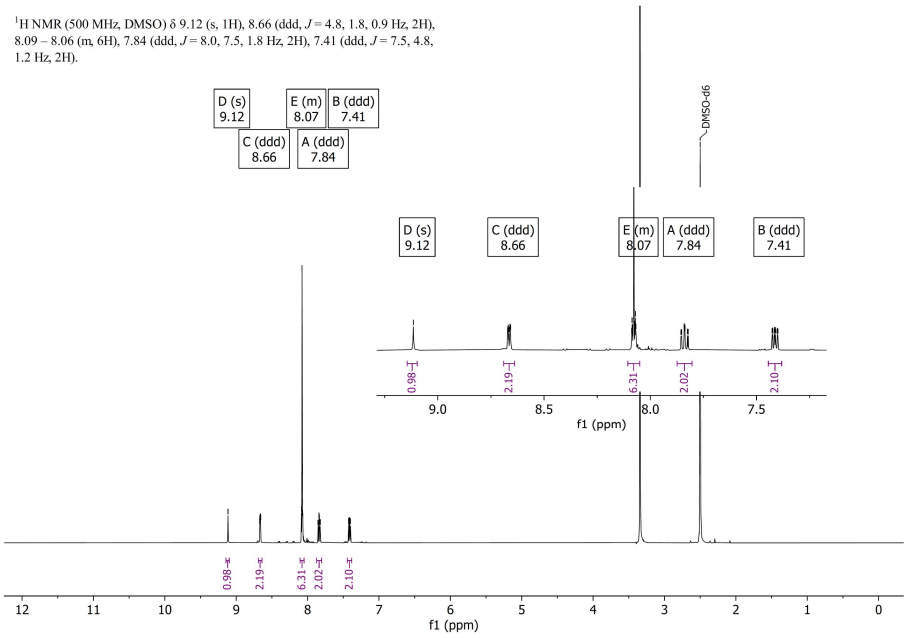

Figure V.17 ^{1}H-NMR of **3b** in DMSO-d_6.

^{13}C NMR (126 MHz, DMSO) δ 154.27, 152.11, 150.15, 149.35, 139.06, 137.28, 124.28, 121.65, 120.39, 115.84.

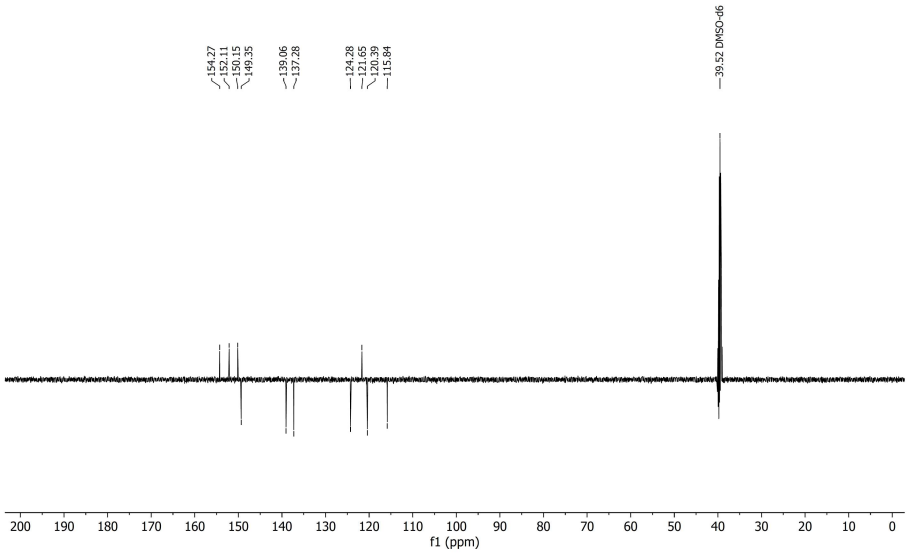

Figure V.18 ^{13}C-APT-NMR of **3b** in DMSO-d_6.

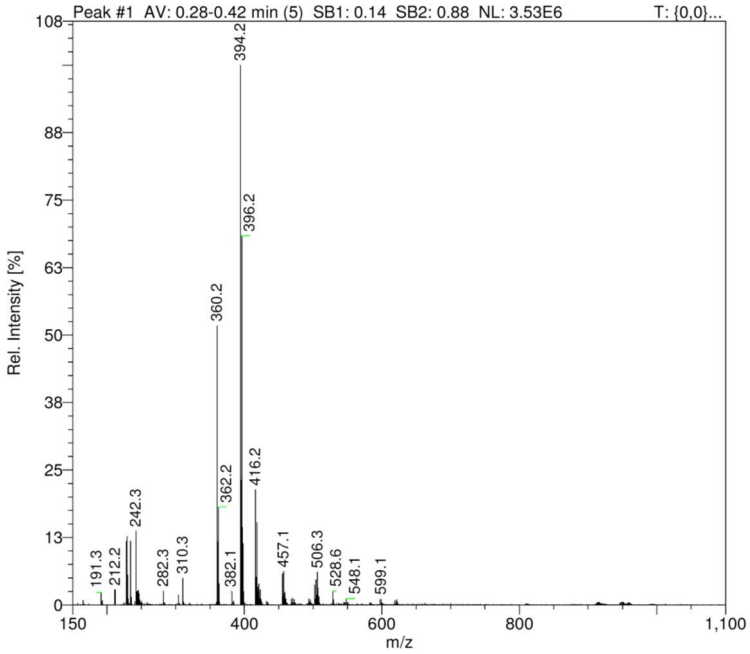

Figure V.19 ESI-MS of **3b**. Calculated for $[C_{20}H_{13}Cl_2N_5 + H^+]^+$: 394.1 m/z.

V

V.4.5 Bis(4-chloro-[2,2'-bipyridin]-6-yl)-*N*-methylamine, 4a

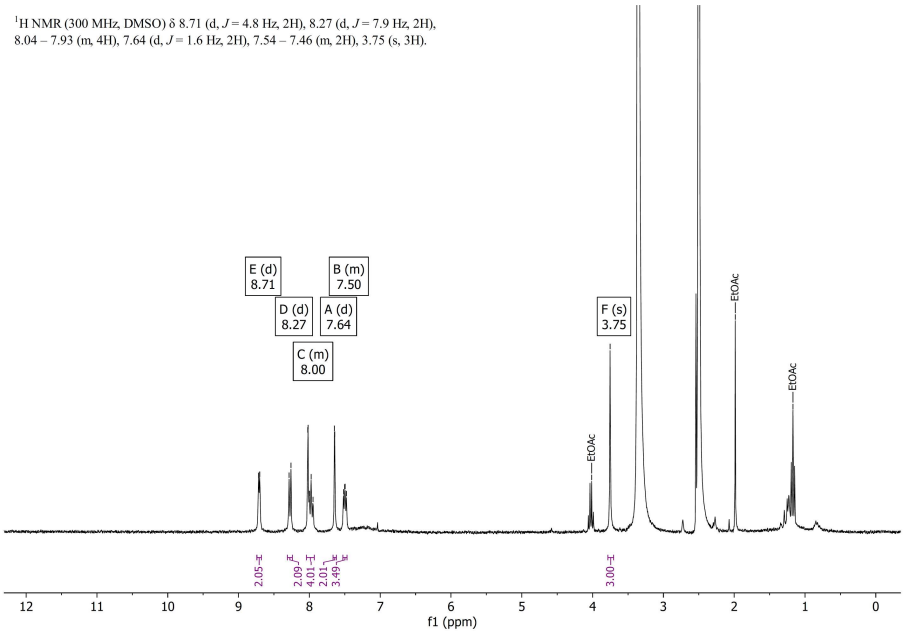

Figure V.20 ^{1}H-NMR of **4a** in DMSO-d_6.

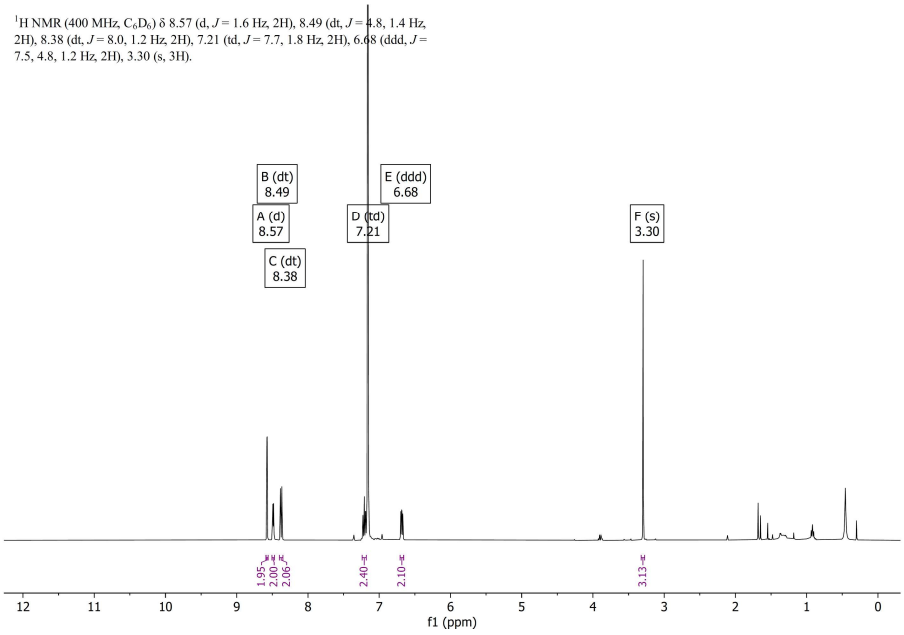

Figure V.21 ^{1}H-NMR of **4a** in benzene-d_6.

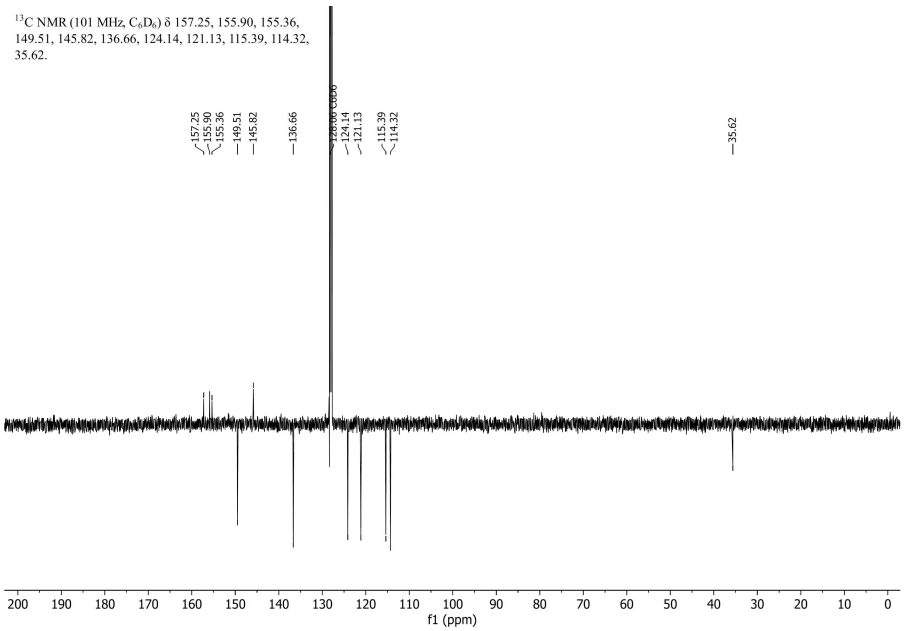

Figure V.22 ^{13}C-APT-NMR of **4a** in benzene-d_6.

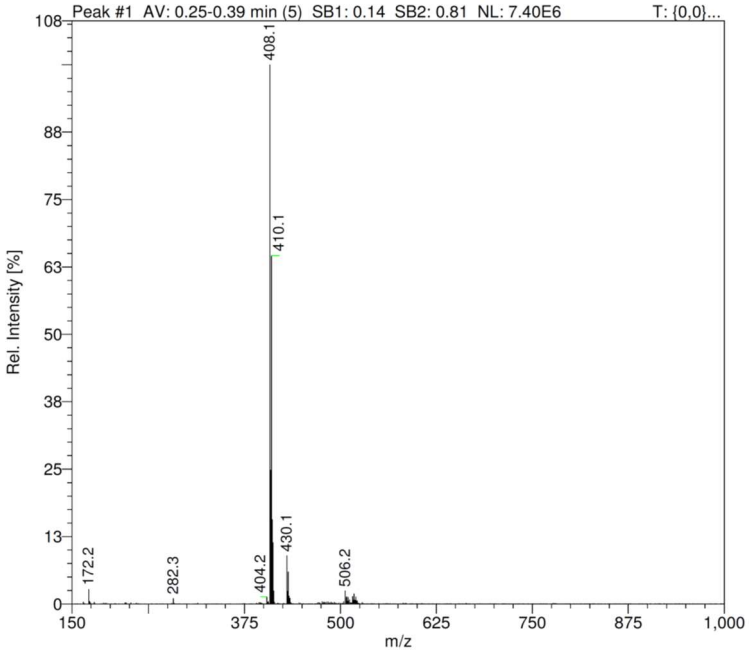

Figure V.23 ESI-MS of **4a**. Calculated for $[C_{21}H_{15}Cl_2N_5 + H^+]^+$: 408.1 m/z.

V.4.6 Bis(5-chloro-[2,2'-bipyridin]-6-yl)-*N*-methylamine, 4b

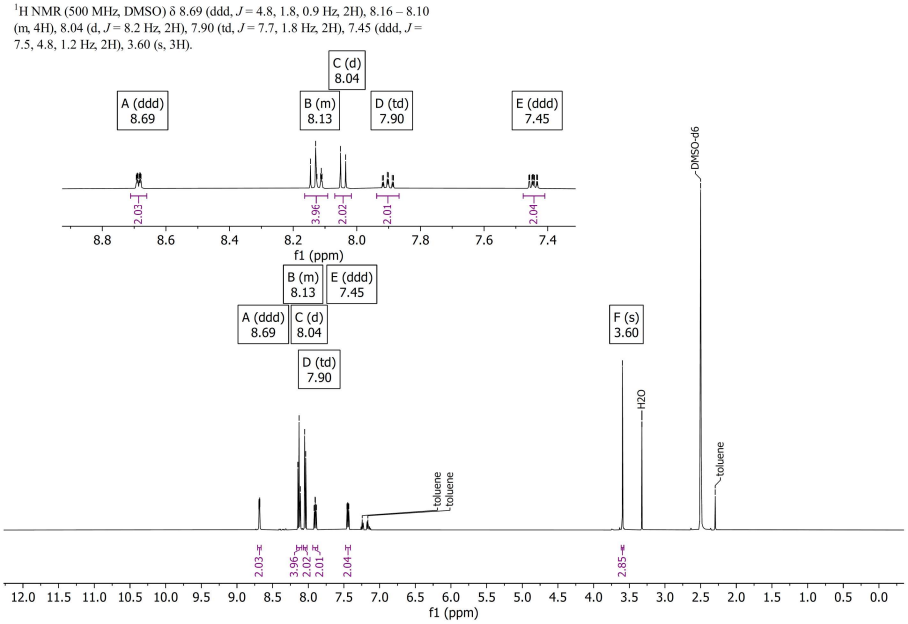

Figure V.24 ^{1}H-NMR of **4b** in DMSO-d_6.

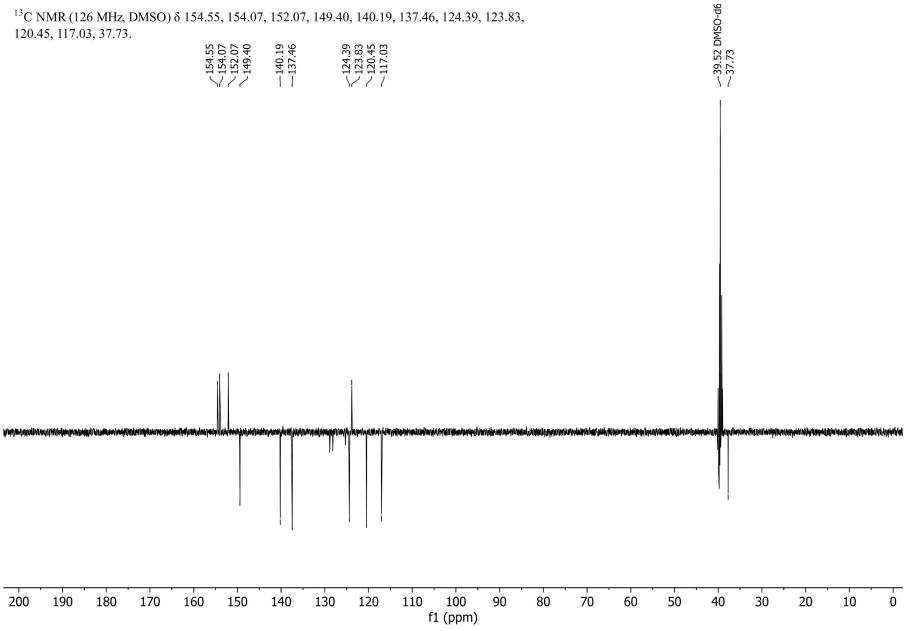

Figure V.25 ^{13}C-APT-NMR of **4b** in DMSO-d_6.

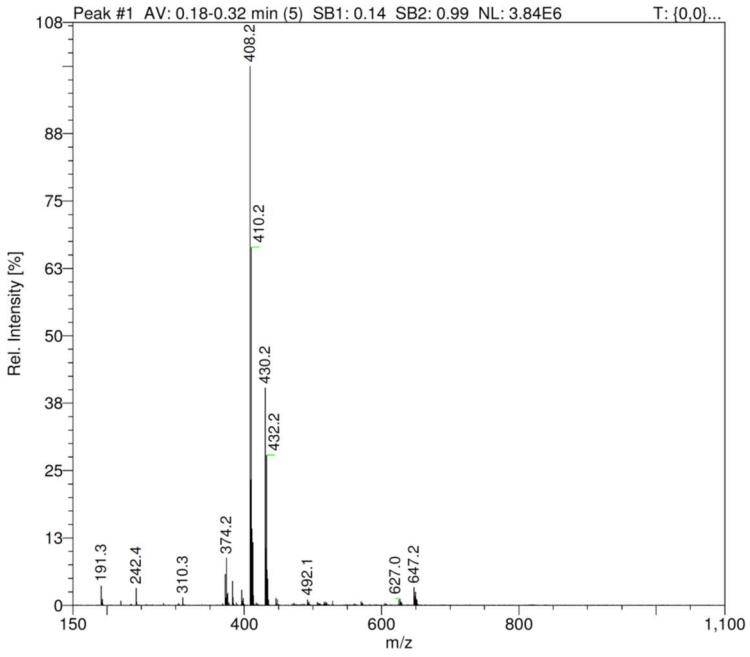

Figure V.26 ESI-MS of **4b**. Calculated for $[C_{21}H_{15}Cl_2N_5 + H^+]^+$: 408.1 m/z.

V.4.7 Bis(4-chloro-[2,2'-bipyridin]-6-yl)-*N*-(2,4-dimethoxybenzyl)amine, 5a

^{1}H NMR (400 MHz, DMSO) δ 8.69 (ddd, J = 4.8, 1.9, 0.9 Hz, 2H), 8.24 (dt, J = 8.0, 1.1 Hz, 2H), 8.00 (d, J = 1.6 Hz, 2H), 7.95 (td, J = 7.7, 1.8 Hz, 2H), 7.59 (d, J = 1.6 Hz, 2H), 7.48 (ddd, J = 7.5, 4.8, 1.2 Hz, 2H), 7.18 (d, J = 2.1 Hz, 1H), 6.96 (dd, J = 8.3, 2.0 Hz, 1H), 6.85 (d, J = 8.3 Hz, 1H), 5.55 (s, 2H), 3.66 (s, 3H), 3.63 (s, 3H).

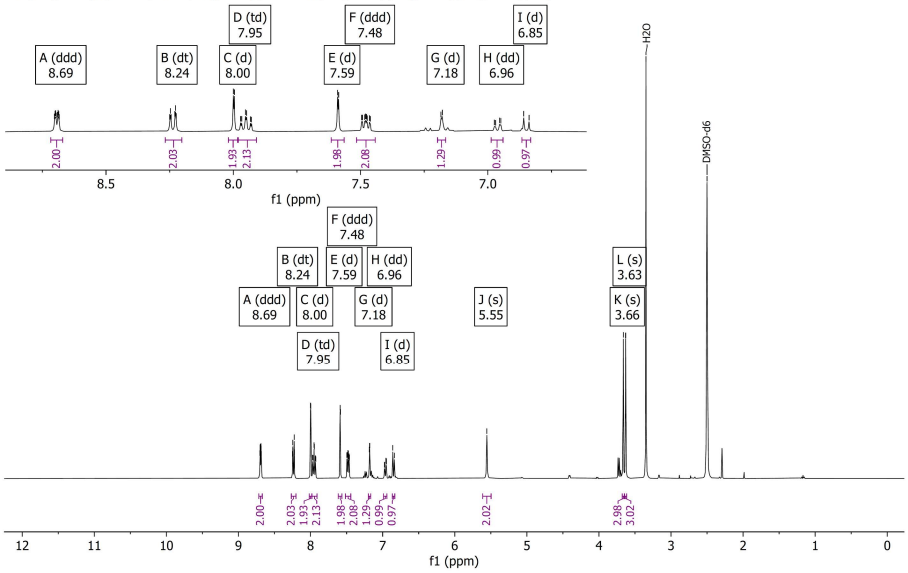

Figure V.27 ^{1}H-NMR of **5a** in DMSO-d_6.

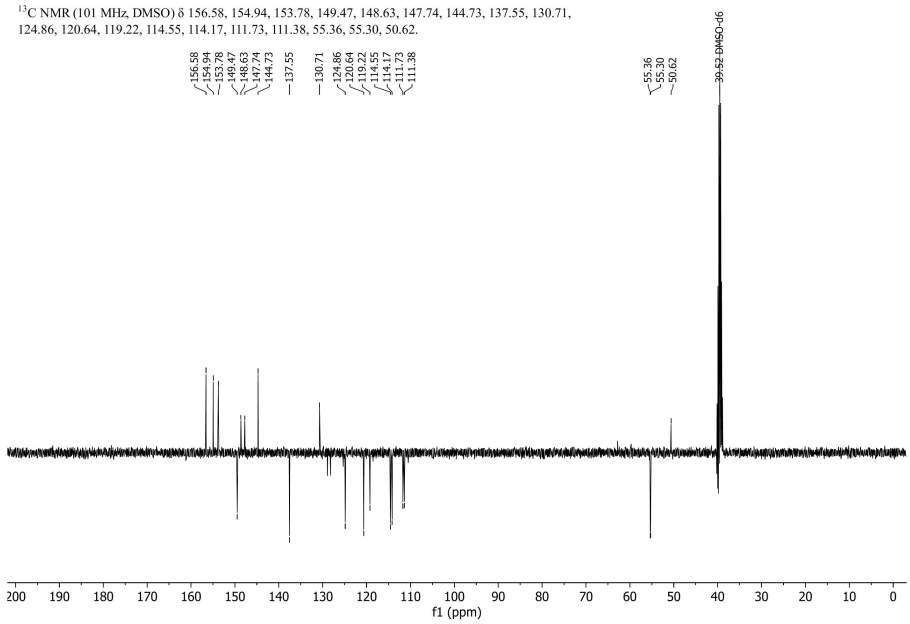

Figure V.28 ^{13}C-APT-NMR of **5a** in DMSO-d_6.

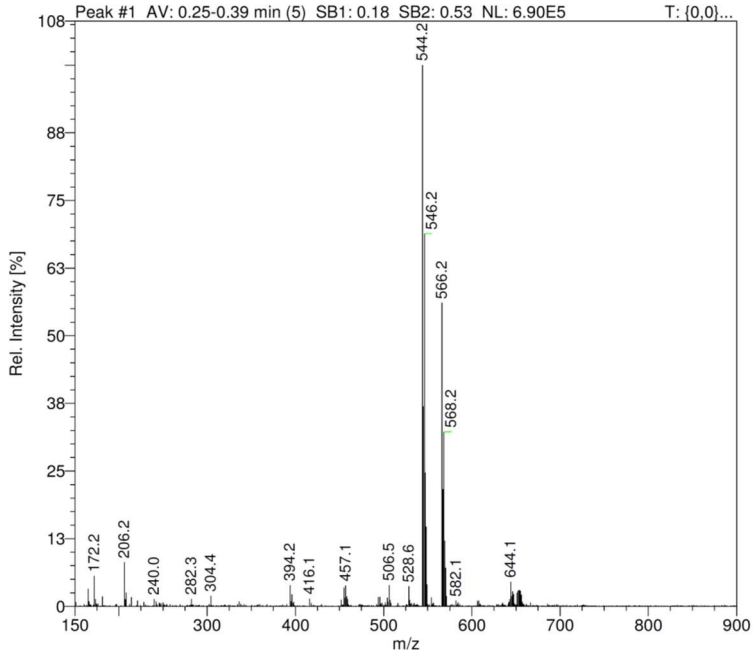

Figure V.29 ESI-MS of **5a**. Calculated for $[C_{29}H_{24}Cl_2N_5O_2 + H^+ + MeOH]^+$: 544.2 m/z.

V.4.8 Compound 6'

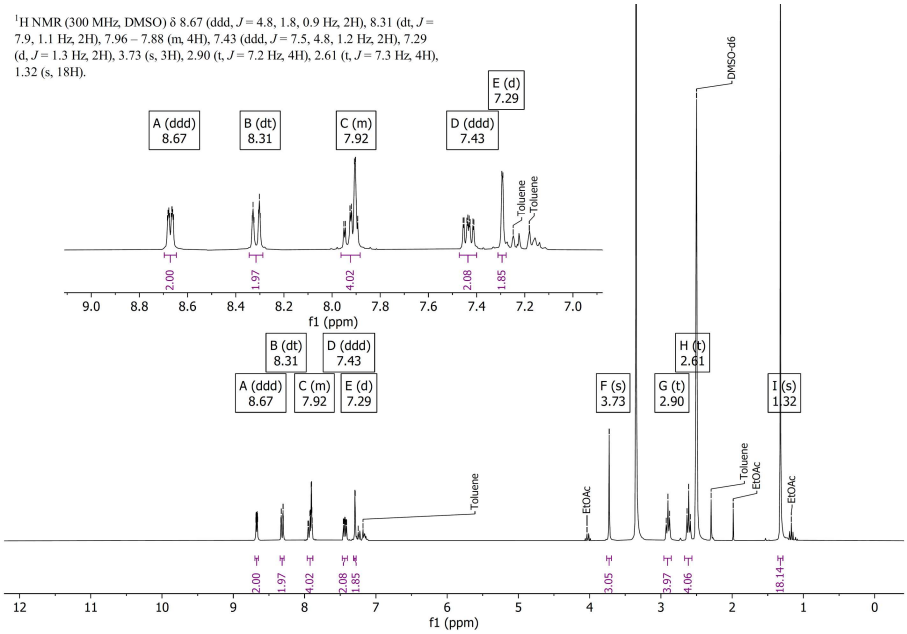

Figure V.30 ^{1}H-NMR of **6'** in DMSO-d_6.

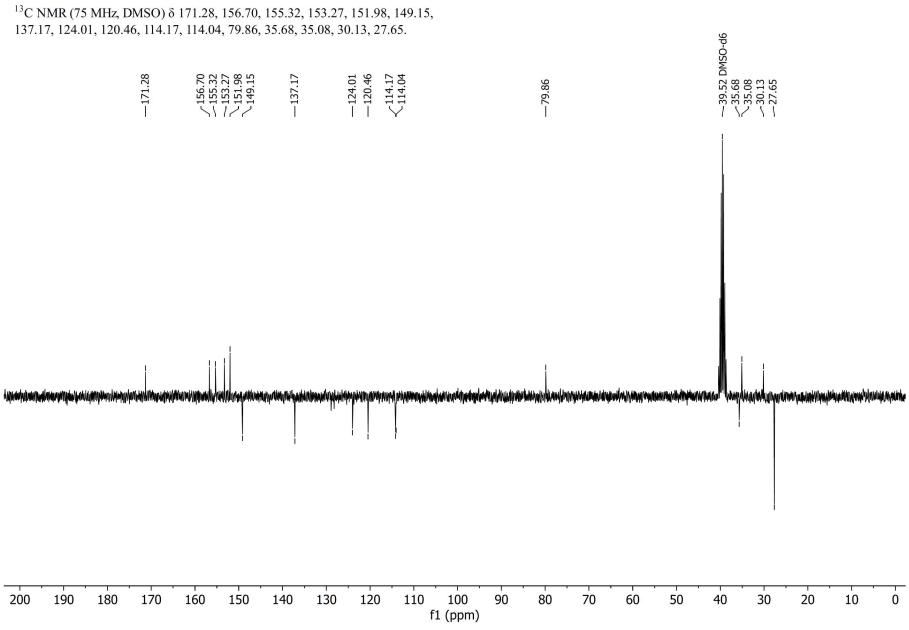

Figure V.31 ^{13}C-APT-NMR of **6'** in DMSO-d_6.

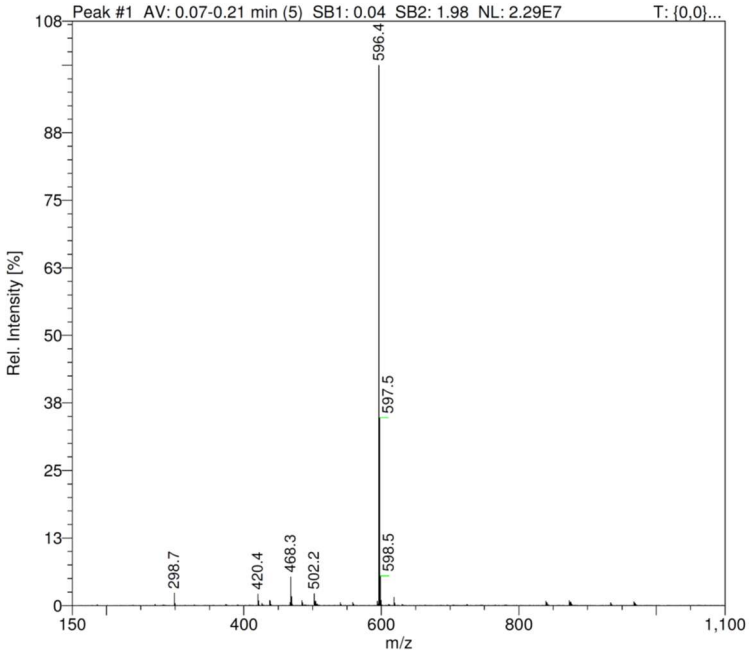

Figure V.32 ESI-MS of **6'**. Calculated for $[C_{35}H_{41}N_5O_4 + H^+]^+$: 596.3 m/z.

V.4.9 Compound 7'

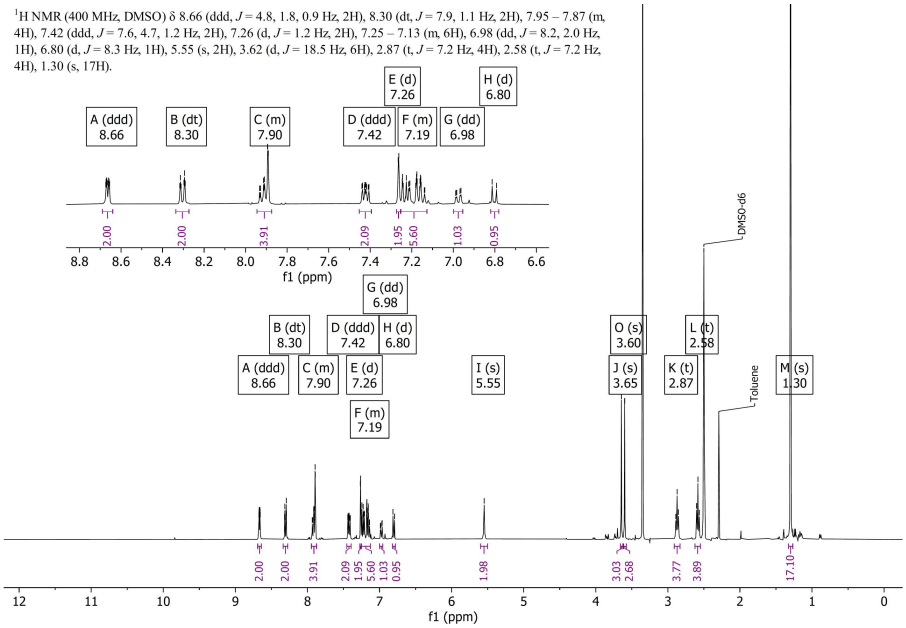

Figure V.33 ^{1}H-NMR of **7'** in DMSO-d_6.

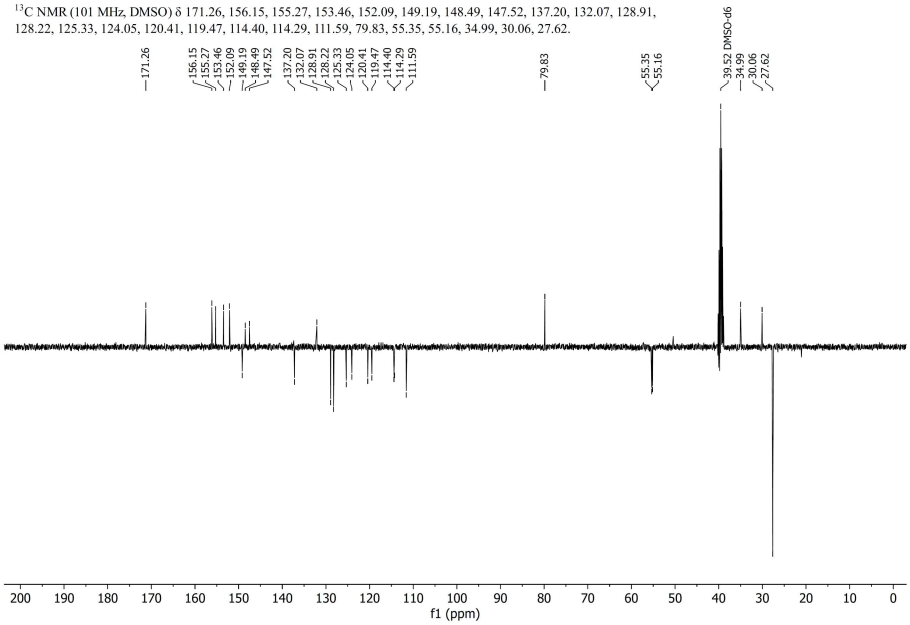

Figure V.34 ^{13}C-APT-NMR of **7'** in DMSO-d_6.

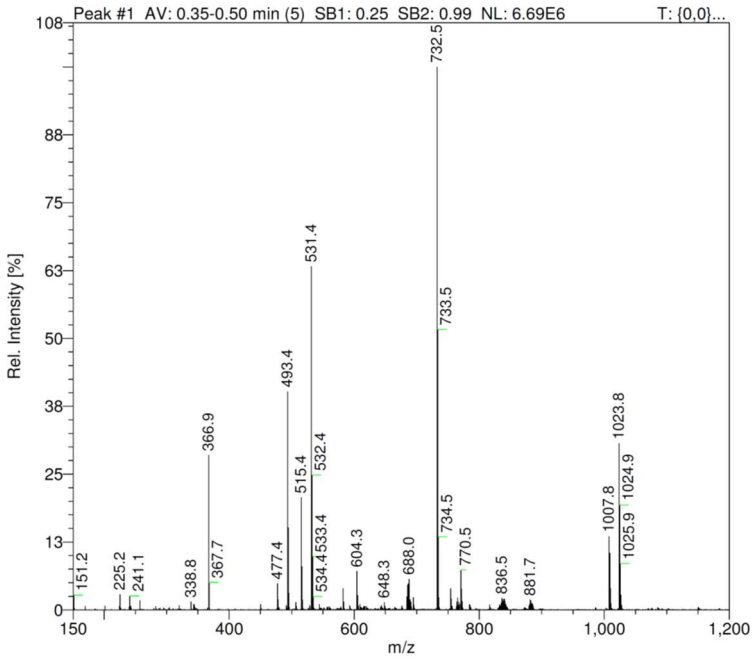

Figure V.35 ESI-MS of **7'**. Calculated for $[C_{43}H_{49}N_5O_6 + H^+]^+$: 735.4 m/z.

V.4.10 Compound 6

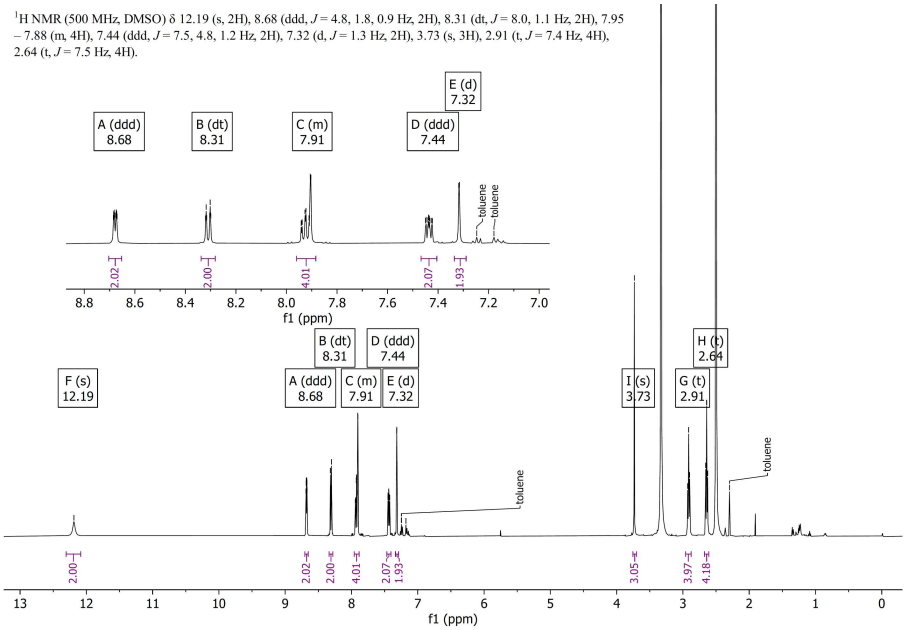

Figure V.36 ^{1}H-NMR of **6** in DMSO-d_6.

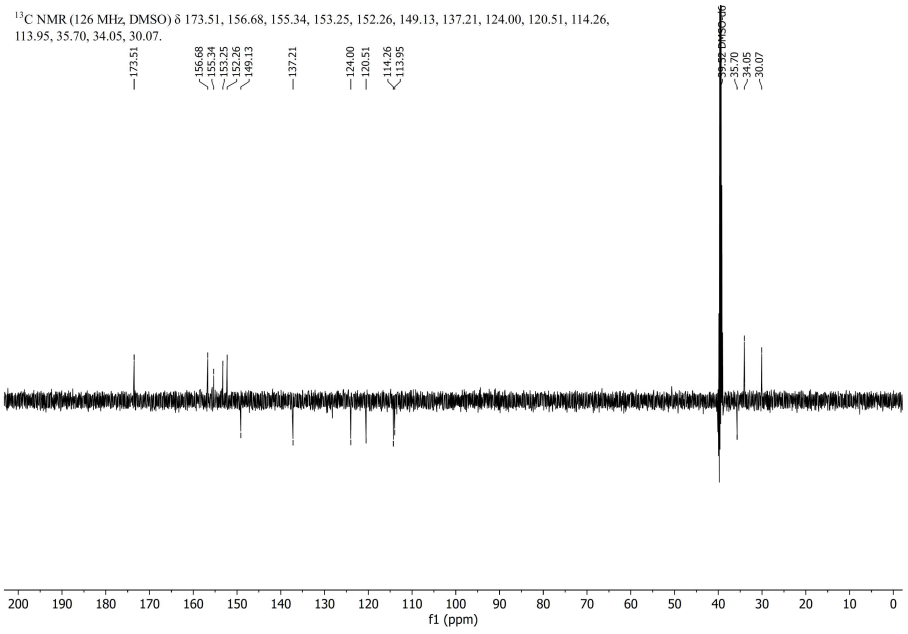

Figure V.37 ^{13}C-APT-NMR of **6** in DMSO-d_6.

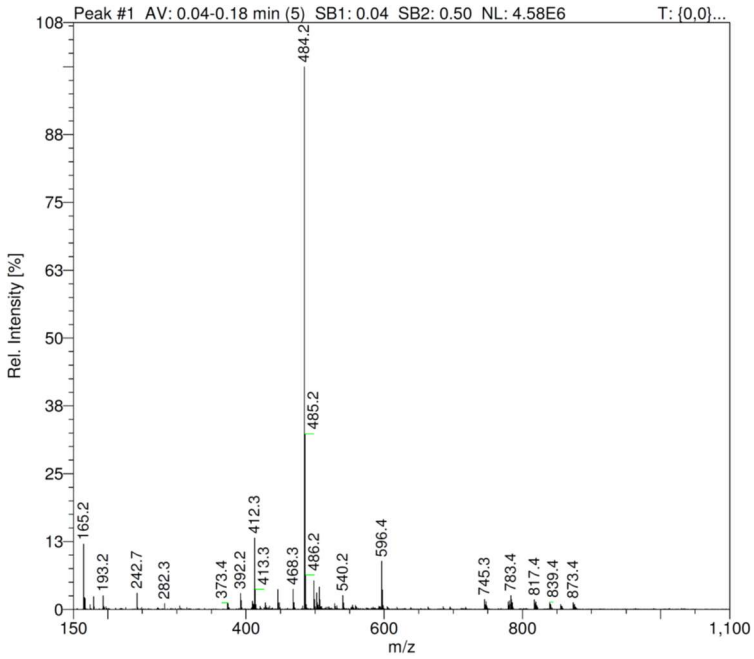

Figure V.38 ESI-MS of **6**. Calculated for $[C_{27}H_{25}N_5O_4 + H^+]^+$: 484.2 m/z.

V.4.11 Compound 7

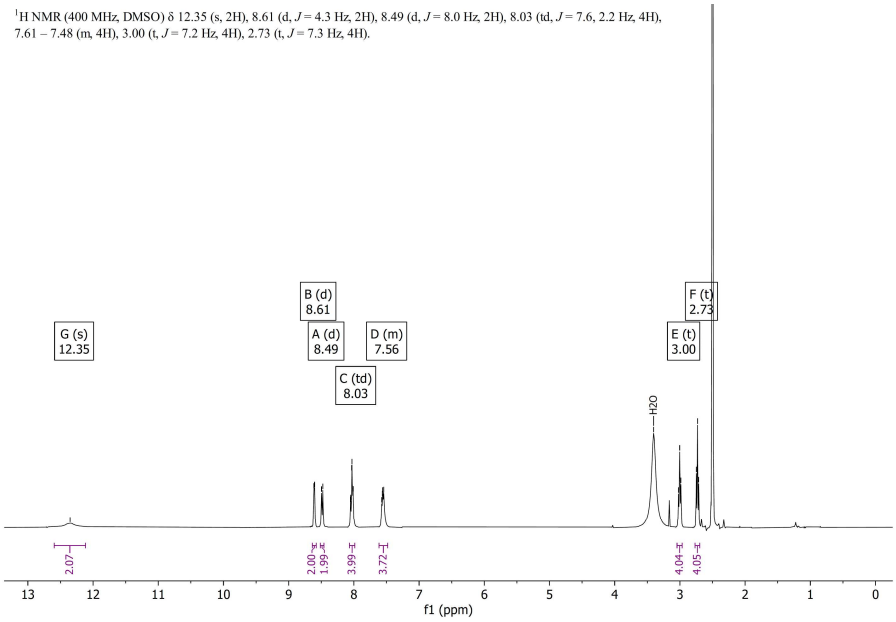

Figure V.39 ^{1}H-NMR of **7** in DMSO-d_6.

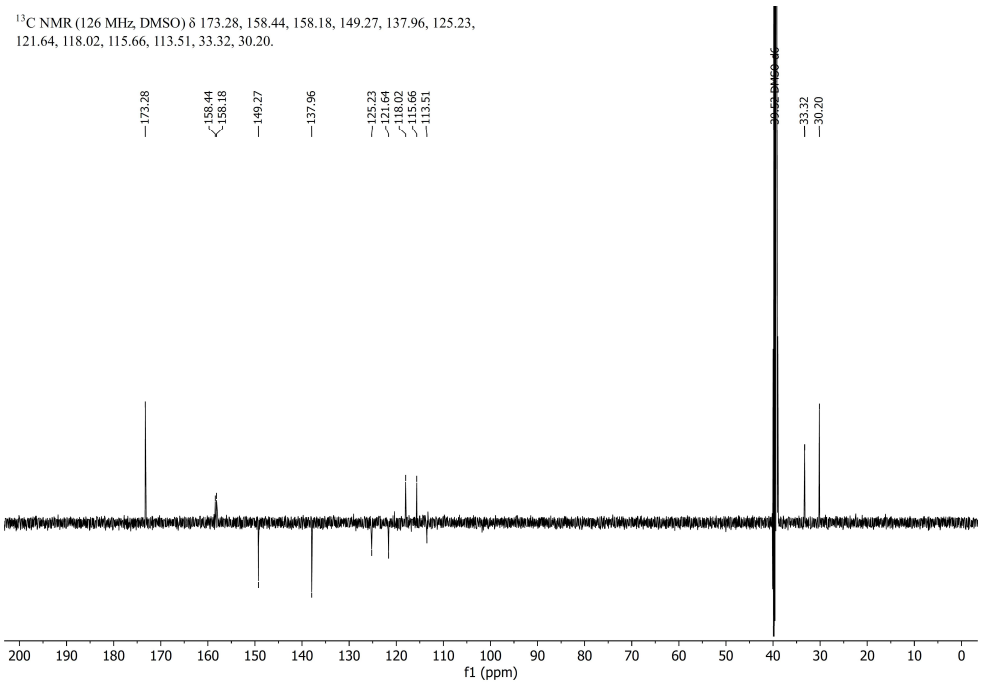

Figure V.40 ^{13}C-APT-NMR of **7** in DMSO-d_6.

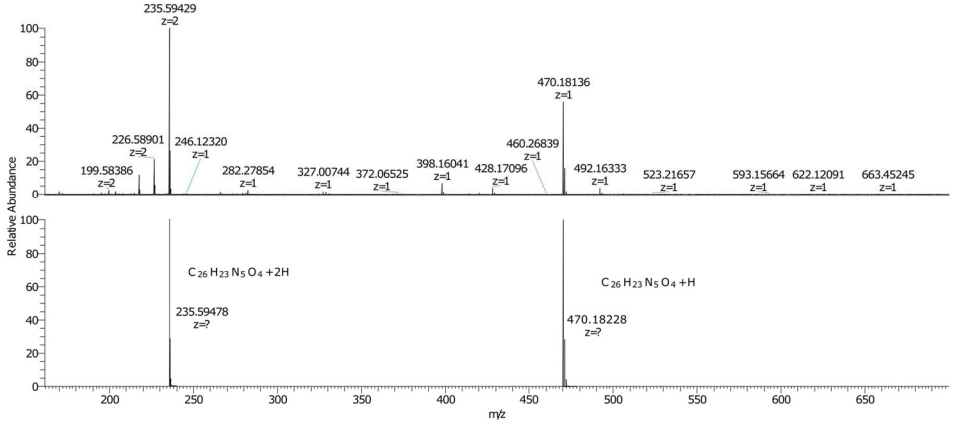

Figure V.41 ESI-HRMS of **7**. Calculated for $[C_{26}H_{23}N_5O_4 + H^+]^+$: 470.1823 m/z and $[C_{26}H_{23}N_5O_4 + 2H^+]^{2+}$: 235.5948 m/z.

V.4.12 6-bromide-5-methyl-2,2'-bipyridine, 17b

^{1}H NMR (400 MHz, $CDCl_3$) δ 8.64 (ddd, J = 4.8, 1.9, 1.0 Hz, 1H), 8.37 (dt, J = 8.0, 1.1 Hz, 1H), 8.27 (d, J = 7.7 Hz, 1H), 7.80 (td, J = 7.7, 1.8 Hz, 1H), 7.63 (dd, J = 7.8, 0.9 Hz, 1H), 7.30 (ddd, J = 7.5, 4.8, 1.2 Hz, 1H), 2.44 (s, 3H).

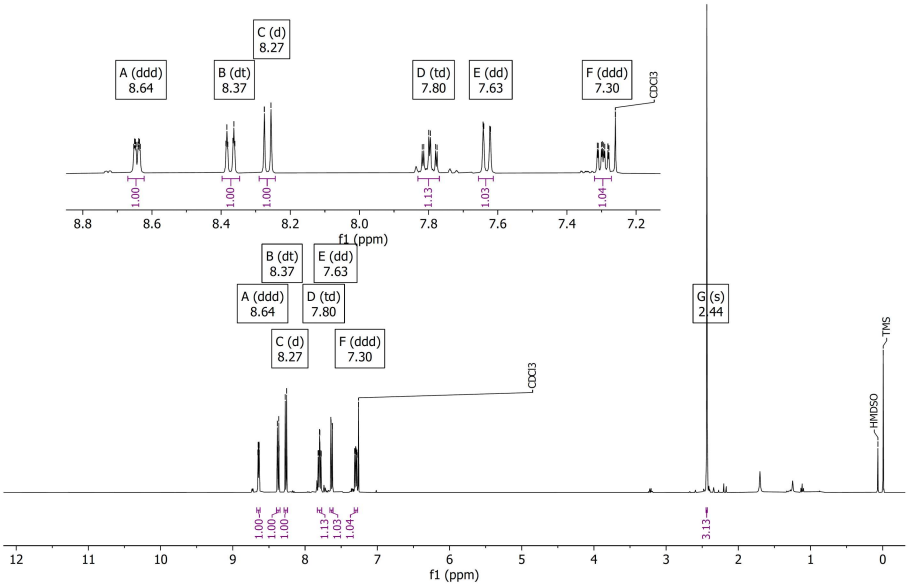

Figure V.42 ^{1}H-NMR of **17b** in $CDCl_3$.

^{13}C NMR (101 MHz, $CDCl_3$) δ 154.82, 154.76, 149.26, 144.20, 139.72, 137.11, 135.30, 124.06, 121.34, 119.99, 22.10.

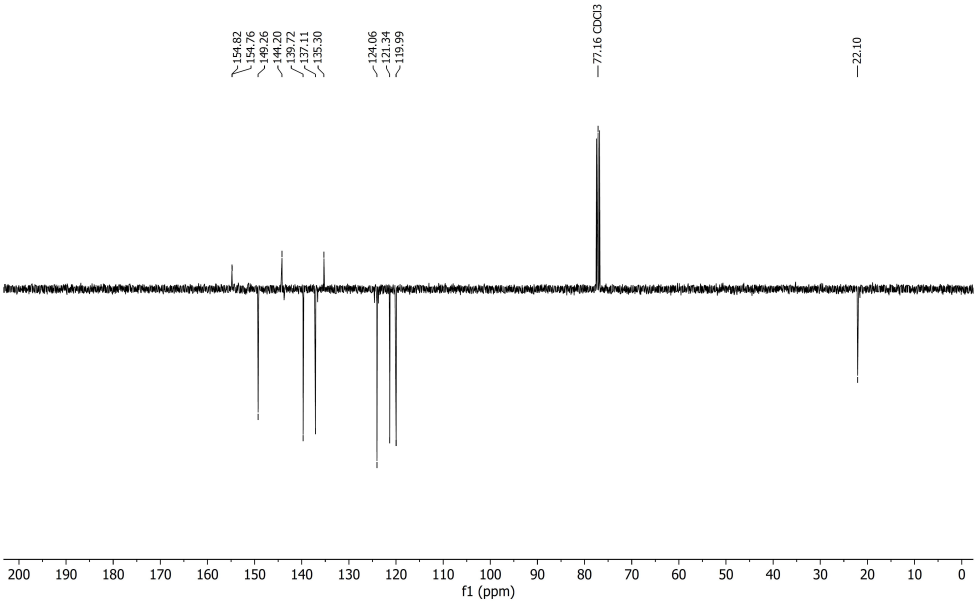

Figure V.43 ^{13}C-APT-NMR of **17b** in $CDCl_3$.

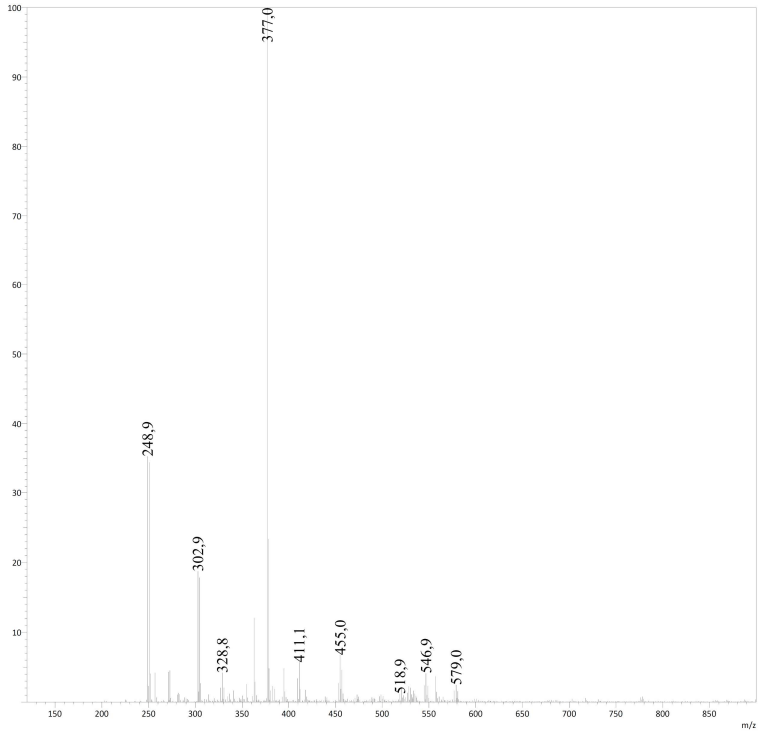

Figure V.44 ESI-MS of **17b**. Calculated for [$C_{11}H_9BrN_2$ + H^+]: 249.0 m/z.

V.4.13 Bis(5-methyl-[2,2'-bipyridin]-6-yl)amine, 18

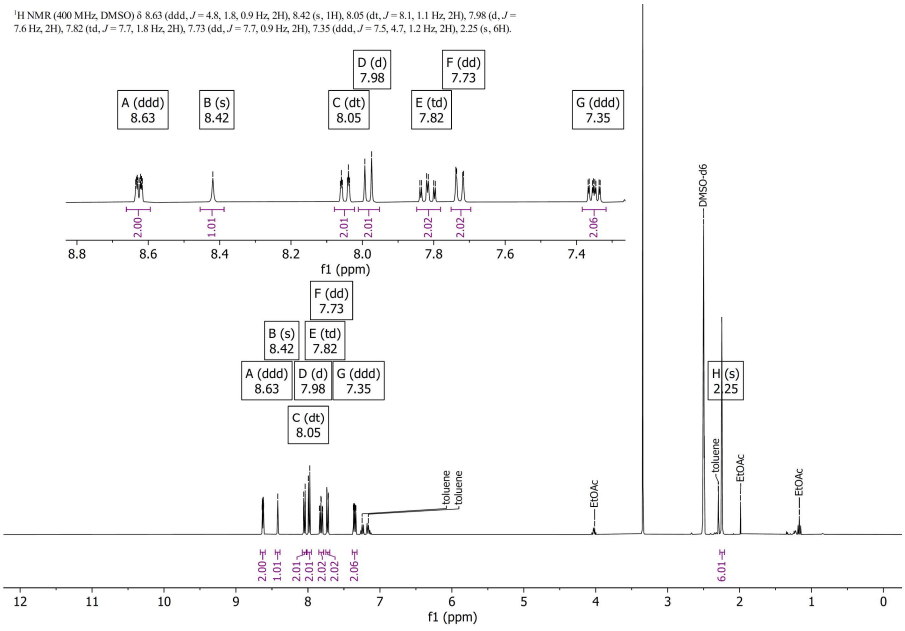

Figure V.45 ^{1}H-NMR of **18** in DMSO-d_6.

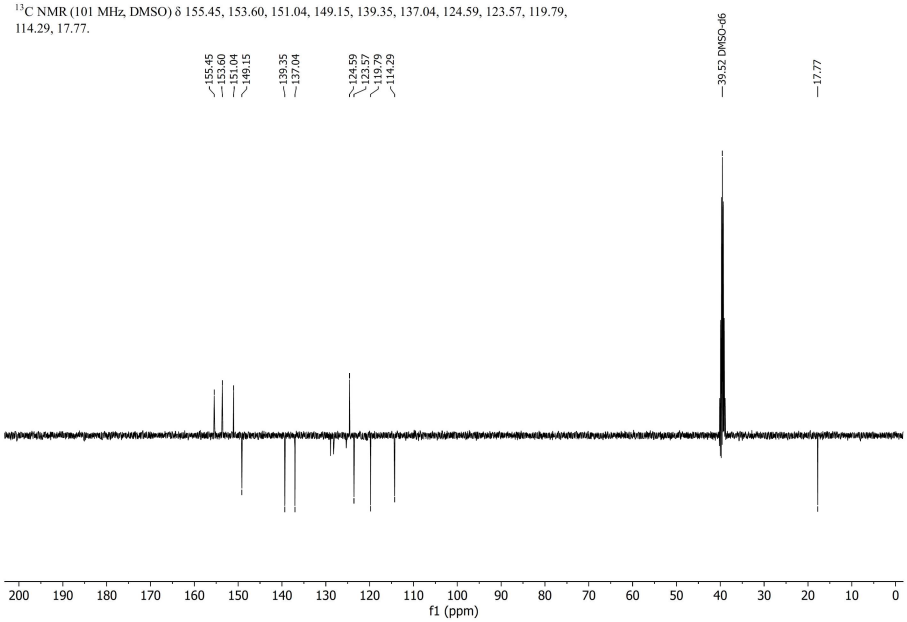

Figure V.46 ^{13}C-APT-NMR of **18** in DMSO-d_6.

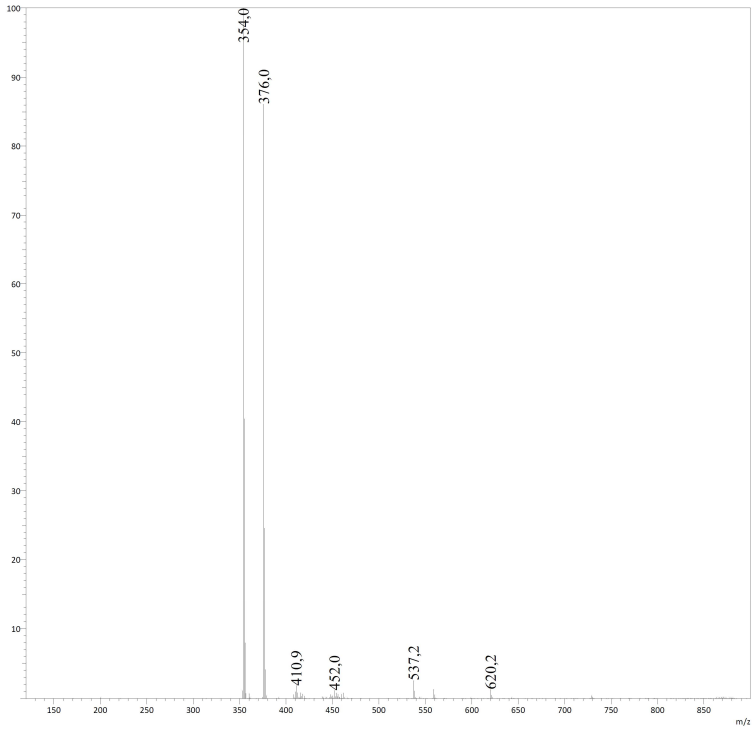

Figure V.47 ESI-MS of **18**. Calculated for $[C_{22}H_{19}N_5 + H^+]^+$: 354.2 m/z.

V

V.4.14 Bis(5'-methyl-[2,2'-bipyridin]-6-yl)amine, 19

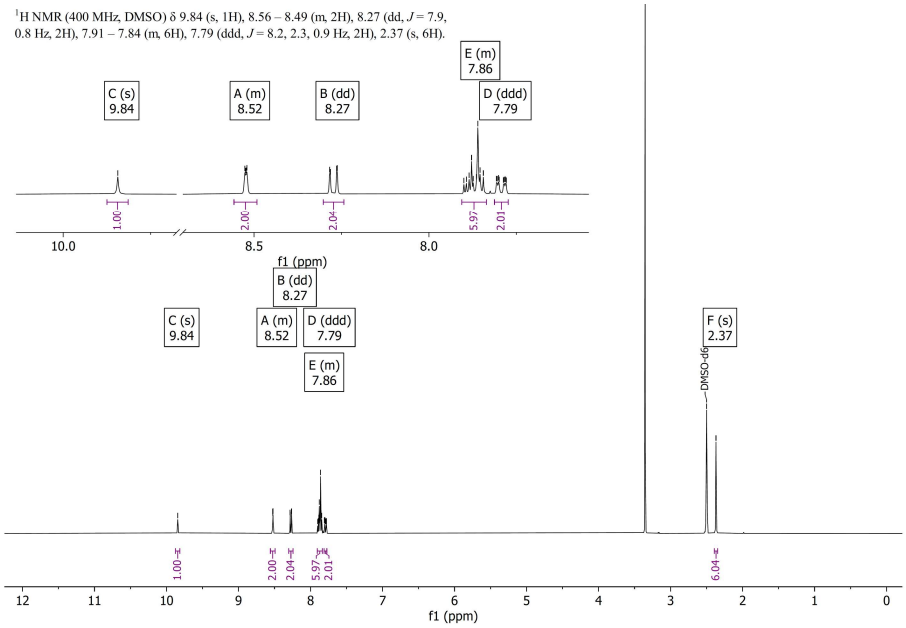

Figure V.48 ^{1}H-NMR of **19** in DMSO-d_6.

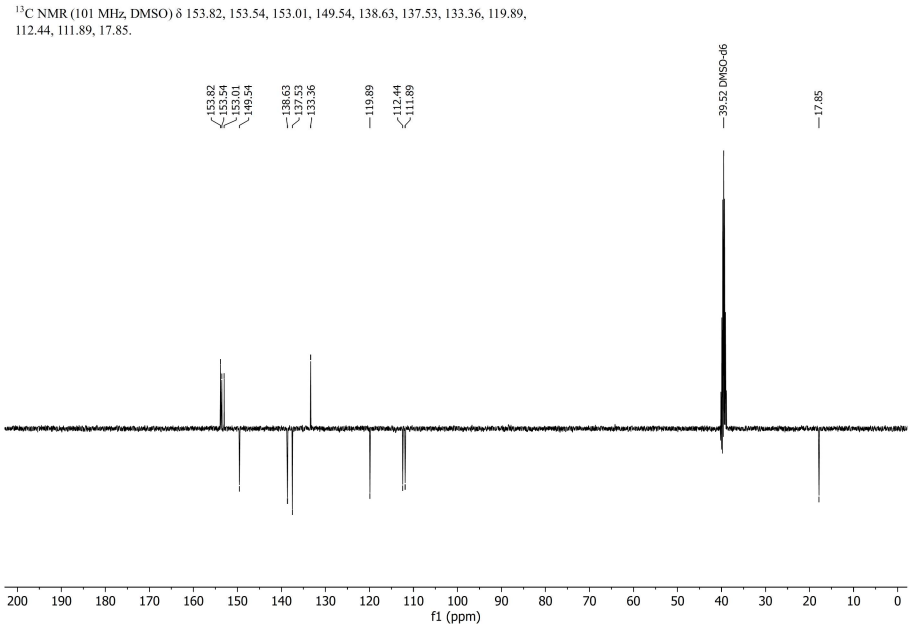

Figure V.49 ^{13}C-APT-NMR of **19** in DMSO-d_6.

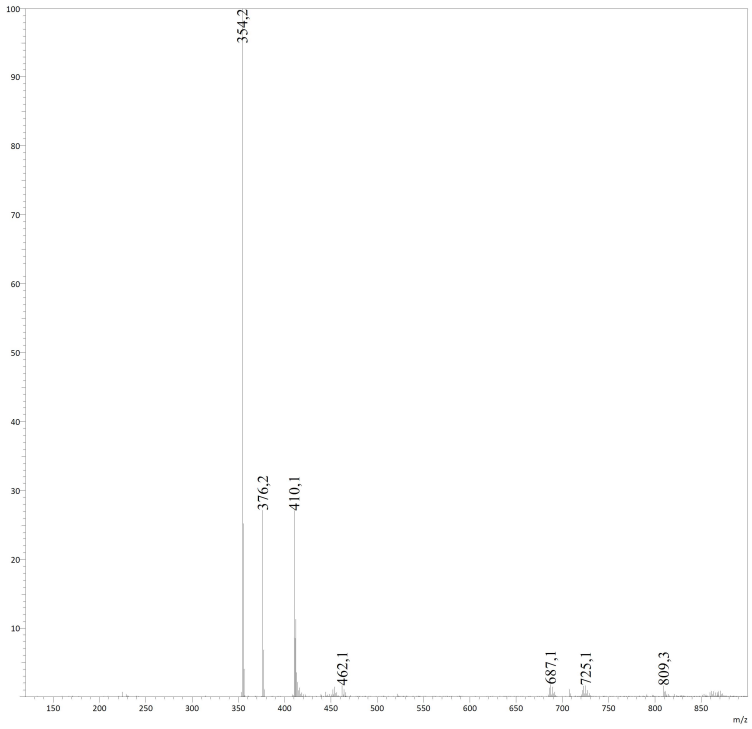

Figure V.50 ESI-MS of **19**. Calculated for $[C_{22}H_{19}N_5 + H^+]^+$: 354.2 m/z.

V.4.15 Bis(5'-methyl-[2,2'-bipyridin]-6-yl)-*N*-methylamine, 20

^{1}H NMR (400 MHz, DMSO) δ 8.51 (dt, *J* = 2.4, 0.9 Hz, 2H), 8.20 (dd, *J* = 7.9, 0.8 Hz, 2H), 7.96 (dd, *J* = 7.5, 0.8 Hz, 2H), 7.82 (dd, *J* = 8.2, 7.5 Hz, 2H), 7.74 (ddd, *J* = 8.1, 2.3, 0.8 Hz, 2H), 7.37 (dd, *J* = 8.2, 0.8 Hz, 2H), 3.73 (s, 3H), 2.35 (s, 6H).

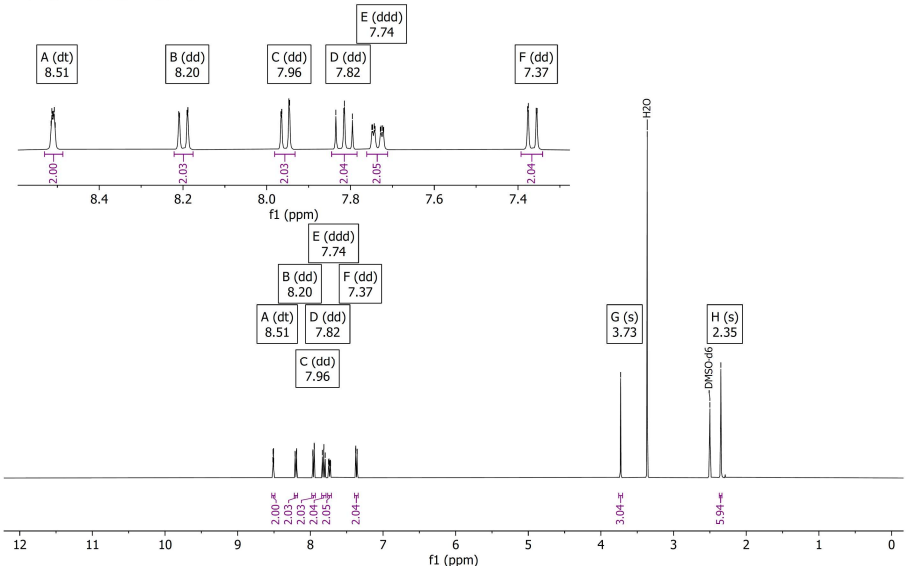

Figure V.51 ^{1}H-NMR of **20** in DMSO-d_6.

^{13}C NMR (101 MHz, DMSO) δ 156.43, 153.62, 152.85, 149.51, 138.47, 137.55, 133.46, 119.89, 114.18, 113.29, 35.62, 17.86.

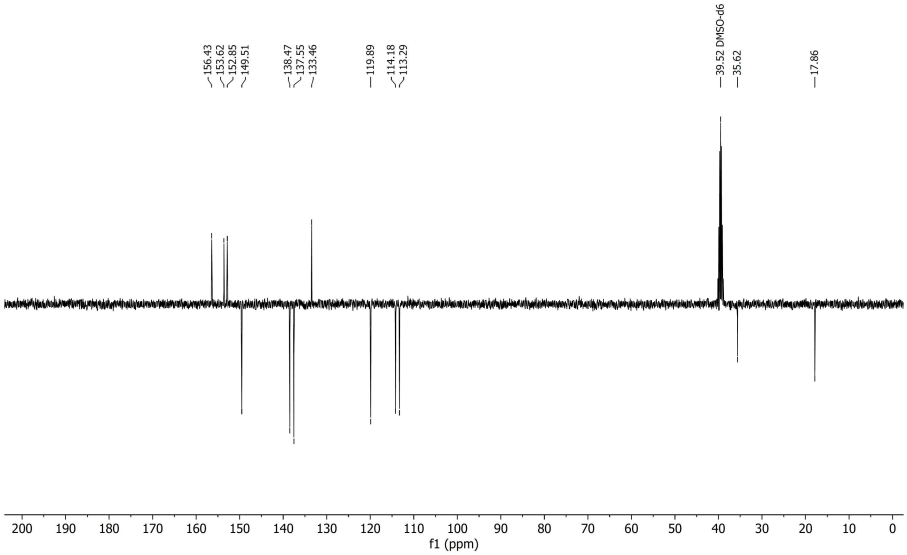

Figure V.52 ^{13}C-APT-NMR of **20** in DMSO-d_6.

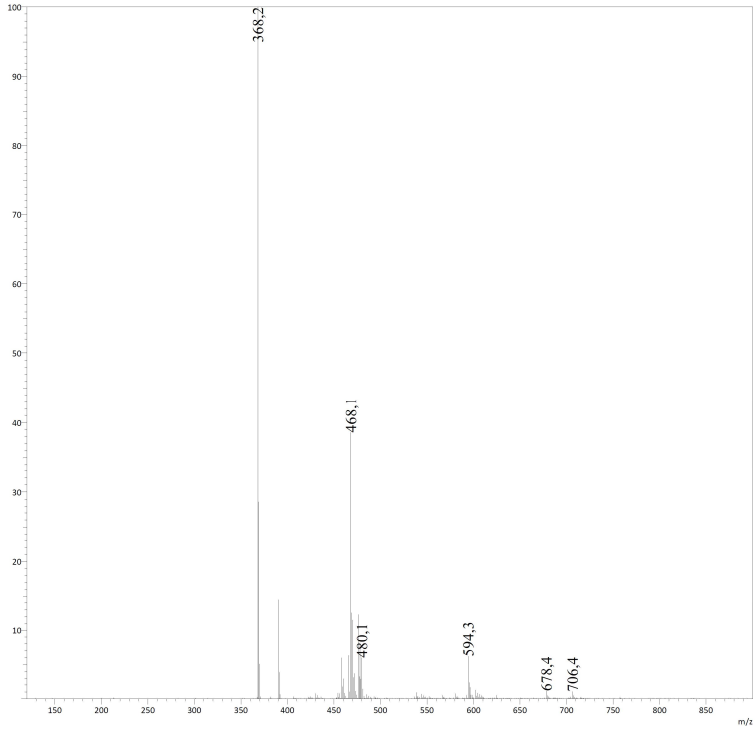

Figure V.53 ESI-MS of **20**. Calculated for $[C_{23}H_{21}N_5 + H]^+$: 368.2 m/z.

V.4.16 Compound 21

^{1}H NMR (400 MHz, $CDCl_3$) δ 8.53 (d, J = 1.5 Hz, 2H), 8.31 (dd, J = 8.1, 0.8 Hz, 2H), 8.00 – 7.95 (m, 2H), 7.71 – 7.62 (m, 4H), 7.28 (dd, J = 8.3, 0.8 Hz, 2H), 4.14 (q, J = 7.1 Hz, 4H), 3.82 (s, 3H), 3.01 (t, J = 7.6 Hz, 4H), 2.67 (t, J = 7.6 Hz, 3H), 1.27 – 1.23 (m, 9H).

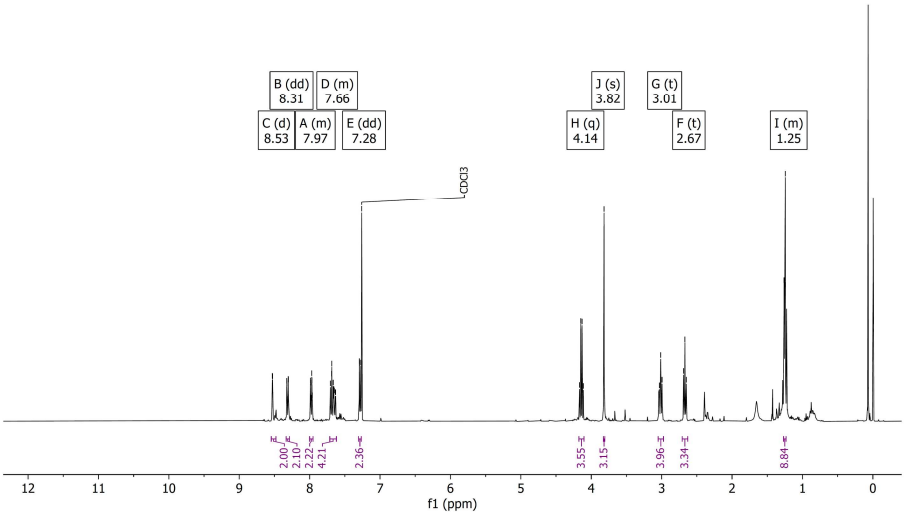

Figure V.51 ^{1}H-NMR of **21** in DMSO-d_6.

^{13}C NMR (101 MHz, $CDCl_3$) δ 172.54, 157.18, 154.78, 154.39, 149.22, 138.10, 136.87, 136.01, 120.92, 114.38, 113.87, 60.79, 36.03, 35.59, 28.12, 14.35.

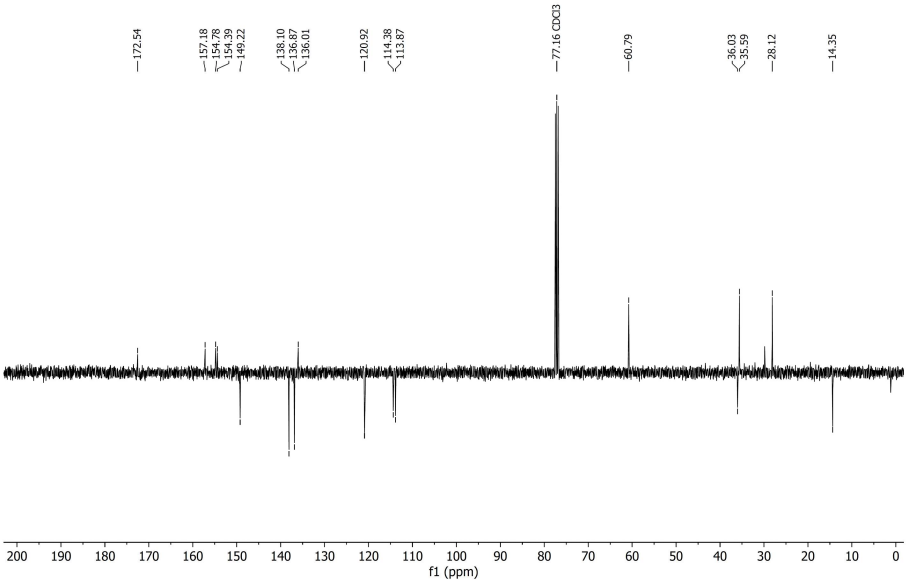

Figure V.52 ^{13}C-APT-NMR of **21** in DMSO-d_6.

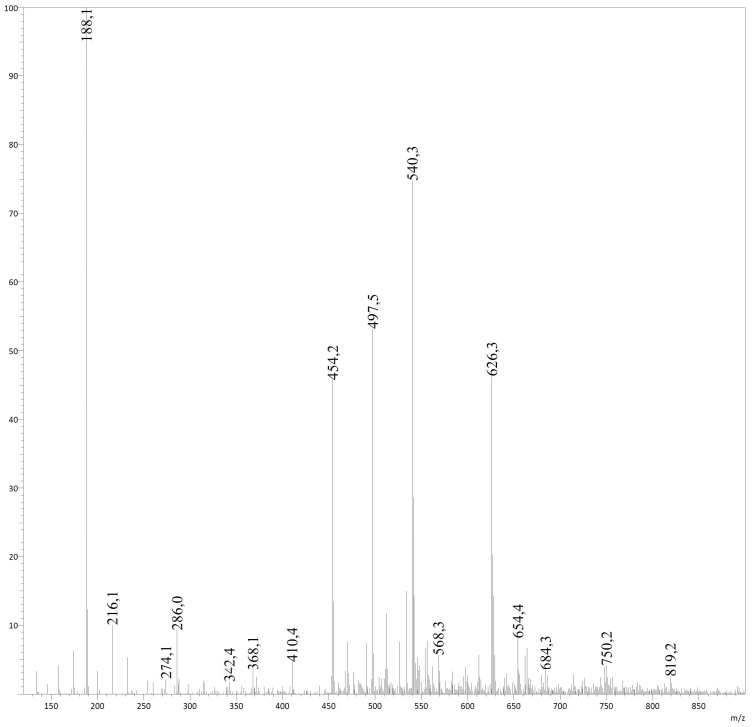

Figure V.53 ESI-MS of **21**. Calculated for $[C_{31}H_{33}N_5O_4 + H]^+$: 540.3 m/z

V.4.17 $[Ru(Mebbpya)(QC82)_2]^{2+}$, $[24]^{2+}$:

^{1}H NMR (400 MHz, Acetone) δ 9.98 (ddd, *J* = 5.6, 1.5, 0.7 Hz, 2H), 8.69 (dt, *J* = 8.0, 1.1 Hz, 2H), 8.41 (dd, *J* = 7.9, 0.9 Hz, 2H), 8.30 – 8.17 (m, 4H), 7.99 – 7.89 (m, 4H), 6.94 (t, *J* = 1.4 Hz, 2H), 6.69 (t, *J* = 1.6 Hz, 2H), 6.06 (t, *J* = 1.5 Hz, 2H), 4.89 (s, 4H), 4.18 (s, 3H), 1.93 (q, *J* = 3.2 Hz, 6H), 1.74 – 1.57 (m, 25H).

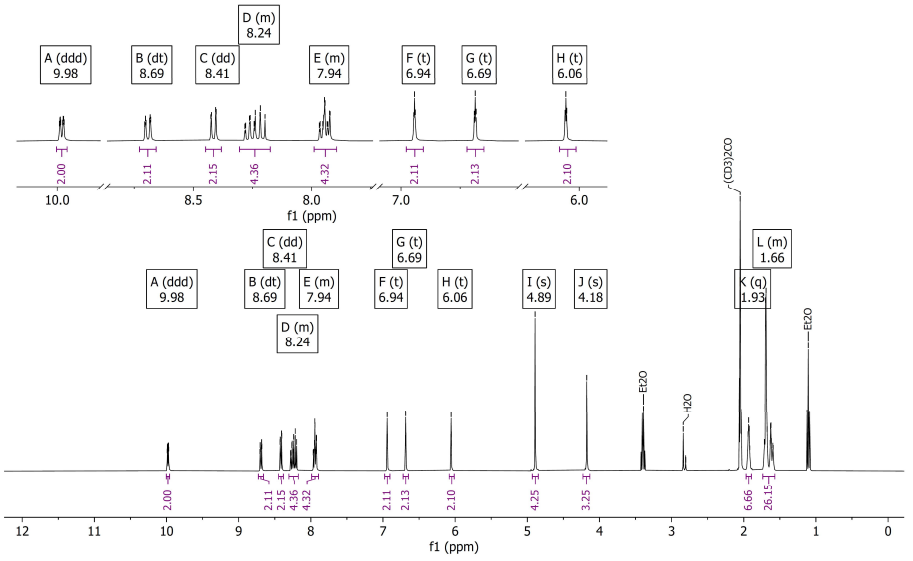

Figure V.54 ^{1}H-NMR of [**24**]$(PF_6)_2$ in Acetone-d_6.

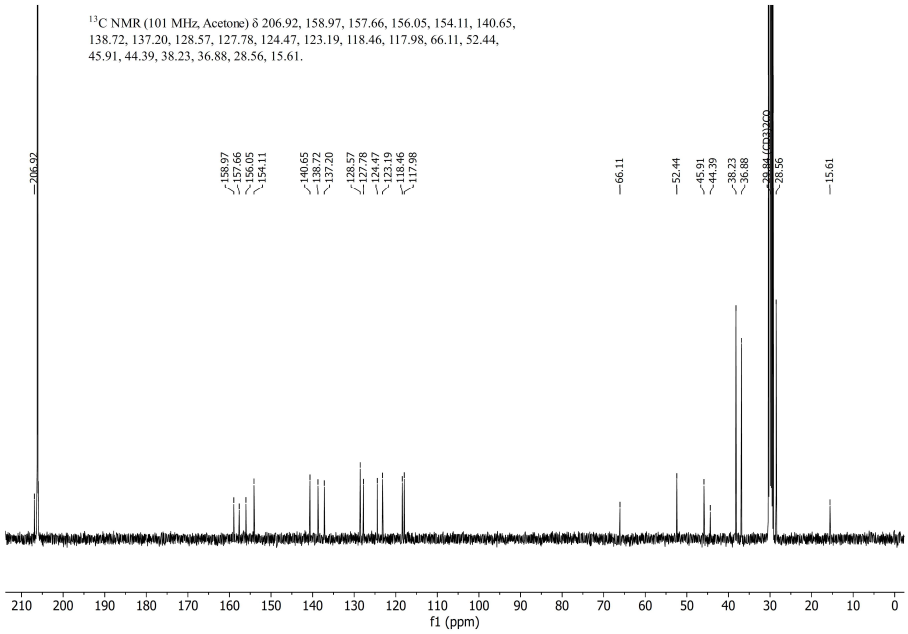

Figure V.55 ^{13}C-NMR of [**24**](PF$_6$)$_2$ in Acetone-d_6.

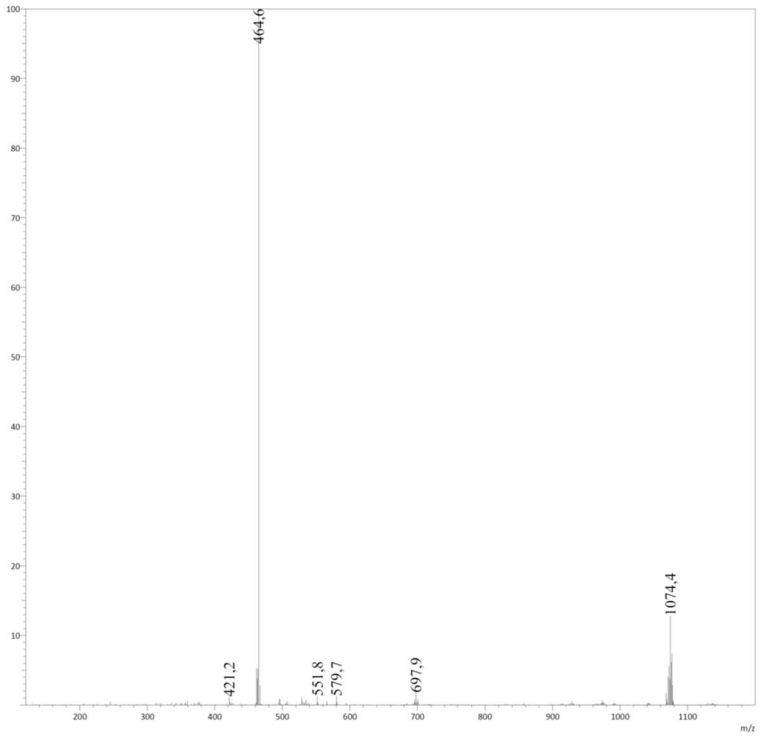

Figure V.56 ESI-MS of [**24**](PF$_6$)$_2$. Calculated for $[C_{51}H_{57}N_9O_2Ru]^{2+}$: 464.7 m/z.

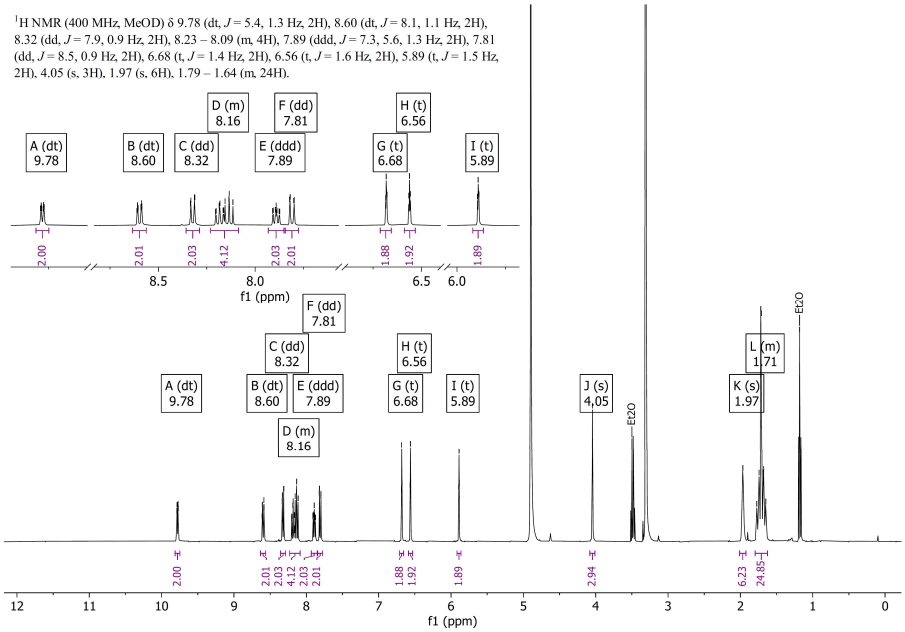

Figure V.57 ^{1}H-NMR of [**24**]Cl_2 in Methanol-d_4.

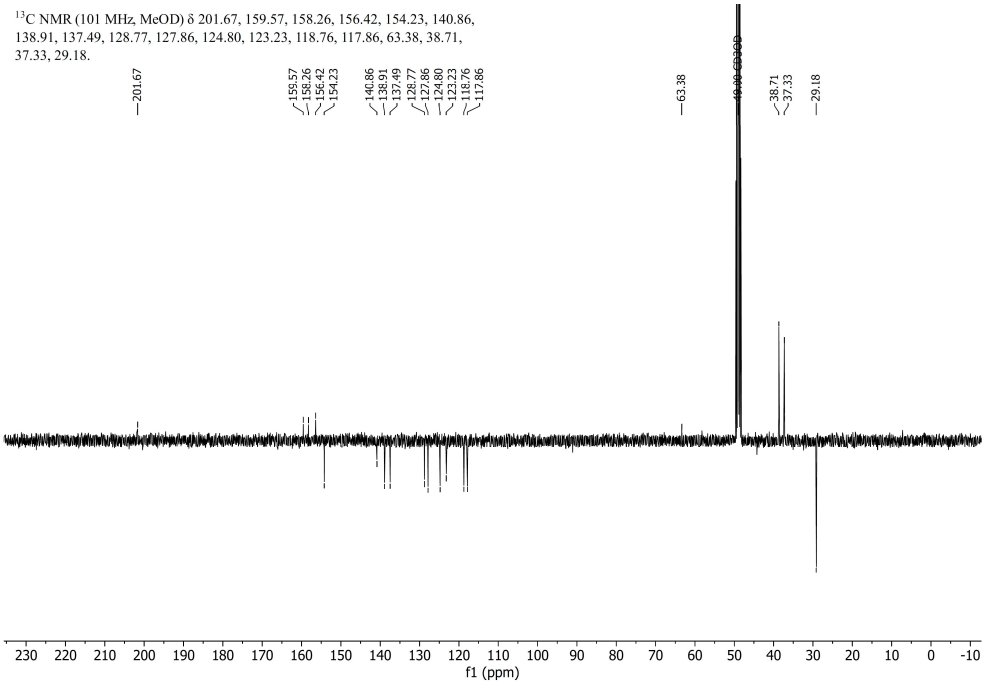

Figure V.58 ^{13}C-APT-NMR of [**24**]Cl_2 in Methanol-d_4.

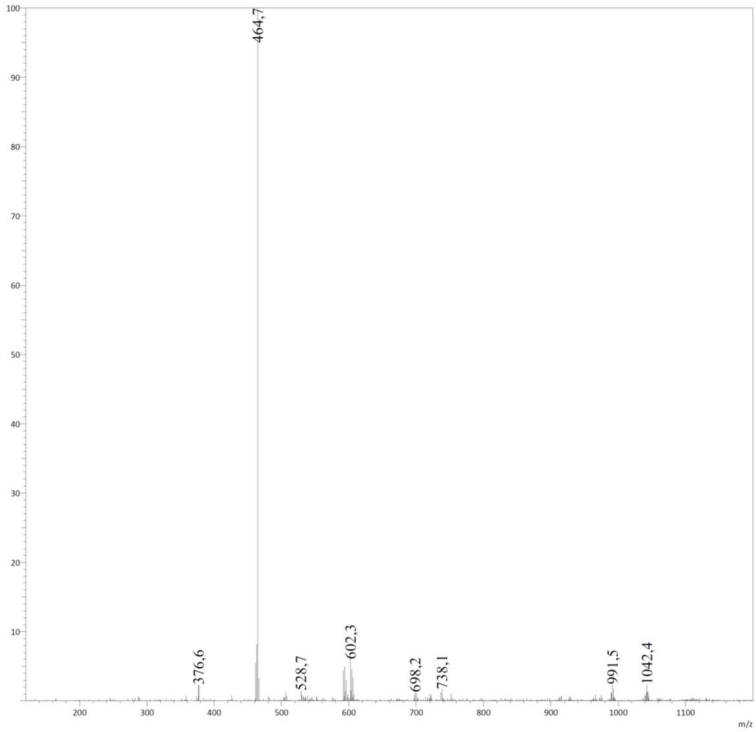

Figure V.59 ESI-MS of [**24**]Cl_2. Calculated for $[C_{51}H_{57}N_9O_2Ru]^{2+}$: 464.7 m/z.

V.4.18 [Ru(Mebbpya)(QC82)(STF-31)]$^{2+}$, [25]$^{2+}$:

^{1}H NMR (850 MHz, Acetone) δ 10.04 (dd, *J* = 5.0, 0.8 Hz, 2H), 9.50 (s, 1H), 8.72 (td, *J* = 7.0, 1.6 Hz, 3H), 8.46 (d, *J* = 7.3 Hz, 2H), 8.30 (td, *J* = 7.7, 1.4 Hz, 2H), 8.27 (dd, *J* = 8.5, 7.6 Hz, 2H), 8.04 (dd, *J* = 8.6, 0.9 Hz, 2H), 8.02 (ddd, *J* = 7.3, 5.5, 1.3 Hz, 2H), 7.77 – 7.75 (m, 2H), 7.70 (d, *J* = 7.7 Hz, 4H), 7.59 (dd, *J* = 8.5, 1.9 Hz, 2H), 7.40 (d, *J* = 8.4 Hz, 2H), 7.05 – 7.00 (m, 2H), 6.93 (t, *J* = 1.4 Hz, 1H), 6.68 (t, *J* = 1.6 Hz, 1H), 6.03 (t, *J* = 1.6 Hz, 1H), 4.88 (s, 2H), 4.25 (s, 3H), 4.20 – 4.17 (m, 2H), 1.94 (d, *J* = 3.2 Hz, 3H), 1.73 – 1.68 (m, 9H), 1.64 – 1.60 (m, 4H), 1.33 (s, 9H).

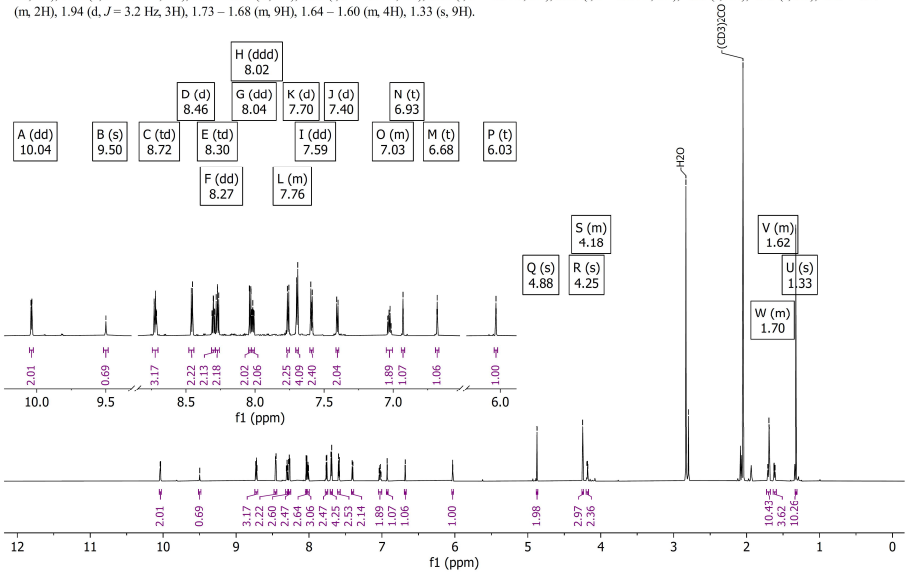

Figure V.60 ^{1}H-NMR of [**25**]$(PF_6)_2$ in Acetone-d_6.

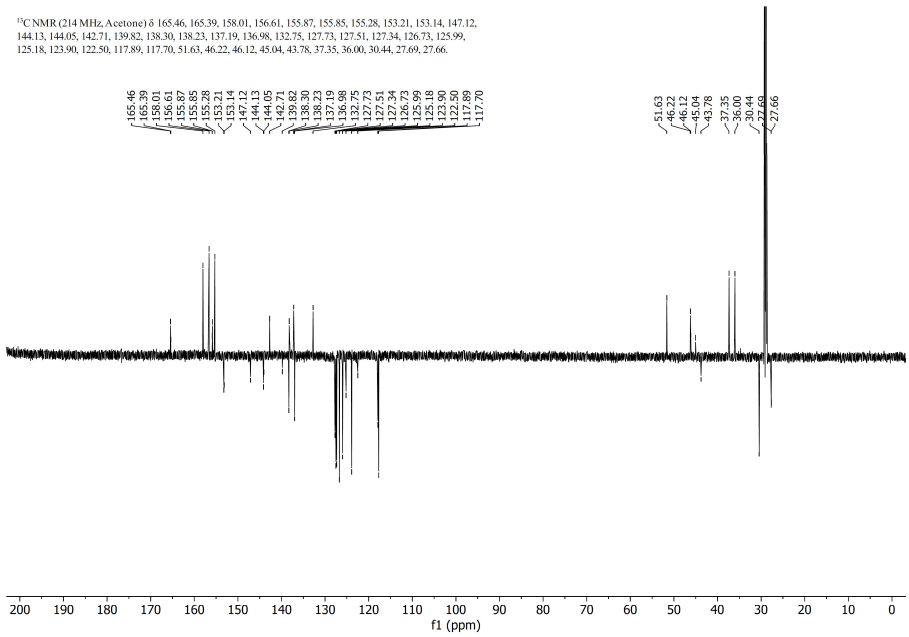

Figure V.61 ^{13}C-NMR of [**25**](PF$_6$)$_2$ in Acetone-d_6.

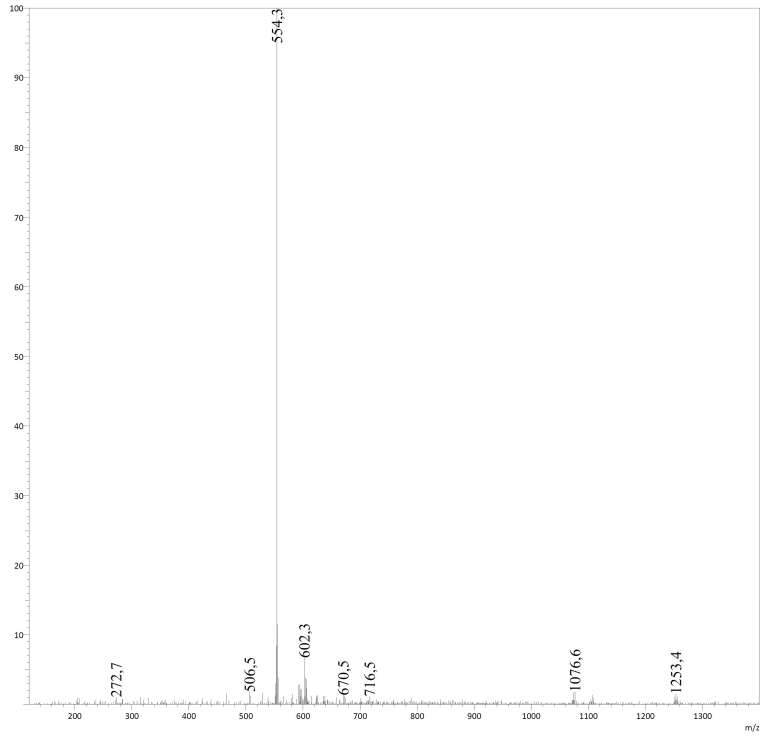

Figure V.62 ESI-MS of [**25**](PF$_6$)$_2$. Calculated for $[C_{59}H_{62}N_{10}O_4RuS]^{2+}$: 554.2 m/z.

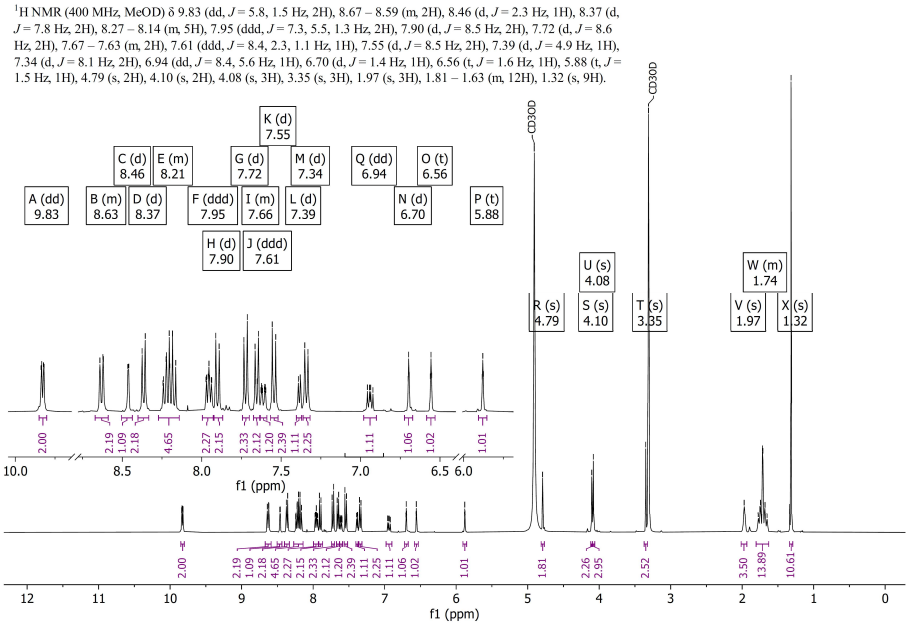

Figure V.63 ^{1}H-NMR of [**25**]Cl_2 in Methanol-d_4.

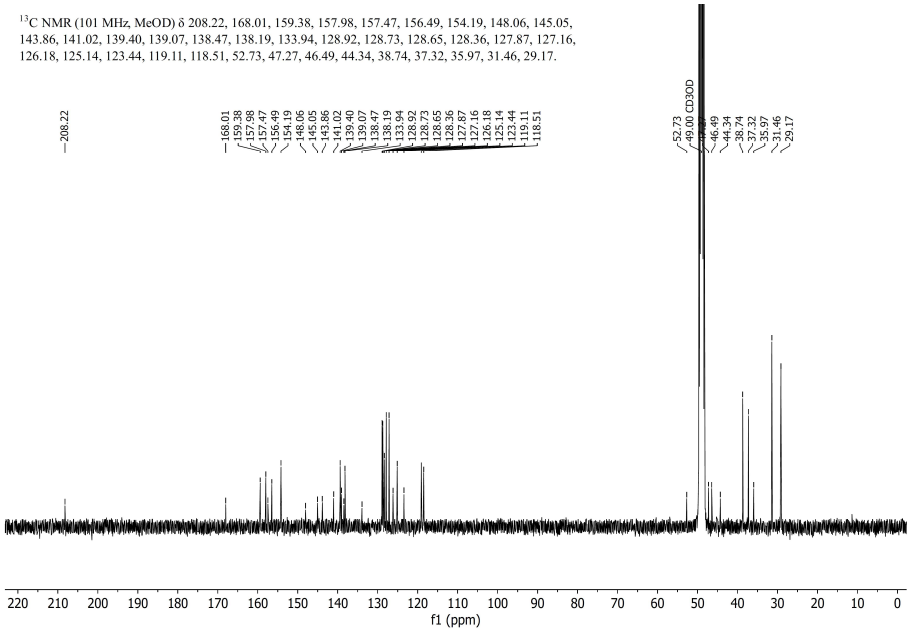

Figure V.64 ^{13}C-NMR of [**25**]Cl_2 in Methanol-d_4.

V

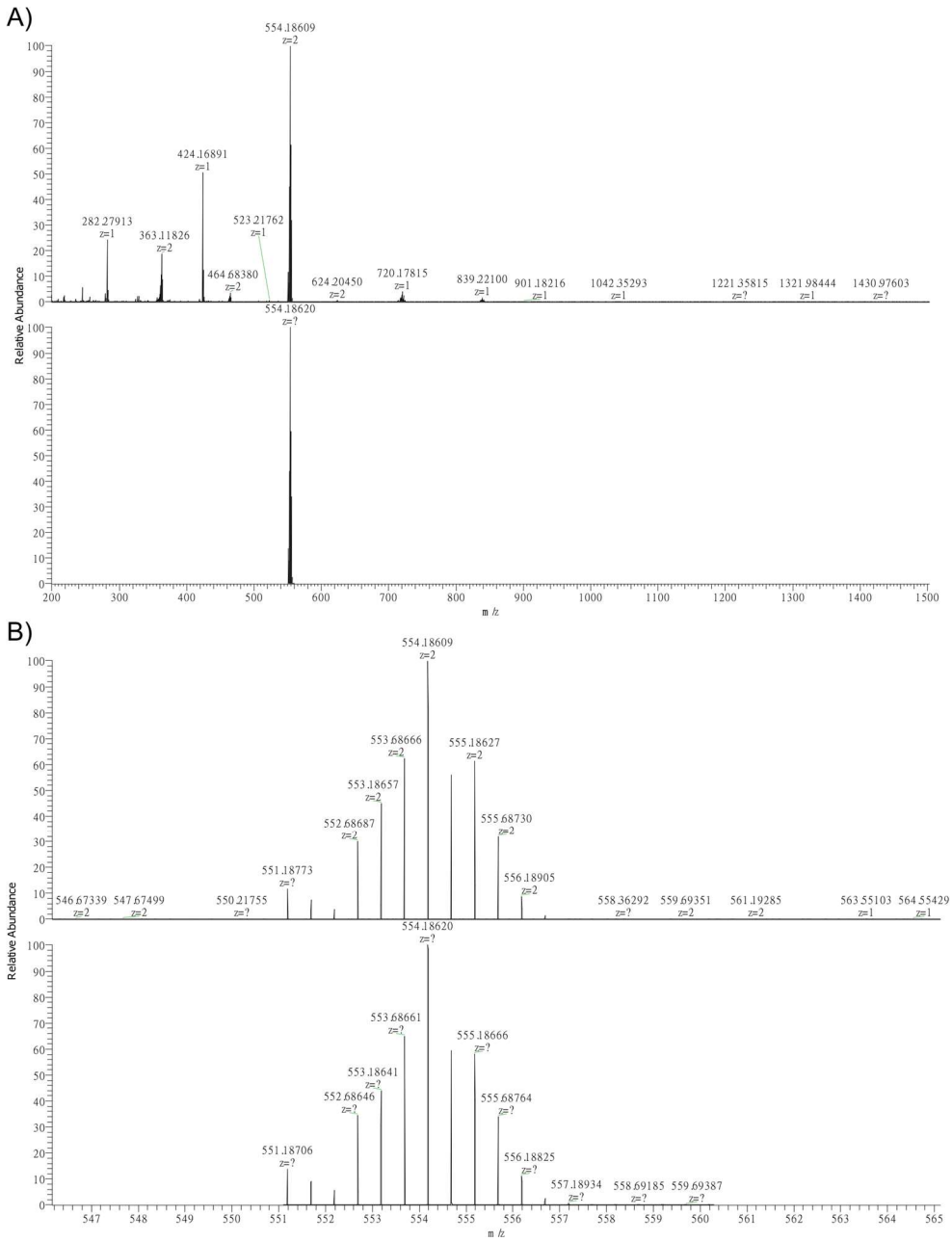

Figure V.65 ESI-HRMS of [**25**]Cl_2. Calculated for $[C_{59}H_{62}N_{10}O_4RuS]^{2+}$: 554.1862 m/z. Mass spectrum shown with range 200-1500 m/z (a) and 546-565 m/z (b).

V.4.19 [Ru(Mebbpya)(QC82)(Py)]$^{2+}$, [26]$^{2+}$:

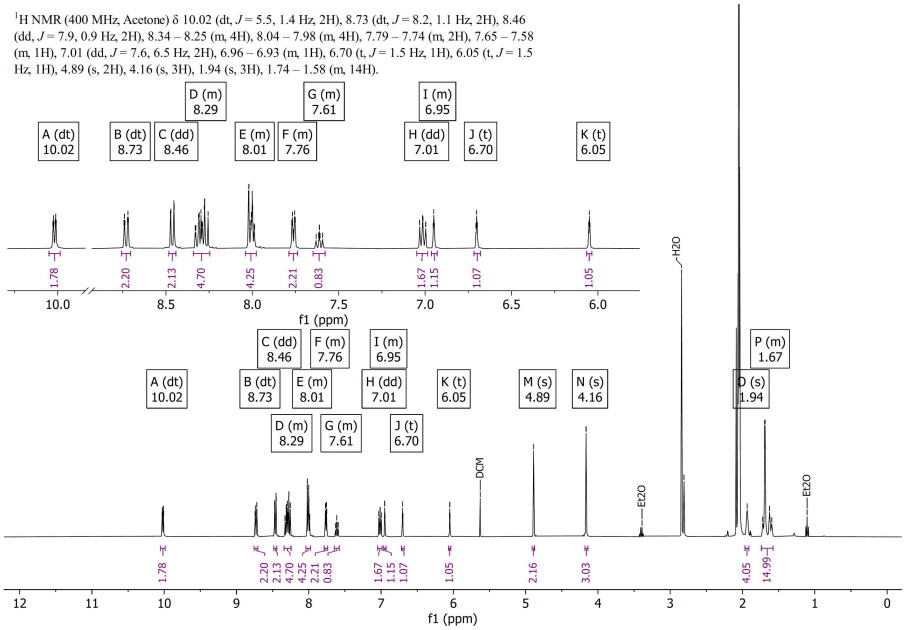

Figure V.66 ^{1}H-NMR of [**26**](PF$_6$)$_2$ in Acetone-d_6.

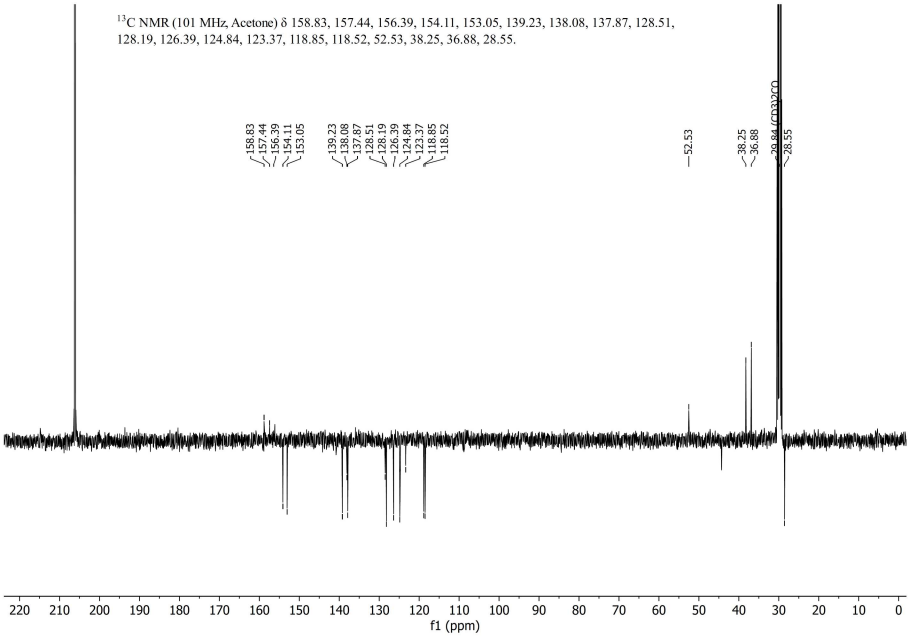

Figure V.67 ^{13}C-NMR of [**26**](PF$_6$)$_2$ in Acetone-d_6.

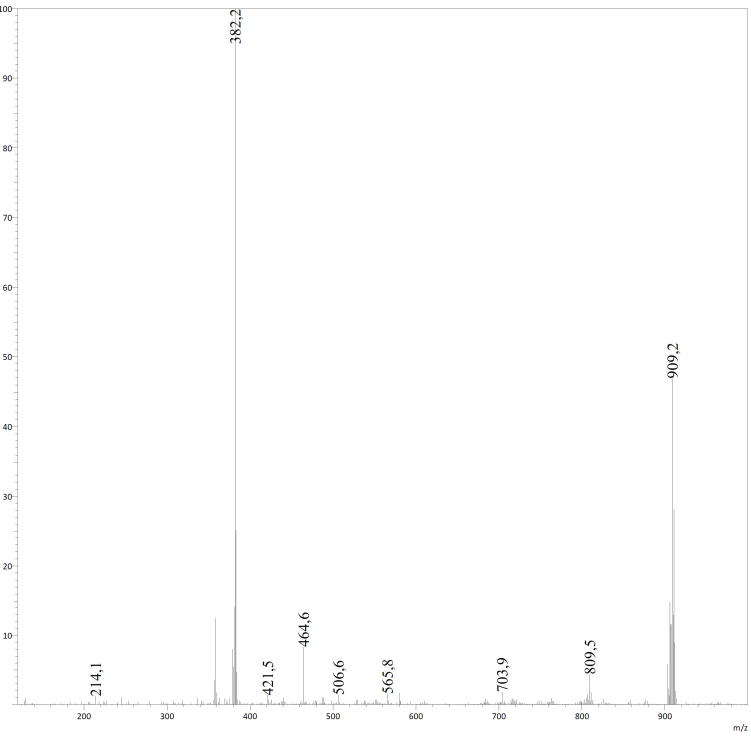

Figure V.68 ESI-MS of [**26**]$(PF_6)_2$. Calculated for $[C_{41}H_{42}N_8ORu]^{2+}$: 382.1 m/z

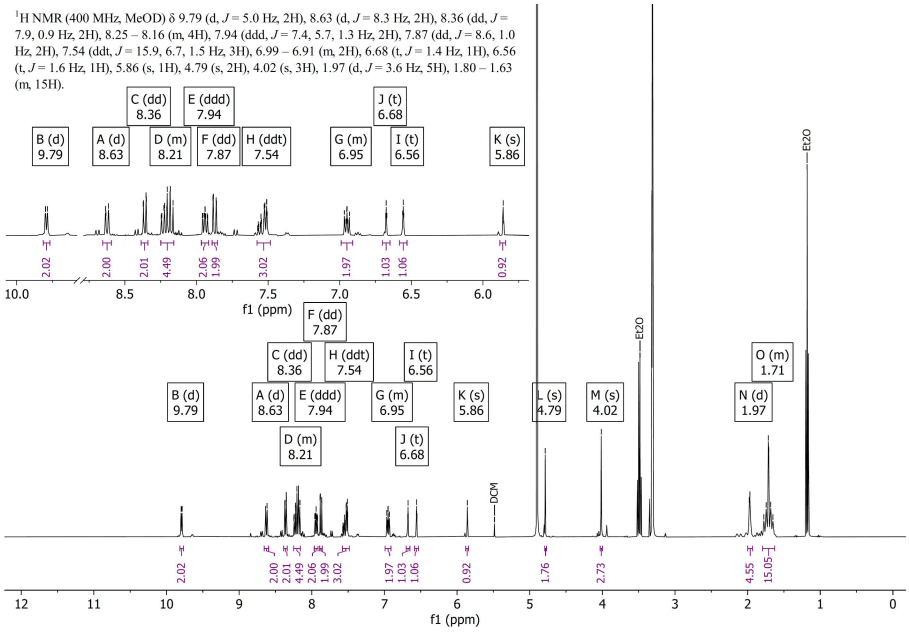

Figure V.69 ¹H-NMR of [**26**]Cl_2 in Methanol-d_4.

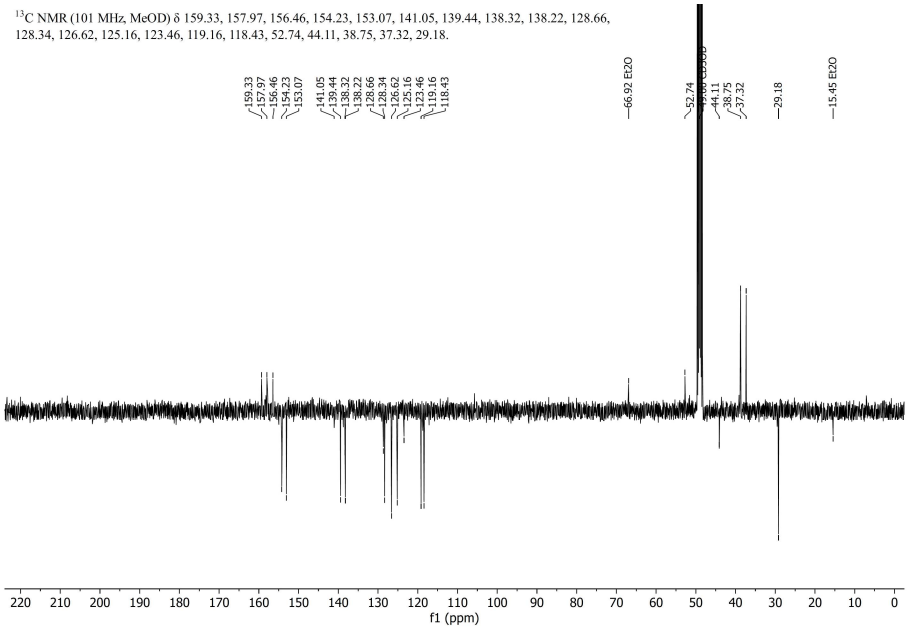

Figure V.70 ^{13}C-APT-NMR of [**26**]Cl_2 in Methanol-d_4.

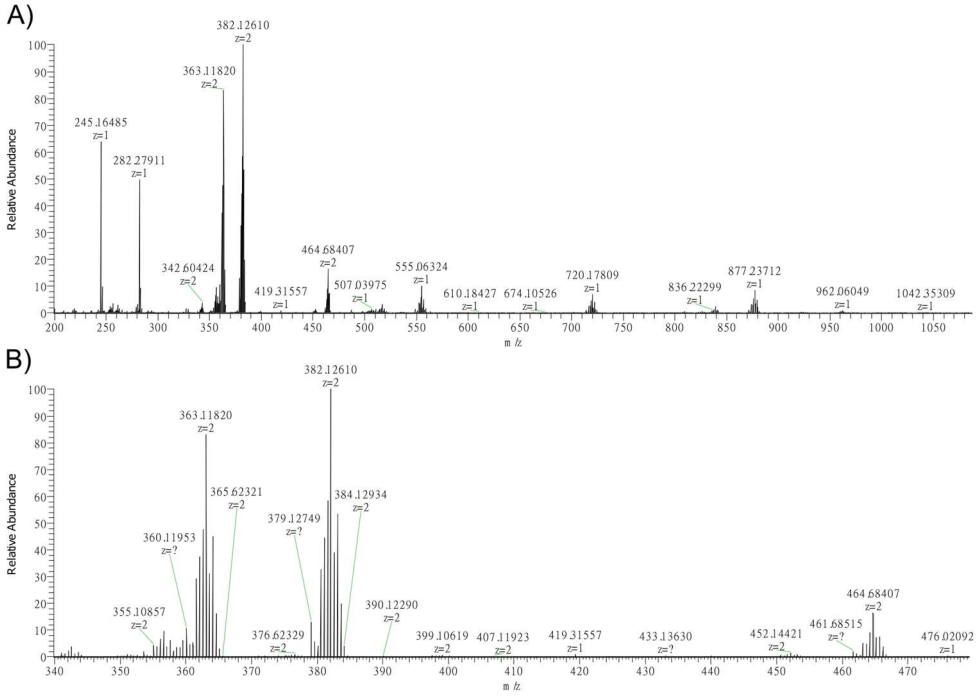

Figure V.71 ESI-MS of [**26**]Cl_2. Calculated for $[C_{41}H_{42}N_8ORu]^{2+}$: 382.1257 m/z. Mass spectrum shown with range 200-1100 m/z (a) and 340-480 m/z (b).